Effects of Coarse Aggregate Morphological Characteristics on Mechanical Performance of Stone Matrix Asphalt

Yufeng Liu

Dissertation submitted to the faculty of the Virginia Polytechnic Institute and State University in partial fulfillment of the requirements for the degree of

Doctor of Philosophy
In
Civil Engineering

Linbing Wang, Chair
Joseph E. Dove
Reza Mirzaeifar
David Mokarem

May 16th, 2017

Blacksburg, Virginia

Keywords: Improved Fourier Transform Interferometry (FTI) system, Stone Matrix Asphalt (SMA), aggregate morphological characteristics, mechanical properties, discrete element modeling

Effects of Coarse Aggregate Morphological Characteristics on Mechanical Performance of Stone Matrix Asphalt

Yufeng Liu

ABSTRACT

This research focused on three main objectives: (1) quantify coarse aggregate morphological characteristics using an improved FTI (Fourier Transform Interferometry) image analysis system, (2) evaluate the effects of morphological characteristics of coarse aggregates of various mineral compositions on the mechanical performances of stone matrix asphalt (SMA) mixtures constituted; (3) investigate the relationship between the uncompacted void content of coarse aggregates and morphological characteristics. To achieve the first research objective, a Fourier Transform Interferometry (FTI) system was adopted to capture three-dimensional high-resolution images of aggregates. Based on these digital images, the FTI system uses the two-dimensional Fast Fourier Transform (FFT2) method to rapidly measure aggregate morphological characteristics, including sphericity, flatness ratio, elongation ratio, angularity, and surface texture. The computed shape characteristics of all aggregates were in good agreement with manual measurement results, demonstrating the accuracy and reliability of this image analysis system. For the second objective, a series of simple performance laboratory tests were performed on eight types of SMA mixtures with different morphological characteristics. Test included wheel-track loading, dynamic modulus, flow number, and beam fatigue. The wheel tracking test included asphalt pavement analyzer (APA) and Model mobile load simulator (MMLS). In the APA test, samples included eight types of SMA mixtures that consisted of aggregates of 22 fractions. In the MMLS test, six types of SMA mixture samples that consist of coarse aggregate of 15 fractions were tested. Regression analyses were then conducted between weighted mean morphological characteristics and performance parameters. The fatigue performance parameters include $|E^*|\sin\varphi$, where $|E^*|$ is complex modulus obtained from dynamic modulus test, the number of loading cycles to failure, and the seismic modulus difference. The rutting performance parameters include $|E^*|/\sin\varphi$, flow number, flow number slope, rut depth and creep slope. For the third objective, different coarse aggregate fractions from different quarries in Virginia were analyzed using the improved FTI system. Regression analyses were performed to investigate the correlation between morphological characteristics and uncompacted void content of coarse aggregates at the size ranges of 4.75-9.5mm and 9.5-12.5 mm, respectively. Aggregate morphological characteristics were found to play an important role in the mechanical performance of stone matrix asphalt mixture and the uncompacted air void content of the coarse aggregates. Both the experimental results and simulation results demonstrated that using more of equi-dimensional, less flaky and elongated coarse aggregates with angular and rougher-textured aggregates is favorable to the mechanical performances of SMA mixtures. Recommended values for each morphological characteristic are provided.

Effects of Coarse Aggregate Morphological Characteristics on Mechanical Performance of Stone Matrix Asphalt

Yufeng Liu

GENERAL AUDIENCE ABSTRACT

Asphalt concrete pavement is used in roads around the world. Keeping this pavement in working condition requires routine maintenance, which can be costly. Therefore, a key problem in civil engineering is the design of resilient asphalt concrete that requires less maintenance. This dissertation experimentally investigates the relationship between the composition of asphalt concrete and its performance. To determine the relationship, several samples of asphalt concrete were collected. Aggregates from these samples were then scanned, and software was used to determine the properties of these aggregates. These asphalt concrete samples were then experimentally tested to determine their mechanical properties. A relationship was then established between the software-determined properties of the aggregates and the mechanical properties of the asphalt concrete samples.

ACKNOWLEDGEMENTS

I would like to sincerely thank my advisor, Dr. Linbing Wang, for his valuable guidance and continuous encouragement and support though my Ph. D study. He has kept me motivated and helped me overcome the challenges of my Ph.D.

I would like to thank Dr. Joseph E. Dove, Dr. Reza Mirzaeifar and Dr. David Mokarem for serving as my committee members and for their valuable suggestions.

I would like to thank my family. Their continuous support and encouragement make me move forward.

I would like to thank my friends and all the staff at Virginia Tech. They make Virginia Tech a happy and relaxing place to study.

This research reported here was a collaboration between Virginia Tech and the Virginia Transportation Research Council (01468785). I would like to express my gratitude for the generous help and strong support given by Dr. Wenjuan Sun, Dr. Harikrishnan Nair and Mr. D. Stephen Lane.

Table of Contents

LIST OF FIGURES

LIST OF TABLES

CHAPTER 1 INTRODUCTION

Problem Statement

Hot-mix asphalt (HMA) concrete is composed of up to approximately 90%-95% mineral aggregates by weight and up to 80% to 90% aggregates by volume. The mineral aggregate plays a vital role in mechanical performances of asphalt concrete and asphalt pavement. Depending on the aggregate gradation, asphalt concrete mixtures can be classified as dense graded, coarse graded, or stone mastic asphalt (SMA). SMA is a gap-graded HMA with high concentrations of coarse aggregate and high asphalt content. There is a common consensus among pavement engineers that mechanical performance of asphalt mixtures such as fatigue and rutting will be greatly improved by the selection of coarse aggregates with appropriate morphological characteristics. Selection of aggregates with proper morphological properties is essential in mix design. Aggregate morphological characteristics, including sphericity, flatness ratio, elongation ratio, angularity, and texture, have been recognized as major factors influencing mechanical performances of both aggregates and asphalt mixture. The quantification of aggregate morphological characteristics becomes essential to measure the aggregate geometric irregularity. Advanced imaging technology with computer-automated system becomes a promising tool that is capable to directly measure aggregate morphological characteristics with good accuracy at high speed. Mechanical performances of SMA mixtures can be measured by laboratory experiments, such as simple performance tests and wheel tracking tests. Regression analysis can be performed to link the measured mechanical performances of SMA mixtures and the measured aggregate morphological characteristics. Based on the regression results, we can better understand the effect of aggregate morphology on the performance of asphalt mixtures, for achieving long-term pavement performances at a low life-cycle cost.

Research Objectives

The main objective of this project is to evaluate the effects of coarse aggregate morphological characteristics on the mechanical performances of SMA mixtures, to provide more comprehensive understanding of the effects of coarse aggregate morphology on the performance of asphalt pavements in Virginia. In this study, the improved Fourier Transform Interferometry (FTI) system was adopted to measure aggregate morphological characteristics through high resolution images. In order to measure the mechanical behavior of SMA mixtures and effectively evaluate the rutting and fatigue performances of SMA mixtures, simple performance tests and wheel-tracking tests were performed. In this study, simple performance tests include dynamic modulus test, flow number test, and beam fatigue test; wheel-tracking tests include asphalt pavement analyzer (APA) test and model mobile load simulator (MMLS) test. The uncompacted void contents of coarse aggregates at different fractions were measured using a cylindrical metal measure with a diameter of 152 mm and a height of 160 mm. Specifically, the following work is conducted in this study.

1. Quantify coarse aggregate morphological characteristics, including sphericity, flatness ratio, elongation ratio, angularity and texture using the improved FTI image analysis system.
2. Perform simple performance tests, wheel-tracking tests, and uncompacted void content test to evaluate the performance potential of the SMA mixtures with different coarse aggregate

blends.

3. Correlate aggregate morphological characteristics captured by the improved FTI system with mechanical performance of SMA mixtures obtained from the laboratory performance-based tests.
4. Correlate aggregate morphological characteristics captured by the improved FTI system with the uncompacted void content of coarse aggregates.

Report Outline

This report is composed of eight chapters. Chapter 1 is the introduction, explaining motivations, objectives and research content of this project. Chapter 2 presents research background associated with measurement methods of aggregate morphological characteristics, and laboratory experiments for measuring mechanical performances of SMA mixtures. Chapter 3 presents the analysis method of the improved FTI image analysis system. Chapter 4 shows the materials and mixture design, such as volumetric mix design results of all SMA mixtures, with the discussion on the determination of aggregate sample size for statistical stable results and the validation of the shape characteristics measured using the improved FTI morphology by manual measurements via a caliper. Chapter 5 presents measurement results of dynamic modulus test, flow number test, beam fatigue test, APA test, MMLS test, and uncompacted void content. Chapter 6 presents the regression analysis results between all mechanical properties of SMA mixtures from laboratory experiments and aggregate morphological characteristics obtained from the improved FTI system. Chapter 7 presents the discrete element method (DEM) simulation of a series of axial compression tests. Finally, Chapter 8 summarizes research findings and conclusions of this study. Some of these contents are from three journal papers published. The first one is titled as “Quantification of aggregate morphologic characteristics as related to mechanical properties of asphalt concrete with Improved FTI system”, the second one is titled as “Quantification of aggregate morphologic characteristics with the correlation to uncompacted void content of coarse aggregates in Virginia”. The third one is titled as “Effect of coarse aggregate morphology on the mechanical properties of Stone Matrix Asphalt”. The MMLS test was done by Romaric Komedja.

CHAPTER 2 LITERATURE REVIEW

Introduction

Numerous studies have been conducted to characterize the morphological properties of aggregates and to analyze the effect of aggregate morphology on mechanical performances of asphalt mixtures and pavement. Mechanical performances of asphalt mixture can be measured using laboratory experiments, such as simple performance tests and wheel-tracking tests. With regard to the quantification of aggregate morphology, both direct and indirect methods have been used. Among these methods, imaging analysis techniques have been widely used as a promising tool to objectively and accurately quantify geometric characteristics (i.e., form, angularity, texture, etc.) of aggregates at high speed. To further identify the effects of aggregate morphological characteristics on mechanical performances of asphalt mixtures and pavements, numerous laboratory performance-based tests have been conducted to measure the mechanical behavior and assess the fatigue and rutting resistance ability of asphalt mixtures.

Methods for Measuring Aggregate Morphology

There are three types of measurement methods for the quantification of aggregate morphology: manual measurement method, image analysis method, and indirect measurement method. Manual measurement method uses a caliper to measure three dimensions of aggregates (ASTM D3398 2006) and a proportional caliper device to measure the flatness ratio and elongation ratio (ASTM D4791). Indirect measurement method determines the void content of uncompact aggregate samples to infer the angularity and texture of aggregates (ASTM D5821). However, manual measurement method and indirect measurement method are time-consuming, tedious, inaccurate, and subjective (Fletcher et al., 2003; Rao and Tutumluer, 2000).

Motivated by advancements in digital imaging techniques and the availability of cost-effective image processing software, image analysis techniques have been widely employed to effectively and accurately quantify aggregate morphological characteristics (Masad et al., 2000; Rao et al., 2001; Fletcher et al., 2003; Al-Rousan et al., 2007). Various mathematical algorithms and experimental setups have been developed to quantify the size, shape, angularity, surface texture, surface area, and volume of aggregates (Fernlund, 2005; Fletcher et al., 2003; Rao and Tutumluer, 2000; Sime and Ferguson, 2003; Wang et al., 2005). Image-processing techniques often determine aggregate morphological characteristics based on two-dimensional images, which cannot represent the three-dimensional characteristics accurately (Wang et al., 2005). Therefore, an improved FTI system, which was developed using the Fourier transform interferometry (FTI) system (Wang et al., 2005; Lally, 2010; Lally et al., 2010), is adopted to measure aggregate morphological properties, based on three-dimensional coordinates of aggregate surfaces that are determined from digital images. The reliability and accuracy of the FTI measurements, including sphericity, flatness ratio, elongation ratio, angularity, and texture, have been validated in previous research (Lally et al., 2010; Wang et al., 2012; Liu et al., 2016).

Effects of Aggregate Morphologies on HMA Performance

Aggregate morphological characteristics such as shape factors (i.e., sphericity, flatness ratio and elongation ratio), angularity and surface texture significantly affect physical properties and

mechanical performances of asphalt mixtures (Kandhal and Parker, 1998; Saeed et al. 2001; Meininger, 1998; Unal and Mimaroglu, 2014; Li, Y. et al 2015; Pan et al, 2006; Naidu et al, 2011; Wang et al; 2016; Francisco et al, 2016). Aggregate shape significantly influences mechanical properties (Krumbein, 1941; Akbuluta et al., 2011; Chen et al., 2005; Bessa et al., 2014), such as permanent deformation, fatigue and friction resistance. It was found that spherical particles are preferable for providing proper aggregate internal friction and improving rutting performance (Chen et al, 2013). Flat and elongated aggregates tend to break down and reduce the particle-to-particle interlock, which mostly contributes to mechanical properties of aggregate structure (Buchanan, 2000). In addition, because aggregate angularity is crucial for this interlocking effect, asphalt mixtures with angular aggregates exhibit stronger shear resistance than those without (Mahmoud 2005; Kim and Souza 2009; Souza, 2009). Aggregates with rougher surfaces promote interface adhesion between particles and asphalt binder, leading to better workability and fatigue performance of asphalt mixtures (Fletcher, 2002; Tutumluer et al, 2005; Bessa et al, 2014). In addition, angularity and surface texture of aggregates affect mutual interactions between aggregates and interactions of aggregates with stabilizers (i.e., asphalt, cement and lime) (Al-Rousan et al. 2006; Tafesse et al. 2013), playing a vital role in durability, rheological properties, bonding potential, and interlocking strength of cement concrete and asphalt concrete (Smith and Collis, 1993; Masad et al., 2001). In summary, it is preferable to have more equal-dimensional, rougher and more angular aggregates than flat and elongated aggregates in mix design for better mechanical performances. To quantitatively evaluate the influence of aggregate morphological characteristics on mechanical performances of asphalt mixtures, there have been some studies that linked shape properties by various imaging techniques with the performance of asphalt mixtures (Janoo, 1998; Rao et al., 2002; Masad et al., 2003; Little et al., 2003; Al-Rousan, 2005).

Laboratory Performance-based Tests for Measuring the Mechanical Performance of Asphalt Mixtures

Fatigue and rutting are the most common distresses that occur in asphalt mixtures. For SMA mixtures, rutting occurs early in service life. Numerous laboratory tests can be used to measure mechanical performances of asphalt mixture, such as simple performance tests such as the static creep test, dynamic modulus test, flow number test, indirect tensile test, beam fatigue test, Marshall stability test, and wheel tracking tests such as asphalt pavement analyzer (APA) test, model mobile load simulator (MMLS) test, Hamburg test, and accelerated pavement tests (Mohammad et al., 1999; Stiady et al., 2001; Pan, 2005; Huang et al., 2009; Prowell et al., 2009). Dynamic modulus test has been used widely for measurement of resilient modulus, which characterizes the elastic part of the stiffness of the asphalt mixture under repeated loading, therefore reflecting the stiffness of asphalt mixtures (Pan et al., 2005; Tutumluer, et al., 2005). Flow number test is also a popular simple performance test for measuring the rutting performance of asphalt mixtures, thereby assessing the resistance of the mixtures to permanent deformation (Pan, et al., 2006; Francisco et al., 2016). Beam fatigue test is a strain-controlled test to determine the fatigue life of asphalt mixtures subjected to repeated flexural bending until failure (Shu et al., 2008). In beam fatigue test, fatigue life is traditionally defined as the number of cycles corresponding to a 50% reduction of initial stiffness.

Wheel-tracking devices such as APA and MMLS have shown as promising testing methods for measuring the rutting and fatigue resistance ability of SMA mixtures. APA and MMLS are two important tools for simulating traffic and environmental conditions in field. APA is one of the most common and popular loaded wheel testers for evaluating the rutting resistance of HMA mixtures (VDOT, 2009). MMLS also has been used widely for effective evaluation of permanent deformation or rutting and fatigue failure of scaled asphalt concrete pavement (Walubita et al., 2000; Huang et al., 2016). Rut depth obtained from APA typically is indicative of permanent deformation on the pavement surface at high temperatures. On the other hand, the seismic modulus or stiffness difference obtained during MMLS trafficking using Portable Seismic Pavement Analyzer (PSPA) generally is a reliable indicator to evaluate fatigue life of SMA mixtures at intermediate and low temperatures.

In this research, dynamic modulus test, flow number test, beam fatigue test, APA test, and MMLS test were conducted on eight types of SMA mixtures that were used in Virginia highways. The performance obtained from those tests were correlated to the morphological characteristics of aggregates through regression analysis to quantify the influence of aggregate morphological characteristics on the performances of SMA mixtures in Virginia State.

CHAPTER 3 THE IMPROVED FTI IMAGE ANALYSIS SYETEM AND THE IMAGING-BASED MORPHOLOGICAL CHARACTERISTICS

Scanning Program for the Improved FTI System

The Improved FTI system

The Improved FTI system is capable to rapidly characterize aggregate morphologies. It is further improved based on the FTI system (Lally, 2010), which is also a three-dimensional (3-D) surface profilometer with a simple fiber optic coupler in order to form a Young's double-pinhole interferometer. The following improvements are made: (1) a new charge-coupled device (CCD) camera is used to replace the original CCD camera in the FTI system, improving the image resolution from 35.4 μm per pixel to 28.47 μm per pixel on the horizontal plane; (2) computational time per image has been greatly reduced via the application of new programs with a more user-friendly graphical interface.

The Improved FTI system can capture images in either single-particle mode or multiple-particle mode. Laser lights with wave lengths of 675 nm and 805 nm were input through the fiber optic switch. A 45°-angled mirror was used to reflect the fringe projection on the aggregate surface. A higher-resolution CCD camera was used to capture the aggregate surface image. The image was then analyzed through the Fourier transform method to reconstruct the surface profile of each aggregate based on the phases of the fringe pattern on the aggregate surface. The 3-D coordinates of the top surface of the aggregate can be obtained through three images: an image taken with visible light, and two images taken with laser lights of wavelengths of 675 and 805 nm, respectively. In the Improved FTI system, the image resolution in both x-axis and y-axis is 28.47μm per pixel, and the z-axis resolution is 20μm.

Figure 3.1 shows a picture of the Improved FTI aggregate imaging system. Additional details about the FTI system are available (Sun, et al, 2012; Wang, et al, 2012). The surface of the aggregate is represented by a matrix z(x, y), the elements of which represent the height of each coordinate pair (x, y) in the horizontal plane. With the improved image resolution, the output z(x, y) matrix changes from a 1,019×1,371 matrix in the FTI system to a 2448×2046 matrix in the Improved FTI system to represent more morphological details on aggregate surfaces.

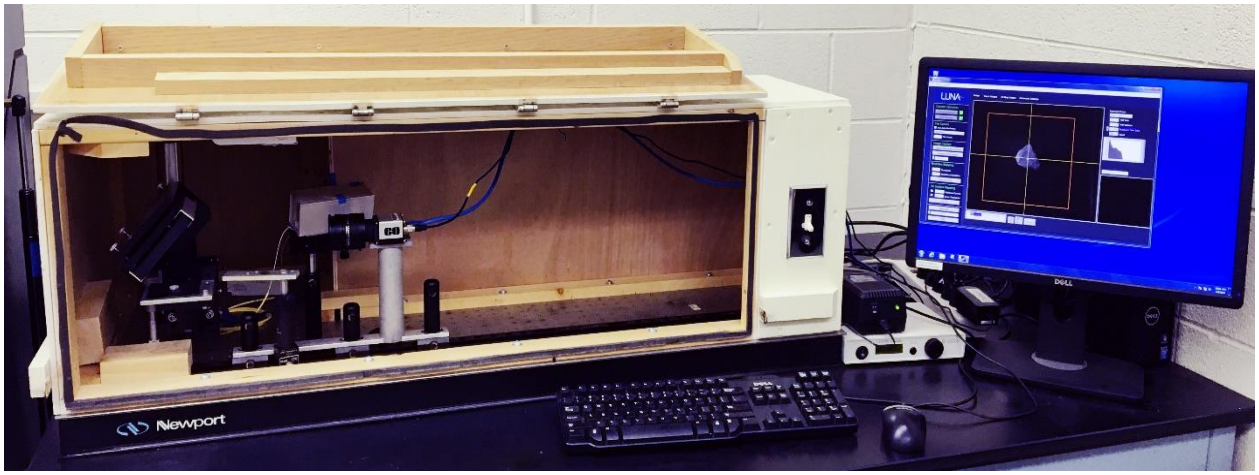

Figure 3.1 The Improved FTI image analysis system

Procedures for scanning

Aggregate samples selected for the study were scanned individually or collectively depending on their size. First, the fiber-optic switch was turned on. Then each aggregate was placed on the platform, where the height was adjusted initially. A clear image of an aggregate can be seen from the graphical user interface of the Improved FTI system. Aggregates were moved on the tray to adjust their positions so that they could be scanned with the best resolution in the Improved FTI software. Three images were taken separately to generate the 3-D coordinates for the surface of an aggregate: an image taken with white light, and two images taken with laser lights. The white light image was captured first, and then the fiber-optic switch was turned off, the two laser light images were captured under laser lights with the wavelength of 675 nm and 805 nm, respectively. Boundary mapping and surface mapping were formed sequentially, and then the 3-D contour plot of an aggregate surface can be output. The image of an aggregate can be output via the graphical user interface in the Improved FTI system. A MATLAB program will process the image to 3-D coordinates and use the 2-D Fourier transform method to analyze the 3-D coordinates for computing morphological characteristics. Figure 3.2 shows photos of the boundary mapping, surface mapping, and 3-D contour plot of an aggregate.

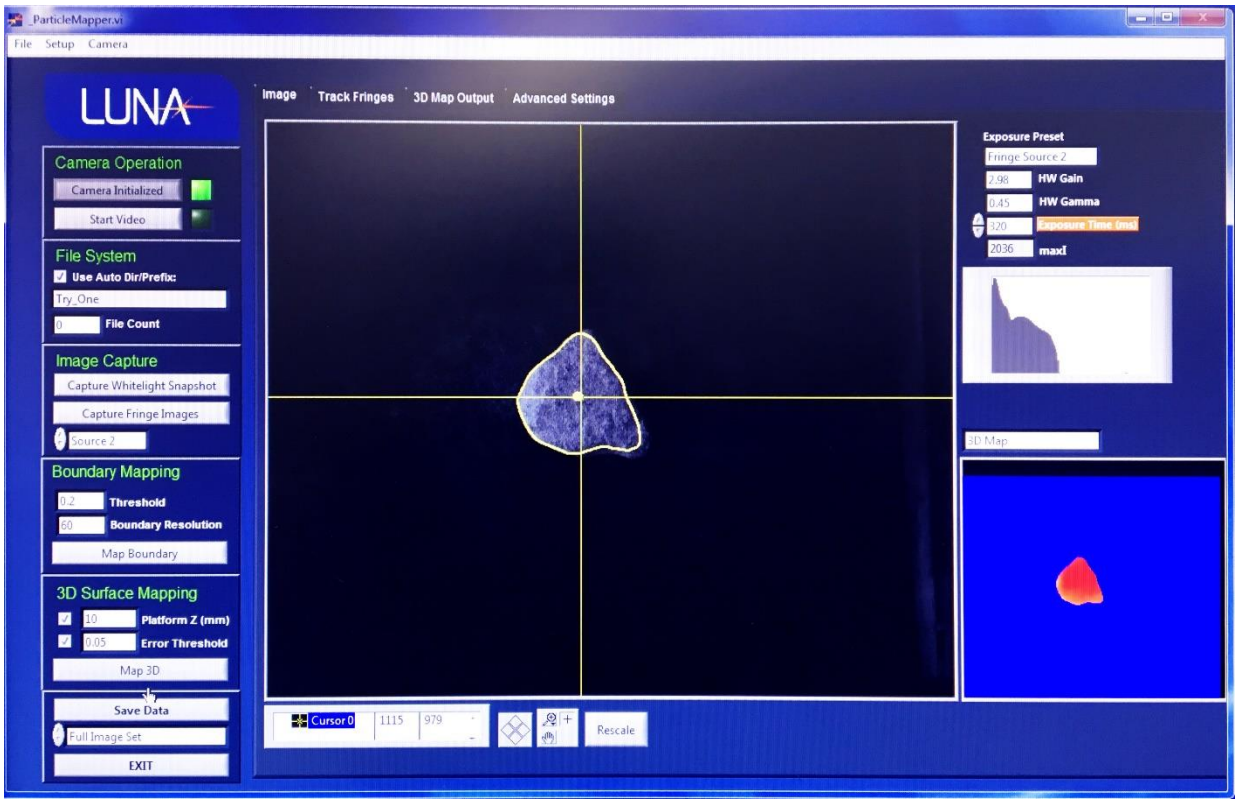

a) The photo of boundary mapping and surface mapping

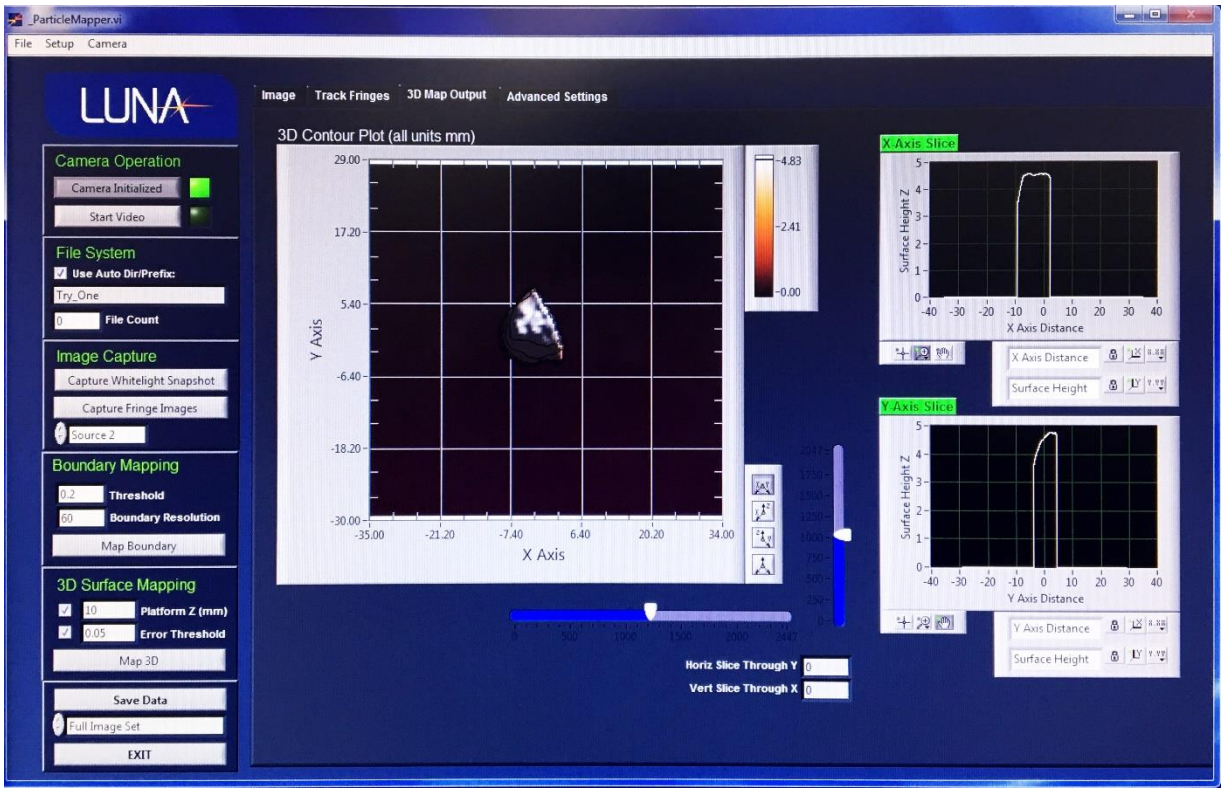

b) The 3-D contour plot of an aggregate

Figure 3.2 Photos of boundary mapping, surface mapping, and 3-D contour of an aggregate

Two-dimensional Fourier Transform Method for Characterizing Aggregate Morphology

The two-dimensional Fourier transform method (FFT2) is used in the Improved FTI system to quantify aggregate morphology, including sphericity, flatness ratio, elongation ratio, angularity and surface texture. It is originated from the one-dimensional Fourier transform method (Wang et al., 2005). The Improved FTI system uses a better camera and improves the operation automaticity and computational efficiency of the FTI software.

The morphological characteristics of aggregates are represented by variations of asperities at multiple dimensional scales, including shape, angularity, and texture. Shape is described by sphericity, flatness ratio, and elongation ratio. Sphericity represents the overall three-dimensional shape of an individual aggregate. Sphericity is defined by Eq. 3.1 and ranges from 0 to 1. A sphericity value of 1 indicates that an aggregate is equidimensional (i.e., cubical or spherical).

$$\text{Sphericity} \quad (S) = \sqrt[3]{\frac{D_s D_m}{D_l^2}} \qquad \text{Eq. 3.1}$$

where S is sphericity; D_s is the shortest dimension of an aggregate; D_m is the intermediate dimension of an aggregate; and D_l is the longest dimension of an aggregate.

The flatness ratio is defined by Eq. 3.2, and the elongation ratio is defined by Eq. 3.3. A greater flatness ratio or elongation ratio indicates that the analyzed aggregate is platy and elongated.

$$\text{Flatness Ratio (FR)} = \frac{D_s}{D_m} \qquad \text{Eq. 3.2}$$

$$\text{Elongation Ratio (ER)} = \frac{D_m}{D_l} \qquad \text{Eq. 3.3}$$

According to ASTM D4791 and VTM-121, the flat and elongated (F&E) ratio of coarse aggregate particles is described as a ratio of length to thickness, which is the ratio of the longest dimension of a coarse aggregate particle to the shortest dimension as follows:

$$\text{Flat and Elongated Ratio (F\&E Ratio)} = \frac{D_l}{D_s} \qquad \text{Eq.3. 4}$$

The described parameter F&E ratio for a particle can be defined in terms of flatness ratio and elongation ratio obtained from the Improved FTI system, which is expressed as follows:

$$\text{Flat and Elongated Ratio (FER)} = \frac{1}{(FR)(ER)} = \frac{D_l}{D_s} \qquad \text{Eq. 3.5}$$

The Improved FTI image analysis system provides an easy and convenient way of calculating the flat and elongated ratio of coarse aggregates instead of performing a complete flat and elongated test. The determination of the percentage of flat and elongated coarse aggregates through the Improved FTI system is more efficient than the manual measurements for coarse

using a caliper device, or measuring particles by determining the uncompacted void content of a sample (ASTM C1252) or the percentage of flat and elongated particles in a sample (ASTM D5821).

The two-dimensional discrete Fourier transform (DFT) is used to quantify angularity and texture from a discrete function $z(x, y)$ that represents the aggregate's surface, and $z(x, y)$ is nonzero over the finite region $0 \le x \le N-1$ and $0 \le y \le N-1$. The DFT transforms spatial domain data into frequency domain data. The relationship between the DFT and the inverse DFT is given by the following equations (Wang, 2007):

$$Z(p,q) = \sum_{x=0}^{N-1}\sum_{y=0}^{N-1} z(x,y) e^{-j(\frac{2\pi}{N}xp+\frac{2\pi}{N}yq)} \quad \text{Eq. 3.6}$$

$$z(x,y) = \sum_{p=0}^{N-1}\sum_{q=0}^{N-1} Z(p,q) e^{j(\frac{2\pi}{N}xp+\frac{2\pi}{N}yq)} \quad \text{Eq. 3.7}$$

$$f_x = \frac{2\pi}{N}x \quad \text{Eq. 3.8}$$

$$f_y = \frac{2\pi}{N}y \quad \text{Eq.3. 9}$$

where N is the size of $z(x, y)$ matrix; $Z(p,q)$ is the DFT coefficient matrix in the frequency domain; $z(x, y)$ is the z coordinate of an aggregate surface; j is the imaginary root; f_x and f_y are frequencies in x and y directions, respectively.

The angularity factor (AF, Eq. 3.10) and texture factor (TF, Eq. 3.11) of an aggregate are defined by the following equations, respectively.

$$\text{Angularity Factor (AF)} = \sum_{p=1}^{N_A}\sum_{q=1}^{N_A}[(\frac{a(p,q)}{a_0})^2 + (\frac{b(p,q)}{a_0})^2] \quad \text{Eq. 3.10}$$

$$\text{Texture Factor (TF)} = \sum_{p=1}^{N}\sum_{q=1}^{N}[(\frac{a(p,q)}{a_0})^2 + (\frac{b(p,q)}{a_0})^2] - \text{AF} \quad \text{Eq. 3.11}$$

where a_0 is the average height of $z(x, y)$; a and b are the real and imaginary parts of the coefficients for the two-dimensional fast Fourier Transform (FFT2), respectively; N is the size of the $z(x, y)$ matrix; N_A is defined as a threshold frequency. The determination of the threshold frequency is a critical step that differentiates angularity from texture. More detailed information to demonstrate how to separate texture from angularity on an aggregate surface by the FFT2 method can be found in (Sun et al, 2012; Wang et al, 2012). A three-dimensional surface is reconstructed using the inverse of FFT2 coefficients that have frequencies smaller

than $2\pi N_A / N$ in either x-direction or y-direction. A set of square matrix $z(x, y)$ varying the matrix size N is sampled on the measured aggregate surface. The FFT2 coefficients are considered to only contribute to angularity if the mean value of distance between the original surface and the reconstructed surface using the inverse of FFT2 is greater than 0.2 mm (Brandon and Kaplan, 1999). The other FFT2 coefficients are considered to contribute to texture only.

The relationship between AF and the size of roughness matrix is plotted for every aggregate particle. You will find that all points in the AF-the size of roughness matrix exactly follow a linear relationship for the same type of aggregate within a certain size range, and that the aggregate with more irregularities has steeper slope in the plot. Therefore, the angularity is defined as the slope in the plot of AF and roughness matrix size. Similarly, texture is defined as the slope in the plot of TF and roughness matrix size. Further information on the elucidation of the definition of angularity and texture can be found in (Wang et al. 2012).

CHAPTER 4 MATERIALS AND IMAGING BASED IMPROVED FTI RESULTS

Materials and Mixture Design

Table 4.1 presents the mix design for all SMA mixtures, including the size, type, and origin of aggregates, and the content of fiber and asphalt binder. These mix designs for SMA mixtures are used in Virginia highways. There are in total 22 types of coarse aggregates in the SMA mixtures. These aggregates were collected from different quarries in Virginia State, including Staunton, Bealeton, Stuarts Draft, Leesburg, Goose Creek, Chantilly, and Garrisonville. These aggregates mainly include the following mineralogical compositions: aplite, limestone, quartzite, arkose, diabase, and granite. These aggregates were representative because they are the most widely used by Virginia pavement contractors.

The Improved FTI system was used to measure coarse aggregates, which are those that were retained on a 2.36 mm sieve after passing through a 12.5 mm sieve. All coarse aggregate samples were sieved into four size ranges, namely, 2.36 to 4.75 mm, and 4.75 to 9.5 mm, 9.5 to 12.5 mm, 12.5 to 19 mm (i.e., #8 to #4, #4 to 3/8 in., 3/8 in. to 1/2 in., 1/2 in. to ¾ in.). In this investigation, a total of 60 particles were scanned at each size range of every type of aggregate. A total of 180 aggregates were scanned for aggregate fractions if there are three size ranges selected for a mix design, and a total of 240 aggregates were scanned for aggregate fractions if four size ranges selected.

SMA mixtures were produced following the specification of the Virginia Department of Transportation (VDOT) SMA mix design. SMA mixture specimens (SMA-9.5 and SMA-12.5) with two different nominal maximum aggregate sizes were fabricated as shown in Table 1. For each type of SMA mixture, three samples were prepared with different weight percentages of crushed coarse aggregate fractions. As shown in Table 4.1, SMA mixtures marked as 13-1070, 13-1081, 14-1021, 14-1047, and 15-1012 were prepared using four aggregate fractions, respectively. SMA mixtures marked as 15-1068, 15-1080, and 15-1084 included three aggregate fractions, respectively. Three different types of asphalt binder were selected: PG 70-22, PG 76-22 and PG 76-28 High Polymer (HP). The asphalt binder content for each SMA mixture varied around 6.5% by weight.

Volumetric analyses were performed to determine fundamental mixture properties. 150-mm diameter gyratory pills were compacted to 65 gyrations for volumetric determination in accordance with VDOT specifications. Data collected included asphalt content for each type of mixture and gradations of all types of aggregates, bulk and Rice specific gravities (G_{mb} and G_{mm}), voids in total mixture (VTM), voids in mineral aggregate (VMA), voids filled with asphalt (VFA), aggregate bulk and effective specific gravities (G_{sb} and G_{se}), dust/asphalt ratio, percent binder absorbed (P_{ba}), and effective binder content (P_{be}). Table 4.2 summarizes the volumetric information of all SMA mixtures. These SMA mixtures exhibited diversity with regards to morphological characteristics and nominal maximum aggregate size of coarse aggregates, performance grade and content of asphalt binder.

SMA is a gap-graded hot mix asphalt (HMA) with high concentrations of coarse aggregate and high asphalt content, which greatly reduces the susceptibility to rutting and improves the durability of SMA mixtures. It is conceivable that fatigue behavior of SMA depends on physical properties of coarse aggregates and asphalt binder. Since all the mixtures prepared are all gap-graded and aggregate gradations of all SMA mixtures are similar as shown in Figure 4.1, aggregate gradation has little influence on mechanical performance of these SMA mixtures, and consequently is not a topic of interest in this study. Since most of the SMA mixtures are SMA-9.5, the nominal maximum aggregate size is not considered as the main influencing factor in the study. Among the other factors, coarse aggregate morphology strongly affects mechanical performance of gap-graded SMA mixtures due to the dominant usage of coarse aggregates. This leads to the main objective of this study, investigation of the influence of coarse aggregate morphology on mechanical performance of SMA mixtures in Virginia.

Table 4.1 SMA Mix Design and Aggregate Basic Information

SMA Mix ID	Materials (Aggregate Fractions ID No., Asphalt Binder, Additive)	Mix Phase (%)	Type	Size	Origin	Crusher
SMA-9.5 /13-1070	13-1071 No.30	13	Diabase	No.57 with 19.05 mm (3/4 in.) removed	Bealeton	Cone Crusher
	13-1071 No.60	34	Diabase	No.8	Bealeton	Cone Crusher
	13-1071 No.78	30	Diabase	No.78	Bealeton	Cone Crusher
	13-1071 RAP	12	Recycled Asphalt Pavement	Recycled-1/2 in.	Bealeton	Cone Crusher
	Filler	11	Diabase	Filler	Bealeton	
	Additive	0.3	Cellulose Fiber			
	Asphalt Binder	6.45	PG 70-22			
SMA-9.5 /13-1081	13-1078 No.8	50	Aplite	No.8	Piney River	Jaw Crusher
	13-1073 No.10	11	Limestone	No.10	Staunton	Impact Crusher
	13-1073 No.68	20	Aplite	N0.68	Piney River	Impact Crusher
	13-1073 No.78	10	Quartzite and Arkose	No.78	Stuarts Draft	Impact Crusher
	Filler	9	Limestone	Filler	Staunton	
	Additive	0.4	Cellulose Fiber			
	Asphalt Binder	6.91	PG 70-22			

SMA-12.5 /14-1021	14-1019 No.8	24	Diabase	No.8	Leesburg	Cone Crusher
	14-1019 No.30	22	Diabase	No. 57 with 19.05 mm (3/4 in.) removed	Goose Creek	Impact Crusher
	14-1019 No.78	29	Diabase	No.78	Leesburg	Cone Crusher
	14-1019 RAP	12	Recycled Asphalt Pavement	Recycled-1/2 in.	Leesburg	Cone Crusher
	Filler	12	Filler	Filler	Goose Creek	
	Additive	0.3	Cellulose Fiber			
	Asphalt Binder	6.29	PG 76-22			
SMA-9.5 /14-1047	14-1048 No.30	13	Diabase	No. 57 with 19.05 mm (3/4 in.) removed	Bealeton	Cone Crusher
	14-1048 No.60	34	Diabase	No.8	Bealeton	Cone Crusher
	14-1048 No.78	30	Diabase	No.78	Bealeton	Cone Crusher
	14-1048 RAP	12	Recycled Asphalt Pavement	Recycled-1/2 in.	Bealeton	Cone Crusher
	Filler	11	Diabase	Filler	Bealeton	
	Additive	0.3	Cellulose Fiber			
	Asphalt Binder	6.7	PG 76-22			
SMA-9.5 /15-1012	15-1013 No.28	12	Diabase	Top Size 1/2 in.	Chantilly	
	15-1013 No.78	61	Diabase	No.78	Chantilly	
	15-1013 No.10	4	Diabase	No.10	Chantilly	
	15-1013 RAP	10	Recycled Asphalt Pavement	Recycled-1/2 in.	Chantilly	
	Filler	13	Filler	Filler		
	Additive	0.3	Adhere HP Plus			
	Asphalt Binder	6.02	PG 76-22			
SMA-9.5 /15-1068*	15-1069 No.8	22	Granite	No.8	Garrisonville	
	15-1069 No.78	52	Granite	No.78	Garrisonville	
	15-1069 RAP	15	Recycled Asphalt Pavement	Recycled-1/2 in.	Garrisonville	
	Filler	10	Filler	Filler	Goose Creek	

	Additive	0.3	Cellulose Fiber			
	Asphalt Binder	6.58	PG 76-28HP			
SMA-9.5 /15-1080*	15-1081 No.8	22	Granite	No.8	Garrisonville	
	15-1081 No.78	52	Granite	No.78	Garrisonville	
	15-1081 RAP	15	Recycled Asphalt Pavement	Recycled-1/2 in.	Garrisonville	
	Filler	10	Filler	Filler	Goose Creek	
	Additive	0.3	Cellulose Fiber			
	Asphalt Binder	6.2	PG 70-22			
SMA-9.5 /15-1084*	15-1085 No.8	22	Granite	No.8	Garrisonville	
	15-1085 No.78	52	Granite	No.78	Garrisonville	
	15-1085 RAP	15	Recycled Asphalt Pavement	Recycled-1/2 in.	Garrisonville	
	Filler	10	Filler	Filler	Goose Creek	
	Additive	0.3	Cellulose Fiber			
	Asphalt Binder	6.45	PG 76-22			

Note: * Aggregates of 15-1069 in SMA-9.5/15-1068 are the same with aggregates of 15-1081 in SMA-9.5/15-1080 and 15-1085 in SMA-9.5/15-1084. No. 8 is the nominal size range of aggregates passing 3/8" sieve and retaining on No. 8 sieve (9.5 mm – 2.36 mm); No. 30 is the nominal size range for aggregates passing the 1" sieve and retaining on the No. 4 sieve (25.4 mm – 4.75 mm), with 3/4 inch (19.5 mm) removed; No. 68 is the nominal size range of aggregates passing ¾" sieve and retaining on the No. 8 sieve (19.0 mm – 2.36 mm); No. 78 is the nominal size range of aggregates passing ½" sieve and retaining on No. 4 sieve (12.75 mm – 4.75 mm).

Table 4.2 Volumetric Information of SMA Mixtures

Property	SMA 13-1070	SMA 13-1081	SMA 14-1021	SMA 14-1047	SMA 15-1012	SMA 15-1068	SMA 15-1080	SMA 15-1084
%AC	6.45	6.91	6.29	6.7	6.02	6.58	6.2	6.45
Rice specific gravity (Gmm)	2.655	2.48	2.669	2.639	2.695	2.615	2.627	2.614
Binder specific gravity (Gb)	1.03	1.03	1.03	1.03	1.03	1.03	1.03	1.03
% Air voids (Va)	3.2	3.3	3	2.5	3.8	2	4.2	2.7
% VMA	19.2	19.1	13	19.1	18.7	18	18.9	18.2
% VFA	83.6	82.7	77.1	87.1	79.8	88.7	78	85.4
VCAMIX	34.6	36.6	39.8	36.7	33.6	33.6	33.9	34.9

Dust/AC	1.49	1.41	2.38	1.8	1.53	1.5	1.61	1.71
Bulk specific gravity (Gmb)	2.572	2.398	2.59	2.574	2.594	2.562	2.518	2.544
Effective specific gravity (Gse)	2.979	2.769	2.989	2.973	3.006	2.933	2.927	2.924
Aggregate specific gravity (Gsb)	2.976	2.759	2.789	2.97	2.998	2.919	2.913	2.91
% Binder absorbed (Pba)	0.03	0.13	2.47	0.04	0.09	0.17	0.17	0.17
Effective % binder (Pbe)	6.42	6.78	3.97	6.66	5.93	6.42	6.04	6.29
Effective film thickness (Feft)	9.6	10.3	5.9	8.5	9.2	9.7	9.1	8.6
% Density @ Nini	85.8	85.3	86.2	86.5	85.9	87	85.1	86.1
% Gmm @ 7 gyr	2.21	2.08	2.22	2.21	2.24	2.27	2.2	2.22
% Gmm @ 65 gyr	1.95	1.83	1.98	1.97	2.01	2.02	1.95	1.99
	Average percent passing							
Sieve size	SMA 13-1070	SMA 13-1081	SMA 14-1021	SMA 14-1047	SMA 15-1012	SMA 15-1068	SMA 15-1080	SMA 15-1084
3/4 in. (19.0 mm)	100	100	100	100	100	100	100	100
1/2 in. (12.5 mm)	88.9	92.4	83.9	89.5	92.9	88.7	89.6	90.8
3/8 in. (9.5 mm)	66.9	78.2	61.4	70.3	71.1	70.7	71.2	72.4
No. 4 (4.75 mm)	26.7	32.9	26.7	29.4	31.5	28.4	26.8	29
No. 8 (2.36 mm)	19.5	21.8	18.1	21.9	18.7	19.2	18.4	20.3
No. 16 (1.18 mm)	17.2	18.1	16	19.5	16.4	17.1	16.4	18.4
No. 30 (600 µm)	15.8	15.8	14.5	17.8	15.1	15.5	15	16.9
No. 50 (300 µm)	14.5	13.9	13.3	16.3	13.9	14	13.8	15.5
No. 100 (150 µm)	12.8	11.8	12.1	14.7	12	12.4	12.3	13.9
No. 200 (75 µm)	9.56	9.59	9.45	11.97	9.09	9.65	9.71	10.78

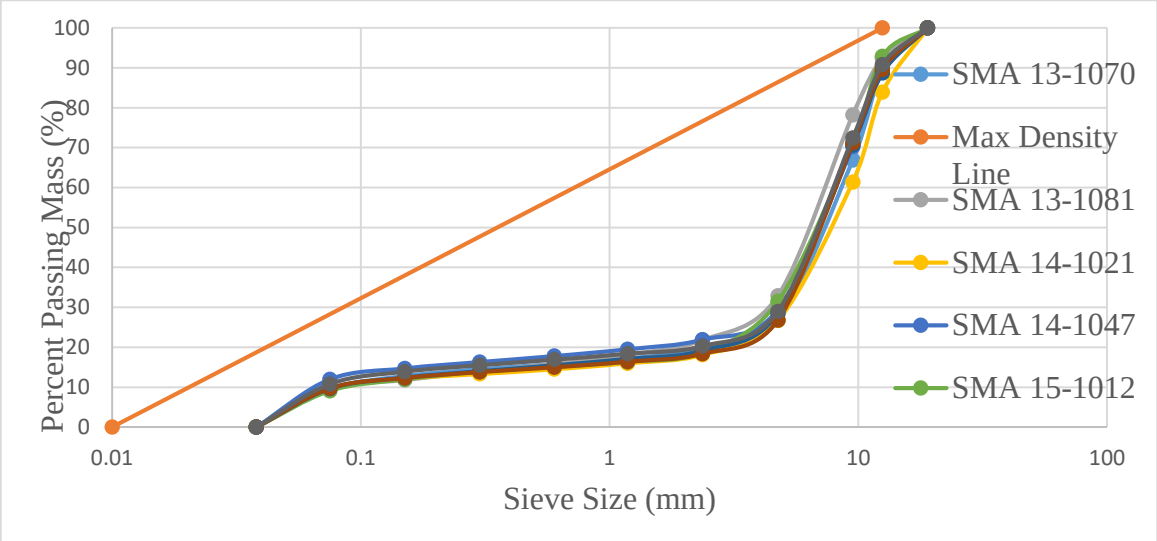

Figure 4.1 Gradation Curves of SMA mixtures

Selection of Aggregate Particles

The first sixteen types of aggregates were selected for statistical analysis to determine the rational of the aggregate sample size. The selected aggregate samples cover a wide range of morphological characteristics. Figure 4.2 shows a photo of sample aggregates selected for the first sixteen types of aggregates. These sixteen aggregate fractions contain aggregates with the size ranging from #8 (2.36 mm) to 1-in (25.4 mm), mostly between 4.75 mm and 19 mm. 13-1071 Staunton #10 is the smallest aggregate fraction. Aggregates from each type of aggregate fraction were randomly selected without sieving the aggregates.

Statistical analysis of aggregate morphological characteristics was performed to validate that the sample population is adequate for all sixteen aggregate fractions. A sample size of 120 particles was randomly selected for each aggregate fraction to ensure that the sample population was large enough to reach statistically stable results of aggregate morphological characteristics. All the aggregates were imaged and analyzed using the improved FTI system. Five morphological parameters, including sphericity, flatness ratio, elongation ratio, angularity and texture were measured for each aggregate particle.

Quantile-quantile plots are generated using Rstudio. If the data is normally distributed, the points in the QQ-normal plot line lie on a straight diagonal line. It can be seen from Figure 4.3 that all the QQ-normal plots almost follow straight lines, which provide the evidence that the distributions of sphericity and elongation ratio for all aggregate fractions follow normal distributions. Statistical analysis of the other morphological characteristics shows similar linear trends in QQ-normal plots, indicating that the other morphological characteristics closely follow normal distributions. Consequently, an entire population of 120 particles for each aggregate fraction is sufficient. Therefore, 120 aggregates were imaged for each aggregate fraction. Literatures also showed that the selection of 120 aggregate particles for scanning was appropriate (Mahmoud et al., 2014).

The flat and elongate aggregate particles tend to lock up more readily during compaction and have a tendency to break up easily, the amount of the flat and elongated aggregates should be limited in use for ensuring the quality of aggregates and the performance of asphalt concrete pavements. The F&E ratio at which the aggregate is considered as too flat or too elongated differs from specification to specification. The SHRP Superpave mix design specification allows less than 10% by weight of particles having an F&E ratio greater than 5:1 for aggregate blends in asphalt mixtures. The other literature shows that the asphalt mixtures with F&E ratios greater than 3:1 are not harmful to the mechanical behavior of asphalt mixtures (Buchanan, 2000). In this study, the amount of aggregates having an F&E ratio greater than 3:1 was limited to 20% and the amount of aggregates having an F&E ratio greater than 5:1 was limited to 5% based on the current VDOT specification. Figure 4.4 plots the cumulative percentage versus the F&E ratio obtained from the Improved FTI system for 16 types of aggregates. As shown in figure 4.4, the percentages of aggregates having F&E ratios greater than 3:1 are less than 20%, the percentages of aggregates having F&E ratios greater than 5:1 are less than 5%, indicating that the requirement for the allowable percentage of the flat and elongated aggregates with F&E ratios greater than 3:1 and 5:1 is mostly satisfied as specified by VDOT specification. This demonstrates an easier way of assessing the F&E ratio of an aggregate than the conventional manual measurements. The Improved FTI system captures images of aggregates, develops a 3-D shape of each particle, and measures the three dimensions of each aggregate particle, the shortest, the intermediate and the longest dimensions of each aggregate, then the flat and elongated ratios of particles can be automatically calculated based on the three dimensions. The Improved FTI has the potential to measure the flat and elongated ratio and can analyze large quantities of aggregate particles in a short time. The system provides a detailed analysis of morphological characteristics for aggregates.

Figure 4.2 A photo of sixteen aggregate fractions

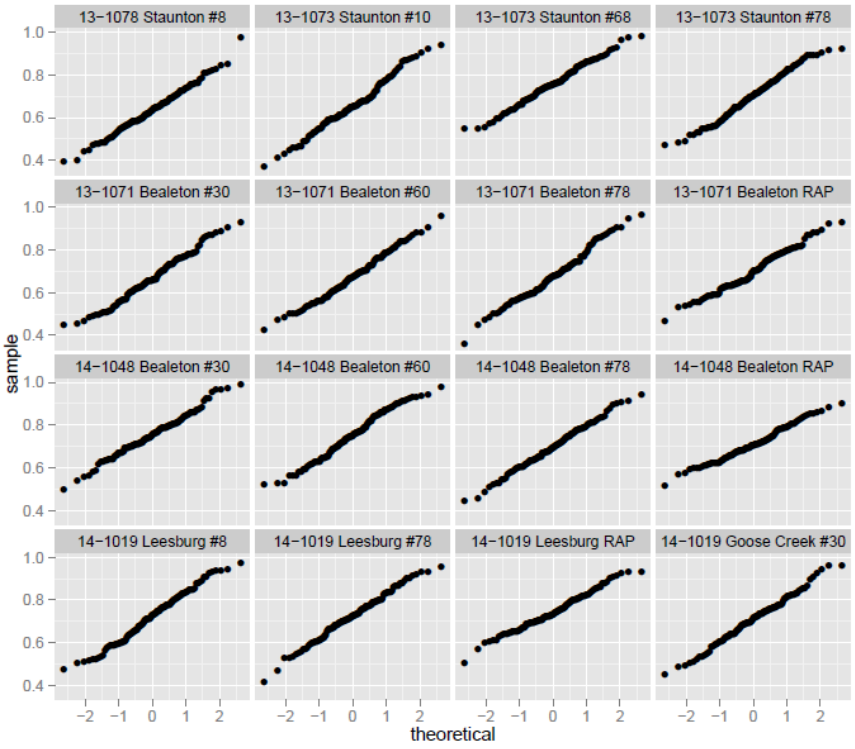

a) Quantile-Quantile plot of sphericity for sixteen aggregate fractions

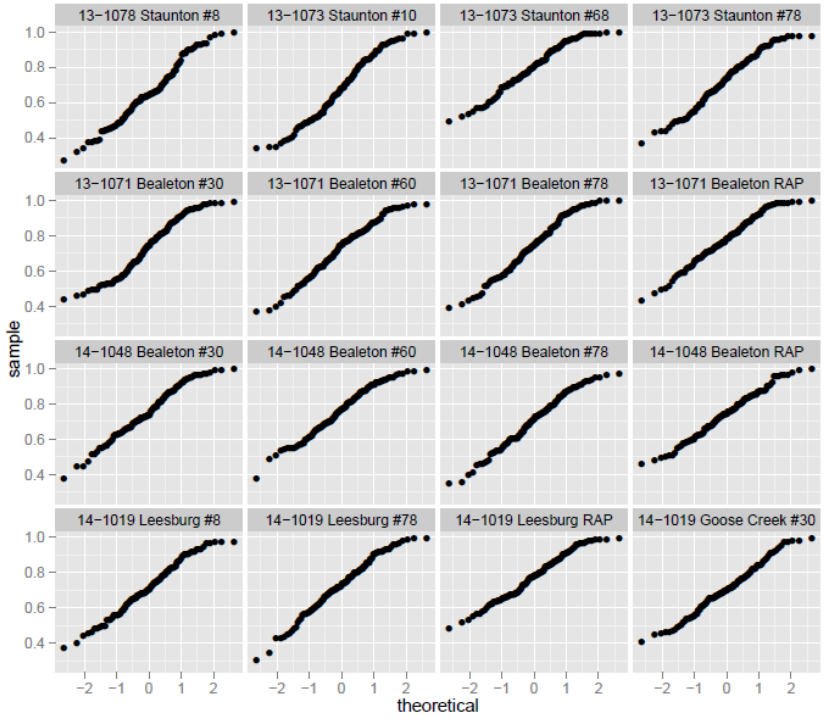

b) Quantile-Quantile plot of elongation ratio for sixteen aggregate fractions

Figure 4.3 Quantile-Quantile plots of sphericity and elongation ratio for sixteen aggregate fractions

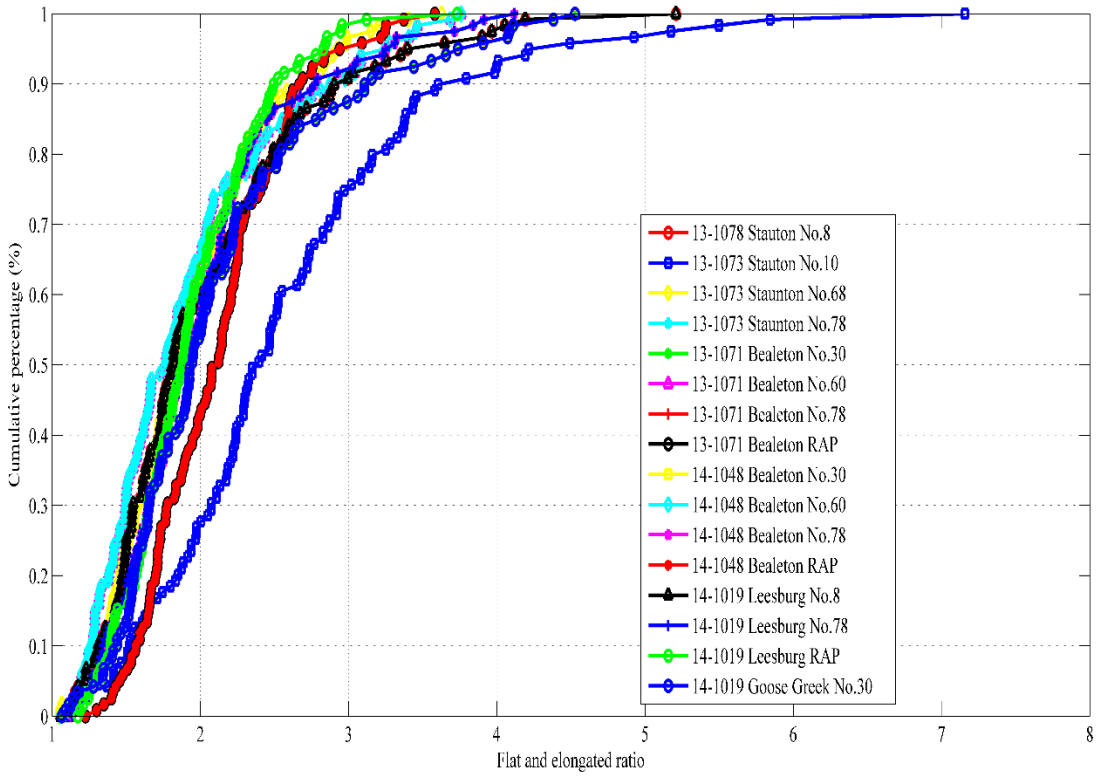

Figure 4.4 FTI flat and elongated ratio distribution of sixteen aggregate fractions

Statistical Analysis of Aggregate Morphological Characteristics

Further statistical analysis was performed to compare the five morphological characteristics of aggregates in eight aggregate fractions. A total of 120 aggregates selected randomly without sieving were analyzed for each aggregate fraction in this section. Staunton No. 68 has the greatest mean value of sphericity, indicating aggregates of Staunton No. 68 are more equidimensional; Staunton No. 8 has the smallest mean value of sphericity. Staunton No. 68 has the greatest mean values of both flatness ratio and elongation ratio, indicating that aggregates of Staunton No. 68 are very flat and elongated. On the contrary, Culpeper No. 30 has the smallest mean value of flatness ratio, and Staunton No. 8 has the smallest mean value of elongation ratio. Staunton No. 68 has the greatest mean angularity value and texture value, indicating the most angular aggregates with the roughest texture.

Figure 4.5 presents the distributions of different morphological characteristics for each aggregate fraction. *X*-axis represents different FTI morphological characteristics, i.e., sphericity, flatness ratio, elongation ratio, angularity and texture, respectively, whereas y-axis represents the cumulative percentage by number for each morphological characteristic.

Figure 4.5(a) plots sphericity distributions for eight aggregate fractions. As shown in this figure, Staunton No. 68 tends to have the greatest values of sphericity, followed by Staunton No. 10; Culpeper No. 30 and Culpeper No. 60 have analogous sphericity distributions. Conversely, Staunton No. 8 has the smallest sphericity value among the eight aggregate fractions.

Figure 4.5(b) presents flatness ratio distributions of eight aggregate fractions. In this figure, it can be identified that Staunton No. 68 has the largest flatness ratios. Both Staunton No. 68 and Staunton No. 78 have greater flatness ratios in comparison with other aggregate fractions, which reveals that these two fractions of aggregates are platy, whereas Culpeper RAP has the smallest flatness ratio values, followed by Culpeper No. 78 and Culpeper No. 30.

Figure 4.5(c) shows the distribution of elongation ratio of all the aggregate fractions. Staunton No. 68 has the largest value of elongation ratio, followed by Culpeper RAP. Staunton No. 8 has the smallest elongation ratio values, followed by Staunton No. 10. The elongation ratio distributions of the other fractions of aggregates are very close to each other.

Figure 4.5(d) presents the FTI angularity distributions of eight aggregate fractions. Staunton No. 68 has the greatest angularity values, followed by Staunton No. 78. Conversely, Culpeper RAP and Staunton No. 10 have the smallest angularity values. The angularity distributions of all the other fractions of aggregates are similar to each other.

Figure 4.5(e) shows the FTI texture distributions of eight aggregate fractions. As expected, Culpeper RAP has the roughest surface due to the fact that RAP is a mixture of aggregate particles and asphalt binder that have been pulled apart. Staunton No. 68 has the second roughest aggregate surfaces. Staunton No.78 has the smoothest surfaces. The other fractions of aggregates have very similar surface textures.

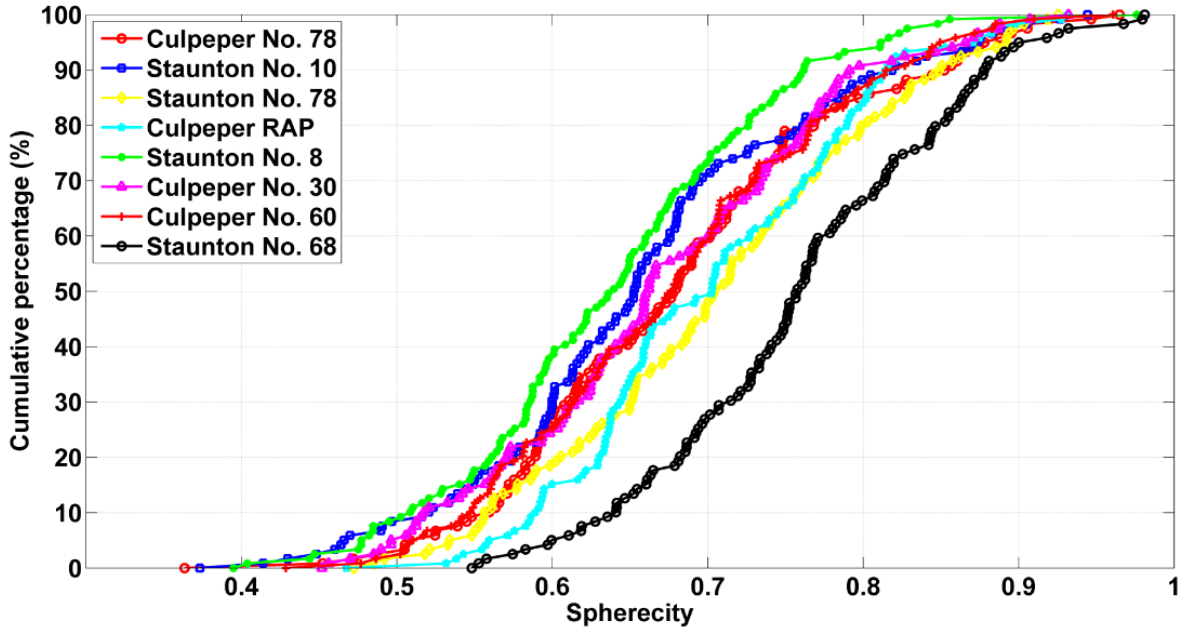

(a) FTI sphericity distributions of eight aggregate fractions.

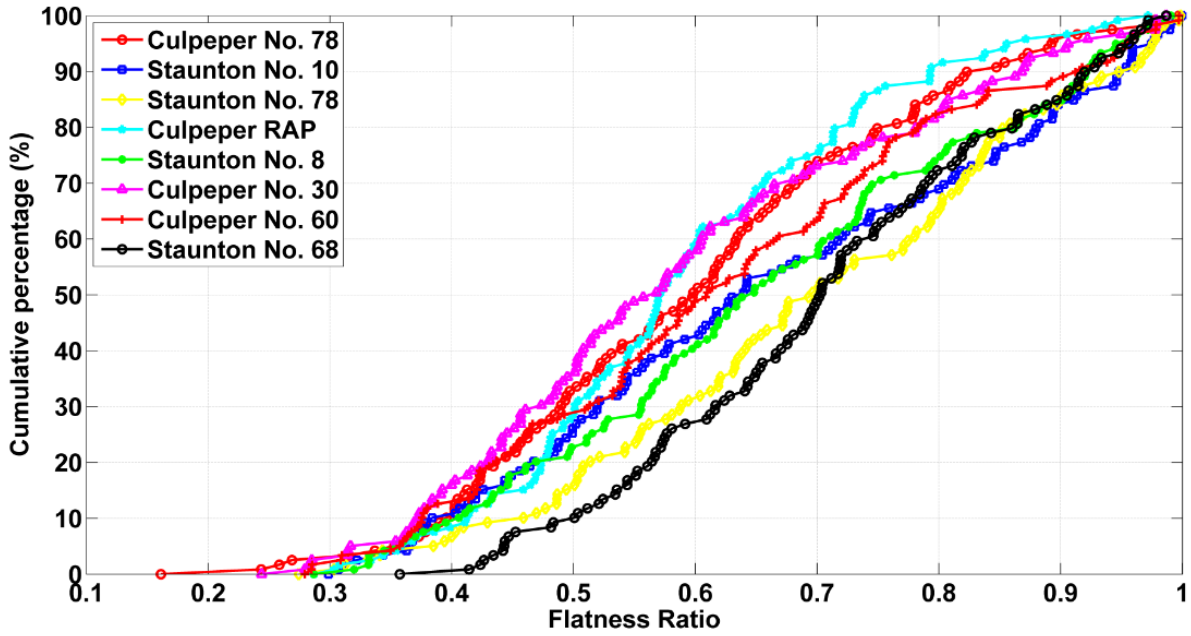

(b) FTI flatness ratio distributions of eight aggregate fractions.

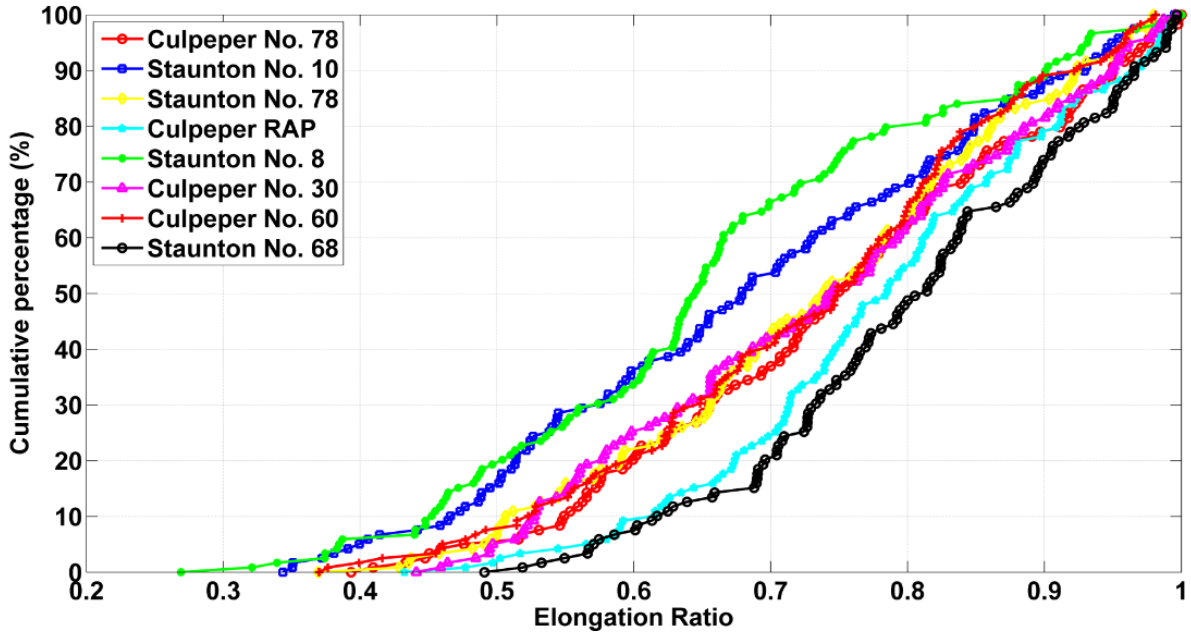

(c) FTI elongation ratio distributions of eight aggregate fractions.

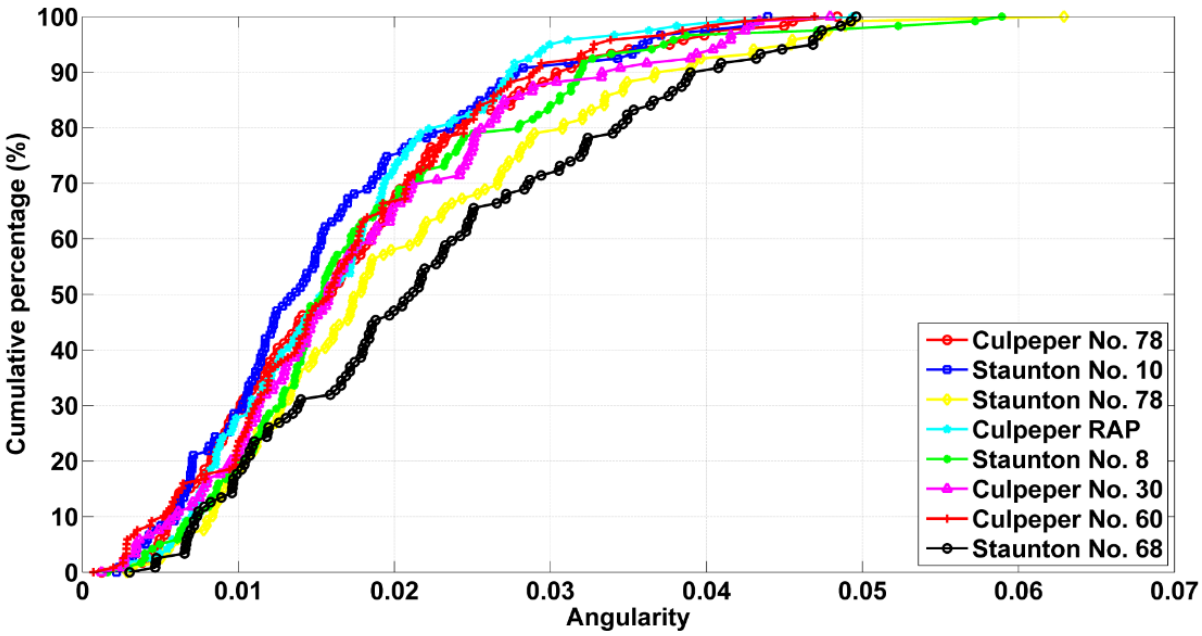

(d) FTI angularity distributions of eight aggregate fractions.

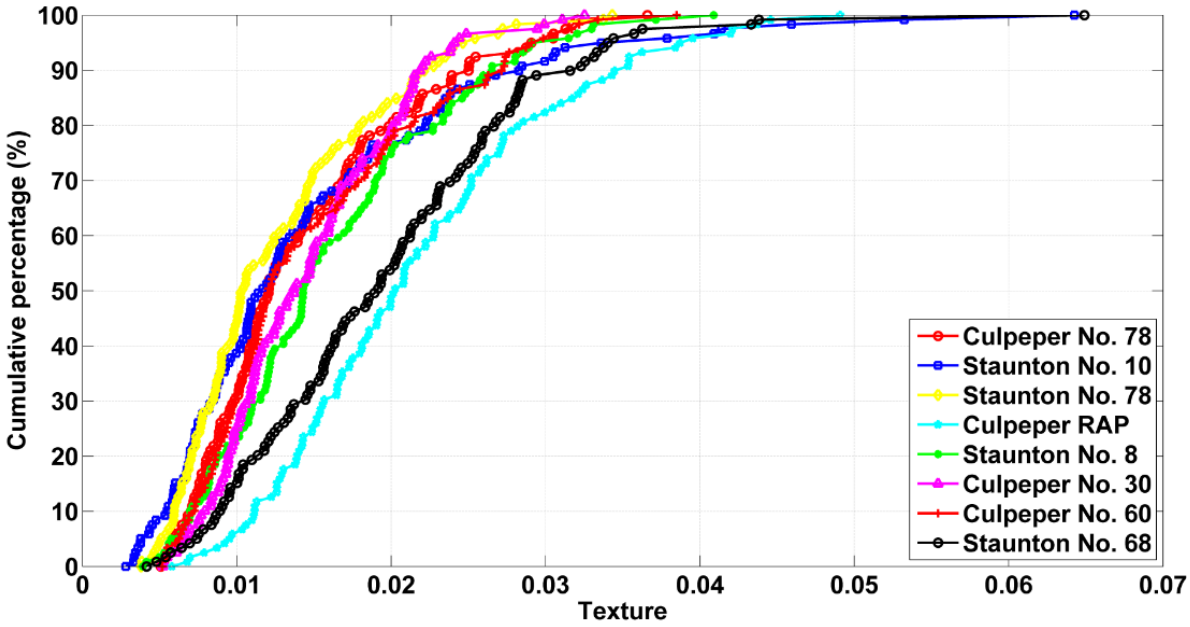

(e) FTI texture distributions of eight aggregate fractions.

Figure 4.5 FTI morphological characteristics distributions of eight aggregate fractions

Comparison between the Improved FTI Shape Results and Manual Measurements

For the verification of the accuracy and reliability of the Improved FTI system, three dimensions of the first eight types of aggregates (960 particles) were manually measured using the Vernier caliper for further comparison with the results from the Improved FTI system. It was found that the mean values of shape descriptors measured by the Improved FTI system were very close to the ones obtained from manual measurements for every fraction of each type of aggregate. Figure 4.6 presents the relationship between the Improved FTI-calculated shape descriptors and the manually measured shape descriptors, including the sphericity and

elongation ratio. The manually measured shape descriptors are labeled as *x*, and the shape descriptors quantified using the Improved FTI system are labeled as *y* for the same aggregate. As shown in Figure 4.6, the relationship between the Improved FTI shape results and the manual measured results for these eight aggregate fractions follows a linear relationship of $y=x$ with the corresponding R^2 value approaching to 1.0, indicating a good agreement between the Improved FTI results and the manual measurements. The consistency of shape descriptors measured by the Improved FTI system and the manual measurement method validates the accuracy and reliability of the Improved FTI system.

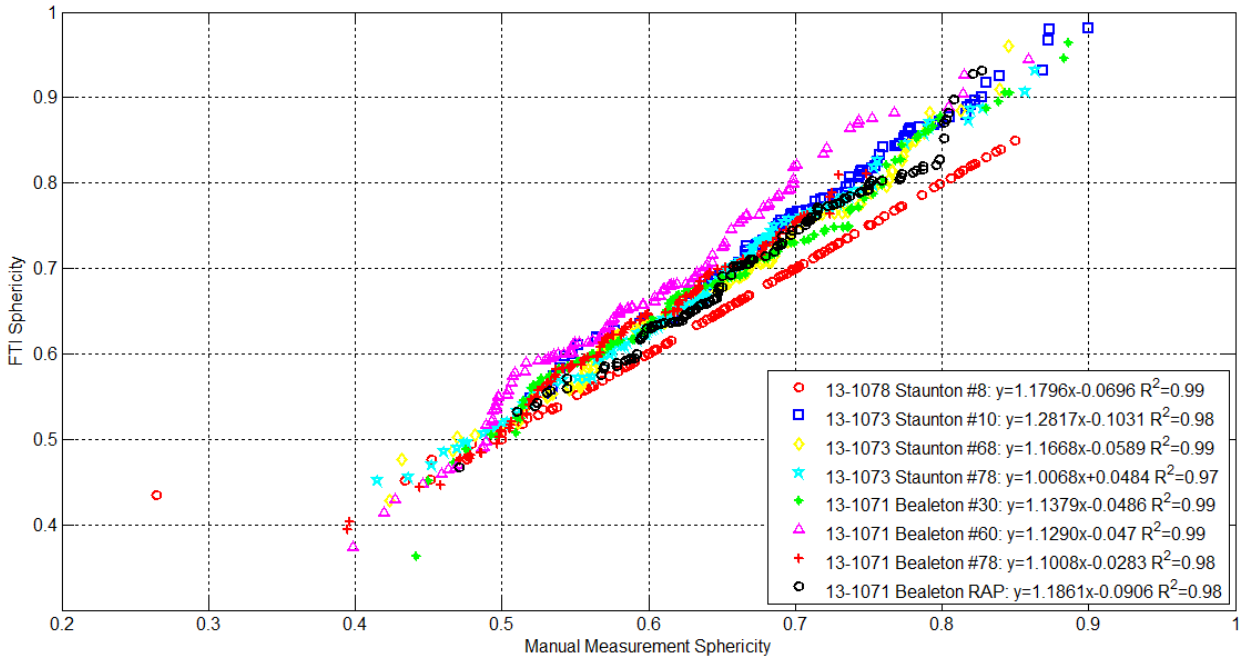

(a) Manually measured sphericity versus the Improved FTI sphericity.

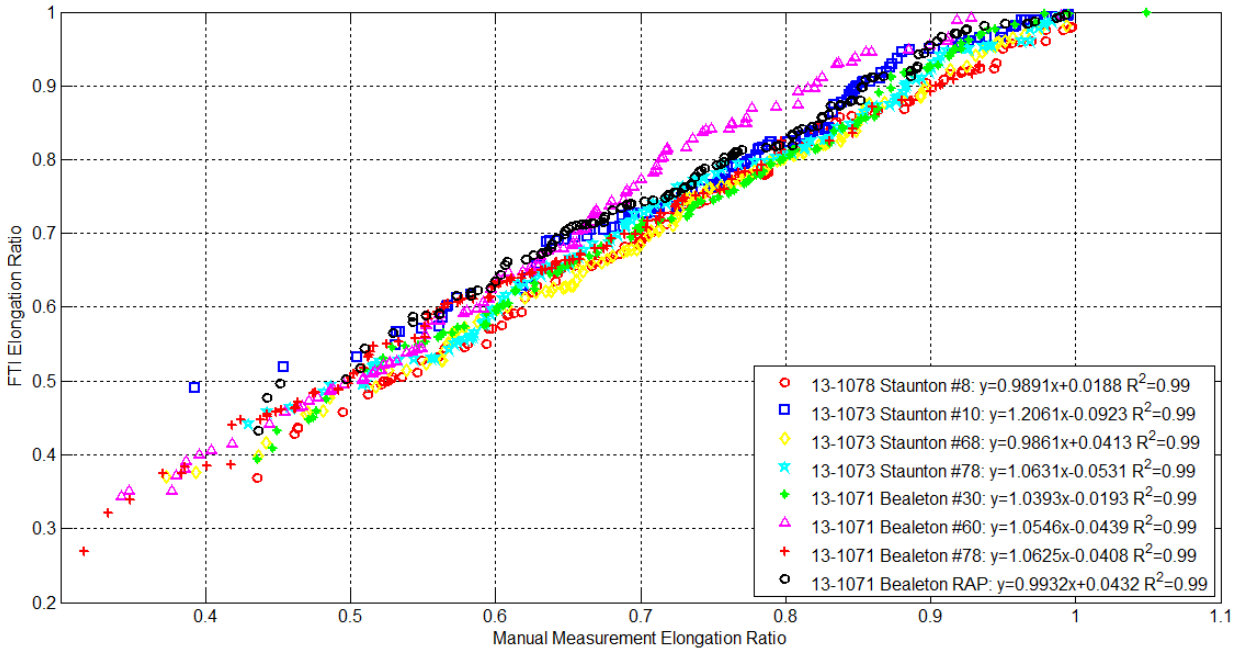

(b) Manually measured elongation ratio versus the Improved FTI elongation ratio

Figure 4.6 Manually measured shape results versus the Improved FTI shape results

Imaging-Based Improved FTI Morphological Characteristics Results

A total of 22 types of aggregates collected from a wide range of sources were image analyzed using the Improved FTI system. Aggregates are separated into different fractions before the imaging analysis through sieving. For each aggregate fraction, 60 aggregates were scanned for each size range, including 2.36 to 4.75 mm, and 4.75 to 9.5 mm, 9.5 to 12.5 mm, 12.5 to 19 mm (#8 to #4, #4 to 3/8 in., 3/8 in. to 1/2 in., 1/2 in. to ¾ in.). A total of 180 aggregates were selected for aggregate fractions with three size ranges of samples, a total of 240 aggregates were selected for aggregate fractions with four size ranges of samples. Morphological characteristics were measured for each coarse aggregate using the Improved FTI system in terms of sphericity, flatness ratio, elongation ratio, angularity and texture. Considering various blends of coarse aggregate fractions used in each type of SMA mixture, the weighted mean aggregate morphological index is proposed to account for the relative weight percentages of constituted coarse aggregate fractions in the SMA mixture:

$$\text{Weighted mean index} = \sum_{i=1}^{n}[(p_i)(index_i)] \quad \text{Eq. 4.1}$$

where the weighted mean index is the composite aggregate morphological index for each coarse aggregate blend used in a certain SMA mix design; p_i is the percentage by weight of the i^{th} coarse aggregate fraction used in the mix design, as shown in Table 1; $index_i$ is the mean morphological characteristic value of the corresponding i^{th} coarse aggregate fraction; and n is the number of coarse aggregate fraction in each SMA mixture. For example, there are 4 aggregate fractions in the first five types of SMA mixtures and n is 4; similarly, n is 3 for the last three types of SMA mixtures as shown in Table 4.1. The mean morphological value $index_i$ determined for each type of aggregate fraction are listed in Table 4.3, followed by the weighted mean index for each aggregate blend shown in bold. The results indicate that different blends of aggregate fractions show distinct morphological characteristics in terms of weighted mean index. The weighted mean values were based on the weight fraction from gradation, without counting fillers.

Table 4.3 Mean morphological value and weighted mean index for coarse aggregates used in each SMA mixture

SMA mixture ID	Aggregate Fractions	D_s	D_m	D_l	Sphericity	Flatness Ratio	Elongation Ratio	Flat and Elongated Ratio	Angularity	Texture
	13-1071 No.30	6.9574	12.6669	18.2666	0.6425	0.5683	0.7067	2.4899	0.0200	0.0206

SMA-9.5/13-1070	13-1071 No.60	5.7763	9.4302	13.3975	0.6675	0.6108	0.7143	2.2920	0.0180	0.0216
	13-1071 No.78	5.6941	9.8892	13.4935	0.6717	0.5716	0.7469	2.3423	0.0171	0.0216
	13-1071 RAP	5.8412	10.2698	13.4045	0.6952	0.5831	0.7716	2.2226	0.0185	0.0285
	Weighted Mean Value	**5.2776**	**9.0521**	**12.5864**	**0.5954**	**0.523**	**0.6514**	**2.9353**	**0.0161**	**0.0199**
SMA-9.5/13-1081	13-1078 No.8	5.2758	9.7004	13.863	0.6405	0.5491	0.7142	2.5499	0.0187	0.0227
	13-1073 No.10	2.7047	6.4275	8.7809	0.6078	0.4312	0.7479	3.1008	0.0134	0.0159
	13-1073 No.68	8.1832	12.9927	16.6504	0.7309	0.6489	0.7878	1.9562	0.0259	0.0286
	13-1073 No.78	5.6228	9.6254	12.979	0.6807	0.5809	0.7525	2.2877	0.017	0.0235
	Weighted Mean Value	**5.1343**	**9.1183**	**12.5254**	**0.6014**	**0.5098**	**0.6722**	**2.9181**	**0.0177**	**0.0212**
SMA-12.5/14-1021	14-1019 No.8	5.91	9.0686	11.9335	0.7142	0.6449	0.7678	2.0196	0.0216	0.026
	14-1019 No.30	8.0731	12.0999	16.519	0.7129	0.6796	0.747	1.9698	0.0254	0.0252
	14-1019 No.78	6.0874	9.6079	13.1671	0.6923	0.6335	0.7411	2.1300	0.0208	0.0244
	14-1019 RAP	6.4378	9.8916	12.2562	0.7501	0.6534	0.8136	1.8811	0.0226	0.033
	Weighted Mean Value	**5.8131**	**8.9327**	**11.9526**	**0.6262**	**0.5732**	**0.6686**	**2.6093**	**0.0198**	**0.0231**
SMA-9.5/14-1047	14-1048 No.30	7.5897	12.0489	17.2611	0.6787	0.6364	0.7182	2.1879	0.0214	0.0232
	14-1048 No.60	6.0334	9.8848	13.3285	0.6937	0.6191	0.7536	2.1434	0.0203	0.025
	14-1048 No.78	5.8255	9.7063	13.4785	0.6701	0.6	0.7278	2.2900	0.0203	0.0238
	14-1048 RAP	6.1235	10.1016	12.7041	0.7221	0.6048	0.803	2.0591	0.0222	0.03
	Weighted Mean Value	**5.5205**	**9.0513**	**12.3437**	**0.6118**	**0.5458**	**0.6643**	**2.7581**	**0.0184**	**0.0223**
	15-1013 No.28	4.2717	9.1398	12.4166	0.6209	0.4608	0.7443	2.9157	0.0178	0.0203

SMA-9.5/15-1012	15-1013 No.78	7.5084	10.2491	12.9949	0.7626	0.7223	0.794	1.7437	0.0269	0.0276
	15-1013 No.10	2.4468	6.9657	9.2224	0.5837	0.3546	0.7708	3.6586	0.0106	0.0155
	Weighted Mean Value	**5.1906**	**7.6273**	**9.7858**	**0.563**	**0.5101**	**0.6045**	**3.2430**	**0.019**	**0.0199**
SMA-9.5/15-1068*	15-1069 No.8	5.4936	8.3257	11.1504	0.7022	0.6507	0.749	2.0518	0.0234	0.0251
	15-1069 No.78	6.6165	10.6196	14.0412	0.691	0.6007	0.7617	2.1855	0.0264	0.0244
	15-1069 RAP	6.8625	12.43	15.5994	0.697	0.5496	0.7984	2.2789	0.0215	0.0255
	Weighted Mean Value	**5.7335**	**9.3016**	**12.2059**	**0.6253**	**0.5444**	**0.6881**	**2.6695**	**0.0223**	**0.0223**

Note: * SMA 15-1080 and SMA 15-1085 used the same aggregate blend as SMA 15-1068, as shown in Table 4.1.

CHAPTER 5 LABORATORY PERFORMANCE-BASED TESTS

To further evaluate the influence of aggregate morphological characteristics on the mechanical performance of SMA mixtures, laboratory experiments were performed on SMA mixtures. Laboratory performance-based test results such as dynamic modulus, flow number, flow number slope, the number of loading cycles to failure, rut depth, APA creep slope and seismic modulus were compared to better address how rutting and fatigue performances vary in different SMA mixtures with aggregate morphological properties. Aggregate morphology was characterized by sphericity, flatness ratio, elongation ratio, flat and elongated ratio, angularity and texture. SMA mixture performance was represented by dynamic modulus, flow number, flow number slope, the number of loading cycles to failure, rut depth, APA creep slope and seismic modulus. The dynamic modulus test, beam fatigue test and MMLS test were performed to evaluate the fatigue performance of SMA mixtures. The flow number test and APA test were performed to evaluate the rutting performance. The effects of the weighted mean morphological characteristics on the rutting and fatigue performance were analyzed in the next section. This section focuses on describing these laboratory tests and summarizing the results of laboratory tests.

Dynamic Modulus Test

The dynamic modulus is a stiffness indicator of asphalt mixtures and reflects the resilient response of asphalt mixtures. Dynamic modulus tests were performed with an Industrial Process Controls, Inc. (IPC) universal testing machine (UTM 100) with a 25 to 100 kN loading capacity in accordance with AASHTO T 342 (2011). Tests were performed on specimens prepared from gyratory compacted asphalt samples (100-mm diameter by 150-mm deep). A VTM of 7% ± 0.5% was obtained for each test specimen. Five testing temperatures ranging from -10°C to 54°C and six testing frequencies ranging from 0.1 Hz to 25 Hz were used. Tests were performed from the coldest to the warmest temperature. At each test temperature, the tests were performed from the highest to the lowest frequency. The dynamic modulus test device UTM 100 was adjusted to apply repeated haversine load cycle with a load duration of 0.1 s and a rest period of 0.9 s on the prepared eight types of SMA specimens. Load levels were selected in such a way that at each temperature-frequency combination, the applied strain was in the range of 75 to 100 microstrains. All tests were conducted in the uniaxial mode without confinement. Stress versus strain values were captured continuously to calculate dynamic modulus. Dynamic modulus was computed automatically using IPC |E*| software. The computer connected to the UTM testing device recorded the load and deformation automatically, and dynamic modulus was thereafter output. The dynamic modulus results at each temperature-frequency combination for each mixture type were reported for three replicate specimens. The average dynamic moduli of all SMA mixture specimens were calculated.

Figure 5.1 shows the dynamic modulus master curves of all types of SMA mixtures. The |E*| sin φ parameter at 10 Hz and 21°C (70°F) related to fatigue cracking from the dynamic modulus test was used to characterize the cracking potential of the mixtures. The parameter |E*|/sin φ at 10 Hz and 54.4°C (130°F) related to rutting from the dynamic modulus test was used for rutting

evaluation in this study. Similar to the field condition, a frequency of 10 Hz was selected as it most closely approximates a highway speed of about 60 miles per hour. The dynamic modulus test results under temperature 21.1°C and 54.4°C were selected to analyze the effects of coarse aggregate morphological characteristics on the mechanical performance of SMA mixtures. Table 5.1 and Table 5.2 list the dynamic modulus test results at temperatures of 21.1°C and 54.4°C for all types of SMA mixtures, respectively.

Table 5.1 Dynamic modulus test results under temperature of 21.1 °C

Mix ID	Dynamic Modulus |E*| of Specimen #1 (MPa)						φ	sin φ	|E*| sin φ
	25 Hz	10 Hz	5 Hz	1 Hz	0.5 Hz	0.1 Hz	10Hz	10Hz	10Hz
13-1070	9853.00	8350.00	7272.00	5092.00	4304.00	2852.00	18.70	0.32	2675.81
13-1081	7235.00	6121.00	5318.00	3660.00	3103.00	2034.00	19.08	0.33	1999.91
14-1021	8257.00	6976.00	6039.00	4260.00	3602.00	2320.00	18.61	0.32	2225.13
14-1047	7336.00	6191.00	5412.00	3789.00	3236.00	2107.00	18.54	0.32	1967.57
15-1012	7528.00	6311.00	5511.00	3740.00	3180.00	2022.00	19.71	0.34	2127.41
15-1068	7915.00	6535.00	5528.00	3683.00	3067.00	1968.00	21.70	0.37	2415.13
15-1080	8871.00	7595.00	6688.00	4762.00	4113.00	2771.00	18.33	0.31	2387.38
15-1084	7393.00	6190.00	5362.00	3683.00	3121.00	2028.00	19.93	0.34	2108.97
Mix ID	Dynamic Modulus |E*| of Specimen #2 (MPa)						φ	sin φ	|E*| sin φ
	25 Hz	10 Hz	5 Hz	1 Hz	0.5 Hz	0.1 Hz	10Hz	10Hz	10Hz
13-1070	7639.00	6411.00	5542.00	3815.00	3223.00	2129.00	19.29	0.33	2116.84
13-1081	7739.00	6465.00	5578.00	3808.00	3211.00	2106.00	19.68	0.34	2176.14
14-1021	7717.00	6523.00	5698.00	3973.00	3380.00	2180.00	18.33	0.31	2050.41
14-1047	7709.00	6473.00	5632.00	3924.00	3328.00	2137.00	18.86	0.32	2091.42
15-1012	6691.00	5526.00	4736.00	3119.00	2591.00	1574.00	21.53	0.37	2027.00
15-1068	7719.00	6425.00	5553.00	3783.00	3180.00	2028.00	20.28	0.35	2225.88
15-1080	10138.00	8660.00	7637.00	5502.00	4755.00	3256.00	17.53	0.30	2607.16
15-1084	7138.00	5980.00	5174.00	3544.00	2989.00	1920.00	19.87	0.34	2031.54
Mix ID	Dynamic Modulus |E*| of Specimen #3 (MPa)						φ	sin φ	|E*| sin φ
	25 Hz	10 Hz	5 Hz	1 Hz	0.5 Hz	0.1 Hz	10Hz	10Hz	10Hz
13-1070	8132.00	6843.00	5930.00	4068.00	3435.00	2262.00	19.45	0.33	2277.50
13-1081	7154.00	6071.00	5288.00	3653.00	3128.00	2086.00	19.39	0.33	2014.57
14-1021	7764.00	6579.00	5731.00	3986.00	3373.00	2161.00	18.82	0.32	2121.32
14-1047	7897.00	6719.00	5890.00	4199.00	3593.00	2377.00	17.89	0.31	2063.00
15-1012	7274.00	6033.00	5184.00	3487.00	2920.00	1822.00	20.64	0.35	2125.57
15-1068	7621.00	6409.00	5578.00	3863.00	3281.00	2144.00	19.57	0.33	2145.70
15-1080	10052.00	8546.00	7487.00	5299.00	4531.00	3006.00	18.23	0.31	2672.16
15-1084	6759.00	5706.00	4992.00	3519.00	3029.00	2040.00	18.17	0.31	1778.47
Mix ID	Average Dynamic Modulus |E*| (psi)						φ	sin φ	|E*| sin φ
	25 Hz	10 Hz	5 Hz	1 Hz	0.5 Hz	0.1 Hz	10Hz	10Hz	10Hz
13-1070	1238815.34	1044464.82	906195.55	627288.05	529967.76	350169.35	19.10	0.33	341600.78
13-1081	1069798.08	901989.46	782430.05	537654.75	456481.99	301001.57	19.40	0.33	299459.80
14-1021	1147634.97	970688.98	844506.18	590738.55	500621.79	322032.04	18.60	0.32	309458.88

14-1047	1109151.64	937088.58	818689.47	575896.36	491049.31	320098.20	18.40	0.32	295646.34
15-1012	1039098.43	863941.23	746025.58	500186.68	420174.22	261938.09	20.60	0.35	303823.10
15-1068	1124283.91	936411.74	805394.35	547710.70	460639.74	296843.83	20.50	0.35	327779.20
15-1080	1404980.20	1199026.67	1054520.77	752407.24	647786.71	436708.51	18.00	0.31	370337.99
15-1084	1029284.21	864231.31	750715.14	519525.04	441833.18	289495.25	19.30	0.33	285501.59

Table 5.2 Dynamic modulus test results under temperature of 54.4 °C

Mix ID	Dynamic Modulus |E*| of Specimen #1 (MPa)						φ	sin φ	|E*|/ sin φ
	25 Hz	10 Hz	5 Hz	1 Hz	0.5 Hz	0.1 Hz	10Hz	10Hz	10Hz
13-1070	1495	1195	1006	672.7	621.1	509.9	24.24	0.41	2912.05
13-1081	1217	942.9	765.9	483	437.6	350	24.19	0.41	2302.18
14-1021	1718	1246	972.9	525.9	415.2	226	32.2	0.53	2339.31
14-1047	945.5	666.5	510.5	283.2	231.2	143.4	31.94	0.53	1260.42
15-1012	1452	1038	800.3	442.3	356.6	212.6	31.47	0.52	1989.21
15-1068	1584	1152	923.4	544.5	458.5	287	29.72	0.5	2324.77
15-1080	1740	1278	1011	588.9	481.7	297.1	29.33	0.49	2610.23
15-1084	1107	802.9	632	376.7	315	207.2	29.5	0.49	1631.26
Mix ID	Dynamic Modulus |E*| of Specimen #2 | (MPa)						φ	sin φ	|E*|/ sin φ
	25 Hz	10 Hz	5 Hz	1 Hz	0.5 Hz	0.1 Hz	10Hz	10Hz	10Hz
13-1070	1103	815.5	632.3	270.3	225.4	152.6	28.09	0.47	1732.75
13-1081	1247	959.4	777.8	472.4	426.2	321.2	26.91	0.45	2120.79
14-1021	1076	748.6	574.9	308.8	247.9	147.9	32.02	0.53	1412.52
14-1047	965.9	682.4	525.7	292.1	238.1	146.6	31.23	0.52	1316.77
15-1012	1148	810	619.6	335.4	267.9	156	32.73	0.54	1498.79
15-1068	1503	1083	856.7	494.4	402	241.9	30.29	0.5	2148.19
15-1080	1991	1475	1172	689.4	563.2	345.8	29.07	0.49	3037.15
15-1084	983.9	701.4	550.3	320.4	266.3	172.1	31.15	0.52	1356.56
Mix ID	Dynamic Modulus |E*| of Specimen #3 (MPa)						φ	sin φ	|E*| /sin φ
	25 Hz	10 Hz	5 Hz	1 Hz	0.5 Hz	0.1 Hz	10Hz	10Hz	10Hz
13-1070	1289	978.2	784.1	402.2	346.6	259.2	26.27	0.44	2211.15
13-1081	1110	847.5	680.3	393.9	354	269.8	27.07	0.45	1863.19
14-1021	1259	886.1	676.3	361.4	282.7	160.6	31.95	0.53	1675.24
14-1047	1074	752.5	591.4	339	278.6	176.8	31.1	0.52	1457.49
15-1012	1284	907.7	697.6	374	296.4	170.4	32.53	0.54	1688.75
15-1068	1506	1093	868.2	498	406.4	244.8	29.62	0.49	2212.47
15-1080	2055	1514	1192	677.2	541.9	320.1	30.33	0.5	2999.52
15-1084	1085	787.4	621.1	357.7	293.6	179.8	30.11	0.5	1570.31
Mix ID	Average Dynamic Modulus (psi)						φ	sin φ	|E*| /sin φ
	25 Hz	10 Hz	5 Hz	1 Hz	0.5 Hz	0.1 Hz	10Hz	10Hz	10Hz
13-1070	187920.5	144491.4	117113.1	65034.9	57681.49	44560.42	26.2	0.44	327423.8
13-1081	172788.3	132941.6	107521.3	65233.12	58875.64	313.67	26.1	0.44	302324.2

14-1021	195945.9	139270	107526.1	57826.53	45725.55	25840.88	32.1	0.53	262200.8
14-1047	144331.9	101594.1	78687.79	44202.66	36157.9	22567.87	31.4	0.52	195083.4
15-1012	187775.5	133226.8	102372.4	55679.97	44521.74	26058.44	32.2	0.53	250127.7
15-1068	222052.7	160895.2	128034.5	74302.81	61249.42	37405.22	29.9	0.5	322915.1
15-1080	279729.4	206292	163167.4	94540.41	76715.27	46557.1	29.6	0.49	417836.9
15-1084	153541.7	110794.3	87187	50995.26	42297.83	27030.19	30.3	0.5	219700.9

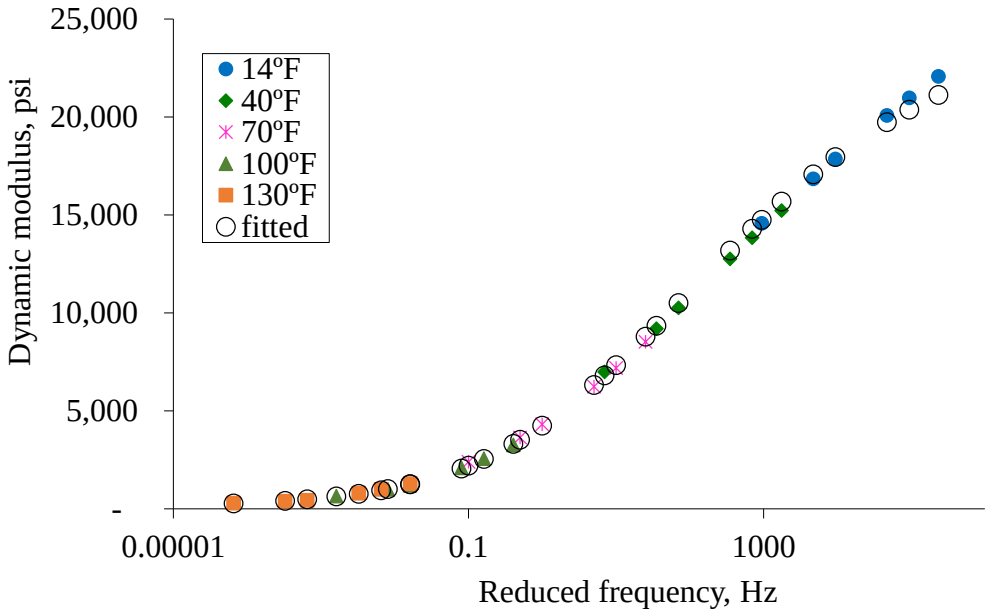

(a)

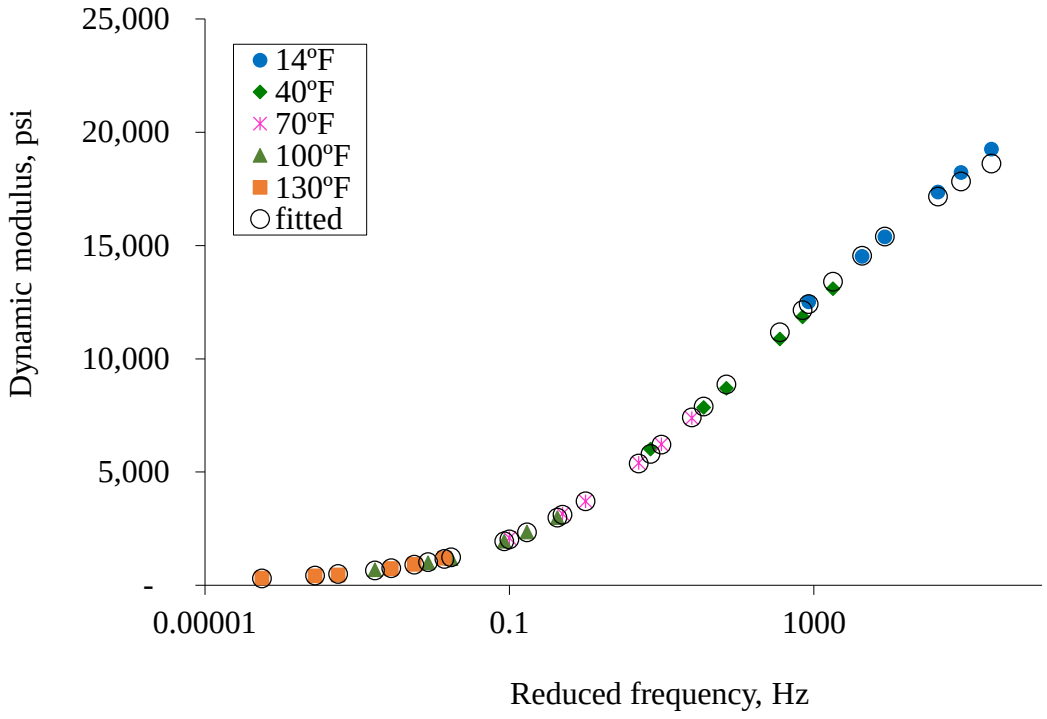

(b)

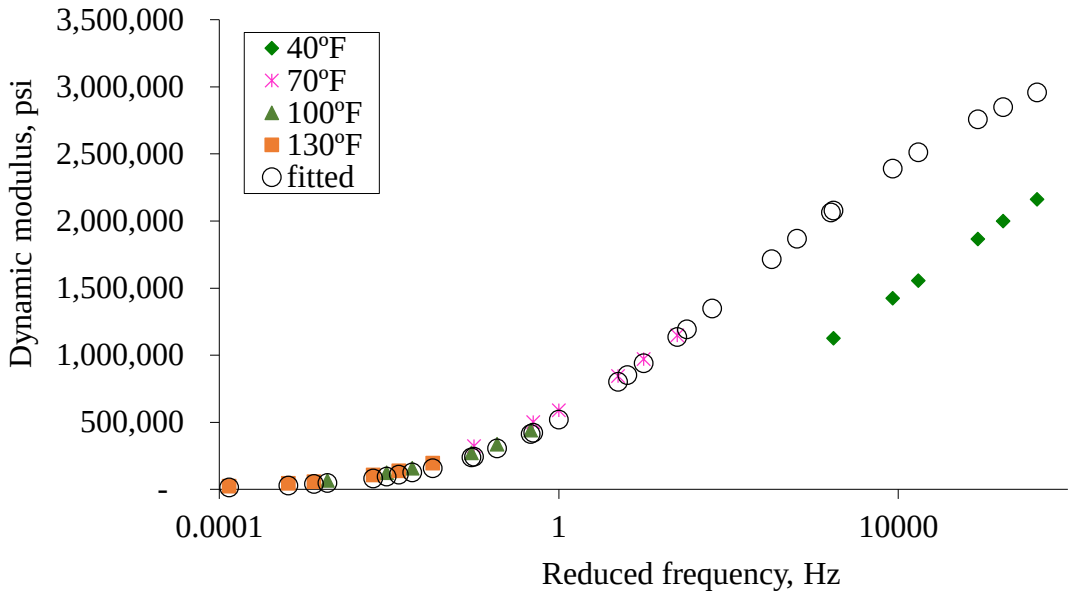
3,500,000
3,000,000
2,500,000
2,000,000
1,500,000
1,000,000
500,000
-
Dynamic modulus, psi
40°F
70°F
100°F
130°F
fitted
0.0001
1
10000
Reduced frequency, Hz

(c)

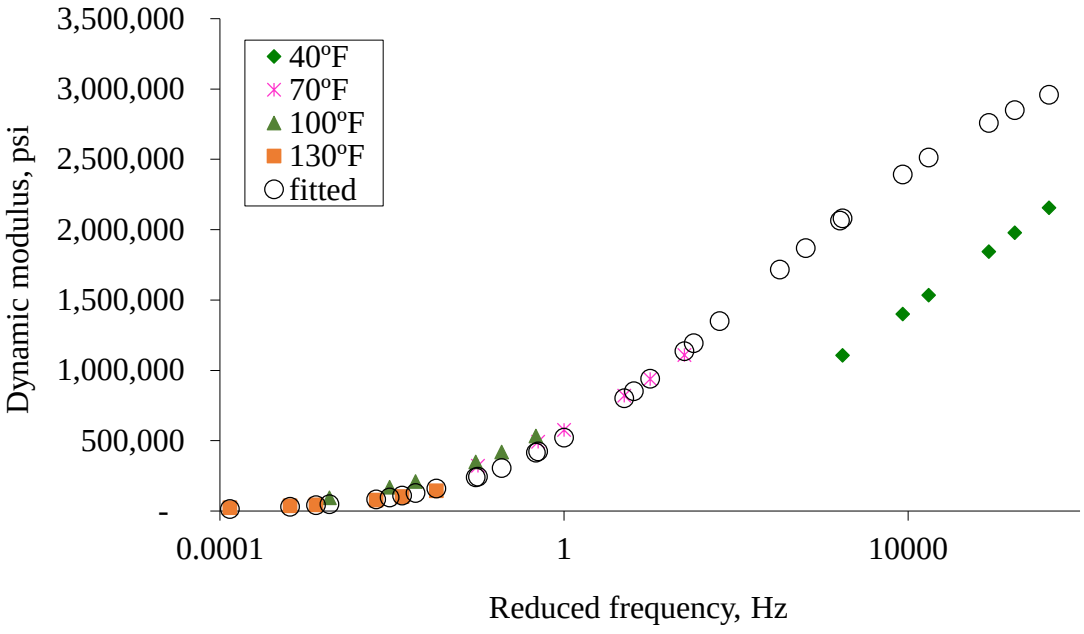
3,500,000
3,000,000
2,500,000
2,000,000
1,500,000
1,000,000
500,000
-
Dynamic modulus, psi
40°F
70°F
100°F
130°F
fitted
0.0001
1
10000
Reduced frequency, Hz

(d)

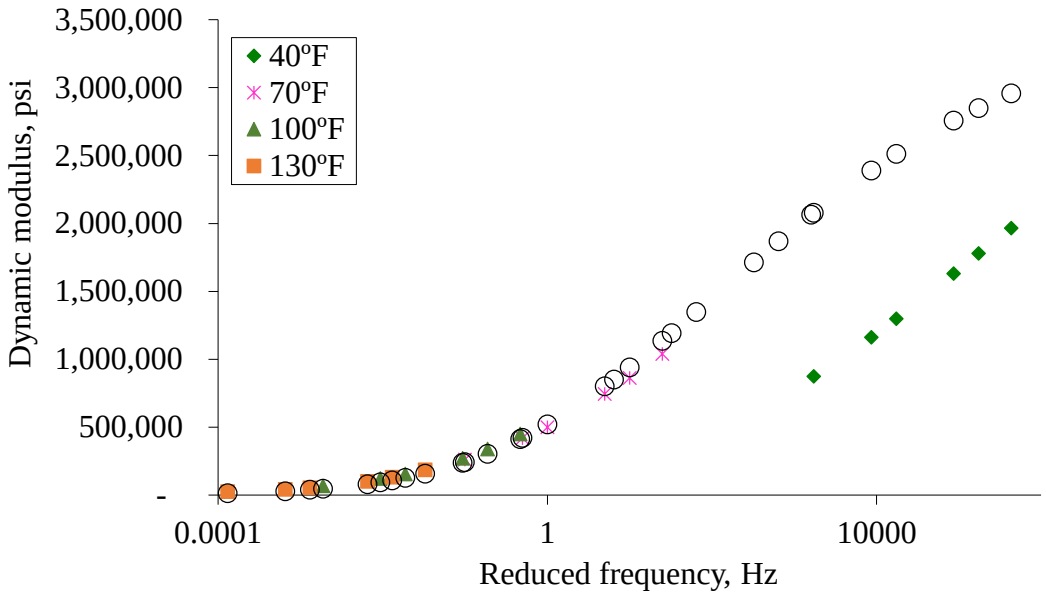
3,500,000
3,000,000
2,500,000
2,000,000
1,500,000
1,000,000
500,000
-
Dynamic modulus, psi
40°F
70°F
100°F
130°F
0.0001
1
10000
Reduced frequency, Hz

(e)

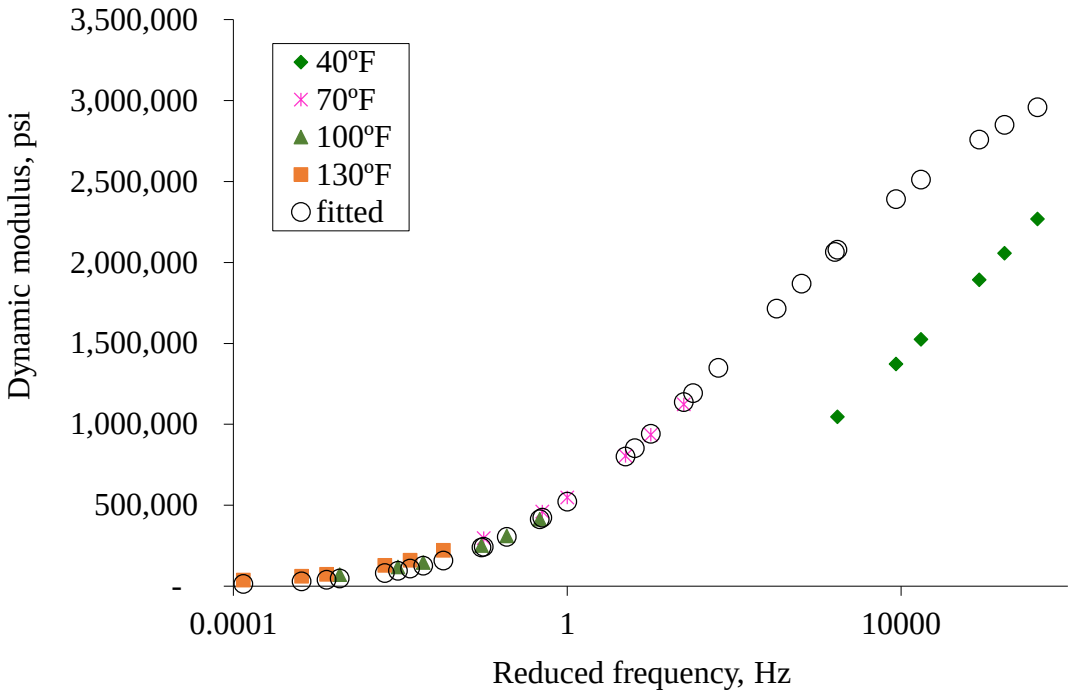
3,500,000
3,000,000
2,500,000
2,000,000
1,500,000
1,000,000
500,000
-
Dynamic modulus, psi
40°F
70°F
100°F
130°F
fitted
0.0001
1
10000
Reduced frequency, Hz

(f)

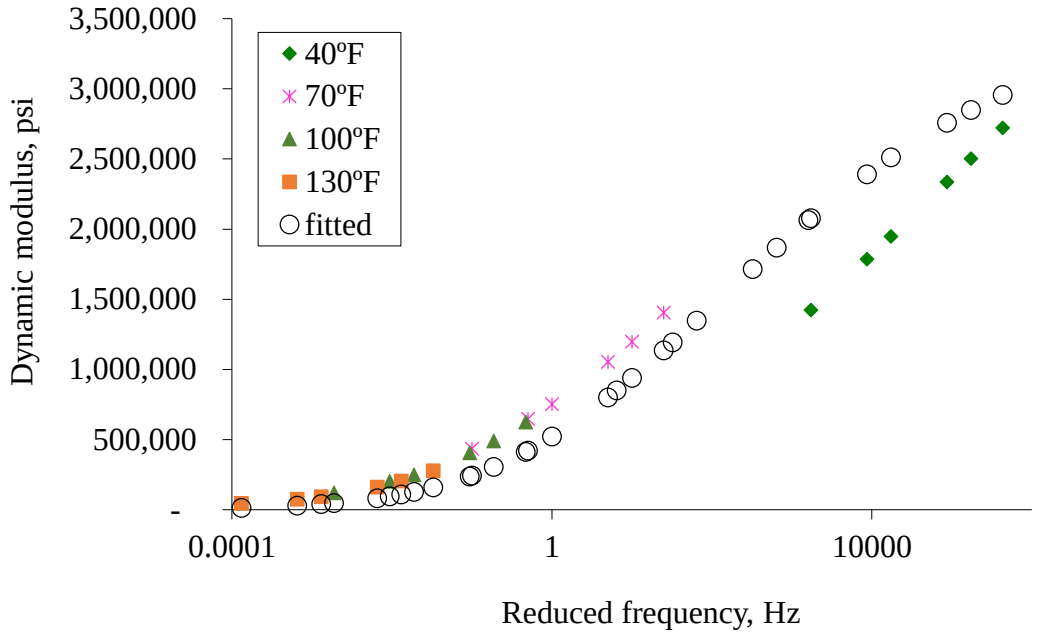

(g)

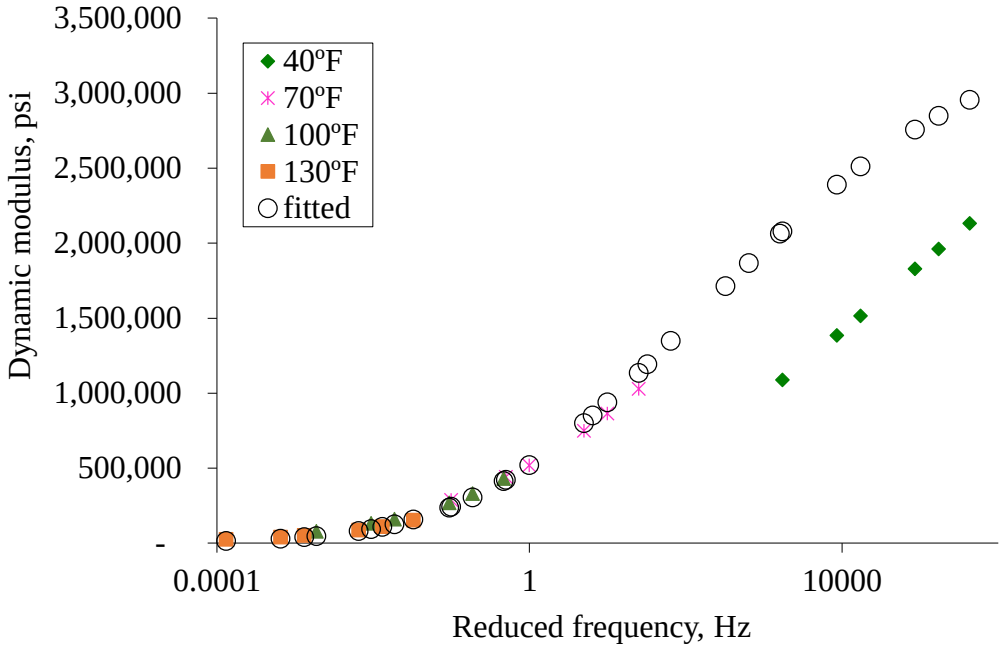

(h)

Figure 5.1 Dynamic modulus master curves of all types of SMA mixtures. (a) SMA 13-1070; (b) SMA 13-1081; (c) SMA 14-1021; (d) SMA 14-1047; (e) SMA 15-1012; (f) SMA 15-1068; (g) SMA 15-1080; (h) SMA 15-1084.

Flow Number Test

The same IPC universal testing machine (UTM 100) was used to conduct the flow number tests. All flow number tests were conducted on the three specimens previously tested for dynamic modulus. The flow number test captures fundamental material properties of an asphalt mixture that evaluate rutting resistance. Tests were conducted at 54°C (130°F), which is based on

LTPPBind software that represents the 50% reliability maximum high pavement temperature at locations in central Virginia. A repeated haversine axial compressive load pulse of 0.1 second followed by a rest or dwell period of 0.9 seconds every 1.0 second was applied to the specimens. This test is different from the flow time test because it applies a dynamic load and provides periodic recovery periods for the test specimen. The repeated load permanent deformation tests were performed in both unconfined and confined modes, which are commonly used in the laboratory. For the unconfined mode, a deviator stress of 600 kPa was applied. The tests were continued for 10,000 cycles or a permanent strain of 5%, whichever came first. During the test, permanent strain (ε_p) versus the number of loading cycles was recorded automatically and then plotted. Figure 5.2 shows the plots of cumulative permanent strain versus number of loading cycles for each type of SMA mixture under unconfined condition. The plots of cumulative permanent strain versus number of loading cycles for all types of SMA mixtures under confined condition are included in appendix A. The results were used to estimate flow number value and flow number slope. The permanent deformation behavior of SMA mixtures can be characterized by these two test parameters. They were proven to have close correlations with the rutting performance in the NCHRP study (Witczak et al, 2002). The general relationship between the cumulative permanent strain and the loading cycles includes three stages: primary, secondary and tertiary as shown in Figure 5.3.

Flow number was determined numerically as the cycle number at which the permanent strain rate is at a minimum based on the Francken model (Roy et al., 2015). Figure 5.4 presents the plots of rate of change of permanent strain versus loading cycles on a log-log scale for flow number test under unconfined condition for all types of SMA mixtures. The plots of rate of change of permanent strain versus loading cycles on a log-log scale for flow number test under confined condition for all types of SMA mixtures are included in appendix B. The point of minimum rate of change corresponds to flow number. Table 5.3 and Table 5.4 provide the flow number value results for unconfined and confined conditions, respectively. The flow numbers obtained from the flow number tests conducted on these eight types of SMA mixtures under unconfined condition varied greatly, indicating the different rutting resistance potentials of these SMA mixtures, while flow number from the confined condition for all types of SMA mixtures are approximately the same. Figure 5.5 shows the flow number of each specimen and the average flow number of each type of SMA mixture under unconfined conditions. SMA 15-1068 has the highest flow number, it may be due to the fact that high-polymer modified asphalt binder was used in this type of SMA mixture.

Flow number slope is the slope of the secondary stage from Figure 5.3. Figure 5.6 shows the same relationship plotted on a log-log scale. The slope represents the rate of permanent strain change as a function of the change in loading cycles. The estimation of the slope parameter is determined from a regression analysis of the linear portion of the permanent strain versus number of cycles curve on a log-log scale. Figure 5.7 shows regression analyses for all types of SMA mixtures under unconfined condition. The dash lines are the regression lines. Regression analyses performed for all types of SMA mixtures under confined condition are included in appendix C. Flow number slope has close relation with simulated rutting in pavement. Table 5.5 and Table 5.6 provide the flow number slope results for unconfined and

confined conditions, respectively. Unconfined flow number test results were used to evaluate the rutting performance of all the SMA mixtures.

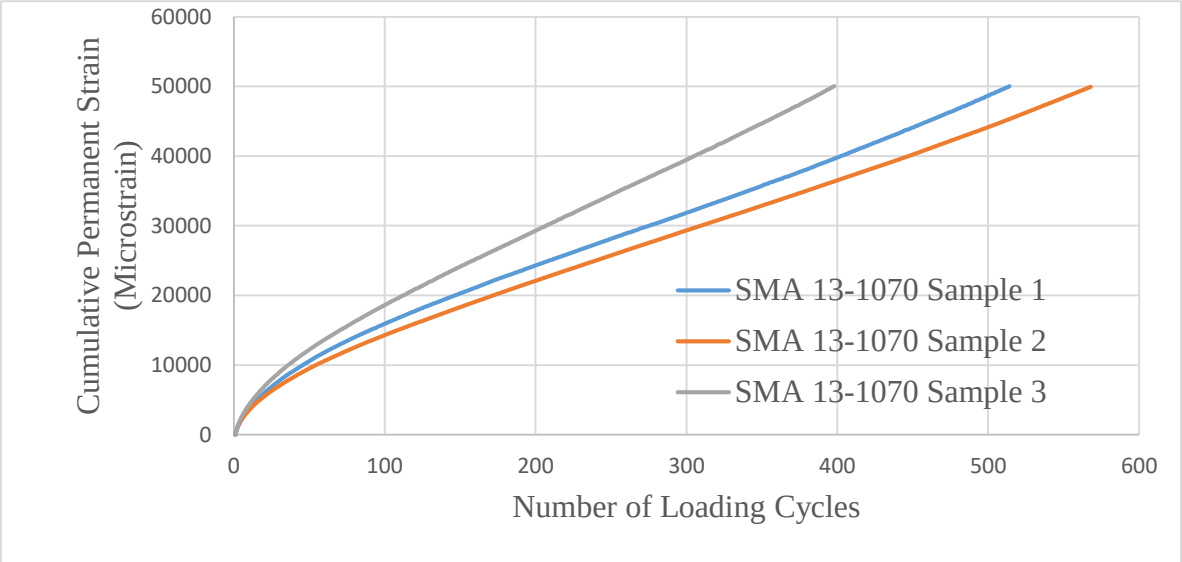

(a)

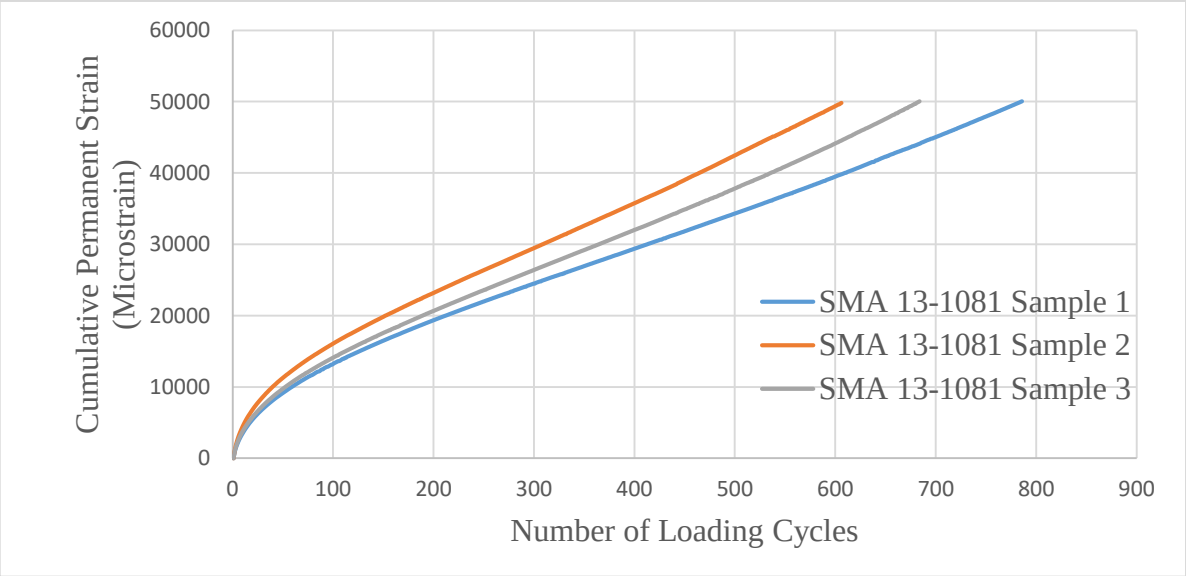

(b)

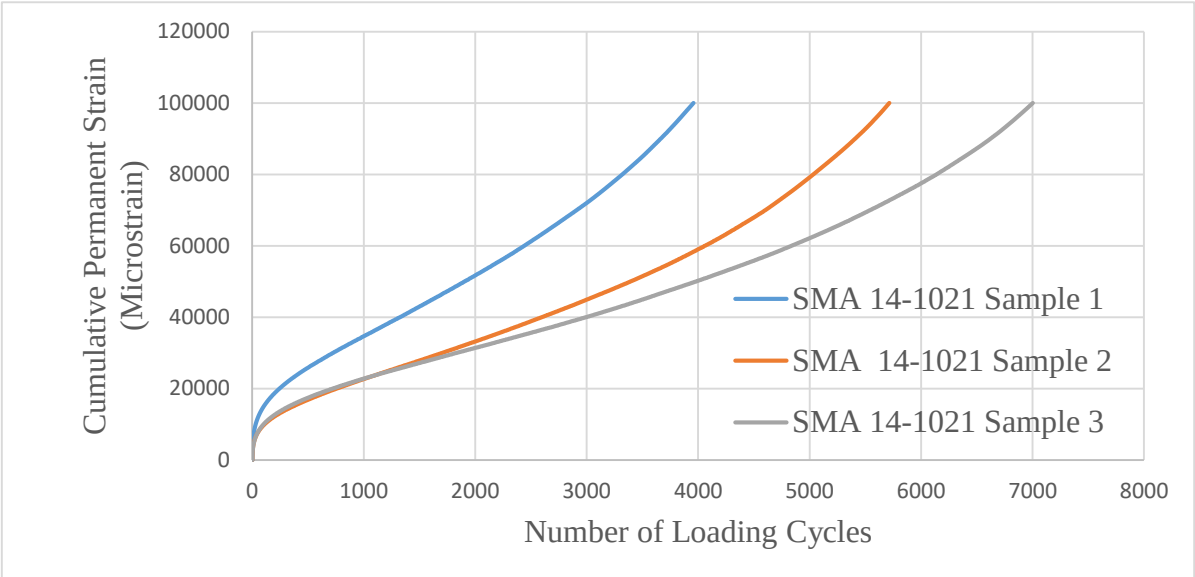
Cumulative Permanent Strain (Microstrain)
120000
100000
80000
60000
40000
20000
0
0
1000
2000
3000
4000
5000
6000
7000
8000
Number of Loading Cycles
SMA 14-1021 Sample 1
SMA 14-1021 Sample 2
SMA 14-1021 Sample 3

(c)

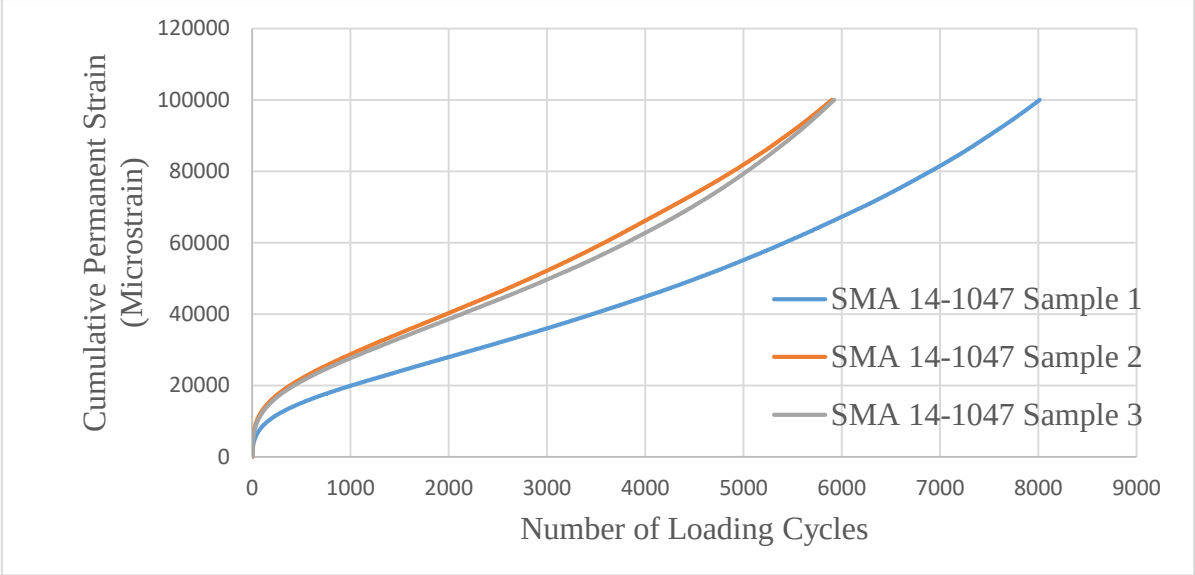
Cumulative Permanent Strain (Microstrain)
120000
100000
80000
60000
40000
20000
0
0
1000
2000
3000
4000
5000
6000
7000
8000
9000
Number of Loading Cycles
SMA 14-1047 Sample 1
SMA 14-1047 Sample 2
SMA 14-1047 Sample 3

(d)

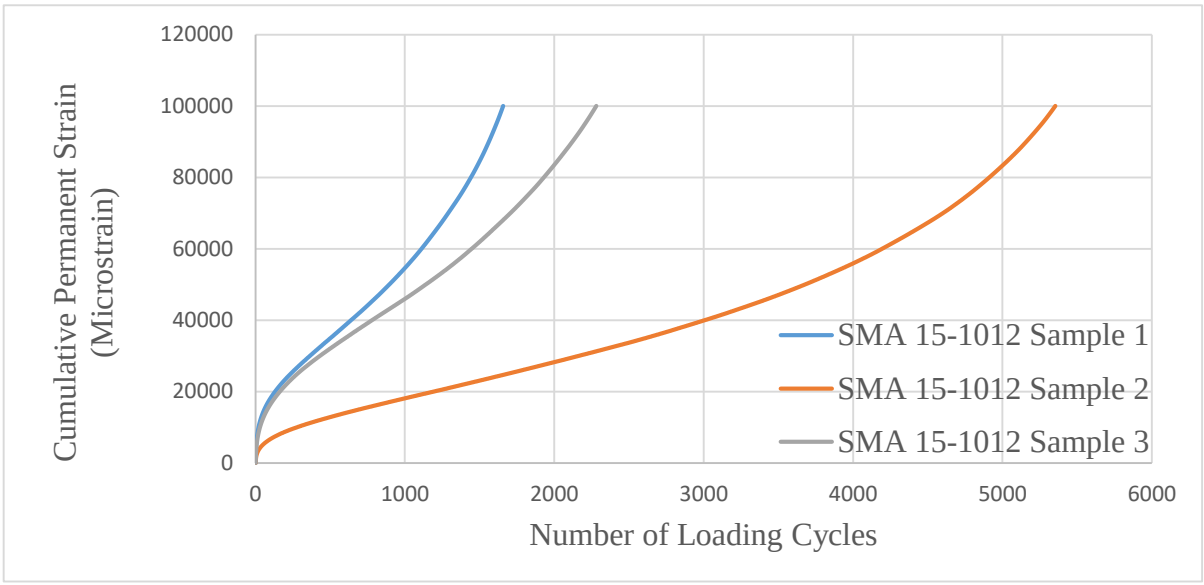
Cumulative Permanent Strain (Microstrain)
120000
100000
80000
60000
40000
20000
0
0
1000
2000
3000
4000
5000
6000
Number of Loading Cycles
SMA 15-1012 Sample 1
SMA 15-1012 Sample 2
SMA 15-1012 Sample 3

(e)

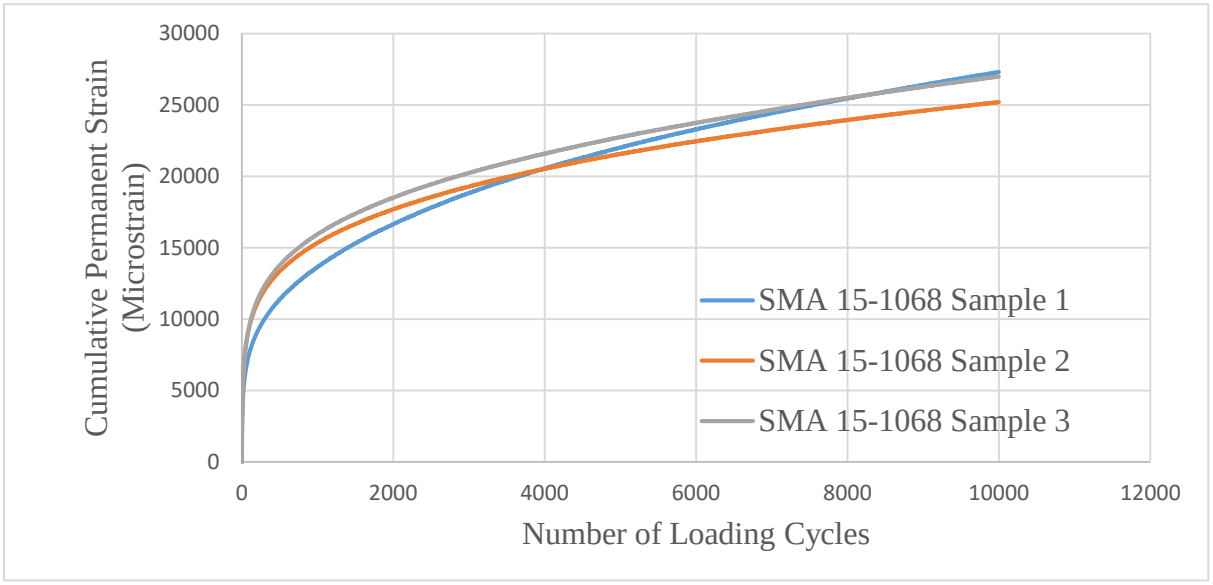
Cumulative Permanent Strain (Microstrain)
30000
25000
20000
15000
10000
5000
0
0
2000
4000
6000
8000
10000
12000
Number of Loading Cycles
SMA 15-1068 Sample 1
SMA 15-1068 Sample 2
SMA 15-1068 Sample 3

(f)

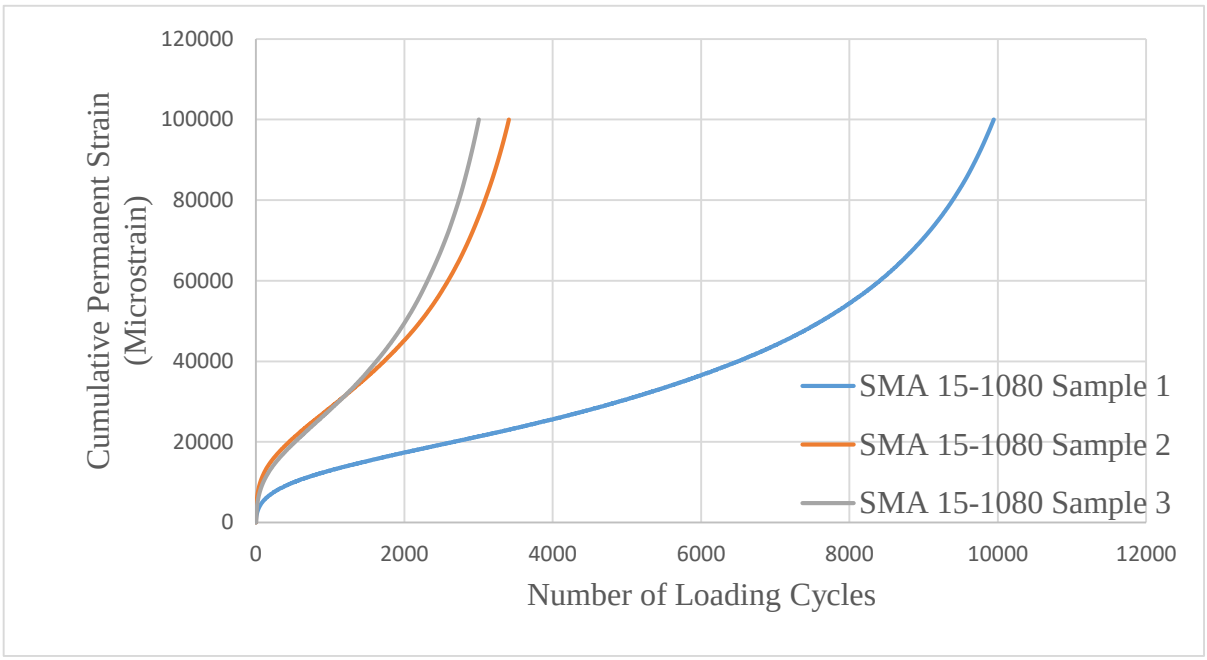

(g)

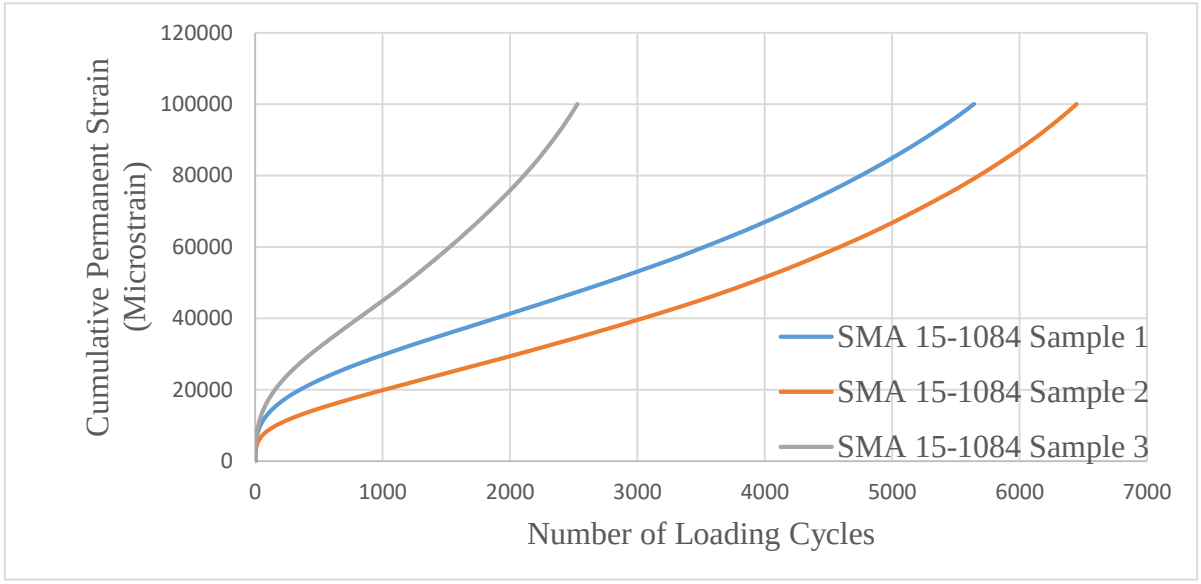

(h)

Figure 5.2 Plots of the cumulative permanent strain versus number of loading cycles for flow number test under unconfined condition for each type of SMA mixture. (a) SMA 13-1070; (b) SMA 13-1081; (c) SMA 14-1021; (d) SMA 14-1047; (e) SMA 15-1012; (f) SMA 15-1068;

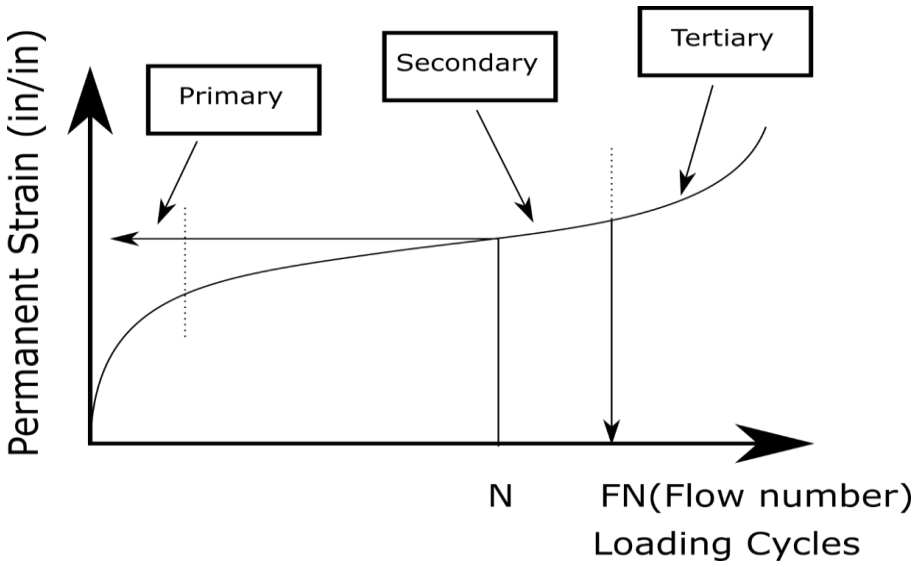

Figure 5.3 General relationship between permanent strain and loading cycles (Witczak et al, 2002)

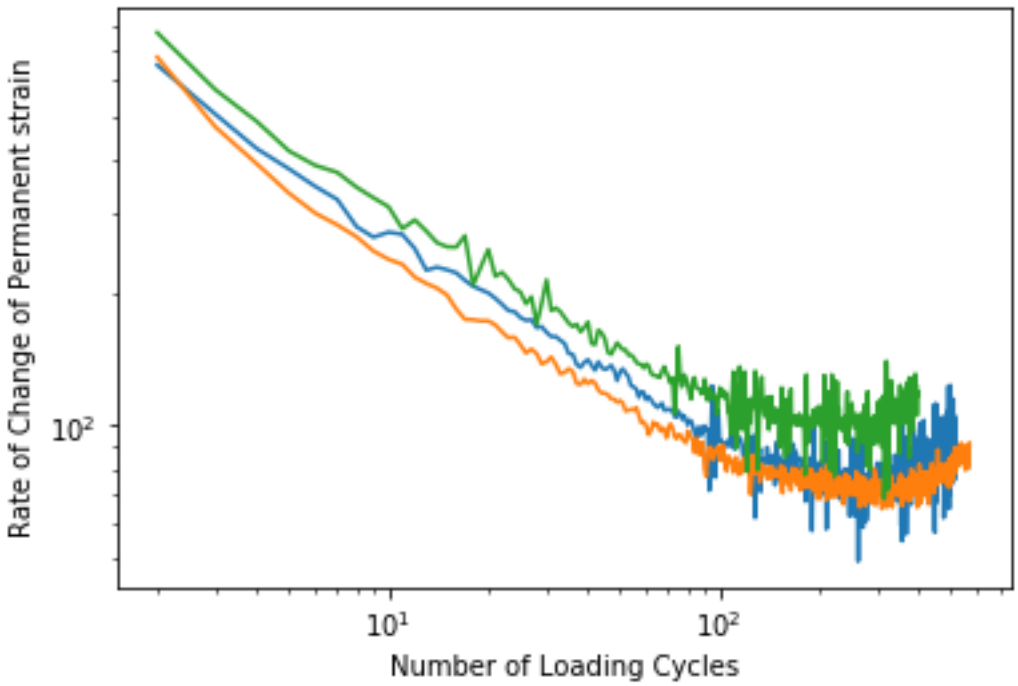

(a) SMA 13-1070

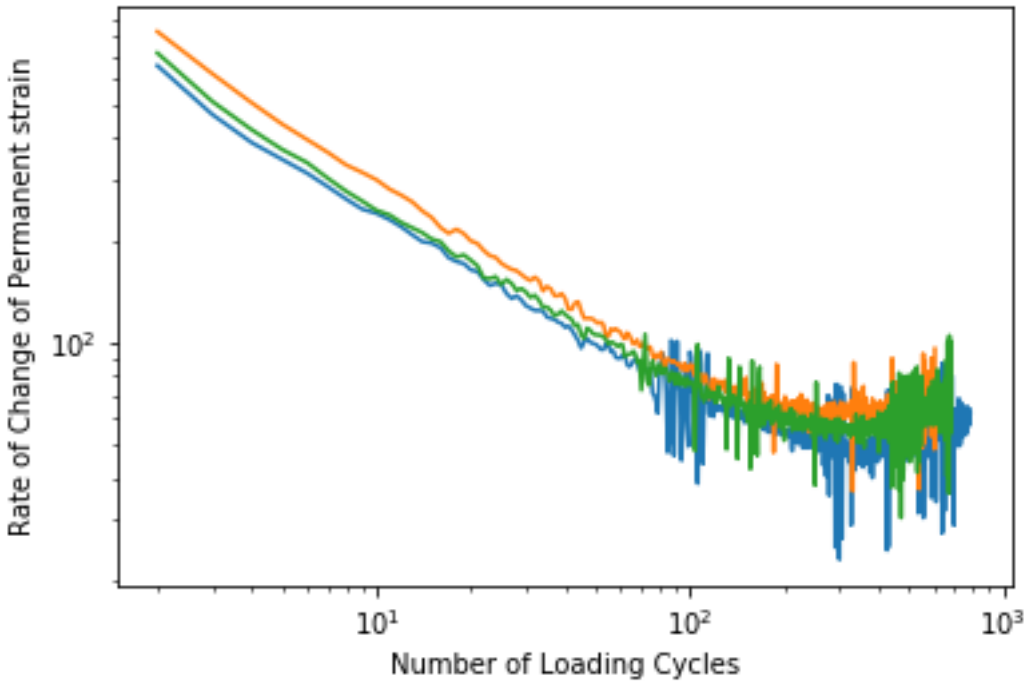

(b) SMA 13-1081

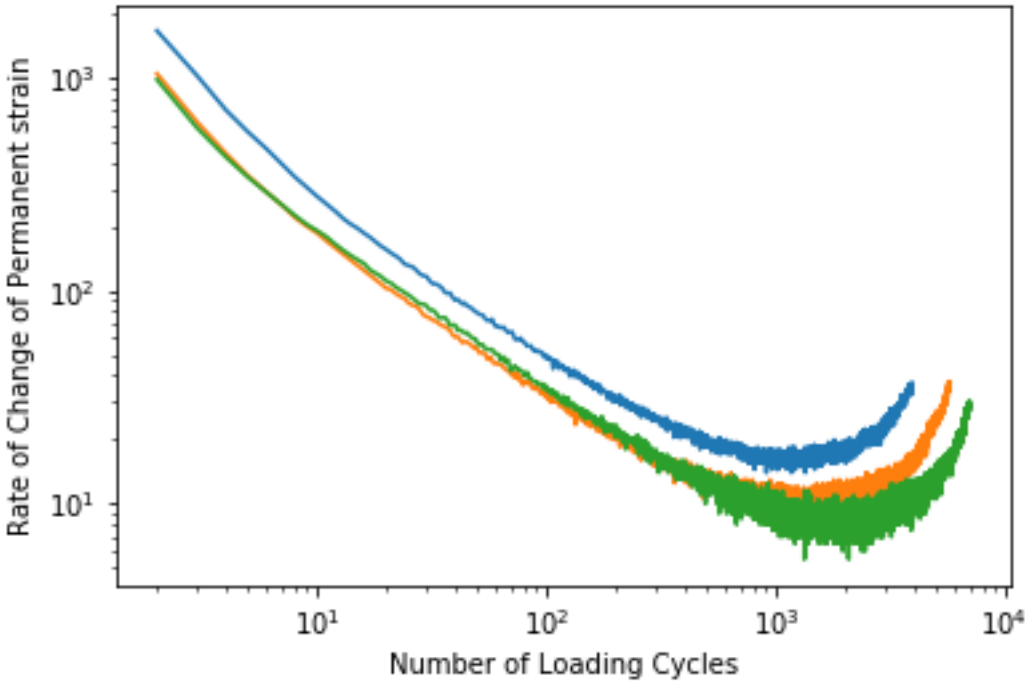

(c) SMA 14-1021

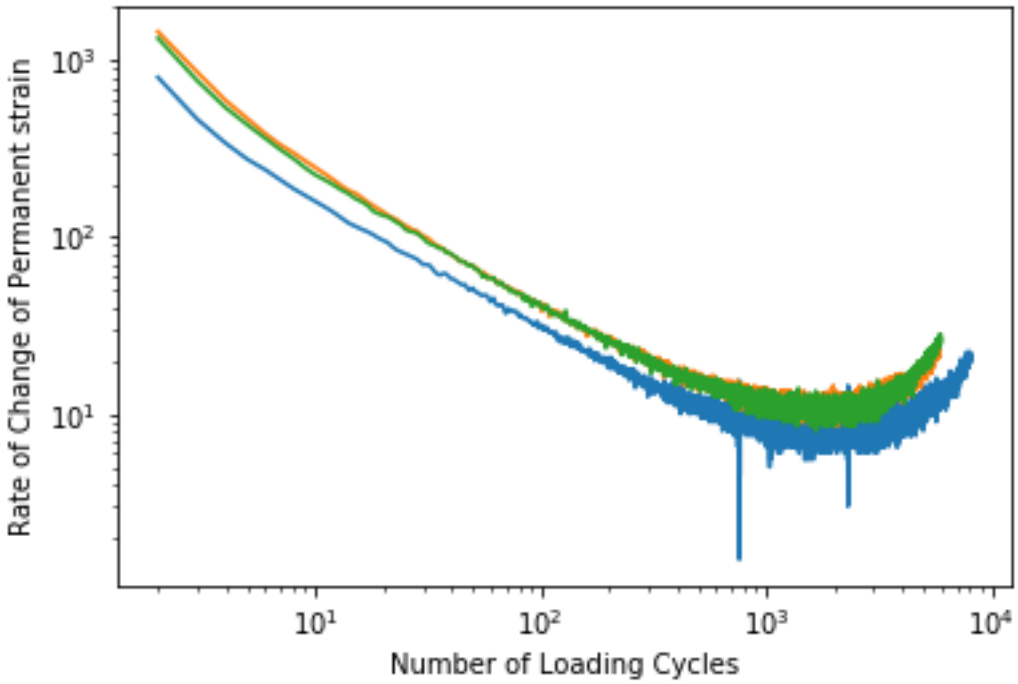

(d) SMA 14-1047

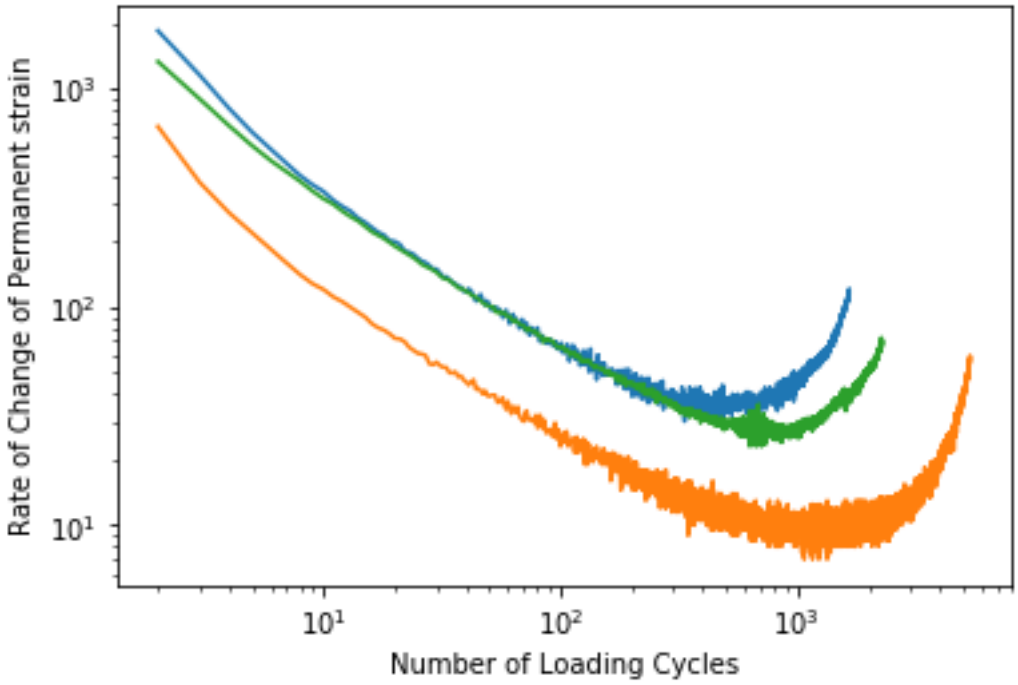

(e) SMA 15-1012

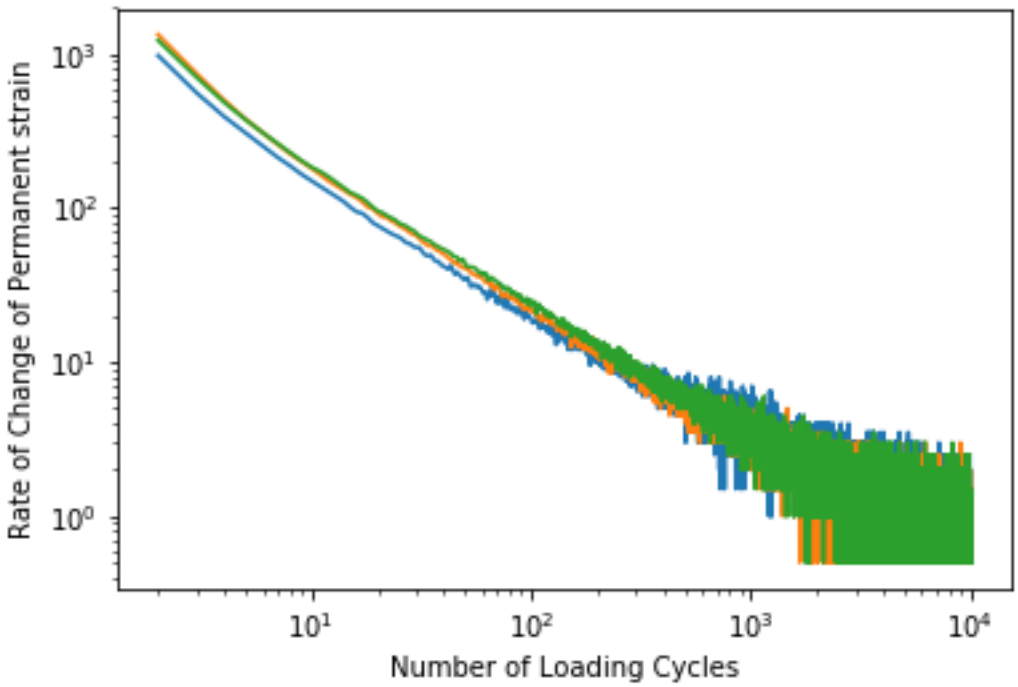

(f) SMA 15-1068

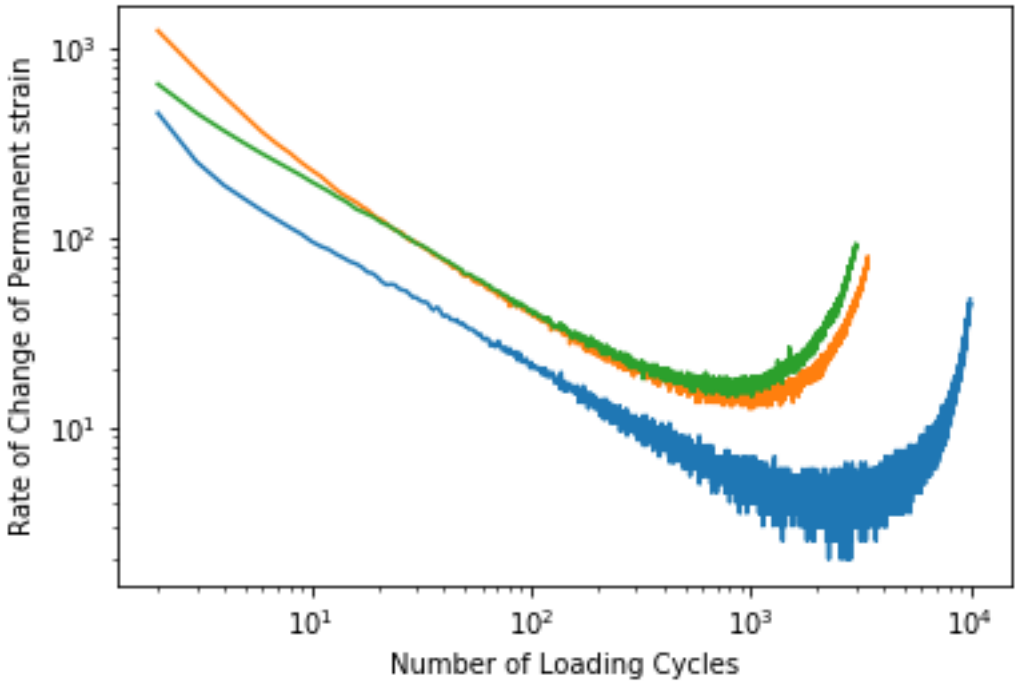

(g) SMA 15-1080

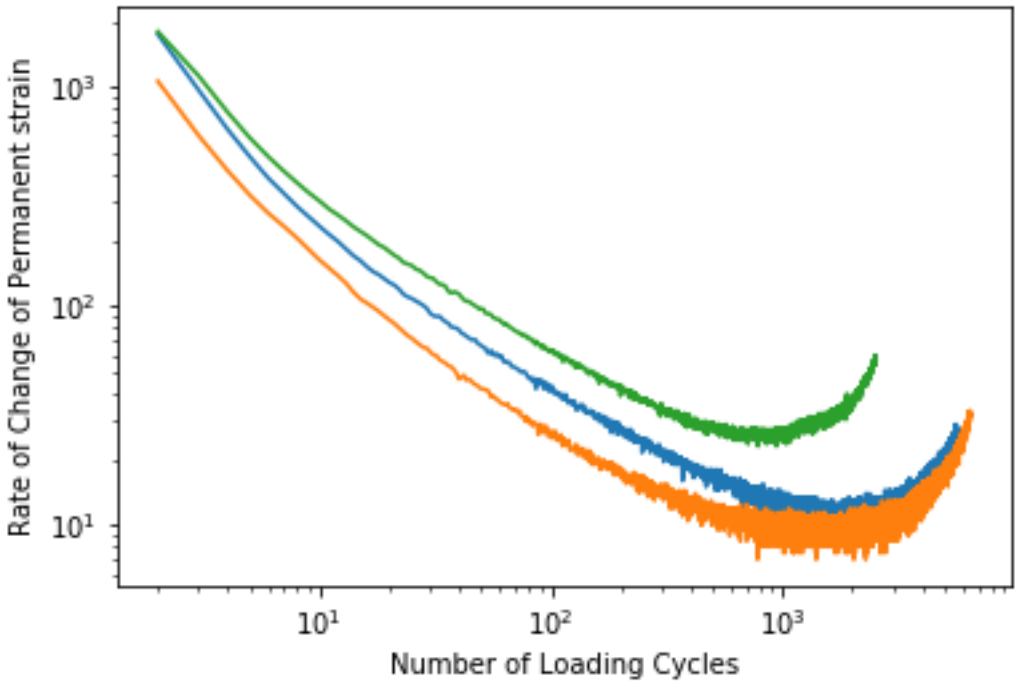

(h) SMA 15-1084

Figure 5.4 Plots of rate of change of permanent strain versus number of loading cycles for flow number test under unconfined condition for each type of SMA mixtures.

.

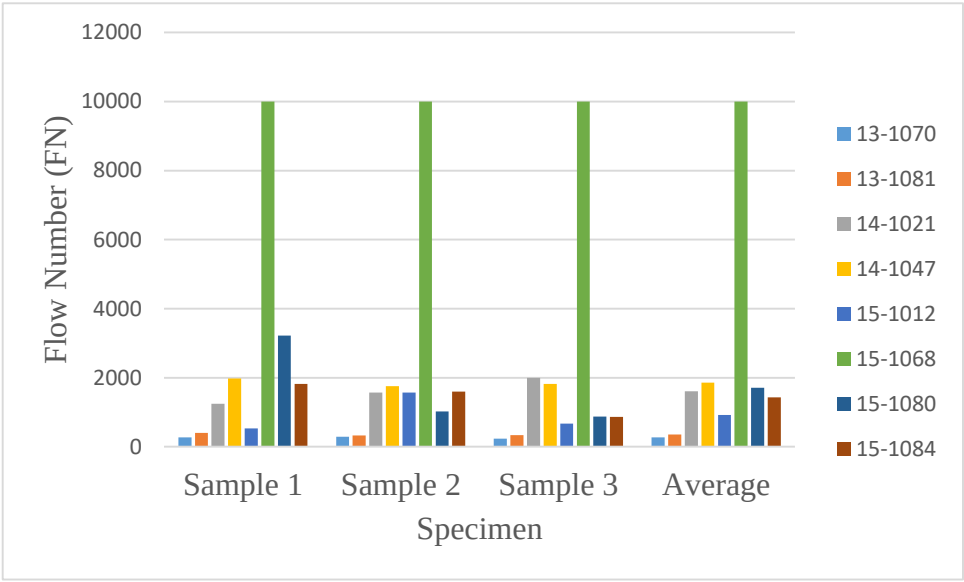

Figure 5.5 Flow numbers of SMA mixtures under unconfined condition

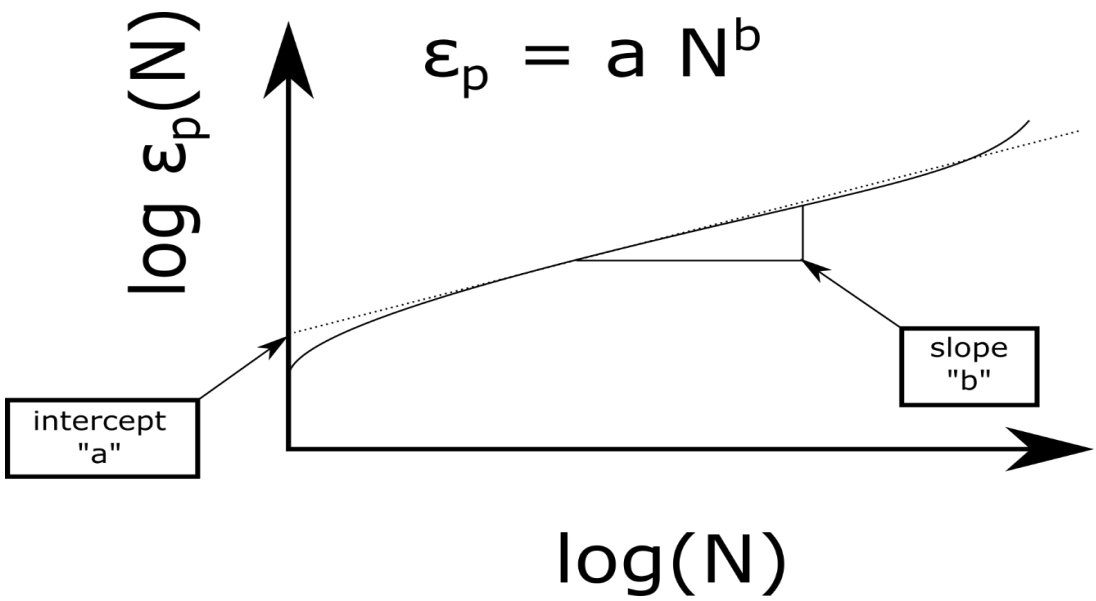

Figure 5.6 Flow number slope when plotted on a log-log scale (Witczak et al, 2002)

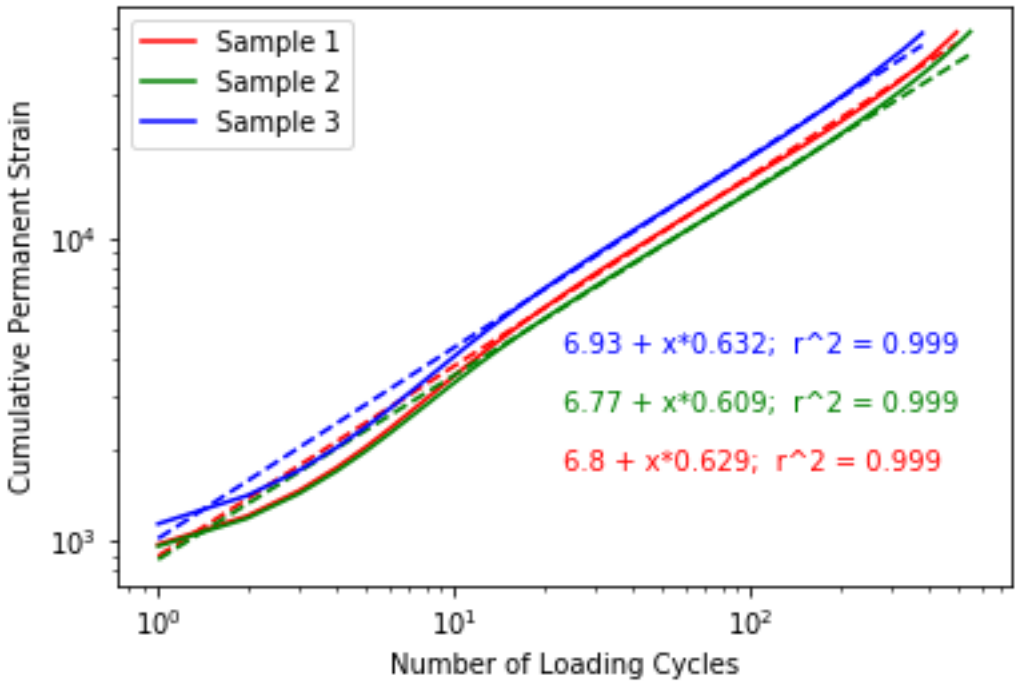

(a) SMA 13-1070

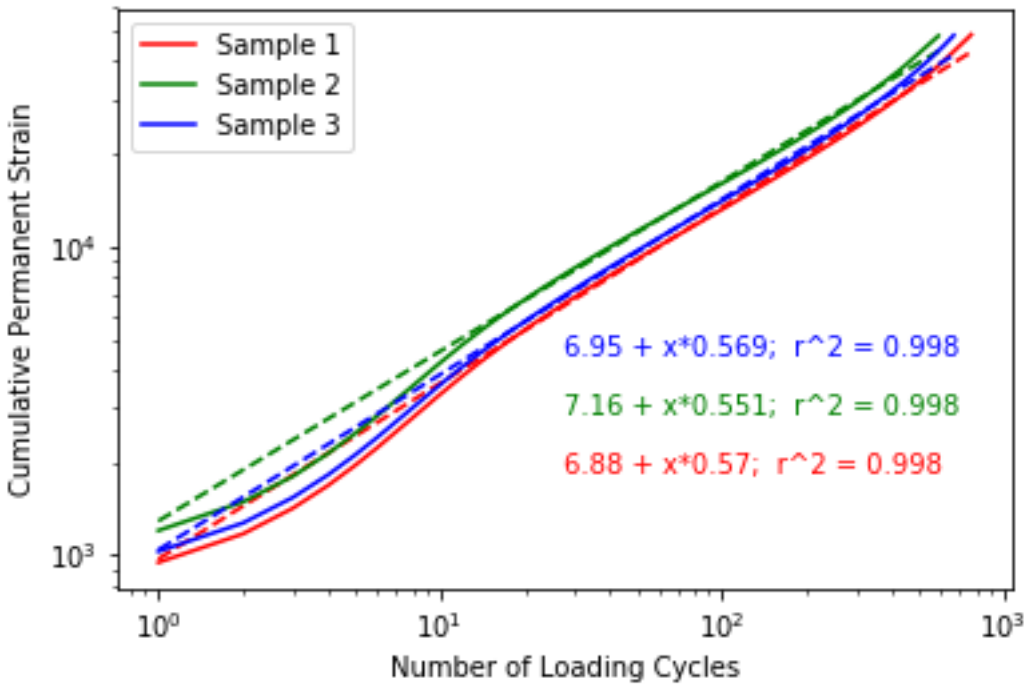

(b) SMA 13-1081

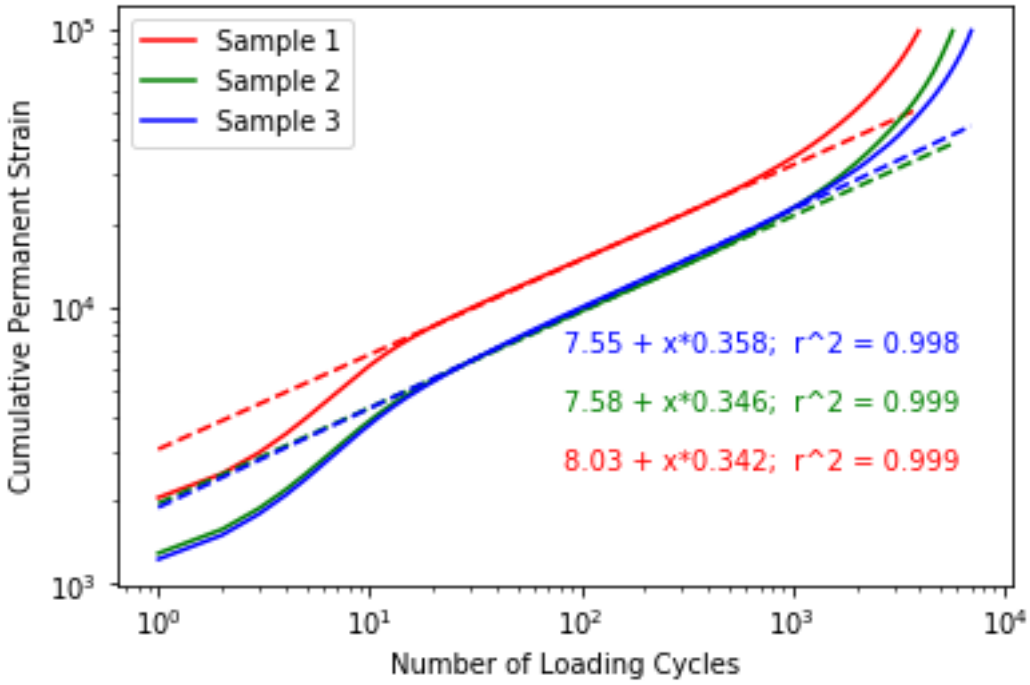

(c) SMA 14-1021

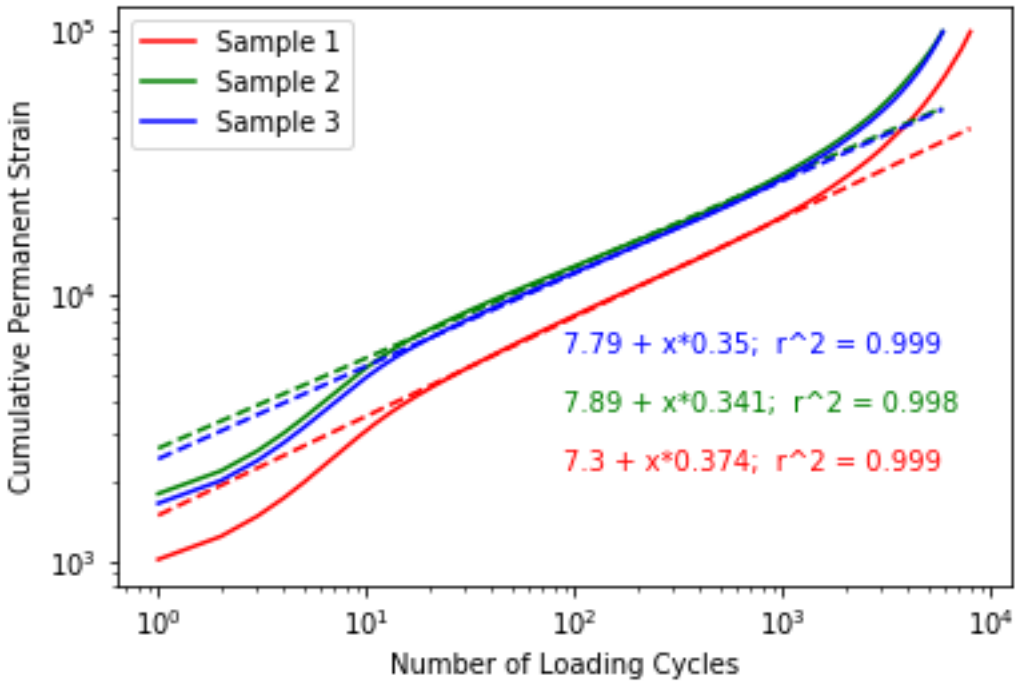

(d) SMA 14-1047

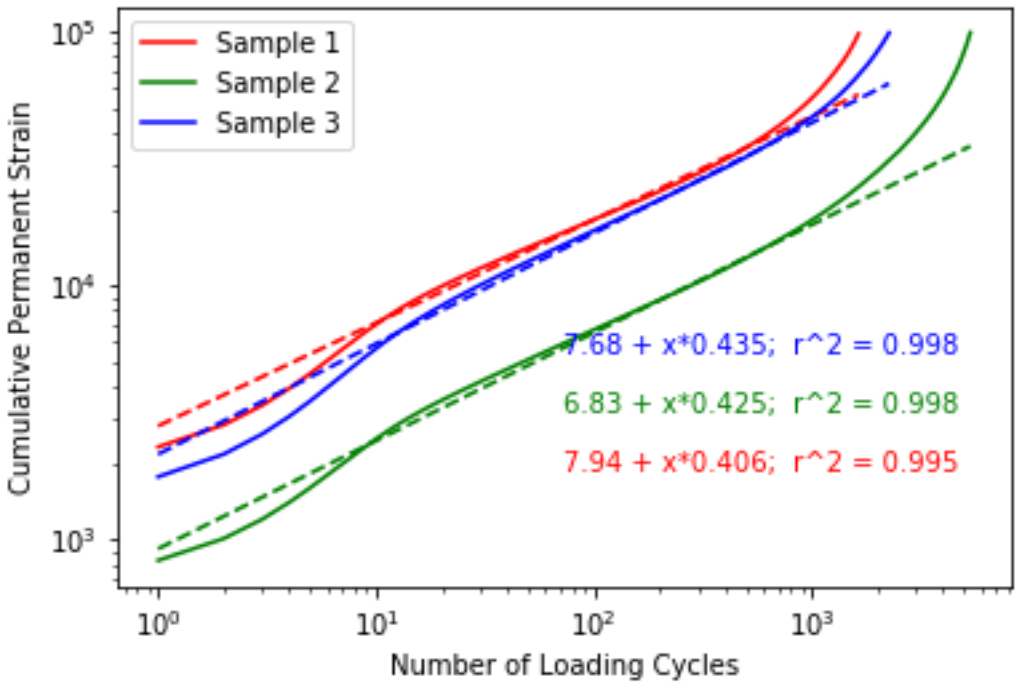

(e) SMA 15-1012

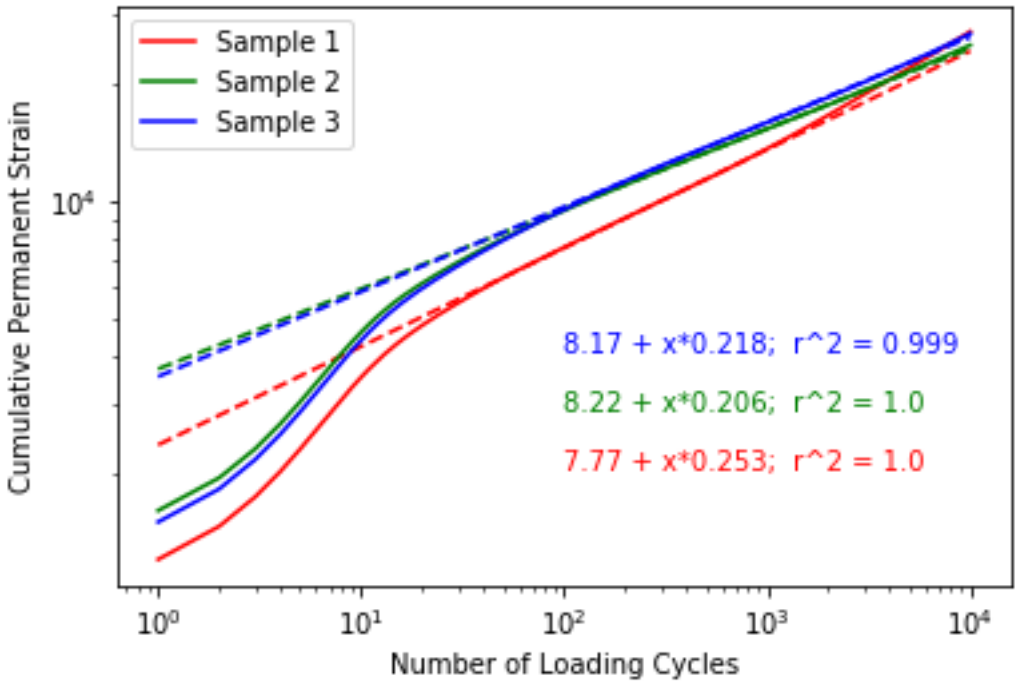

(f) SMA 15-1068

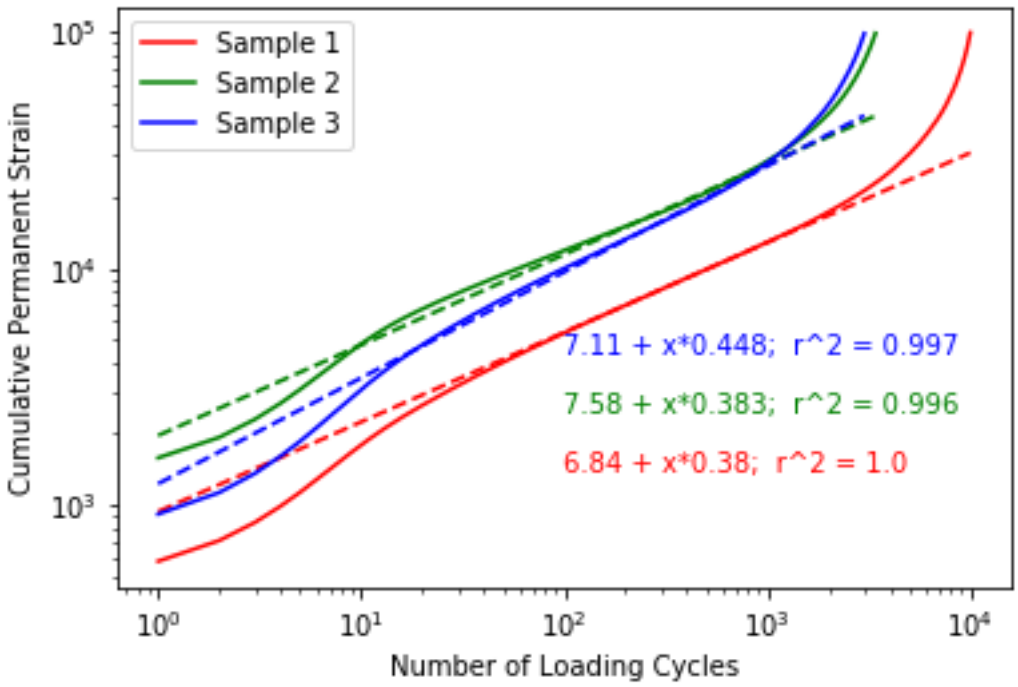

(g) SMA 15-1080

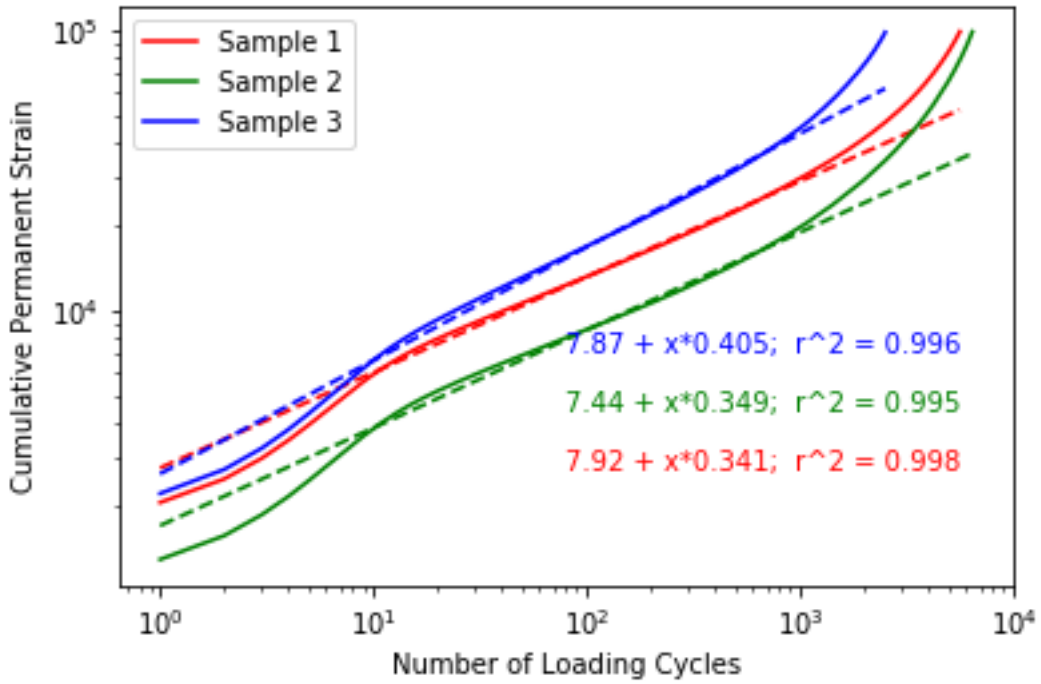

(h) SMA 15-1084

Figure 5.7 Flow number slope from plot of permanent strain versus number of loading cycles on log-log scale for flow number test under unconfined condition for each type of SMA mixture.

Table 5.3 Flow number of SMA mixtures under unconfined condition

Mix ID	unconfined Flow Number (Cycles/Micro strain at flow point)			
	Sample 1	Sample 2	Sample 3	Average
13-1070	275 (30039)	289 (28529)	238 (33185)	267 (30584)
13-1081	400 (29431)	323 (30989)	341 (28712)	355 (29711)
14-1021	1249 (38894)	1572 (28865)	1994 (31491)	1605 (33083)
14-1047	1981 (27857)	1760 (37589)	1823 (36705)	1855 (34050)
15-1012	527 (36032)	1568 (24112)	670 (36988)	922 (32377)
15-1068	10000 (27373)	10000 (25218)	10000 (27032)	1000 (26541)
15-1080	3218 (22778)	1025 (29019)	876 (26078)	1706 (25958)
15-1084	1823 (39302)	1596 (25695)	861 (41469)	1426 (35489)

Table 5.4 Flow number values of SMA mixtures under confined condition

Mix ID	Confined Flow Number (Cycles/Micro strain at flow point)			
	Sample 1	Sample 2	Sample 3	Average
13-1070	10000 (26376)	10000 (24947)	10000 (16825)	10000 (22716)
13-1081	10000 (17357)	10000 (19661)	9472 (49849)	9824 (28956))
14-1021	10000 (79254)	10000 (24662)	10000 (33279)	10000 (45732)
14-1047	10000 (21414)	10000 (27983)	10000 (21280)	10000 (23559)
15-1012	10000 (20395)	10000 (29148)	-	10000 (24772)
15-1068	10000 (18725)	10000 (20376)	10000 (17652)	10000 (18918)
15-1080	10000 (14920)	10000 (22210)	10000 (15691)	10000 (17607)
15-1084	7414 (25385)	10000 (24459)	10000 (18982)	9138 (22942)

Table 5.5 Flow number slopes of SMA mixtures under unconfined condition

Mix ID	Unconfined Flow Number Test			
	Flow Number Slope			
	Sample 1	Sample 2	Sample 3	Average
13-1070	0.629	0.609	0.632	0.623
13-1081	0.570	0.551	0.569	0.563
14-1021	0.342	0.346	0.358	0.349
14-1047	0.374	0.341	0.350	0.355
15-1012	0.406	0.425	0.435	0.422
15-1068	0.253	0.206	0.218	0.226
15-1080	0.380	0.383	0.448	0.404
15-1084	0.341	0.349	0.405	0.365

Table 5.6 Flow number slopes of SMA mixtures under confined condition

Mix ID	Confined Flow Number Test			
	Flow Number Slope			
	Sample 1	Sample 2	Sample 3	Average
13-1070	0.170	0.193	0.198	0.187
13-1081	0.174	0.249	0.287	0.237
14-1021	0.211	0.129	0.172	0.171

14-1047	0.183	0.211	0.145	0.180
15-1012	0.184	0.105	0.194	0.161
15-1068	0.132	0.164	0.125	0.140
15-1080	0.232	0.284	0.097	0.204
15-1084	0.172	0.179	0.219	0.190

Beam Fatigue Test

Another fundamental material property of asphalt mixture is fatigue property, which is important because one of the principal modes of HMA pavement distress is fatigue-related cracking. Therefore, an accurate prediction of HMA fatigue property would be useful in predicting overall pavement life. The flexural test, beam fatigue test, is one of the typical ways of estimating in-place HMA fatigue properties. The beam fatigue test determines the fatigue life of a small-scale HMA beam specimen (380 mm long x 50 mm thick x 63 mm wide) by subjecting it to repeated flexural bending until failure. The beam specimen is sawed from either laboratory or field compacted HMA. Results are usually plotted to show cycles to failure versus applied stress or strain.

In this study, four-point flexural beam fatigue tests were performed in accordance with AASHTO T321 (2007) using three replicate specimens at three strain levels, and that is a total of nine beams for each mixture type. For the fatigue tests, compacted beams measuring approximately 75 mm thick by 125 mm wide by 381 mm long were fabricated. From these compacted beams, the 50.8 mm by 63.5 mm by 381 mm specimens required for the fatigue testing were saw-cut. The target air void level for the fatigue beams was 7±0.5%. IPC beam fatigue test equipment was used. All tests were conducted at a single temperature of 20°C. The tests were conducted in the strain-controlled mode. Applied tensile strain levels ranging from 300 to 800 microstrains were used so that fatigue curves describing strain versus number of cycles to failure could be developed. During the test, repeated application of the specified 600 microstrains was continued until failure occurred in the test specimen. Specimen failure was defined as the number of cycles at which beam stiffness degraded to 50% of the initial flexural stiffness. Table 5.7 presents the fatigue test results of all SMA mixtures under three different strain levels. Figure 5.8 shows the number of loading cycles to failure versus the applied strain curves for the eight types of SMA mixtures.

Table 5.7 Fatigue test results of SMA mixtures

Mix ID	Fatigue test results (cycles)								
	300 Micro strain			450 Micro strain			600 Micro strain		
Air Voids (%)	7.1	6.6	6.7	6.8	6.9	6.4	6.8	6.7	6.2
13-1070	1,440,250	1,826,920	1,121,160	189,220	198,520	140,260	42,280	28,320	23,730
Air Voids (%)	6.9	5.2	5.3	6.2	5.3	5.2	5.2	5.9	5.2
13-1081	3,158,360	3,973,570	3,303,000	231,900	220,860	379,820	48,510	62,980	74,400

Air Voids (%)	6.6	6.5	-	6.2	-	-	7.3	6.7	-
14-1021	4,803,880	6,168,820	-	238,970	-	-	73,420	39,560	-
Air Voids (%)	7.0	7.1	7.5	7	7.1	7.1	7.1	7.2	-
14-1047	6,646,010	8,166,320	5,986,030	414,030	576,020	556,370	116,280	104,200	-
Air Voids (%)	6.6	6.8	-	8	6.7	7.3	6.6	8.3	7.2
15-1012	10,000,000	4,512,300	-	305,790	256,480	179250	69,730	64,650	51,610
Air Voids (%)	6.9	6.7	6.8	6.6	6.8	-	6.8	7.2	7.2
15-1068	10,000,000	10,000,000	6,760,000	2,948,900	2,828,500	-	855,000	507,920	264,580
Air Voids (%)	6.5	-	-	7.0	6.9	7.2	7.0	7.0	6.9
15-1080	2,757,390	-	-	277,160	251,650	332,130	41,960	49,700	47,720
Air Voids (%)	6.6	6.8	7.2	7.5	7.1	7.3	6.7	6.8	6.7
15-1084	3,211,820	5,924,760	5,940,140	-	286,540	274,920	49,690	57,740	90,270

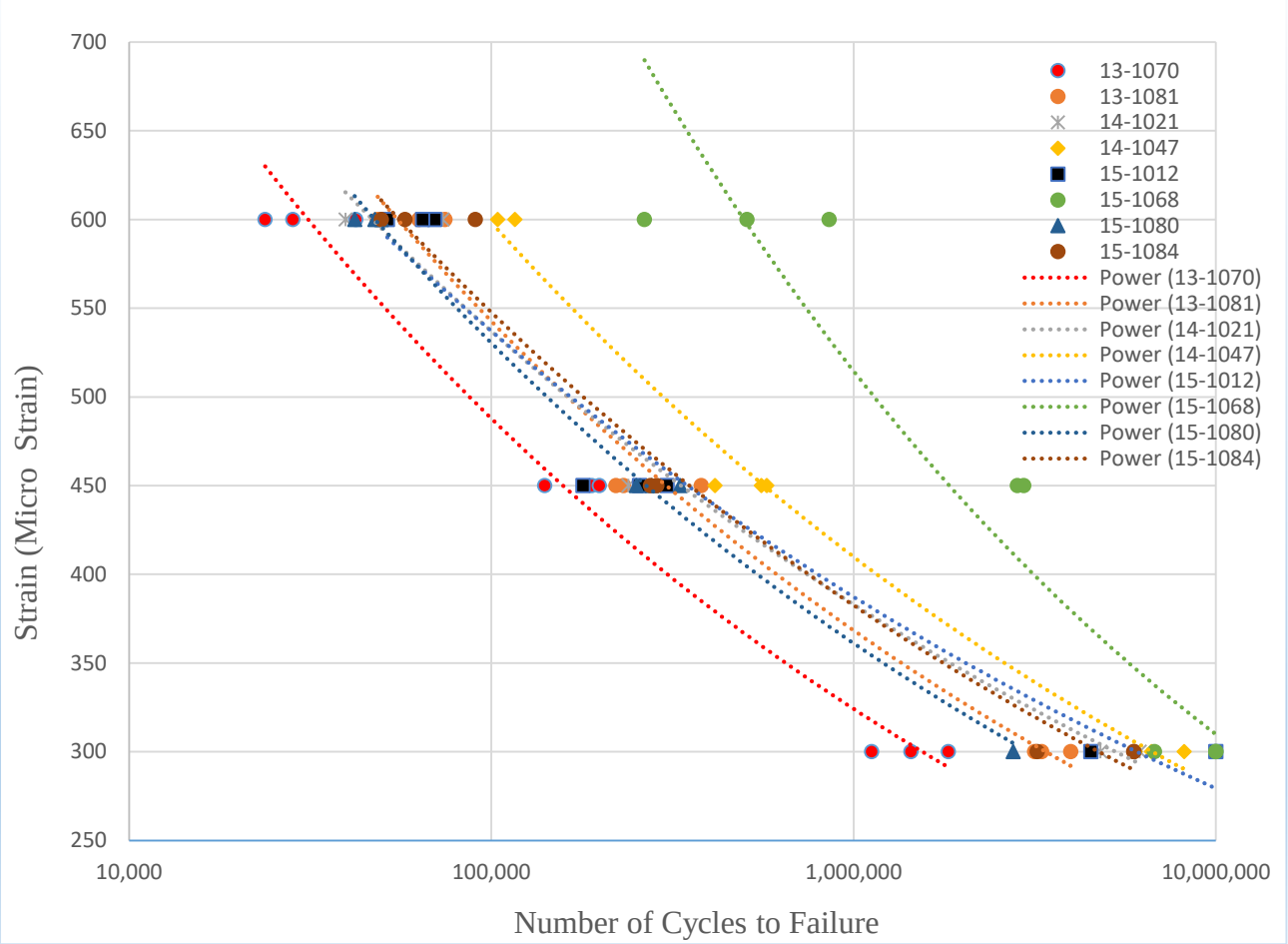

Figure 5.8 Fatigue curve of SMA mixtures

Asphalt Pavement Analyzer Test

In this study, the APA test was conducted in accordance with Virginia Test method 110 (VDOT, 2009). Three beam specimens of 3 inch thick by 5 inch wide by 12 inch long (75 mm x 125 mm x 300 mm) were tested in the APA at a test temperature of 49°C (120 °F) for each type of SMA mixture. The specimens were compacted in laboratory to ensure air void content of 8.0 ± 0.5%. All three specimens for each type of mixture were tested simultaneously. A vertical load of 120 lbf (533N) was applied through a rubber hose filled with compressed air at a pressure of 120 psi (830kPa). The loading wheel speed was 2 ft/sec, and a total of about 135 mins were required to complete 8,000 cycles of load application. The recorded rut depth results after 8,000 cycles of load applications include left, middle, right and average rut depth of the three replicate beams for each mixture type. Figure 5.9 shows plots of number of loading cycles versus rut depth for SMA mixtures. As seen in figure 5.9, SMA mixtures deform rapidly at the initial first or two thousand cycles and the curves become linear with the number of loading cycles after that. Literatures showed that the relevant parameters for evaluating the rutting resistance ability from the APA test results are: 1. the final rut depth after 8,000 loading cycles' application; 2. the creep slope of the linear portion of the plot of rut depth versus number of loading cycles (Amit et al. 2004). APA creep slope can be evaluated from the regression analysis of the linear portion of the rut depth

versus number of loading cycles curve. The plots for APA creep slope determination for SMA mixtures were included in appendix D. Table 5.8 lists rut depths for these 24 SMA mixture replicates after 8,000 cycles' loading application in the APA testing. The rut depths were used to rank the rutting resistance ability of SMA mixtures. The air void content was measured for every SMA replicate sample in the APA tests, and the average value of air void content is listed in the last column in Table 5.8. Table 5.9 lists the APA creep slope values and intercept values obtained from APA curves for SMA mixtures.

Table 5.8 APA rut depth results after 8,000 loading cycles

Mix ID	Rut Depth (mm) (49 °C)				
	Left	Middle	Right	Mean	Average Air Void Content (%)
13-1070	2.01	1.72	1.34	1.69	7.9
13-1081	1.19	1.30	1.40	1.30	8.4
14-1021	1.22	1.37	1.38	1.32	7.5
14-1047	2.44	2.63	2.63	2.57	7.7
15-1012	2.85	3.09	3.57	3.17	7.8
15-1068	1.18	1.43	1.69	1.43	7.8
15-1080	2.34	2.38	2.65	2.46	8.2
15-1084	1.12	1.54	1.34	1.33	-

Table 5.9 APA creep slope results

Mix ID	Creep Slope (49 °C)				
	Left	Middle	Right	Mean	Average Air Void Content (%)
13-1070	1.25E-04	1.16E-04	8.19E-05	1.08E-04	7.9
13-1081	9.80E-05	8.48E-05	8.10E-05	8.79E-05	8.4
14-1021	-	7.96E-05	-	7.96E-05	7.5
15-1012	1.93E-04	-	2.92E-04	2.43E-04	7.8
15-1068	7.34E-05	-	1.19E-04	9.62E-05	7.8
15-1080	1.73E-04	1.02E-04	1.99E-04	1.58E-04	8.2
15-1084	5.33E-05	9.76E-05	7.78E-05	7.62E-05	-

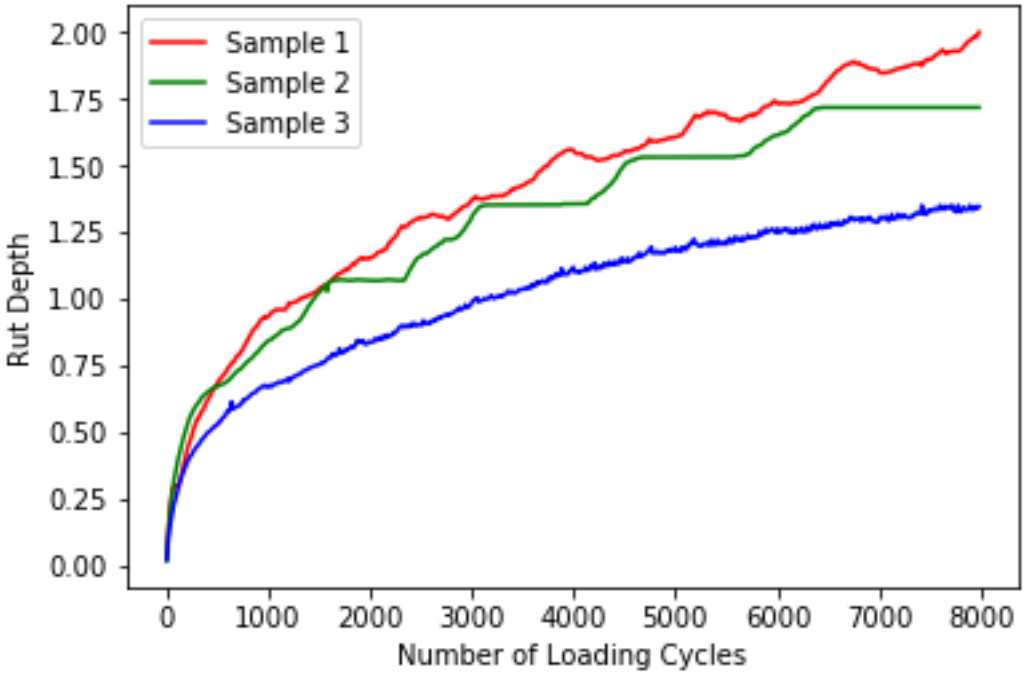

(a) SMA 13-1070

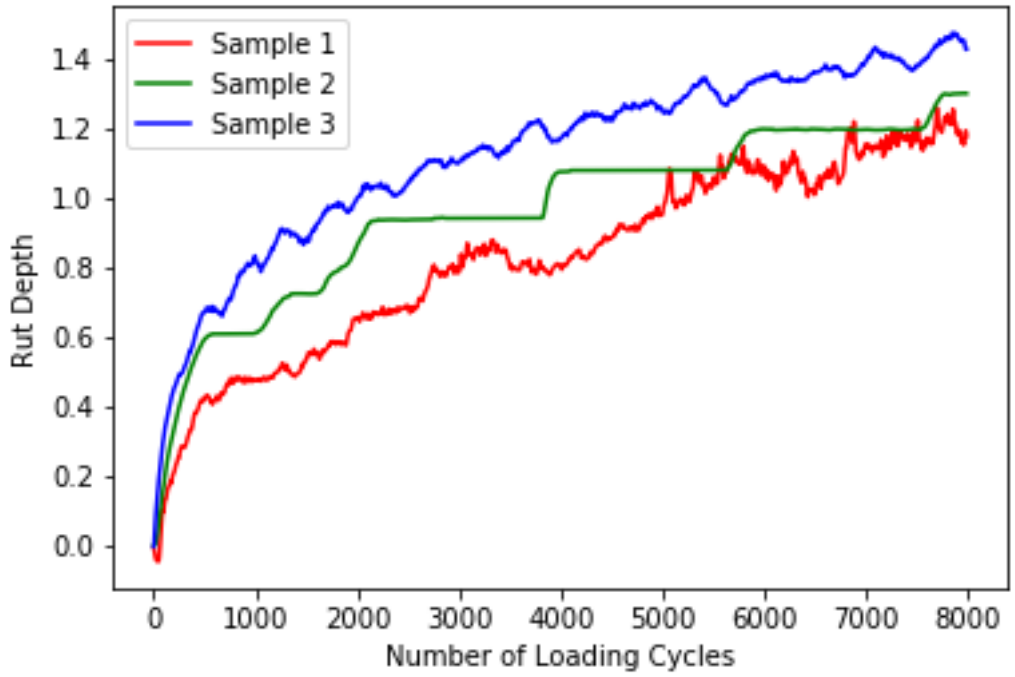

(b) SMA 13-1081

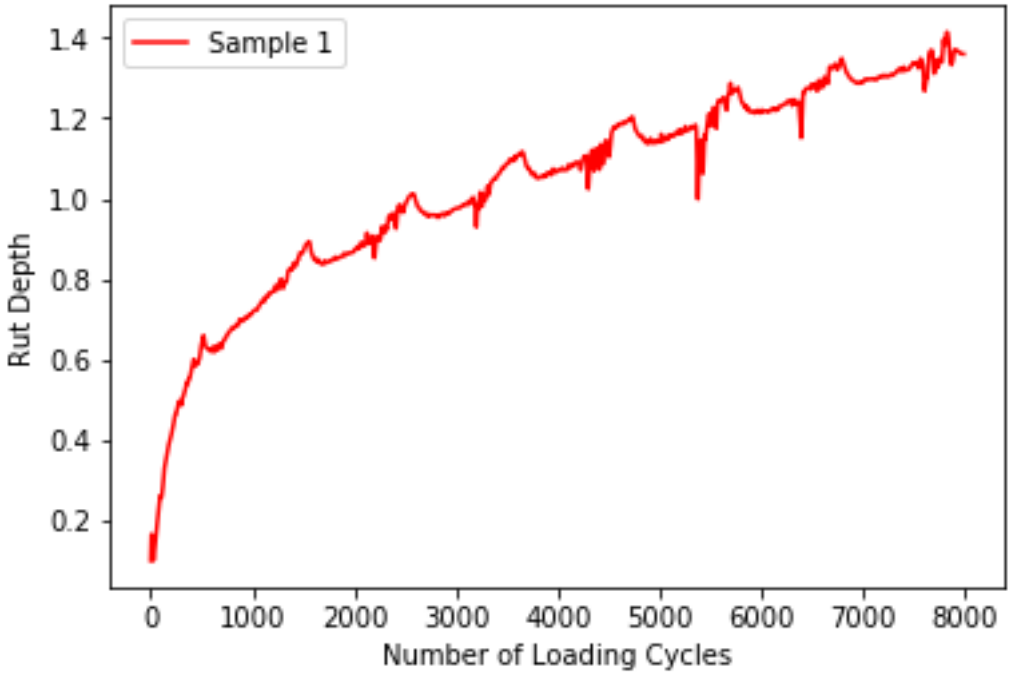

(c) SMA 14-1021

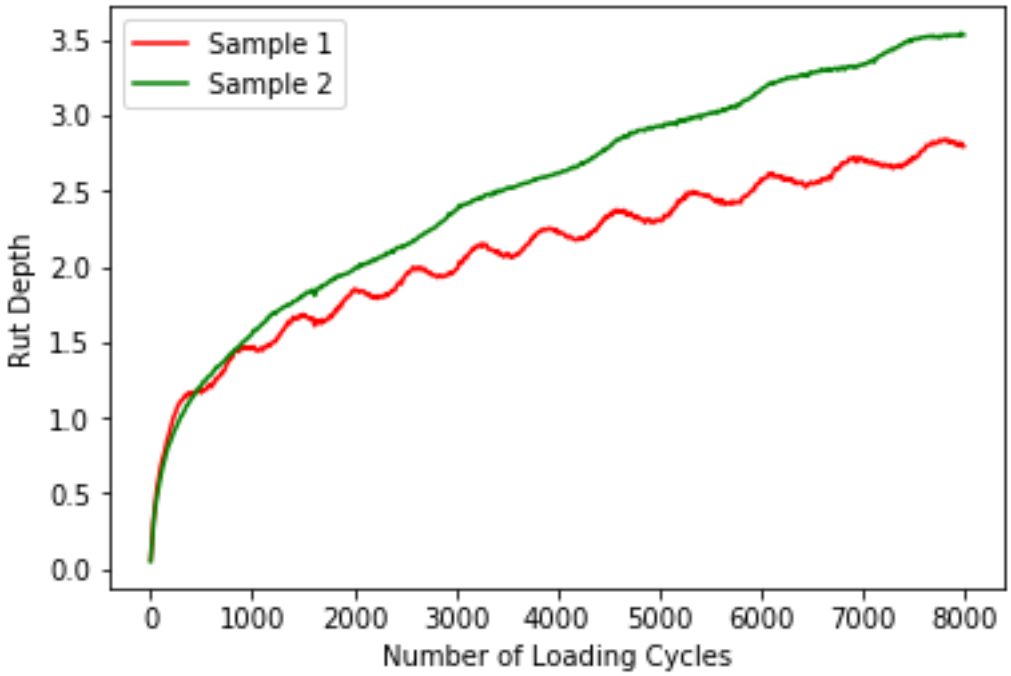

(d) SMA 15-1012

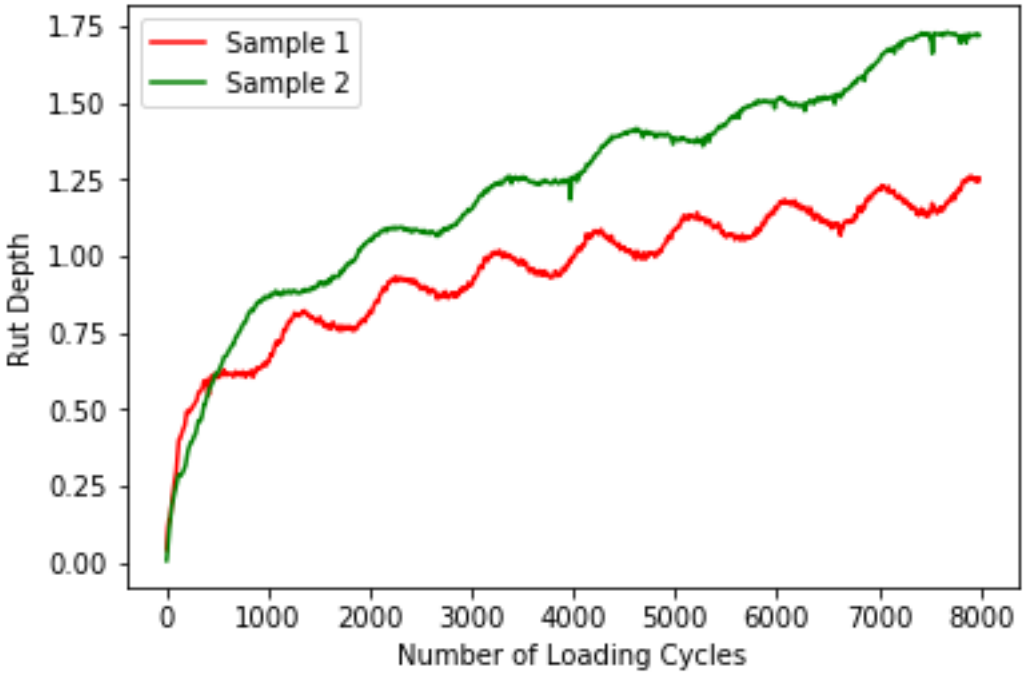

(e) SMA 15-1068

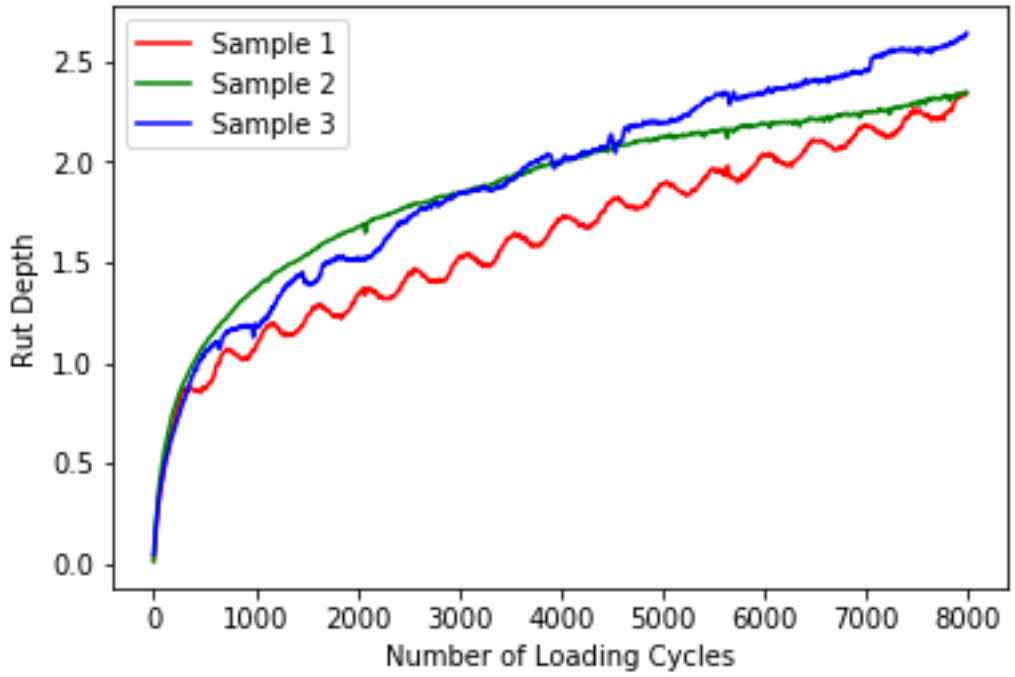

(f) SMA 15-1080

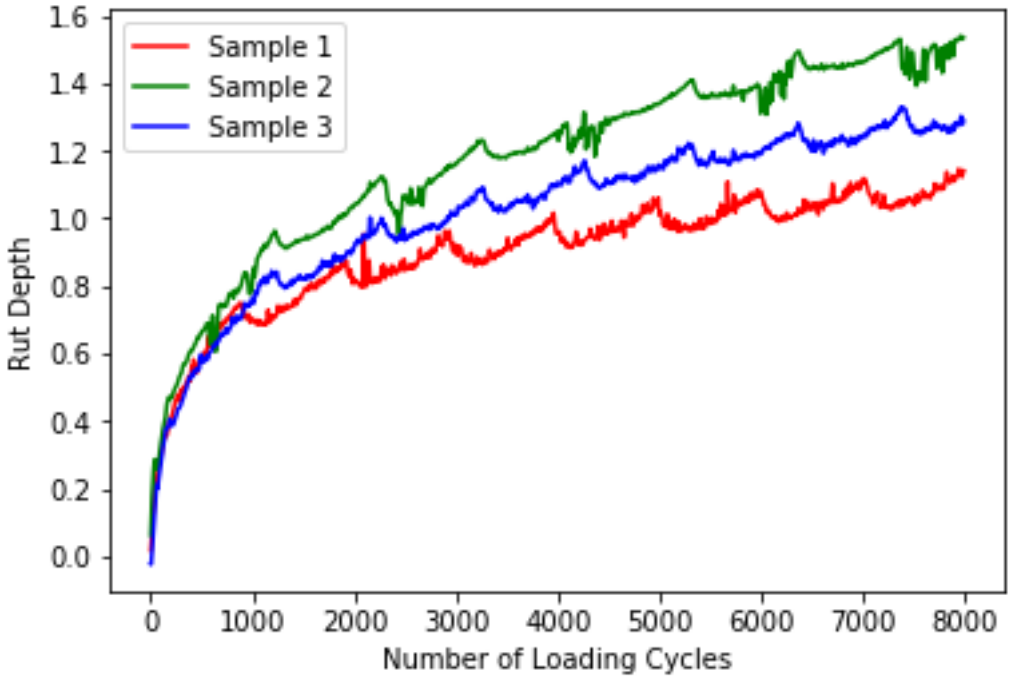

(g) SMA 15-1084

Figure 5.9 Number of loading cycles versus rut depth for SMA mixtures.

Modal Mobile Load Simulator (MMLS) Test

MMLS can evaluate the rutting and fatigue susceptibility of HMA under different environmental and trafficking conditions. In this study, the MMLS3 was used to analyze the fatigue resistance of SMA mixtures. The MMLS3 fatigue testing was carried out at an intermediate temperature of 20 °C. The MMLS3 used in this study is a one-third scale accelerated pavement testing system with four single wheel bogies for simulating realistic dynamic wheel load application to SMA specimens. The MMLS3 has four axles and an electric motor. Each axle is equipped with a single tire of 30 cm diameter, and the electric motor provides power for circulating each axle in a vertical closed loop in such a way that the loads can be applied to the specimens. Each axle of the MMLS3 applies a load of 2.7 kN, and the tire pressure is set to 0.7 MPa. The loads were applied with a loading frequency of 2 Hz, indicating 7200 loading repetitions were finished per hour. The MMLS3 was running on six types of SMA mixtures until a total of 1,000,000 loading cycles were applied for fatigue resistance evaluation. The size of each SMA beam specimen is 12 inch in length, 5 inch in width, and 3 inch in depth (i.e., 30 cm × 12.5 cm × 7.5 cm). The seismic modulus of every SMA sample was measured.

The Portable Seismic Pavement Analyzer (PSPA), a nondestructive device, was used to measure the seismic modulus occurred in SMA. The seismic modulus difference between the initial loading cycle and the 1 million loading cycles is indicative of the integrity change of the SMA. PSPA has become a tool for evaluation of the ability of SMA to resist fatigue during trafficking process. More detailed information about PSPA can be found in (Jurado et al., 2012). The difference of seismic modulus of each specimen after 1,000,000 loading

cycles was recorded in Table 5.10. After 1,000,000 loading cycles' application in the MMLS3 test, SMA mixtures of 13-1081, 14-1047, 15-1068, 15-1080 and 15-1084 show decreasing trends in seismic modulus. Conversely, there were some increases of seismic modulus in SMA mixtures of 13-1070, 13-1081, and 15-1080. The moduli would typically be expected to decrease as a result of anticipated traffic damage. However, material densification during trafficking may offset the effects of traffic damage. Such decreases and increases in normalized PSPA modulus were also found in other MMLS tests (Walbita et al., 2000). The correlation between seismic modulus difference for each type of SMA mixture and coarse aggregate morphology was analyzed in the following section.

Table 5.10 The summary of change of seismic modulus after 1 million loading cycles

SMA Mix ID	Seismic Modulus (GPa)(20 °C)								
	Initial			After 1 million load cycles			Difference (%)		
	Replicate 1	Replicate 2	Replicate 3	Replicate 1	Replicate 2	Replicate 3	Replicate 1	Replicate 2	Replicate 3
13-1070	6.2	5.67	7	6.67	6.867	8.27	7.53	21.17	18.09
13-1081	6.53	7.03	6.23	7.8	5.6	5.43	19.39	-20.38	-12.83
14-1047	9.17	8.00	10.80	5.03	5.37	4.83	-45.09	-32.91	-55.25
15-1068	10.13	9.70	7.57	5.37	4.97	4.67	-47.04	-48.80	-38.33
15-1080	10.05	9.28	8.50	8.57	8.97	9.10	-18.44	-4.79	5.06
15-1084	8.96	8.43	10.48	9.10	4.17	10.13	-2.14	-47.03	-19.87

Uncompacted Void Content Test

Different from previous laboratory performance-based tests conducted on SMA mixtures, the uncompacted void content tests were conducted on the selected aggregate fractions used to constitute SMA mixtures. The uncompacted void content of each aggregate fraction was measured in accordance with AASHTO T326 (Coarse Aggregate). The coarse aggregates were tested using a cylindrical metal measure with a diameter of 152 mm and a height of 160 mm. The uncompacted void content is calculated as the difference between the volume of the calibrated cylindrical measure and the absolute volume of the coarse aggregate collected in the cylinder. The uncompacted void content of coarse aggregate measurement provides an

indication of morphological characteristics such as sphericity, angularity and surface texture. The test is considered as an indirect method for measuring morphology such as angularity. Aggregates with the size ranges of 4.75-9.5mm and 9.5-12.5 mm were analyzed to evaluate the relationship between morphological characteristics and uncompacted void content of coarse aggregates. To examine the effects of the morphological characteristics on the uncompacted void content of coarse aggregates, the void contents were measured for aggregates in two size ranges: particles that pass the 9.5 mm sieve but are retained on the 4.75 mm sieve, and particles that pass the 12.5 mm sieve but are retained on the 9.5 mm sieve. Table 5.11 and Table 5.12 show the uncompacted void test results for aggregates of the aforementioned two size ranges.

Table 5.11 Uncompacted void contents of aggregate fractions passing 12.5 mm and retaining on 9.5 mm sieve size

Aggregate Fractions	Sample 1 (Mass/g)	Sample 2 (Mass/g)	UCV of Sample 1 (%)	UCV of Sample 2 (%)	Average UCV (%)
13-1071 No.30	4401.3	4369.2	49.45868	49.92729	49.6
13-1071 No.60	4524.4	4560.4	48.04509	47.63169	47.8
13-1078 No.8	3782.9	3781.9	53.74727	53.75949	53.8
13-1073 No.68	4121	4200.5	49.61339	48.64136	49.1
13-1073 No.78	3972.4	3912.5	46.41913	47.22708	46.8
14-1019 No.8	4533.4	4516.5	47.94174	48.13581	48.0
14-1019 No.30	4431.6	4410.3	49.28208	49.52585	49.4
14-1019 No.78	4520.8	4551.3	48.08643	47.73619	47.9
14-1048 No.30	4431.6	4410.3	49.11074	49.35533	49.2
14-1048 No.60	4458.2	4465.3	48.80528	48.72375	48.8
14-1048 No.78	4593.8	4544.3	47.24815	47.81657	47.5
15-1013 No.28	4609.8	4573.3	47.59554	48.01048	47.8
15-1013 No.78	4198.8	4216.4	52.26781	52.06774	52.2
15-1069 No.8	4464.9	4486.3	47.12052	46.86707	47.0
15-1069 No.78	4348.6	4373	49.20584	48.92083	49.1

Table 5.12 Uncompacted void contents of aggregate fractions retaining on 4.75 mm sieve size

Aggregate Fractions	Sample 1 (Mass/g)	Sample 2 (Mass/g)	UCV of Sample 1 (%)	UCV of Sample 2 (%)	Average UCV (%)
13-1071 No.60	4391.2	4369.6	49.57466	49.8227	49.7
13-1078 No.8	3755.3	3703.9	54.08473	54.71318	54.4
13-1073 No.68	4188.2	4200.5	48.79175	48.64136	48.7
13-1073 No.78	3840	3833.2	48.20498	48.2967	48.3
14-1019 No.8	4453.5	4466.2	48.85925	48.71341	48.8
14-1019 No.78	4407.9	4432.8	49.38289	49.09696	49.2
14-1048 No.60	4253.7	4279.9	51.15361	50.85275	51.0
14-1048 No.78	4342.7	4388.7	50.1316	49.60337	49.9

15-1013 No.28	4552.2	4593.1	48.25034	47.78539	48.0
15-1013 No.78	4066.7	4072.9	53.76953	53.69905	53.7
15-1069 No.8	4484.6	4502.8	46.88721	46.67166	46.8
15-1069 No.78	4230.8	4221.6	50.58181	50.68927	50.6

CHAPTER 6 RELATIONSHIP BETWEEN MECHANICAL BEHAVIOR OF SMA MIXTURES AND MORPHPLOGICAL CHARACTERISTICS OF COARSE AGGREGATES

Effects of Coarse Aggregate Morphologies on Fatigue and Rutting Performance of SMA Using Dynamic Modulus Test

Dynamic modulus is often loosely defined as the relationship between the applied stress and the measured strain response under different loading frequencies and temperatures. At a low or an intermediate temperature and very short load duration, the dynamic modulus of an asphalt mixture has been found to significantly affect the fatigue performance of the asphalt mixture. At a high temperature, the dynamic modulus has been proven to affect the rutting performance of asphalt mixture. Because the dynamic modulus characterizes the elastic part of the stiffness of the asphalt mixture under dynamic repeated loading, it will inherently relate to the mechanical performance of asphalt mixture. Asphalt mixture stiffness is an important parameter used during pavement design and plays a vital role in the evaluation of pavement mechanical performance. Accordingly, the dynamic modulus of asphalt mixture was selected as a main indicator for investigating the effects of the coarse aggregate morphological characteristics on the fatigue and rutting behaviors of asphalt mixtures. The dynamic modulus tests were conducted on eight types of SMA mixtures constituted by various aggregate blends. A total of three specimens were fabricated for each mix design. Each specimen was tested on five temperatures and six frequencies as discussed in Chapter 5. The dynamic modulus test results at 21.1 ^{o}C were discussed to evaluate the effects of aggregate morphological characteristics on the fatigue performance of asphalt mixtures, while the dynamic modulus test at 54.4 ^{o}C were selected to measure the effects of aggregate morphologies on the rutting performance of asphalt mixtures. All the dynamic modulus test results under a frequency of 10 Hz were selected since this frequency approximately represents a highway speed of about 60 mph. The dynamic modulus was used as an important indicator to relate the fatigue properties and rutting performance of SMA mixtures with the aggregate morphologies. Aggregate morphological characteristics discussed in this chapter include sphericity, flat and elongated ratio, angularity and texture. The flat and elongated ratio was selected instead of flatness ratio or elongation ratio since it reflects both flatness and elongation well. All the morphological characteristics values in the following are weighted mean values.

Correlation between aggregate morphological characteristics and fatigue parameter |E| sin φ under a temperature of 21.1 ^{o}C*

The parameter |E*| sin φ obtained from dynamic modulus test under a temperature of 21.1 ^{o}C and a frequency of 10 Hz was used as an important indicator for evaluating the fatigue performance of SMA mixtures. The correlations between the fatigue parameter |E*| sin φ and both asphalt content and asphalt binder performance grade were analyzed first to demonstrate the effect of asphalt binder on the fatigue performance of SMA mixtures. The statistical t-test results were shown in Table 6.1. The p-value of 0.01342 shown in bold in the bottom row,

which is less than the specified significance level of 0.05, indicated the fatigue parameter has a correlation with the asphalt binder performance grade. To further investigate the possible relationship between the fatigue parameter |E*| sin φ and aggregate morphological characteristics, the test results of fatigue parameter |E*| sin φ were grouped based on different asphalt binder stiffness. The asphalt binder stiffness can still be approximately categorized by the PG grade. The high temperature performance grade of the asphalt binder in °F was considered as binder stiffness criteria due to the fact that binders used in this study had almost the same low temperature grade. The classification of the binder stiffness was finally performed based on the high temperature grade. Then the fatigue parameter data were grouped based on two classes of binder stiffness: PG 70 and PG 76, two separate sets of regression analyses were performed for the different categorized SMA mixtures. The regression analyses then focused on the relationship between aggregate morphology and the fatigue parameter |E*| sin φ grouped according to the asphalt binder performance grade. Second-order polynomials were found to give the highest R^2 values between aggregate morphological characteristics and fatigue parameters grouped by asphalt binder stiffness, and therefore selected as the best fit functions. Correlations of the fatigue parameters |E*| sin φ obtained from dynamic modulus tests with the weighted mean S, FER, AF and TF indices of the aggregate blends showed different trends. As shown in Figure 6.1, *x* represents the mean value of a morphological characteristic, and y represents the fatigue parameters |E*| sin φ. The higher R^2 values for SMA mixtures with asphalt binder PG 70 indicated a good correlation between the fatigue parameter and morphological characteristics**.**

Table 6.1 T-test results of regression analyses between |E|sinφ and asphalt content and performance grade*

Regression Pair	T Stat	P-value
|E*| sin φ-Asphalt Content	-1.328	0.19792
|E*| sin φ-Performance Grade	-2.688	**0.01342**

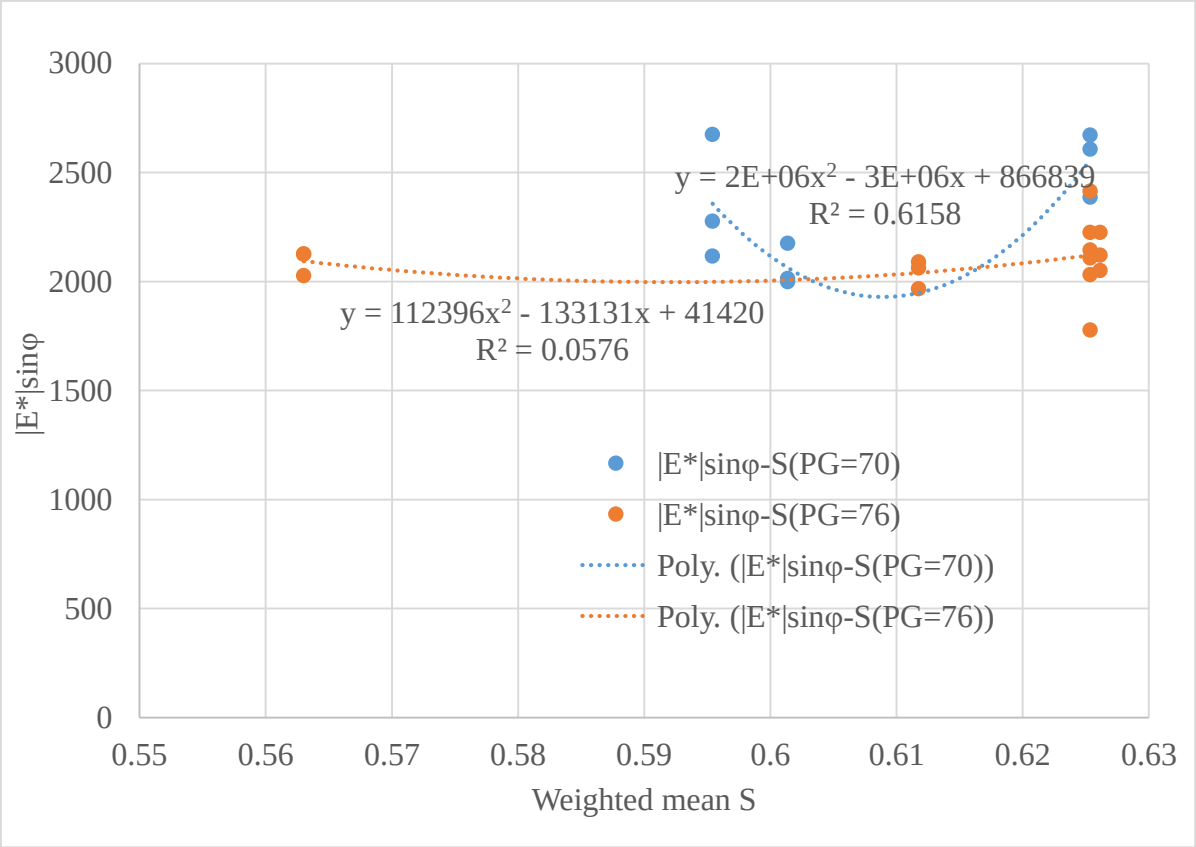
3000
2500
2000
1500
1000
500
0
0.55
0.56
0.57
0.58
0.59
0.6
0.61
0.62
0.63
|E*|sinφ
Weighted mean S
y = 2E+06x² - 3E+06x + 866839
R² = 0.6158
y = 112396x² - 133131x + 41420
R² = 0.0576
|E*|sinφ-S(PG=70)
|E*|sinφ-S(PG=76)
Poly. (|E*|sinφ-S(PG=70))
Poly. (|E*|sinφ-S(PG=76))

(a)

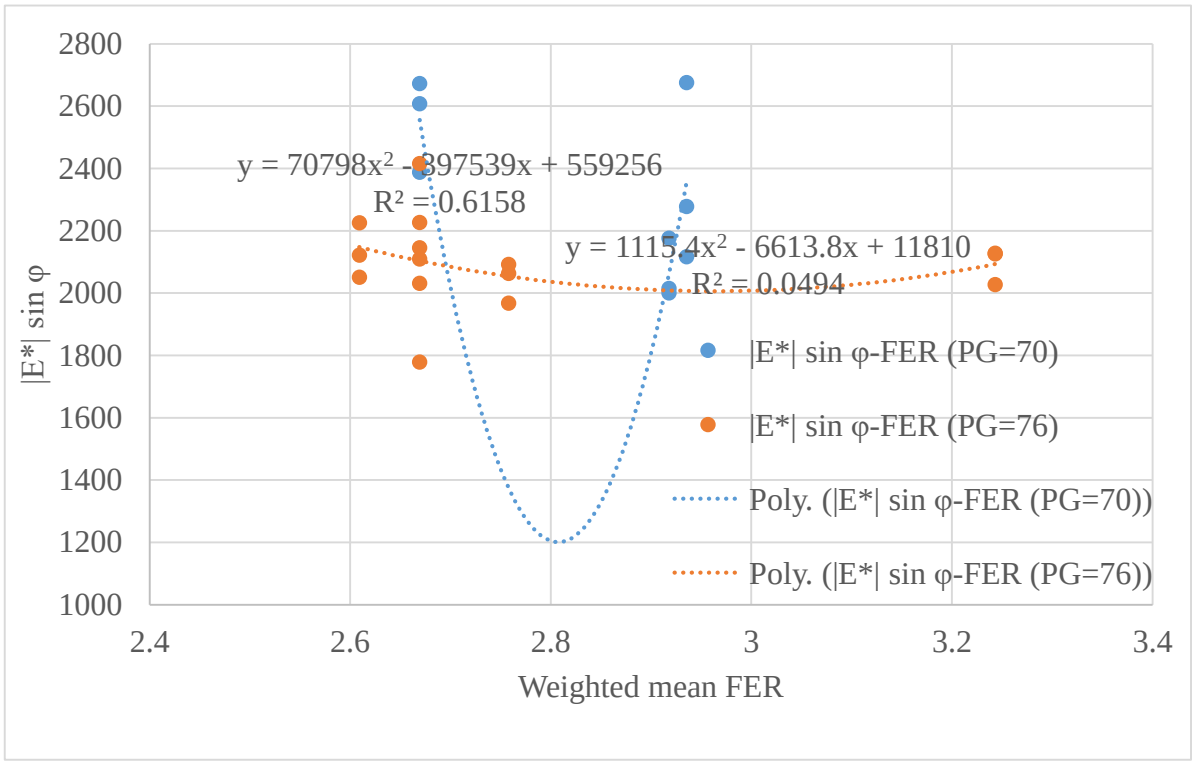
2800
2600
2400
2200
2000
1800
1600
1400
1200
1000
2.4
2.6
2.8
3
3.2
3.4
|E*| sin φ
Weighted mean FER
y = 70798x² - 397539x + 559256
R² = 0.6158
y = 1115.4x² - 6613.8x + 11810
R² = 0.0494
|E*| sin φ-FER (PG=70)
|E*| sin φ-FER (PG=76)
Poly. (|E*| sin φ-FER (PG=70))
Poly. (|E*| sin φ-FER (PG=76))

(b)

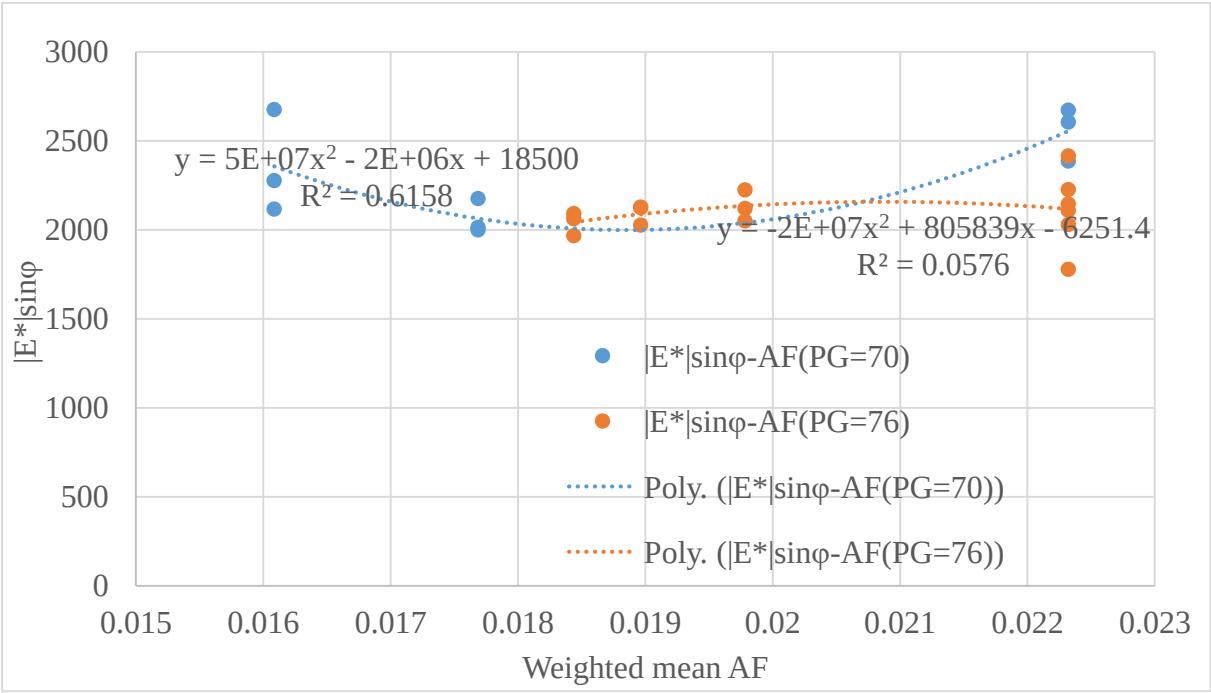

(c)

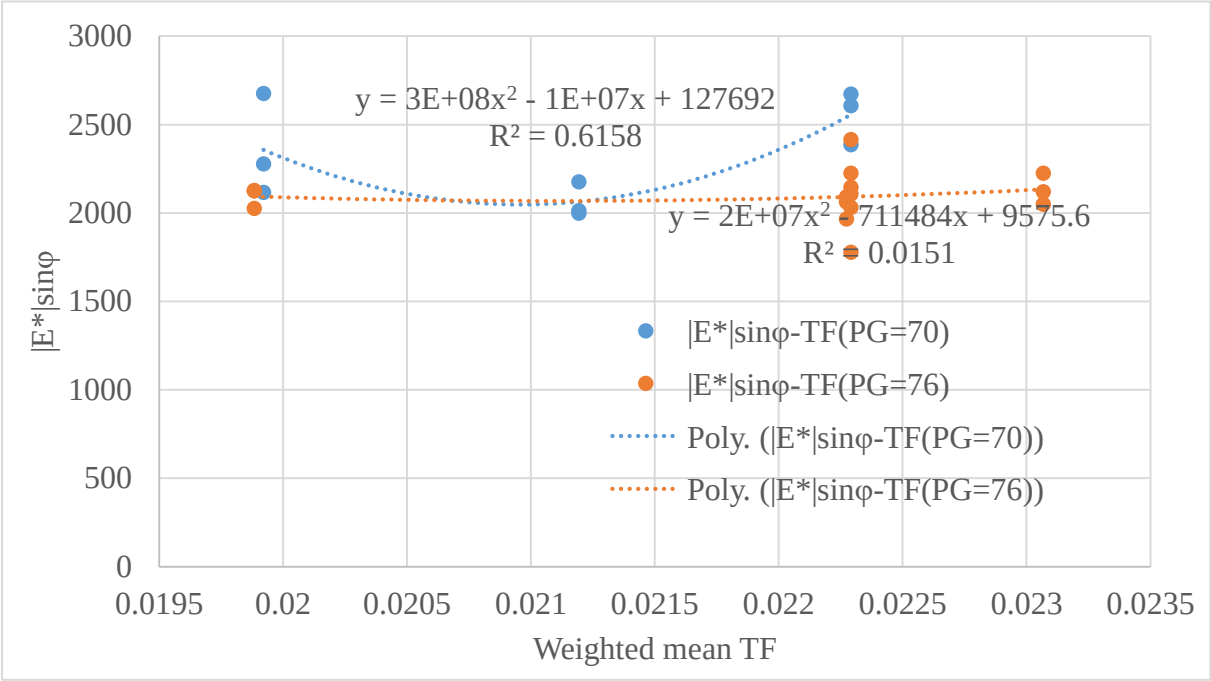

(d)

Figure 6.1 Correlations between fatigue parameter |E|sinφ and weighted mean morphological characteristics for 24 asphalt mixture specimens grouped by asphalt binder performance grade.* (a) |E*|sinφ versus weighted mean sphericity; (b) |E*|sinφ versus weighted mean flat and elongated ratio; (c) |E*|sinφ versus weighted mean angularity; (d) |E*|sinφ versus weighted mean texture;

Correlation between aggregate morphological characteristics and rutting parameter |E| /sin φ under a temperature of 54.4 ºC*

The parameter |E*| /sin φ obtained from dynamic modulus test under a temperature of 54.4 ºC and a frequency of 10 Hz was selected as an indicator for evaluating the rutting potential of SMA mixtures. The correlations between the rutting parameter |E*|/ sin φ and both asphalt content and asphalt binder performance grade were also analyzed first to interpret the effect of asphalt binder on the rutting performance of asphalt mixtures. The statistical t-test results were shown in Table 6.2. The p-value of 0.0007576 shown in bold at the bottom row, which is less than the specified significance level of 0.05, indicated the rutting parameter relates well with the asphalt binder performance grade. To further investigate the possible relationship between the rutting parameter |E*|/sin φ and aggregate morphological characteristics, the rutting parameter |E*|/sin φ data were grouped based on different asphalt binder stiffness, two separate sets of regression analyses were performed for the different categorized SMA mixtures. The regression analyses then focused on the relationship between aggregate morphologies and the rutting parameter |E*| /sin φ according to the asphalt binder performance grade. Second-order polynomials were found to give the highest R^2 values between aggregate morphological characteristics and rutting parameters grouped by asphalt binder stiffness, and therefore selected as the best fit functions. Correlations of the rutting parameters |E*| /sin φ obtained from dynamic modulus tests with the weighted mean S, FER, AF and TF indices of different aggregate blends showed different trends. As shown in Figure 6.2, the higher R^2 values for SMA mixtures with asphalt binder PG 70 indicated a good correlation between the rutting parameter and morphological characteristics**.**

Table 6.2 T-test results of regression analyses between |E|/sinφ and asphalt content and performance grade*

Regression Pair	T Stat	P-value
|E*|/ sin φ-Asphalt Content	-0.688	0.4986
|E*|/ sin φ-Performance Grade	-3.906	**0.0007576**

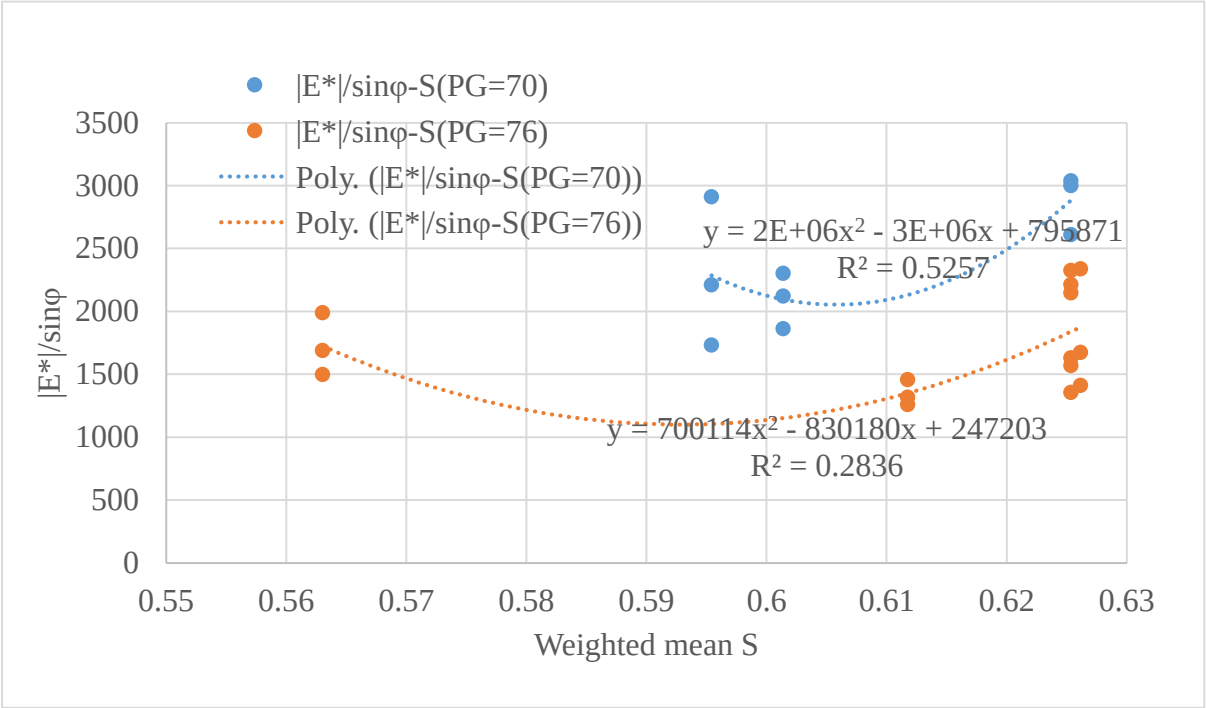
|E*|/sinφ-S(PG=70)
|E*|/sinφ-S(PG=76)
Poly. (|E*|/sinφ-S(PG=70))
Poly. (|E*|/sinφ-S(PG=76))
y = 2E+06x² - 3E+06x + .795871
R² = 0.5257
y = 700114x² - 830180x + 247203
R² = 0.2836
|E*|/sinφ
Weighted mean S
3500
3000
2500
2000
1500
1000
500
0
0.55
0.56
0.57
0.58
0.59
0.6
0.61
0.62
0.63

(a)

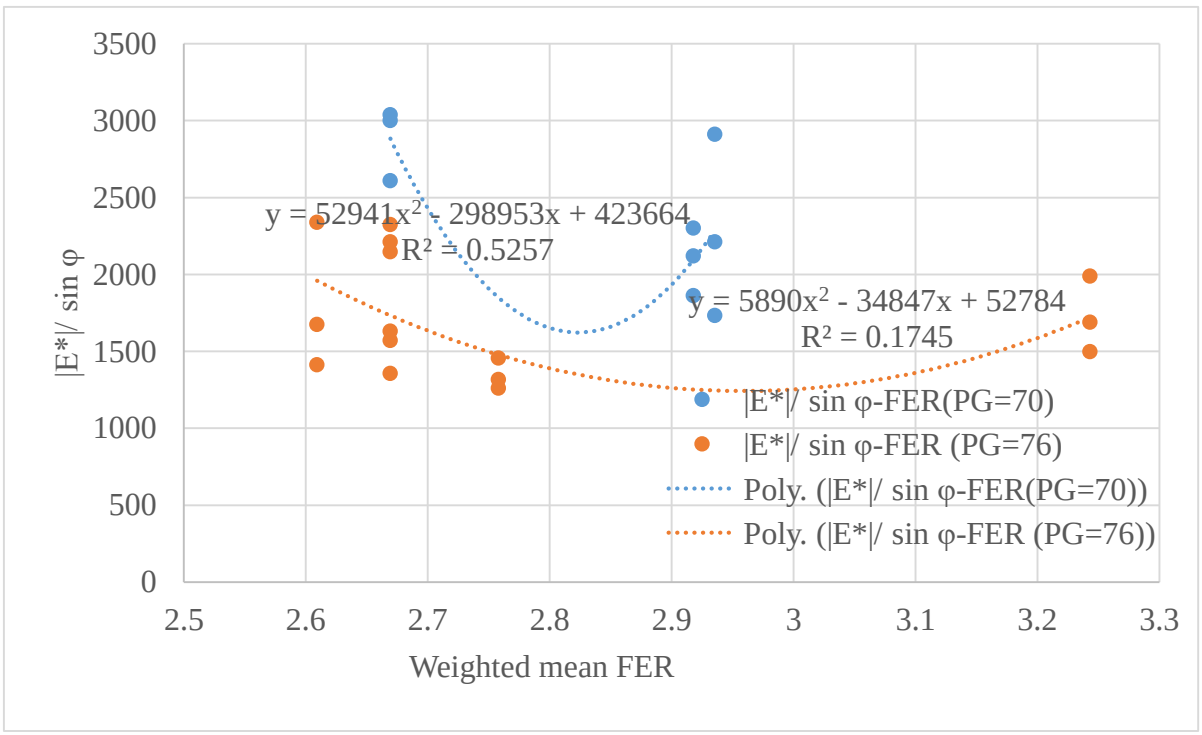
y = 52941x² - 298953x + 423664
R² = 0.5257
y = 5890x² - 34847x + 52784
R² = 0.1745
|E*|/ sin φ-FER(PG=70)
|E*|/ sin φ-FER (PG=76)
Poly. (|E*|/ sin φ-FER(PG=70))
Poly. (|E*|/ sin φ-FER (PG=76))
|E*|/ sin φ
Weighted mean FER
3500
3000
2500
2000
1500
1000
500
0
2.5
2.6
2.7
2.8
2.9
3
3.1
3.2
3.3

(b)

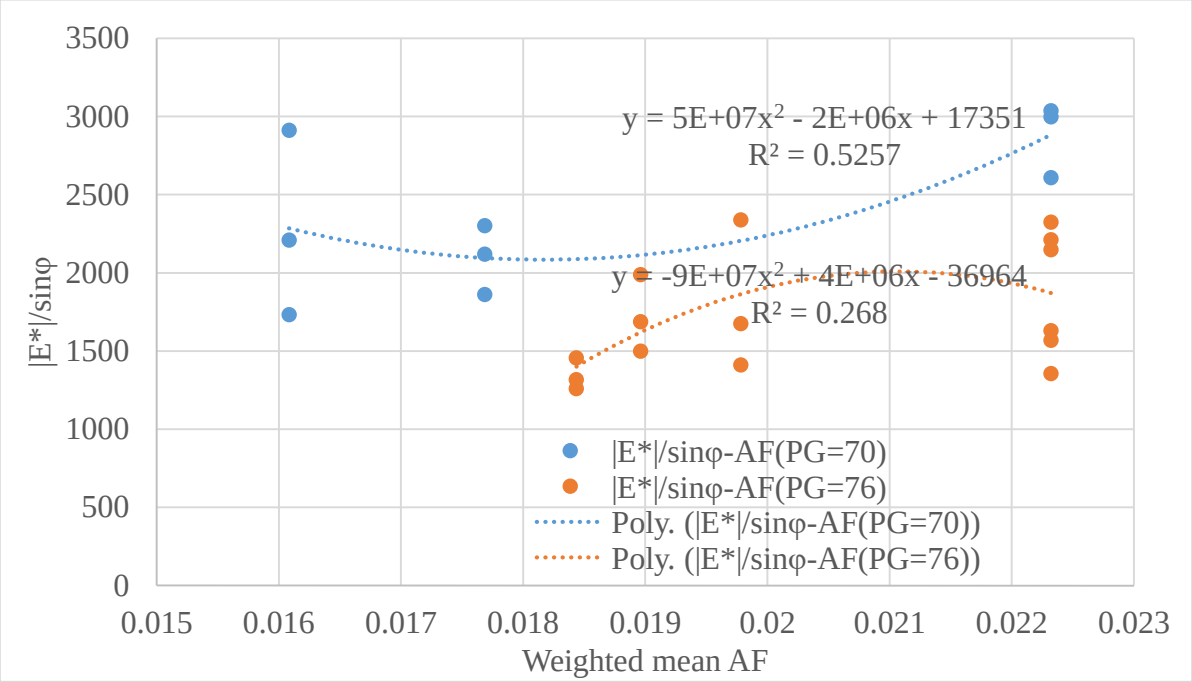

(c)

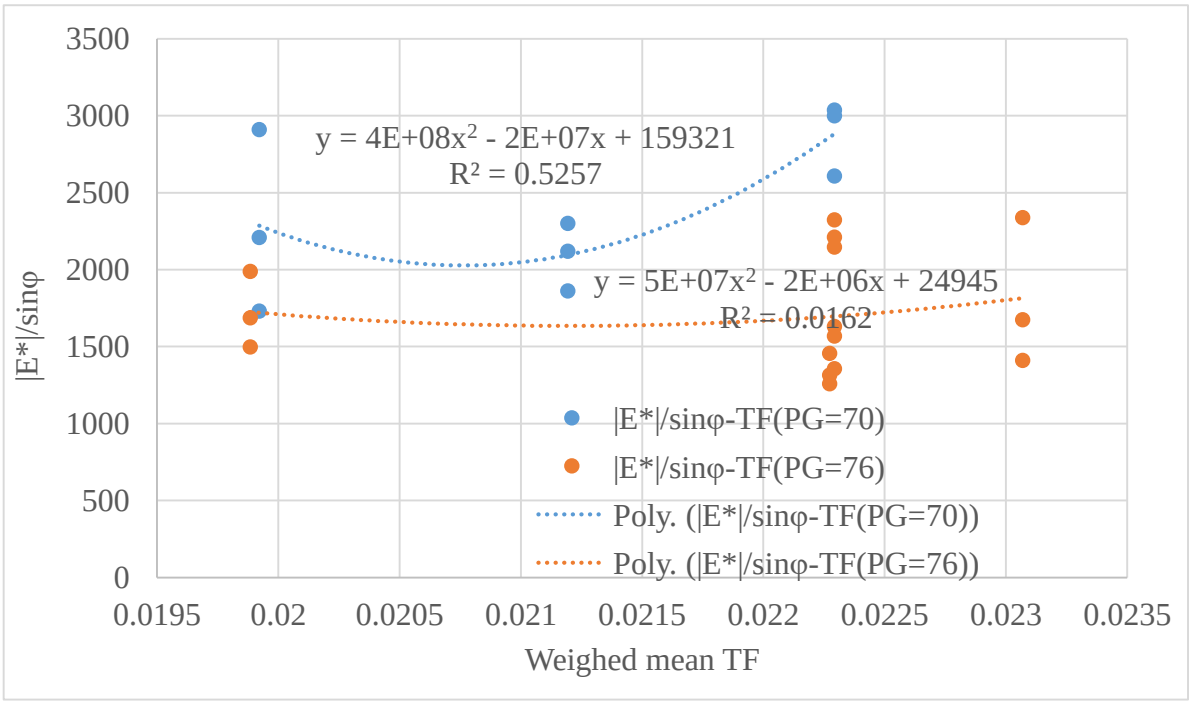

(d)

Figure 6.2 Correlations between rutting parameter |E|/sinφ and weighted mean morphological characteristics for 24 asphalt mixture specimens grouped by asphalt binder performance grade.* (a) |E*|/sinφ versus weighted mean sphericity; (b) |E*|/sinφ versus weighted mean flat and elongated ratio; (c) |E*|/sinφ versus weighted mean angularity; (d) |E*|/sinφ versus weighted mean texture;

Effects of Coarse Aggregate Morphologies on Rutting Performance of SMA Using Flow Number Test

To quantify the permanent deformation behavior of SMA mixtures and correlate them with the aggregate morphological characteristics, the flow number and flow number slope were considered as two major indicators of asphalt mixtures to evaluate the rutting potential. The flow number is recorded as the number of loading cycles where the minimum slope corresponds to in the plot of rate of change of permanent strain versus loading cycles on a log-log scale. Flow number measures the stability of SMA mixtures and has recommended as the most important indicator to characterize the rutting resistance behavior of SMA mixtures. Flow number slope reflects the rate of change of the cumulative permanent strain as a function of the change in loading cycles and has recommended as another important indicator to evaluate the permanent deformation of SMA mixtures.

Correlation between aggregate morphological characteristics and flow number

Using the flow number FN measured from the flow number tests given in Table 5.3 in Chapter 5, the effect of asphalt binder on the permanent deformation behavior of the 24 SMA mixture specimens was first studied. Regression analyses performed between the flow number FN and both the asphalt contents and performance grades of the 24 asphalt mixture specimens reported p-values of 0.5373 and 0.06428, greater than the significance level of 5%, respectively. These high p-values indicated flow number had poor correlations with asphalt content and performance grade, indicating no measurable effect of the asphalt binder was observed on the permanent deformation behavior**.** To better explain the flow number test results, the measured permanent deformation parameters, which are the flow numbers of a total of 24 specimens for the studied eight types of SMA mixtures, were taken logarithms, and the regression analyses were performed between aggregate morphologies and the logarithms of the flow numbers, which are denoted as Log(FN). A total of four regression pairs between the four morphological characteristics and the flow number test parameters Log(FN) were analyzed statistically. The descriptive statistics of the aggregate morphological characteristics and the permanent deformation parameter (Log(FN)) are listed in Table 6.3. The regression pairs that have a p-value higher than the specified significance level of 5% ($\alpha = 0.05$) were considered as having poor correlations between the response and the predictor variables. Regression analyses were only performed on the regression pairs in bold, since they had the meaningful p-values and indicated statistically significant.

Figure 6.3 shows the linear regression analyses conducted between the weighted mean morphological characteristics (S, FER, AF and TF) and the measured permanent deformation parameters Log(FN) of all SMA mixtures. As shown in Figure 6.3, Log(FN) increases with increased weighted mean S, AF and TF values. It is generally accepted that the higher the flow number, the lower the rutting susceptibility. Therefore, using more of the spherical, angular or better-crushed, rough coarse aggregate particles in SMA mixtures, as indicated by higher S, AF, and TF values, can improve the resistance of the SMA to rutting. More angular aggregates in the mixtures improved rutting resistance potential due to better aggregate interlocking.

Rougher textured aggregates in the mixtures improved rutting performance due to stronger aggregate structures and higher stability. In figure 6.3, Log(FN) also increases with decreased weighted mean FER values. Likewise, using less flat and elongated aggregate particles, as indicated by lower FER values, can promote the rutting performance of the SMA mixtures. Flat and elongated aggregates tend to breakdown easily and are considered as undesirable in SMA mixtures. The SMA mixtures consisting of more spherical, less flat and elongated aggregates with more angular and rougher textured surfaces exhibited better rutting resistance.

Table 6.3 Statistical results of regression analyses between aggregate morphologies and flow numbers

Regression Pair	T Stat	P-value
Log(FN)-S	2.801	**0.01041**
Log(FN)-FER	-2.868	**0.008938**
Log(FN)-AF	4.889	**6.889E-05**
Log(FN)-TF	3.741	**0.001133**

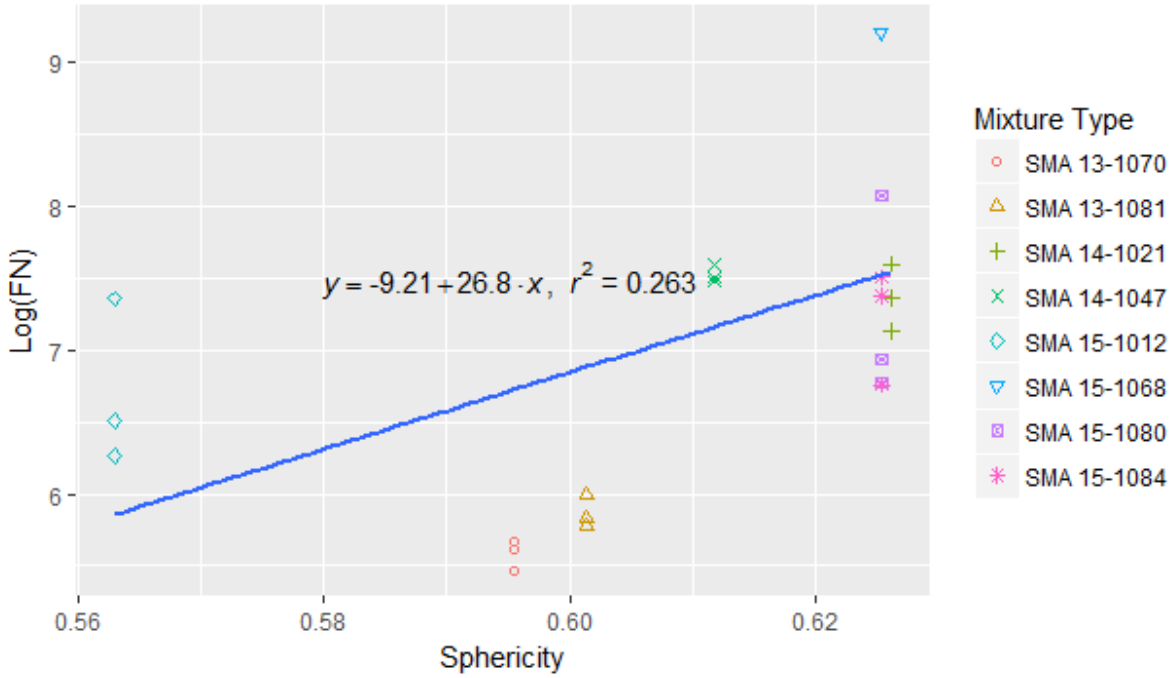

(a) Sphericity versus Log(FN) for all SMA mixtures

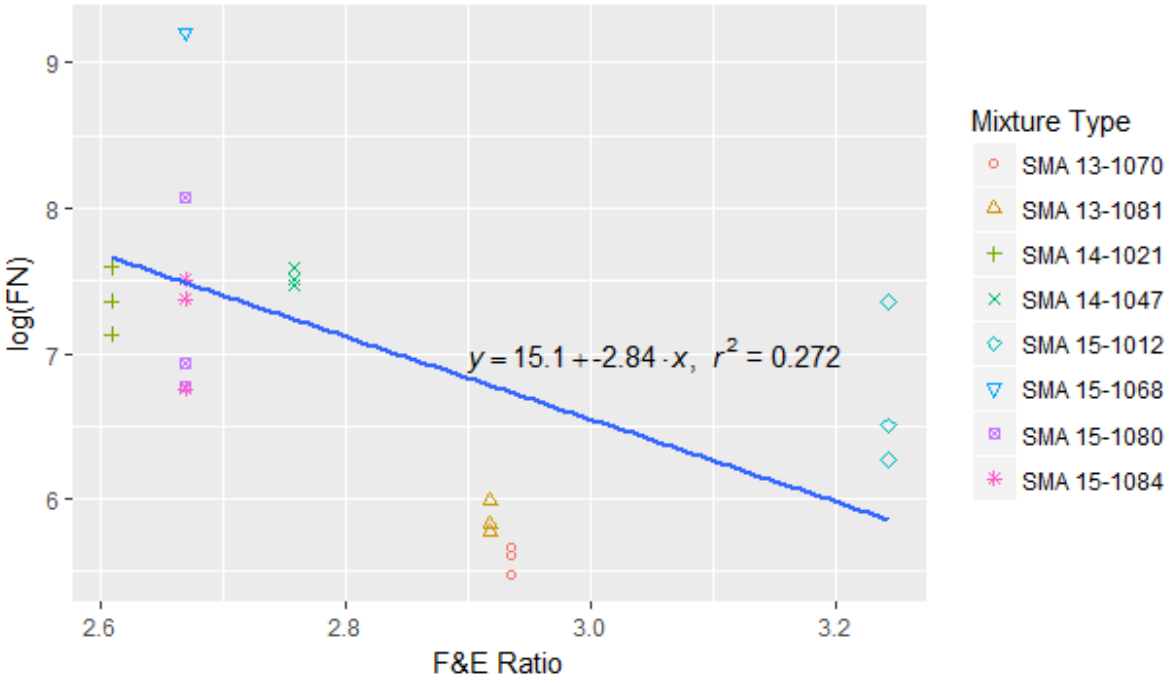

(b) F&E Ratio versus Log(FN) for all SMA mixtures

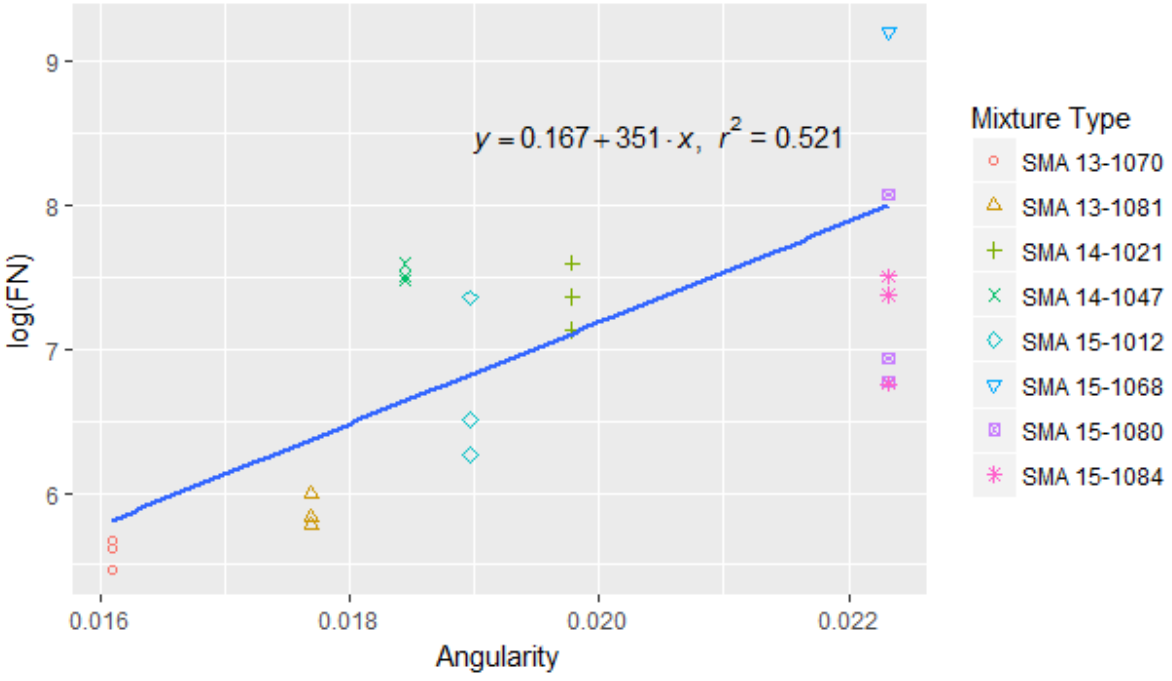

(c) Angularity versus Log(FN) for all SMA mixtures

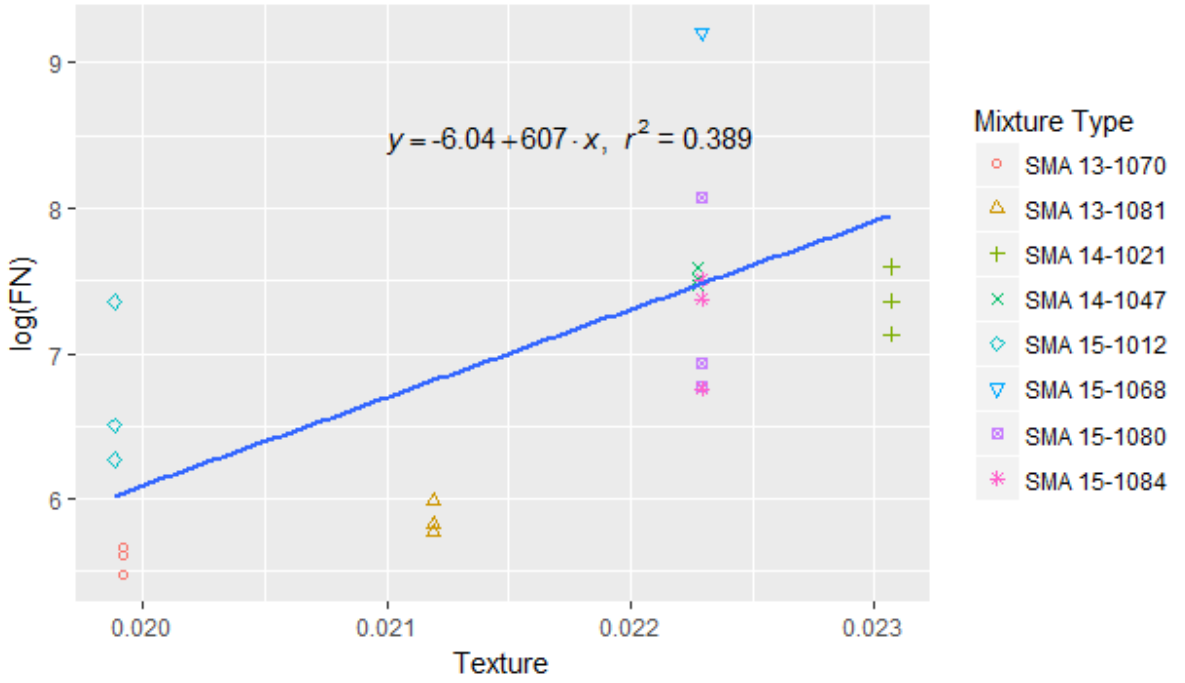

(d) Texture versus Log(FN) for all SMA mixtures

Figure 6.3 Morphological Characteristics versus Log(FN) for all SMA mixtures

Correlation between aggregate morphological characteristics and flow number slope

The flow number slope (FNS) characterizes the rate of change of cumulative permanent deformation under the repeated loading condition and was found to relate well to the rutting performance of asphalt mixture pavements. The flow number slope can be estimated from a regression analysis of the linear portion of the plot of the permanent strain versus the number of loading cycles on a log-log scale. To investigate how aggregate morphology would affect the rate of change of vertical permanent deformation, FNS was used as another important indicator related to the aggregate morphological characteristics. Using the FNS estimated from the flow number tests given in Table 5.5 in Chapter 5, the effect of asphalt content on the permanent deformation behavior of the 24 SMA mixture specimens was studied. Statistical analyses between the FNS and both the asphalt content and performance grades of the 24 asphalt mixture specimens were recorded in Table 6.4. The lower p-value in bold indicated flow number slope had correlations with performance grade of asphalt binder. Figure 6.4 presents the plot of flow number slope versus the performance grade of asphalt binder. As seen in figure 6.4, the stiffer the asphalt binder, the slower the flow number slope, the better the rutting resistance. The flow number slope data were then grouped based on different asphalt binder stiffness (PG 70 and PG 76), two separate sets of regression analyses were performed for the different categorized SMA mixtures. The descriptive statistics of the aggregate morphological characteristics and the flow number slope (FNS) are listed in Table 6.5. The regression pairs that have a p-value higher than the specified significance level of 5% ($\alpha = 0.05$) were considered as having poor correlations between the response and the predictor variables. Regression analyses were only performed on the regression pairs in bold, since they had the meaningful p-values and indicated statistically significant.

Figure 6.5 shows the linear regression analyses conducted between the weighted mean morphological characteristics (S, FER, AF and TF) and the measured permanent deformation parameters FNS of all SMA mixtures with or without grouping FNS data based on PG grades. As shown in Figure 6.5, FNS increases with increased weighted mean FER values. FNS decreases with increased weighted mean S, AF and TF values. It is generally accepted that the lower the flow number slope, the better the rutting resistance. Therefore, using more of the spherical, angular or better-crushed, rough, less flaky coarse aggregate particles in SMA mixtures, as indicated by higher S, AF, and TF values and lower FER values, can improve the resistance of the SMA to rutting. Likewise, more angular aggregates in the mixtures resulted in better aggregate interlocking. Rougher textured aggregates in the mixtures promoted stronger aggregate structures and higher stability. Less flaky aggregates tended to not breakdown easily. The SMA mixtures consisting of more spherical, less flaky aggregates with more angular and rougher textured surfaces exhibited better rutting resistance.

Table 6.4 Statistical results of regression analyses between flow number slope and asphalt content and performance grade

Regression Pair	T Stat	P-value
FNS-AC	0.729	0.4737
FNS-PG	-5.41	**1.965e-05**

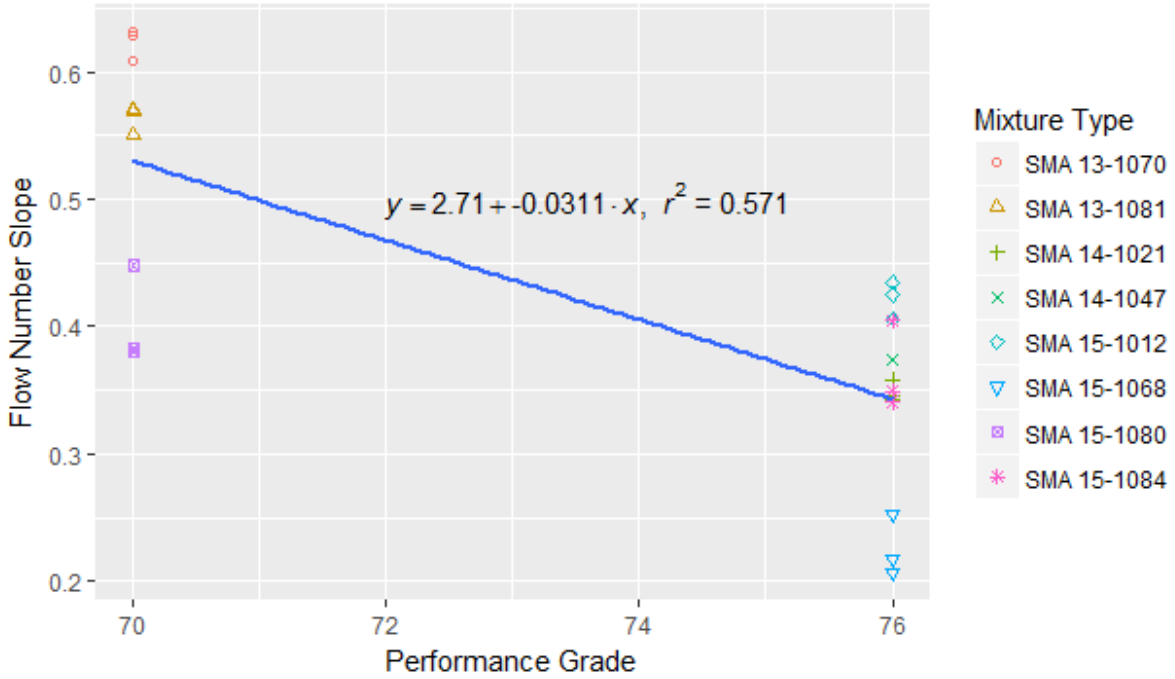

Figure 6.4 Performance grade of asphalt binder versus flow number slope

Table 6.5 Statistical results of regression pairs of aggregate morphologies and flow number slopes with or without grouping based on asphalt binder stiffness

(a) Statistical results of regression pairs between aggregate morphologies and flow

number slopes

Regression Pair	T Stat	P-value
FNS-S	-2.609	**0.01603**
FNS-FER	2.764	**0.01132**
FNS -AF	-5.634	**1.153e-05**
FNS-TF	-4.420	**0.0002162**

(b) Statistical results of regression pairs between aggregate morphologies and flow number slopes When categorized based on asphalt binder stiffness

Regression Pair	T Stat	P-value
FNS-S (PG=70)	-11.64	**7.793e-06**
FNS-FER (PG=70)	8.715	**5.257e-05**
FNS -AF (PG=70)	-12.40	**5.092e-06**
FNS-TF (PG=70)	-6.973	**0.0002167**
FNS-S (PG=76)	-2.891	**0.01262**
FNS-FER(PG=76)	2.663	**0.01954**
FNS-AF (PG=76)	-2.612	**0.02153**
FNS-TF (PG=76)	-2.161	**0.04994**

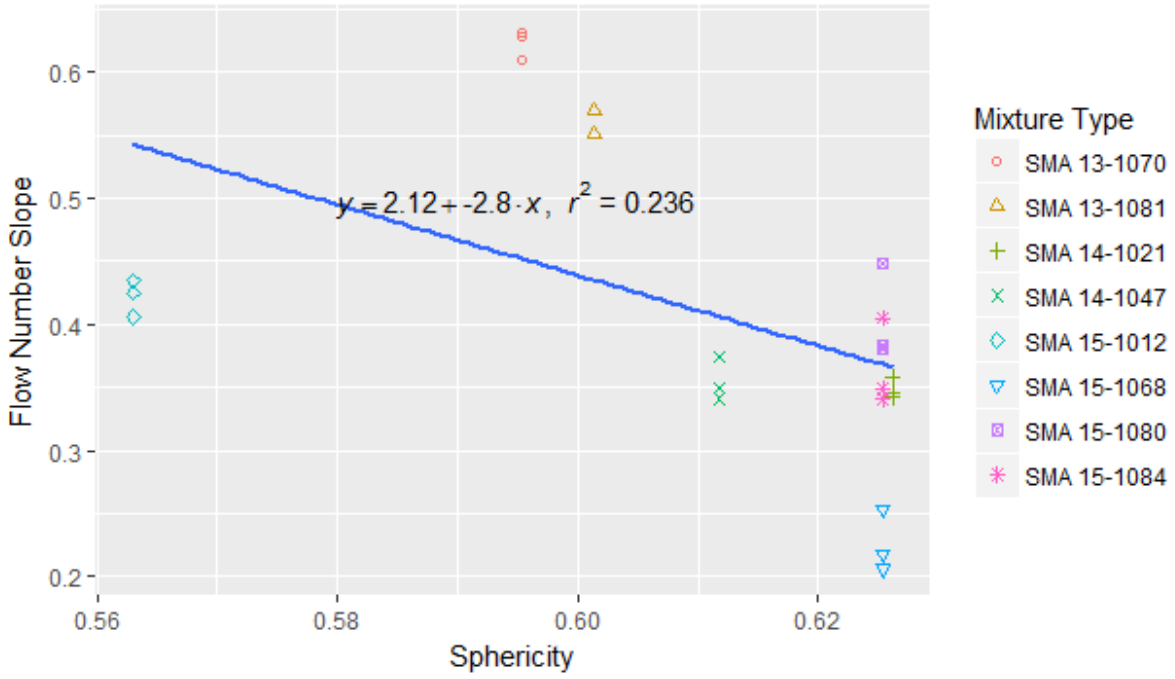

(a1)

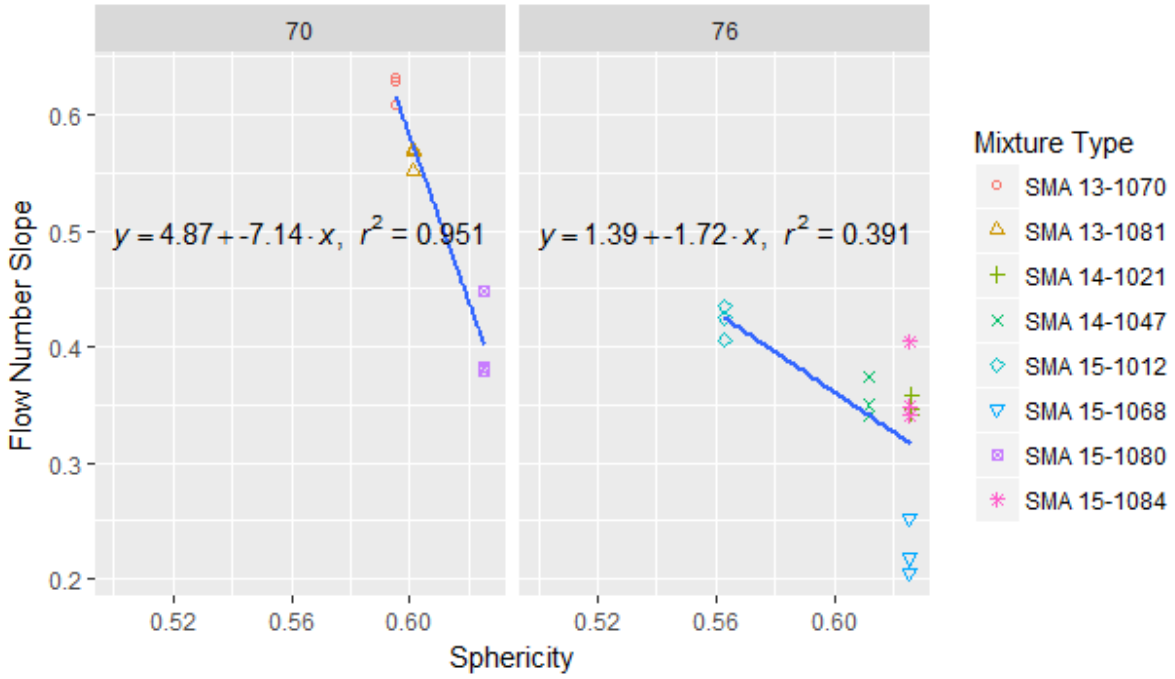

(a2)

(a) Sphericity versus FNS for all SMA mixtures

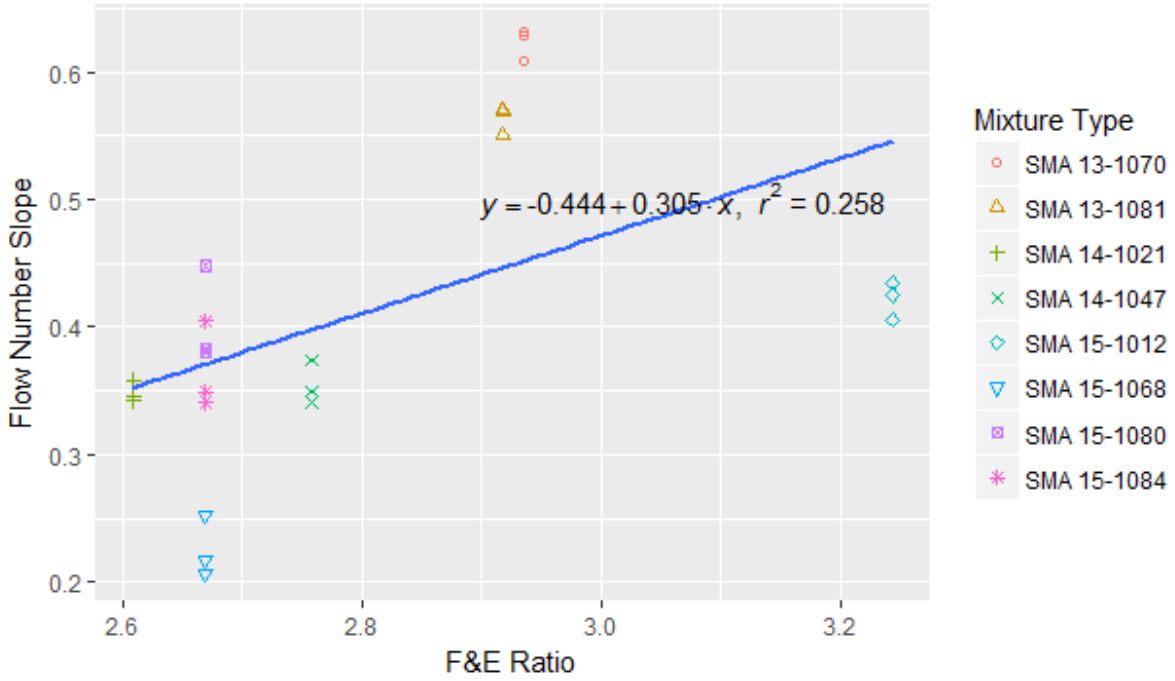

(b1)

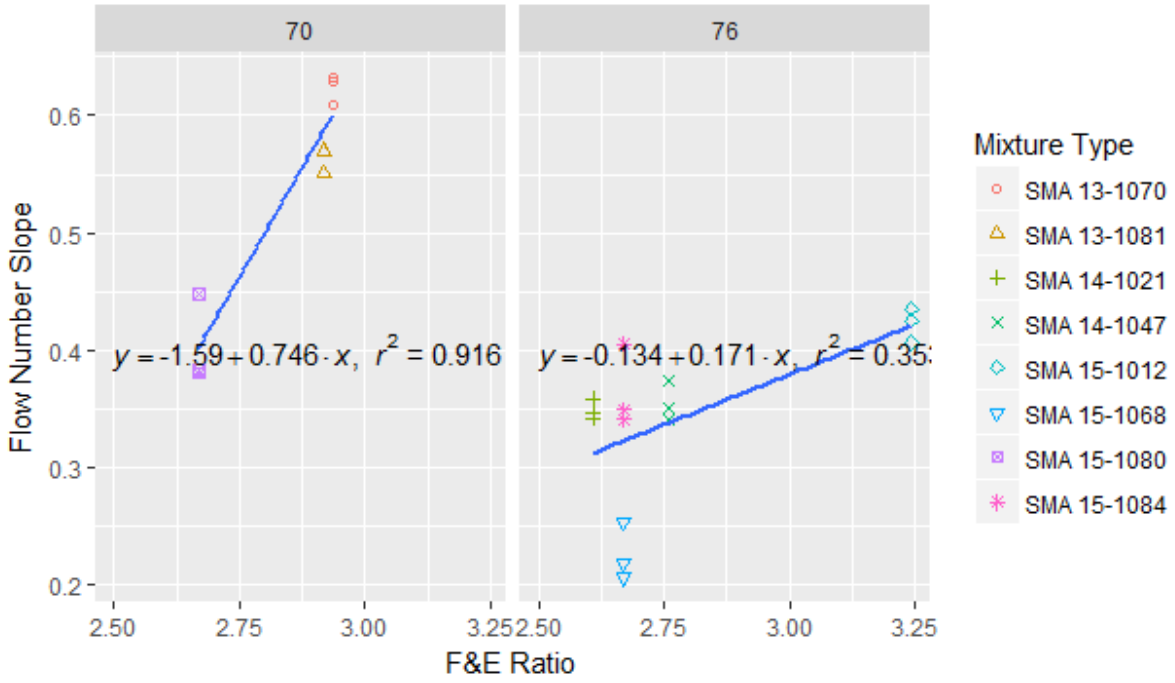

(b2)

(b) Flat and elongated ratio versus FNS for all SMA mixtures

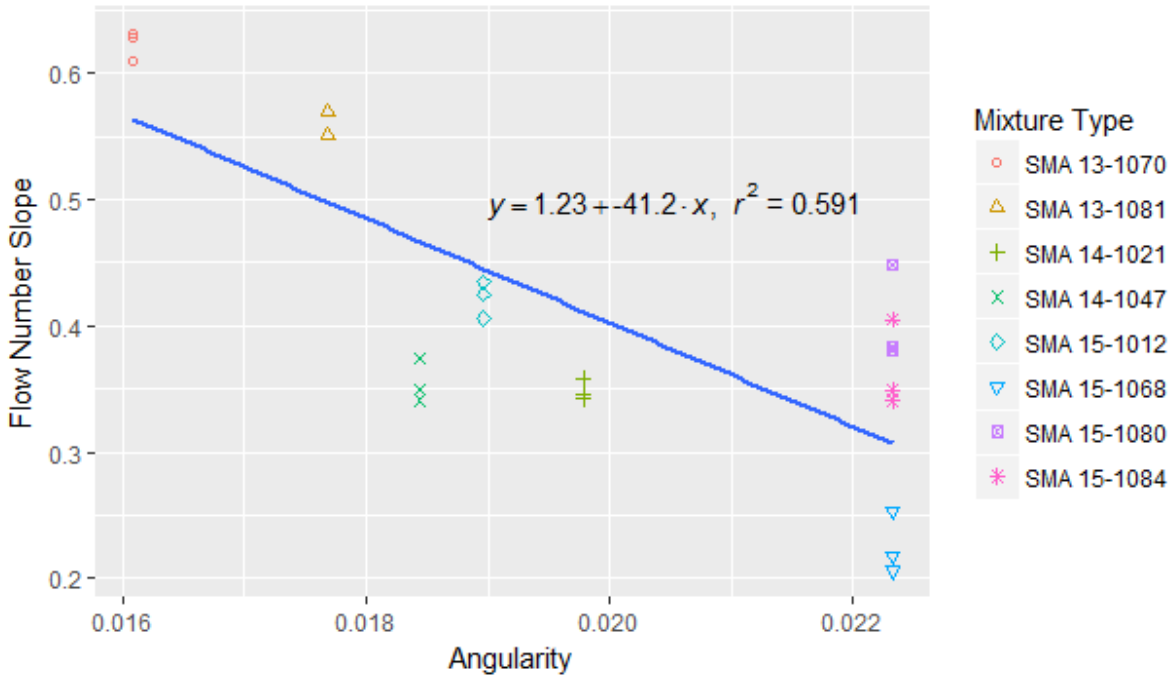

(c1)

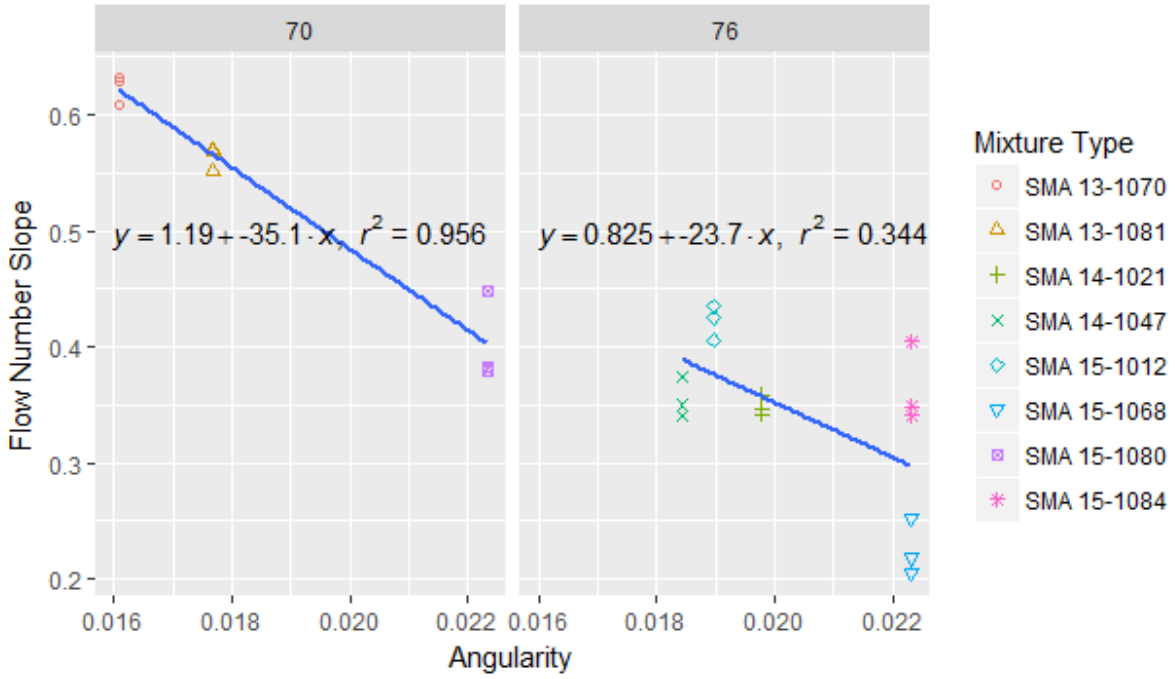

(c2)

(c) Angularity versus FNS for SMA mixtures

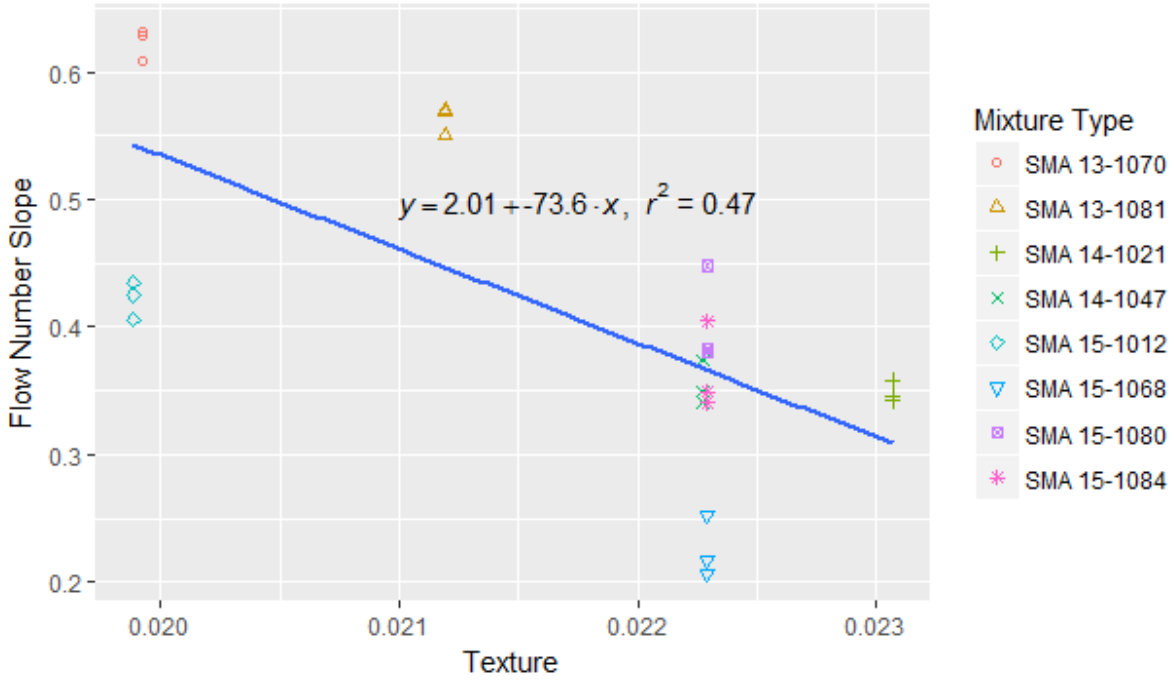

(d1)

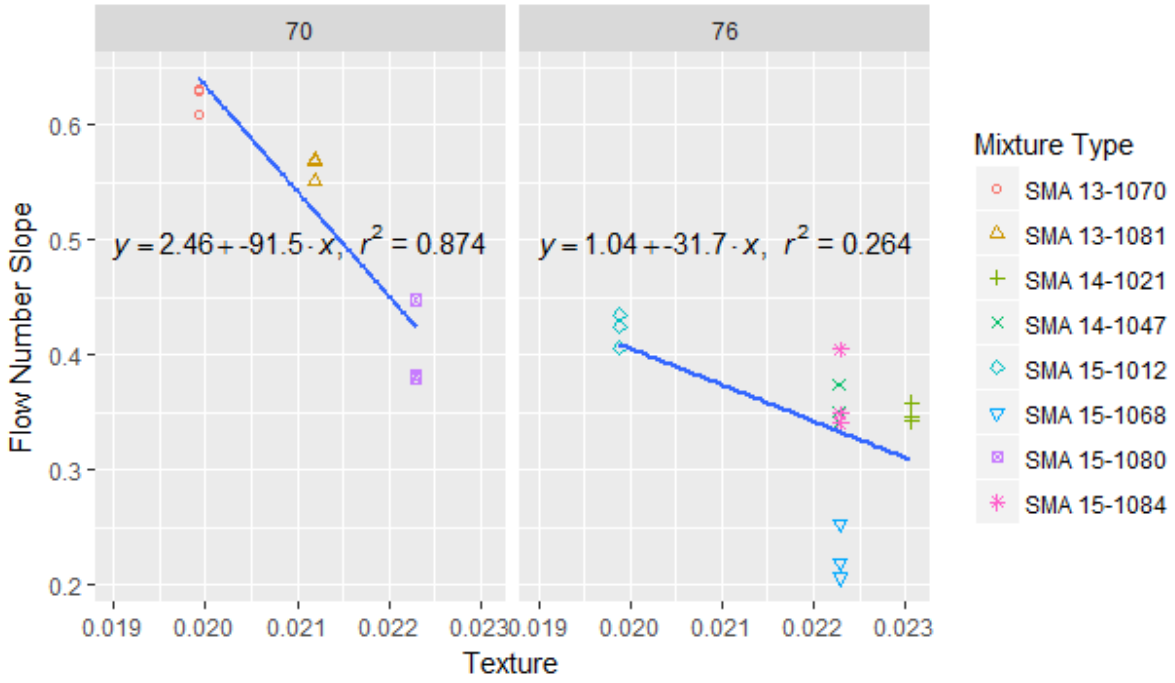

(d2)

(d) Texture versus FNS for SMA mixtures

Figure 6.5 Morphological characteristics versus FNS for SMA mixtures

Effects of Coarse Aggregate Morphologies on Fatigue Performance of SMA under Different Strain Levels Using Beam Fatigue Test

The number of loading cycles to failure under three different strain levels obtained from beam fatigue tests was used as the another important fatigue indicator to measure the fatigue performance ranking of all types of SMA mixtures. The number of loading cycles was defined when the beam stiffness degraded to 50 % of the initial flexural stiffness. Similarly, the statistical analyses were performed between the number of loading cycles to failure under three different strain levels and both the asphalt contents and performance grades of all the mixtures. The statistical results were shown in Table 6.6. As shown in table 6.6, the number-of-loading-cycle and performance-grade regression pairs under 300 and 600 microstrain levels show a p-value smaller than the significance level of 5%, indicating the asphalt binder performance grade can significantly affect the number of loading cycle to failure at 300 and 600 microstrain levels. Figure 6.6 shows that the stiffer the asphalt binder, the more loading cycles the SMA mixtures can withstand until failure.

To better interpret the beam fatigue test results, the measured number of loading cycles to failure under different strain levels, which are denoted as NOCs, were taken logarithms for the studied eight types of SMA mixtures, each with three replicates, and the regression analyses were performed between aggregate morphologies and the logarithms of the number of loading cycles to failure, which are denoted as Log(NOC). A total of twelve regression pairs between the four morphological characteristics and the Log(NOC) under three different strain levels were analyzed statistically.

The descriptive statistics of the aggregate morphological characteristics and the fatigue parameter (Log(NOC)) are listed in Table 6.7. The regression pairs that have a p-value greater than the specified significance level of 5% ($\alpha = 0.05$) were considered as having poor correlations between the dependent and the independent variables. Regression analyses were only performed on the regression pairs in bold, since they had the p-values less than 5%, indicating statistically significant. Linear regression analyses were conducted to investigate the relationships between the weighted mean morphological characteristics (AF and TF) and the measured fatigue parameters Log(NOC) of all SMA mixtures under three different strain levels.

Figure 6.7 shows the correlations of Log(NOC) with the weighted mean AF and TF values under 300 microstrain level. Figure 6.8 shows the regression relationship between Log(NOC) and weighted mean AF and TF values under 450 microstrain level. Figure 6.9 shows the correlation of Log(NOC) with weighted mean TF under 600 microstrain level. As shown in all the figures, the Log(NOC) tends to increase as the angularity and texture increase, indicating that SMA mixtures with more angular and rougher aggregates can withstand more loading cycles until failure and possess better fatigue life. The fatigue properties of SMA mixtures could be greatly improved for aggregate blends with higher AF and TF indices. The effect of angularity on the fatigue resistance of SMA mixtures was positive, because aggregates with greater angularity require more asphalt binder to meet mix design criteria, which reduces cracking due to increased viscoelastic energy dissipation from the binder, while angular particles produce a higher stress concentration that results in potential cracks (Kim, et al, 2009). The effect of texture on the fatigue resistance of SMA mixtures was positive because rough textured aggregates improved inter-particle contact and provided a better binder-aggregate interaction, which makes the SMA mixtures more resistant to fatigue cracking. Fatigue cracking can be decreased by improving the aggregate-binder interactions through using aggregates with rougher texture. Thus angular and rough-textured aggregates in SMA mixtures are crucial and desirable to obtain better fatigue performance. Little (2003) also demonstrated that the granite mixture shows better fatigue performance than the limestone mixture due to the fact that the granite aggregates are rougher, more angular, and retained more bonding with the binder compared to limestone aggregates.

Table 6.6 Statistical results of regression analyses between number of loading cycles to failure and asphalt content and performance grade

Regression Pair	T Stat	P-value	R2
NOC-AC (300 microstrain level)	-0.088	0.9307	0.0004325
NOC-PG (300 microstrain level)	5.674	**2.214e-05**	0.6414
NOC-AC (450 microstrain level)	1.144	0.2675	0.0678
NOC-PG (450 microstrain level)	2.101	0.05001	0.1969
NOC-AC (600 microstrain level)	1.251	0.2253	0.0726
NOC-PG (600 microstrain level)	2.671	**0.01469**	0.2629

Note: NOC mean the number of loading cycles to failure under different strain levels.

Table 6.7 Statistical results of regression pairs between aggregate morphologies and number

of loading cycles to failure under different strain levels

Regression Pair	T Stat	P-value
Log(NOC)-S (300 strain level)	0.994	0.3333
Log(NOC)-FER (300 strain level)	-1.065	0.3009
Log(NOC)-AF (300 strain level)	3.031	**0.007185**
Log(NOC)-TF (300 strain level)	2.757	**0.01299**
Log(NOC)-S (450 strain level)	1.855	0.08
Log(NOC)-FER (450 strain level)	-1.839	0.08248
Log(NOC)-AF (450 strain level)	2.246	**0.03747**
Log(NOC)-TF (450 strain level)	2.268	**0.03585**
Log(NOC)-S (600 strain level)	1.402	0.1763
Log(NOC)-FER (600 strain level)	-1.336	0.1964
Log(NOC)-AF (600 strain level)	2.343	**0.02958**
Log(NOC)-TF (600 strain level)	1.833	0.08177

Note: NOC means the number of loading cycles to failure.

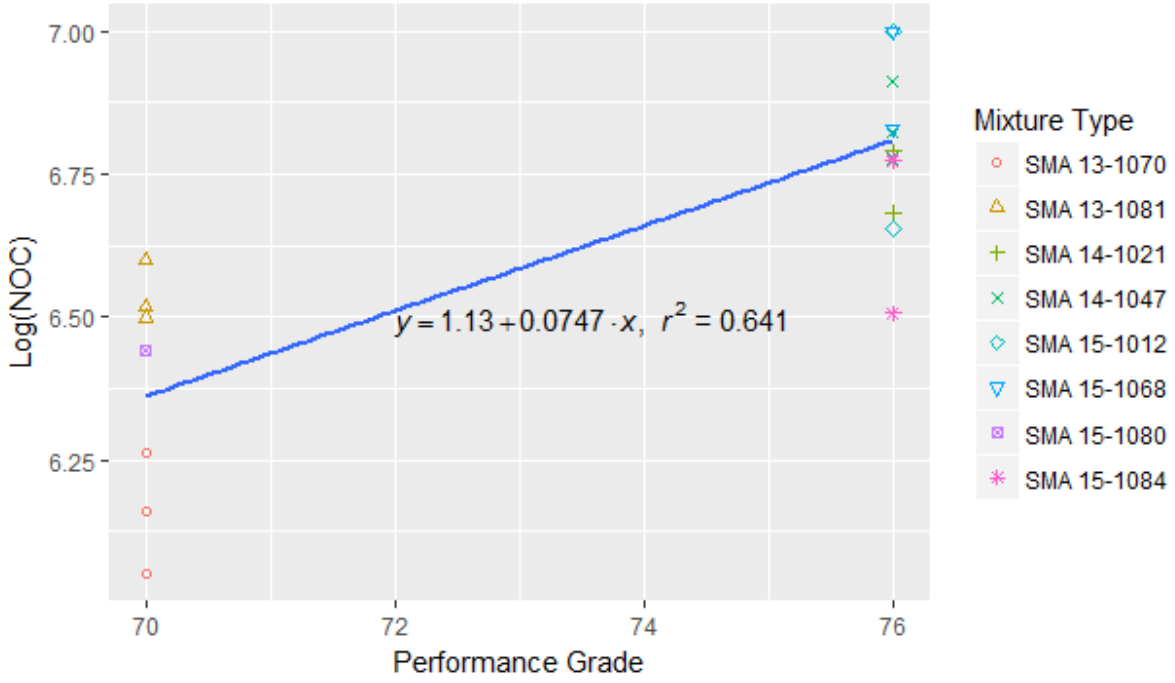

(a) Performance grade of asphalt binder versus number of cycles to failure under 300 microstrain level

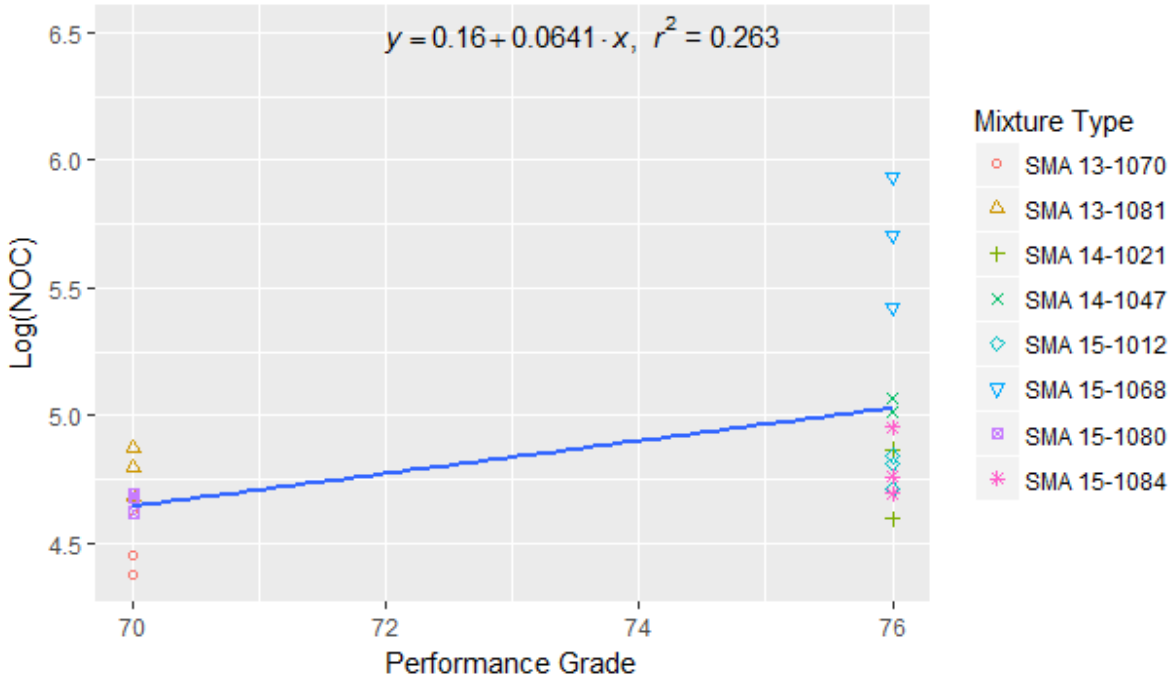

(b) Performance grade of asphalt binder versus number of cycles to failure under 600 microstrain level

Figure 6.6 Performance grade of asphalt binder versus number of cycles to failure under 300 and 600 microstrain levels

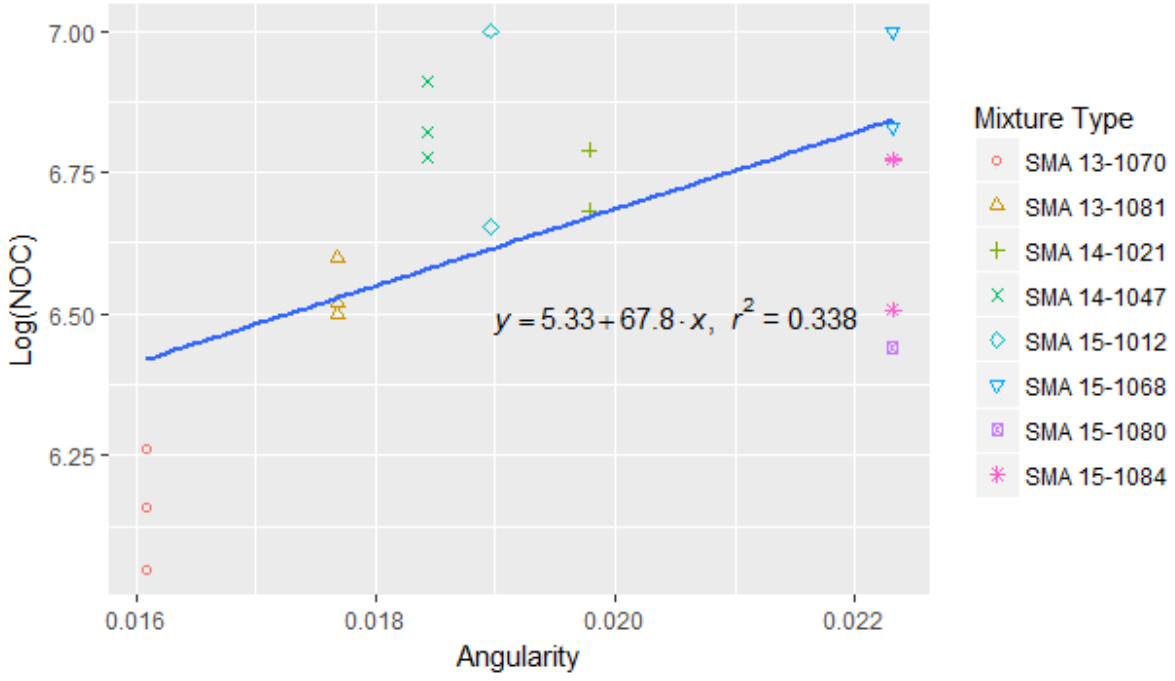

(a) Angularity versus Log(NOC) for all SMA mixtures under 300 microstrain level

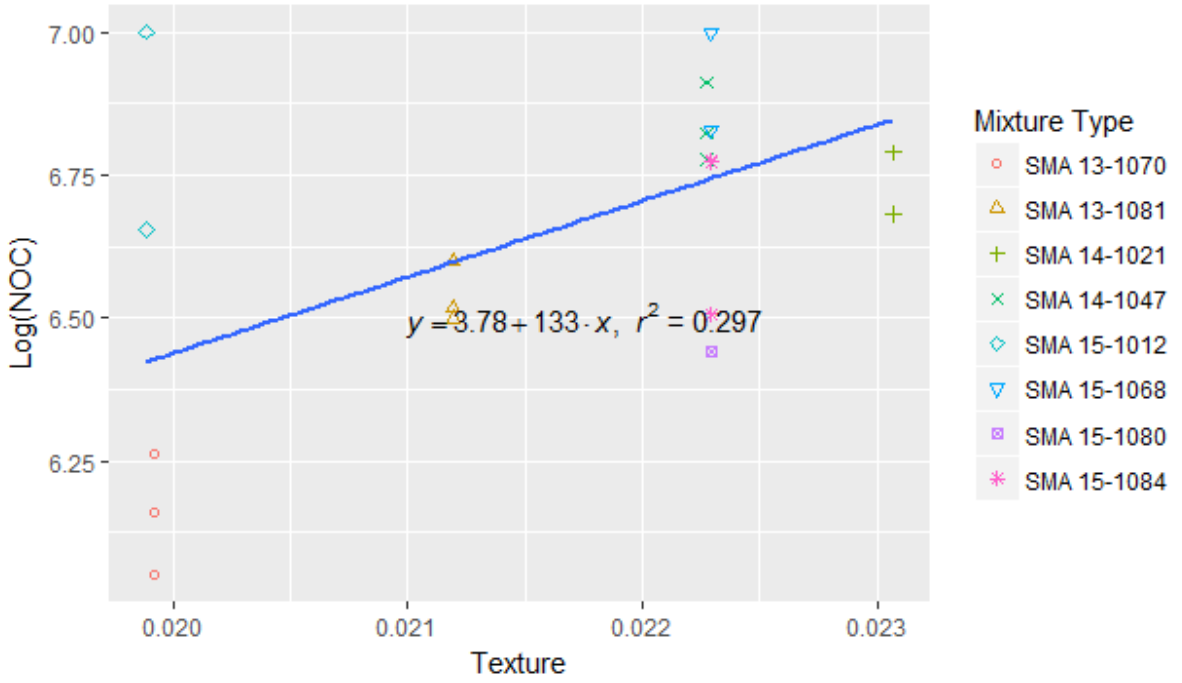

(b) Texture versus Log(NOC) for all SMA mixtures under 300 microstrain level

Figure 6.7 Morphological characteristics versus Log(NOC) for all SMA mixtures under 300 microstrain level

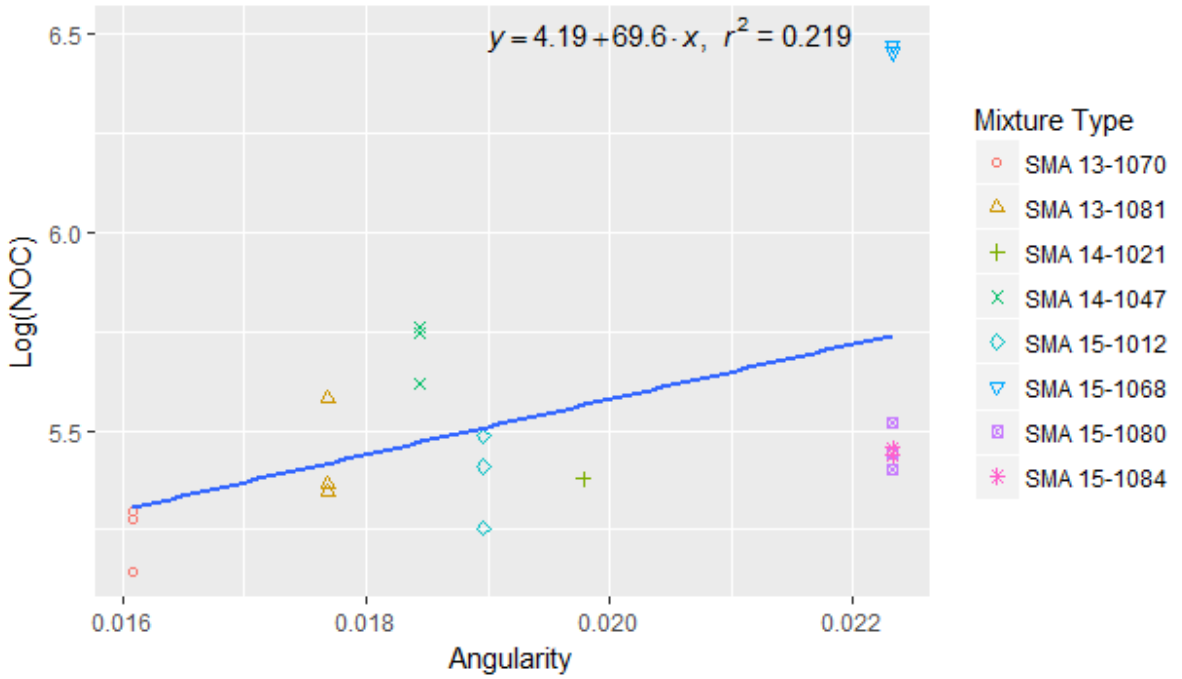

(a) Angularity versus Log(NOC) for all SMA mixtures under 450 microstrain level

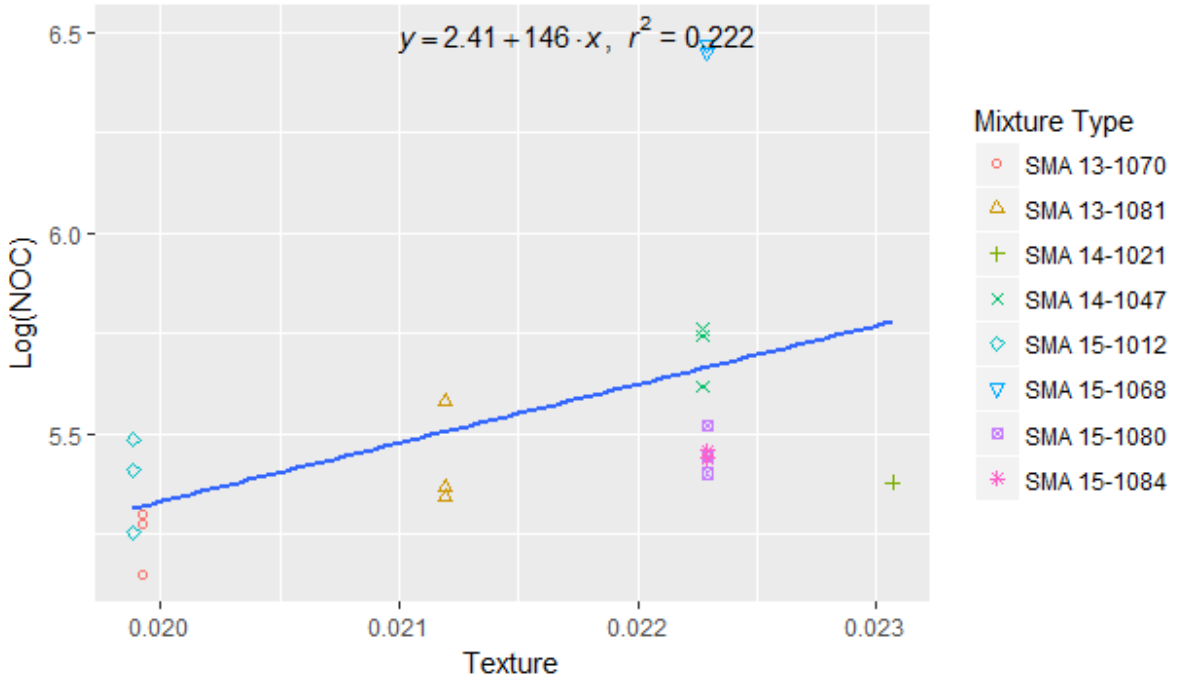

(b) Texture versus Log(NOC) for all SMA mixtures under 450 microstrain level

Figure 6.8 Morphological characteristics versus Log(NOC) for all SMA mixtures under 450 microstrain level

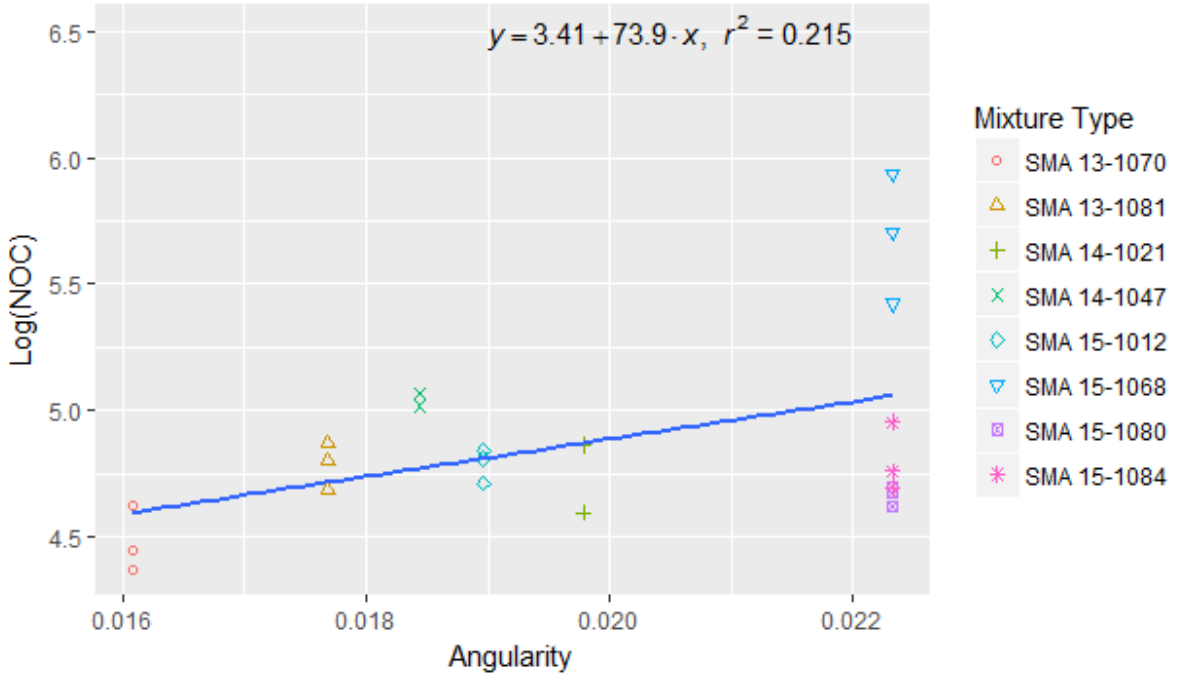

Figure 6.9 Angularity versus Log(NOC) for all SMA mixtures under 600 microstrain level

Effects of Coarse Aggregate Morphologies on Rutting and Fatigue Performance of SMA during Load Trafficking Using Wheel-tracking APA Test and MMLS Test

The effects of asphalt binder content and performance grade on the rutting and fatigue performance of SMA mixtures were analyzed first. The rut depth and the creep slope from

APA test results measure the deformation and the rate of deformation with respect to the number of loading cycles without considering the initial amount of consolidation. The seismic modulus difference from the MMLS test evaluates the stiffness degradation of SMA mixtures. Regression analyses were conducted to determine the effects of asphalt binder content and asphalt binder performance grade on rut depth, APA creep slope and seismic modulus difference first. The linear regressions between performance grade and rut depth and creep slope have correlation coefficients R^2 of 0.01088 and 0.001983, respectively. The linear regression between asphalt binder content and seismic modulus difference has a correlation coefficient of 0.04388. The low correlations between the performance grade and rut depth, creep slope indicated that the performance grade might not be the main influential factor to affect the rutting performance of SMA mixtures. The low correlation between the asphalt content and seismic modulus difference might be due to the fact that asphalt content difference was not significant among different mixtures, which indicated that asphalt content might not be the main factor to affect the fatigue performance of SMA mixtures. Therefore, coarse aggregate morphology predominantly affects the mechanical performance of SMA mixtures.

The effects of coarse aggregate morphological characteristics on the rutting performance of SMA mixtures were examined by correlating the morphological characteristics to rut depth, creep slope of SMA mixtures obtained from the APA test. The effects of coarse aggregate morphological characteristics on the fatigue performance of SMA mixtures were examined by correlating the morphological characteristics to seismic modulus difference of SMA mixtures. A series of regression analyses were conducted between the selected four morphological characteristics and rut depth, creep slope and seismic modulus difference, respectively. These four morphological characteristics, including sphericity, flat and elongated ratio, angularity and texture, were considered as response variables, while the rut depth, creep slope and seismic modulus difference were considered as predictor variables.

Before performing the regression analyses, t-tests were conducted to identify certain morphological characteristics for further regression analyses. A lower p-value (<0.05) suggests that the changes in the predictor are associated with changes in the response, indicating it is statistically significant. A greater coefficient of determination R^2 indicates that the predictor is strongly related with the response. T-tests with higher p-values representing insignificant relationships between the predictor and response variables were screened out. Table 6.8 summarizes the statistical results of a total of 12 regression pairs. The regression pairs in bold were further analyzed on the possible effects of morphological characteristics on the mechanical performance of SMA mixtures, since they had lower p-values and relatively higher R^2-values, indicating good correlation with each other.

Table 6.8 Statistical Results of Regression Analyses

Regression Pair	T Stat	P-value	R^2
Sphericity-RD	-3.282	**0.003406**	0.3287

Sphericity-CS	-2.633	**0.01881**	0.3162
Sphericity -SMD	-2.452	**0.02607**	0.2731
Flat and Elongated Ratio-RD	3.040	**0.006005**	0.2959
Flat and Elongated Ratio-CS	2.548	**0.02228**	0.3021
Flat and Elongated Ratio-SMD	2.764	**0.01383**	0.3232
Angularity-RD	-0.415	0.6818	0.007786
Angularity-CS	-0.047	0.963	0.000148
Angularity-SMD	-1.935	0.07091	0.1896
Texture-RD	-1.869	0.07501	0.137
Texture-CS	-1.612	0.1277	0.1477
Texture-SMD	-3.873	**0.001349**	0.4838

Note: The p-values in bold are less than 0.05, which indicates statistical significance;
RD means rut depth; CS is creep slope in APA test. SMD is seismic modulus difference.

Correlation between aggregate morphological characteristics and APA rut depth

The weighted mean flat and elongated ratio values from the screening t-tests were found to have a statistically significant relation with rut depth for all 24 SMA mixture replicates, the correlations were poor, which indicates that flat and elongated ratio may not play a significant role in the rutting performance of the 24 SMA mixtures in this study. A possible explanation might be because of the low percentages of flat and elongated coarse aggregates that are allowed in the SMA mixtures according to the Virginia Specification for SMA mix design. Flat and elongated aggregates do not have obvious influence on rutting performances of SMA mixtures in this study. From the t-test results, sphericity was found to have better correlation with rut depth with a lower p-value and a higher R^2 value in comparison with flat and elongated ratio although the correlation was just somewhat decent linear relationship.

Figure 6.10 (a) shows the relationship between sphericity and rut depth for all eight types of SMA mixtures. From Figure 6.10 (a), the rut depths of SMA mixtures decrease with increased sphericity, indicating that spherical aggregates are more favorable to the rutting behavior of SMA mixtures. A possible explanation is as follows. Most types of aggregates used in the SMA mixtures were processed using an impact crusher, which tend to produce more equi-dimensional particles compared to aggregates produced by other crushers. Spherical or cubical particles tend to exhibit interlocking effect and strong internal friction, improving rutting performance of asphalt concrete (Jian-Shiuh et al, 2005). Therefore, spherical aggregates are preferable for increased internal friction between aggregates and improved rutting performance. Figure 6.10 (b) shows the correlation between flat and elongated ratio and rut depth for all SMA mixtures. As seen in figure 6.10 (b), the rut depths of SMA mixtures increase with increased flat and elongated ratio, indicating that flat or elongated aggregates are undesirable to the rutting performance of SMA mixtures. Flat and elongated aggregates tend to breakdown and have lower compactibility. Figures 6.10 (c) and

6.10 (d) present the low correlations between angularity, texture, and rut depth with linear regression coefficients of 0.00779 and 0.137, respectively. From Table 6.8, it is observed that both angularity and texture have no measurable effects on the rut depth, as they have high p-values and low R^2 values. However, some trends exist. As the weighted mean angularity and texture indices increase for all the mixtures, the rut depth tends to decrease, indicating better rutting resistance of SMA mixtures. This might be due to the fact that using more angular and rougher coarse aggregates in mixtures can result in higher stability of SMA mixtures and stronger internal aggregate structure, and further improve the rutting performance of SMA mixtures.

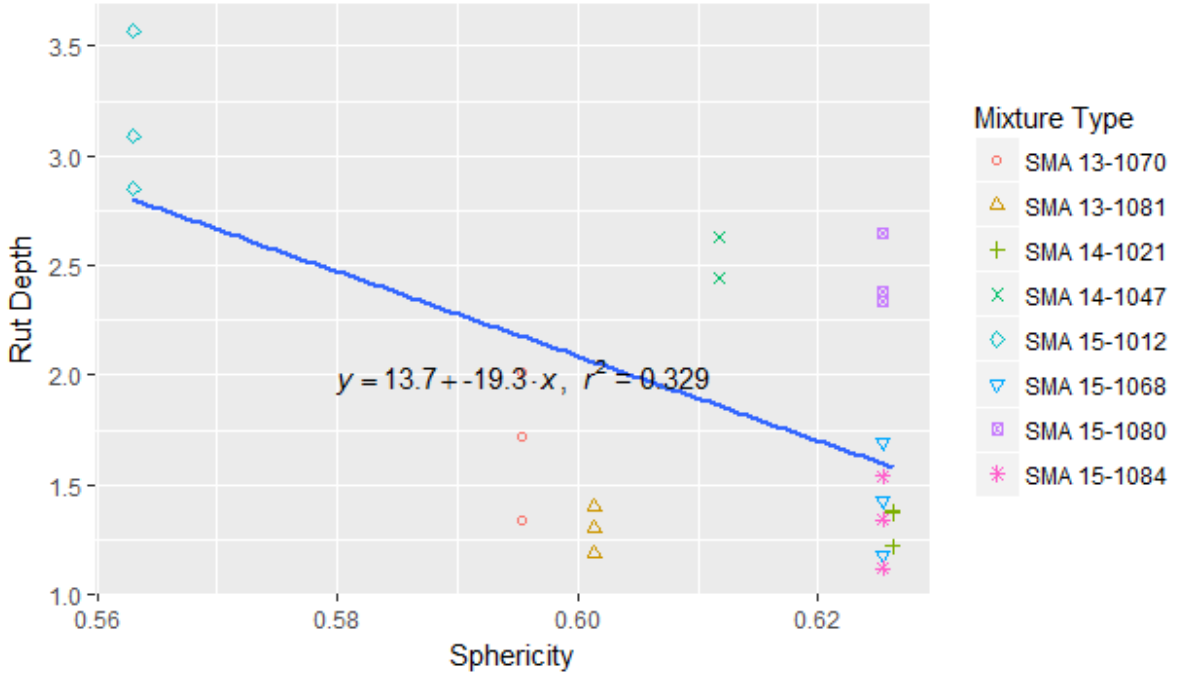

(a)

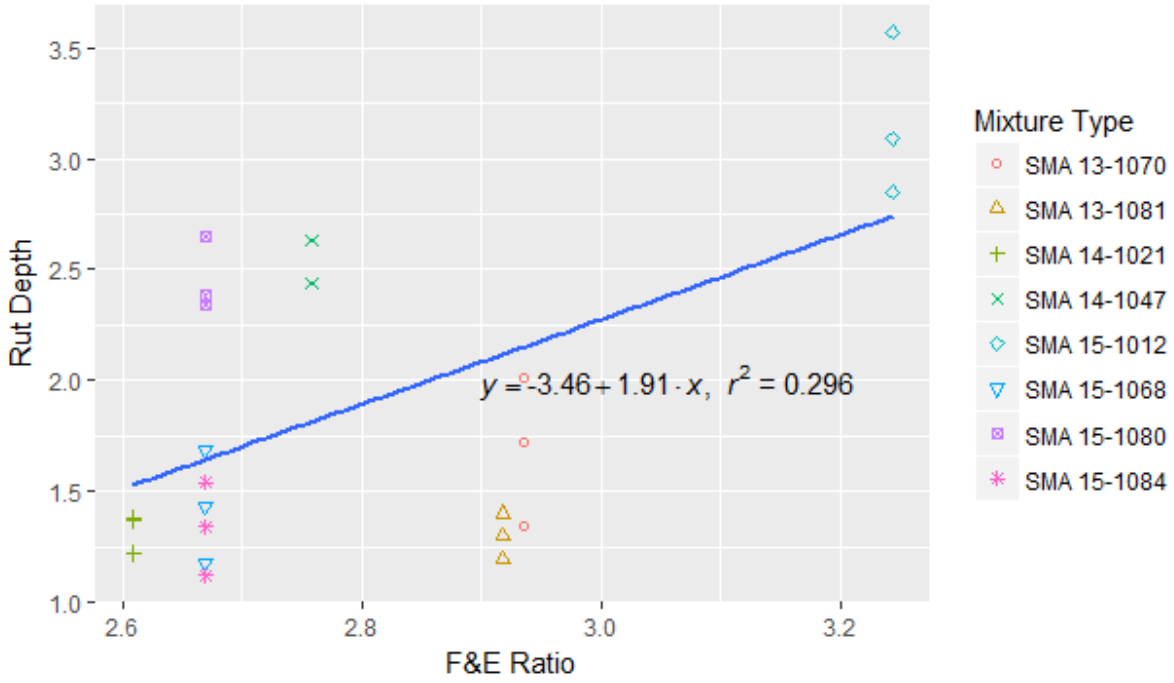
Rut Depth
F&E Ratio
y = -3.46 + 1.91 · x, r² = 0.296
Mixture Type
SMA 13-1070
SMA 13-1081
SMA 14-1021
SMA 14-1047
SMA 15-1012
SMA 15-1068
SMA 15-1080
SMA 15-1084

(b)

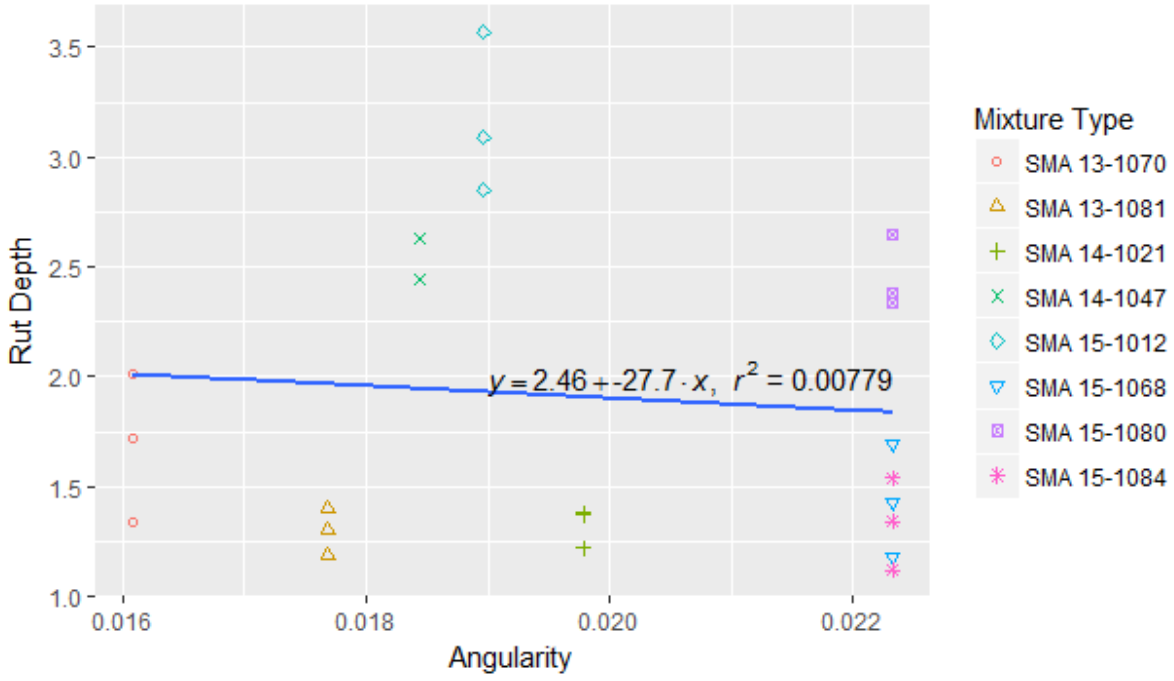
Rut Depth
Angularity
y = 2.46 + -27.7 · x, r² = 0.00779
Mixture Type
SMA 13-1070
SMA 13-1081
SMA 14-1021
SMA 14-1047
SMA 15-1012
SMA 15-1068
SMA 15-1080
SMA 15-1084

(c)

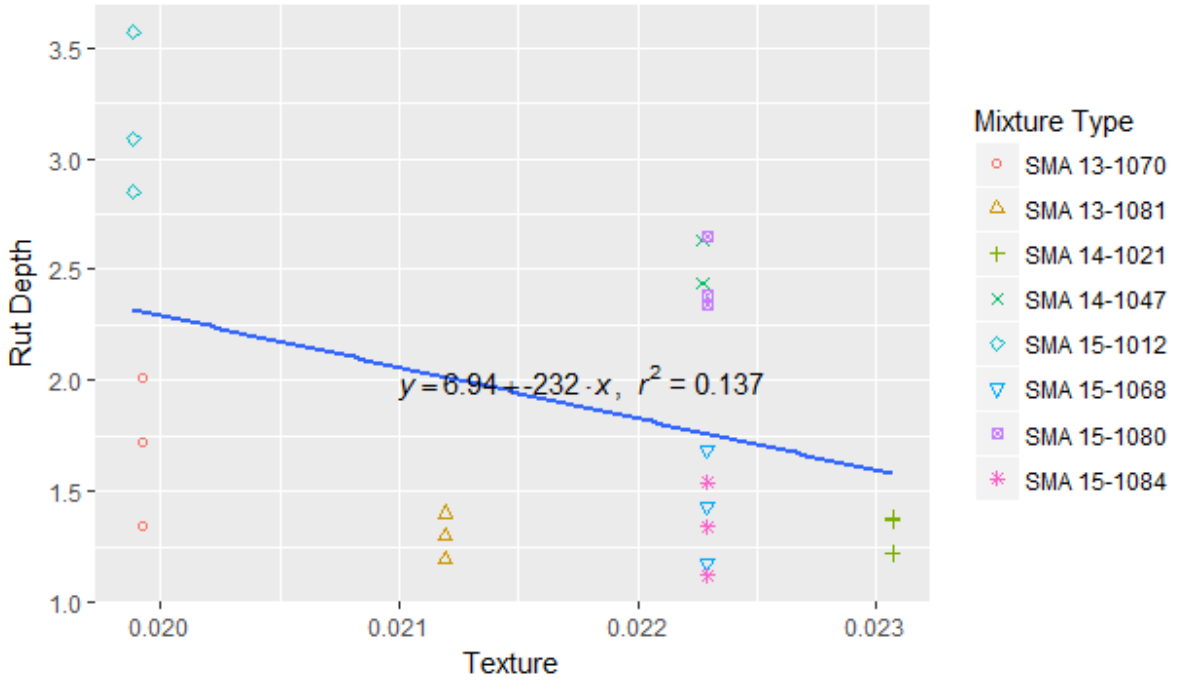

(d)

Figure 6.10 Relationships between rut depth and morphological characteristics. (a) Sphericity; (b)Flat and elongated ratio; (c) Angularity; and (d) Texture.

Correlation between aggregate morphological characteristics and APA creep slope

The weighted mean sphericity, flat and elongated ratio values were found to have statistically significant relations with creep slope for all 24 SMA mixture replicates from the screening t-tests, the correlations were not strong but somewhat decent. Figure 6.10 (a) and 6.10 (b) present the linear relationships with correlation coefficients of R^2 of 0.316 and 0.302 between the creep slope and both the sphericity and flat and elongated ratio, respectively.

Figure 6.11 (a) shows the correlation between sphericity and creep slope for all eight types of SMA mixtures. As shown in figure 6.11 (a), the sphericity index has an inverse correlation with the creep slope for all SMA mixtures, indicating that spherical aggregates are more favorable to the slow rate of change of rut depth of SMA mixtures. The slower the creep slope, the better the rutting resistance ability. SMA mixtures containing spherical and equidimensional particles have better pumpability and finishability, and produce consistent higher strengths and lower shrinkage (Ozen, 2007). Figure 6.11 (b) shows the correlation between flat and elongated ratio and creep slope for all SMA mixtures. As seen in figure 6.11 (b), the creep slopes of SMA mixtures increase with increased flat and elongated ratio, indicating that flat or elongated aggregates are undesirable to the rutting performance of SMA mixtures. Mixtures containing flat and elongated particles may decrease the stability (Doyle, 1971). Figures 6.11 (c) presents the correlation between texture and creep slope with linear regression coefficient of 0.148. From Table 6.8, it is observed that texture has no

measurable effects on the creep slope, as the texture-creep slope regression pair has high p-values and low R^2 values. However, some trends exist. As the weighted mean texture index increases for all the mixtures, the creep slope tends to decrease, indicating better rutting resistance of SMA mixtures. Therefore, using more spherical, less flaky and elongated aggregate particles with rougher texture can lead to better rutting performance, which is consistent with the previous conclusions.

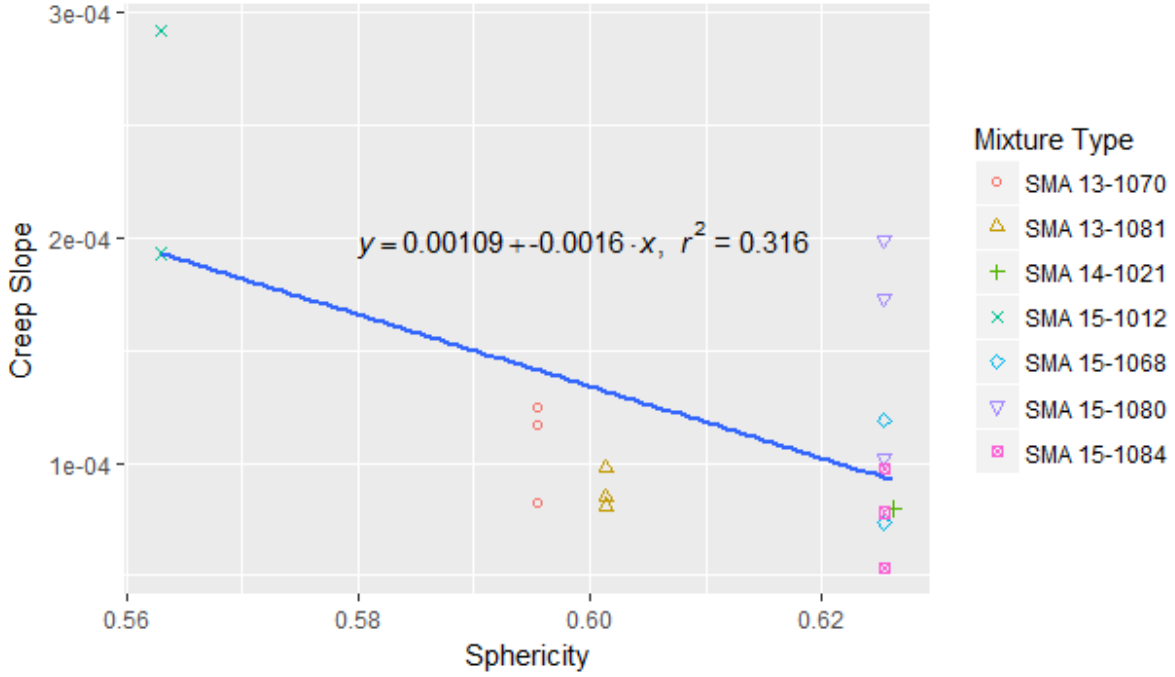

(a)

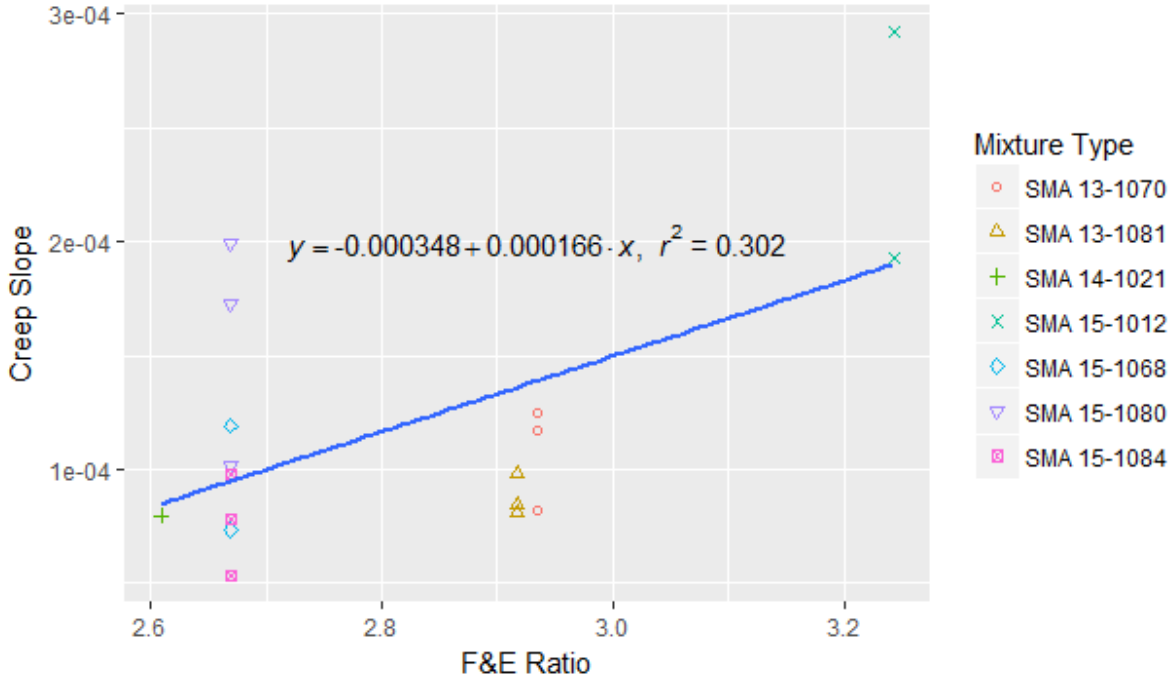

(b)

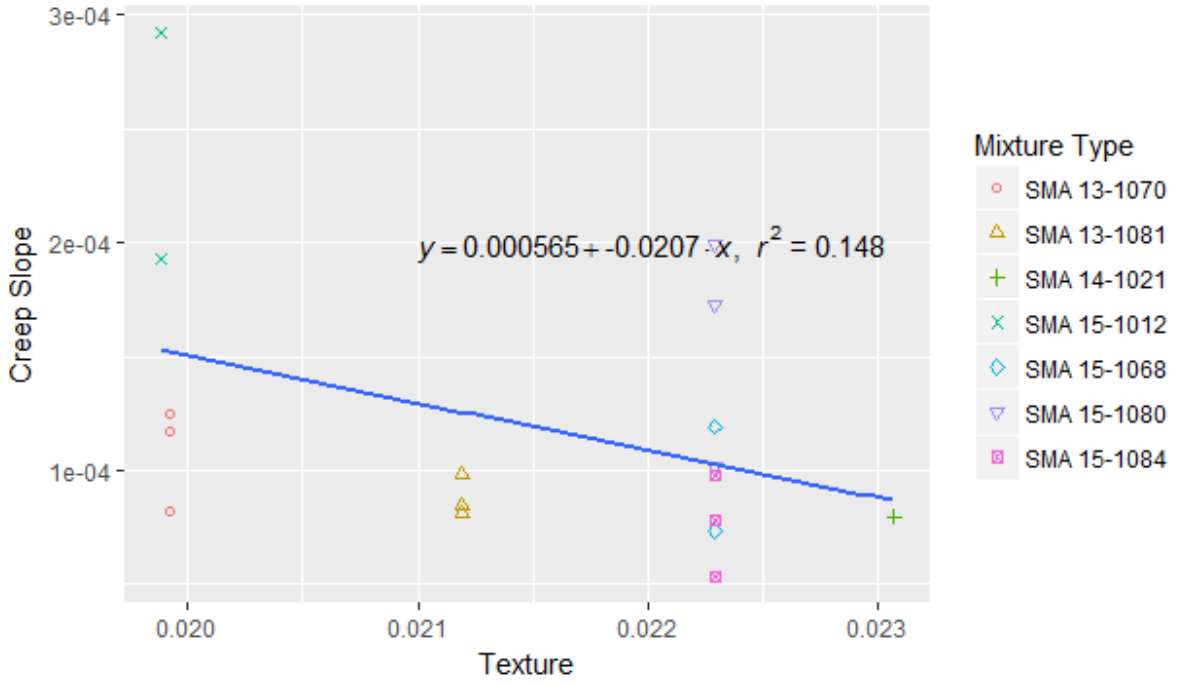

(c)

Figure 6.11 Relationships between APA creep slope and morphological characteristics. (a) Sphericity; (b)Flat and elongated ratio; and (c) Texture.

Correlation between aggregate morphological characteristics and MMLS seismic modulus difference

In the t-test, p-value was much greater than 0.05 for the regression pair between angularity index and seismic modulus difference. This indicated that it was not statistically significant for the correlation between angularity and seismic modulus difference. R^2-value for this regression pair was 0.1896, indicating no significant linear regression. This demonstrated that angularity has little impact on the seismic modulus difference, which means this morphological characteristic may not be the main contributor to the degradation of SMA stiffness after 1 million loading cycles.

The sphericity and seismic modulus difference regression pair, the flat and elongated ratio and seismic modulus difference regression pair, and the texture and seismic modulus difference regression pair were all found to have p-values lower than the specified significance level of 0.05, and so these regression pairs are statistically significant. R^2 values of 0.273, 0.323 and 0.484 for these pairs indicated that some pronounced trends exist although there were no measurable effects of sphericity, flat and elongated ratio and texture on seismic modulus difference in linear regressions.

Figure 6.12 (a) show the plot of sphericity versus seismic modulus difference for SMA mixtures. As shown in Figure 6.12 (a), as the sphericity increases for all the SMA mixtures, the seismic modulus difference tends to decrease, indicating that SMA mixtures with more spherical coarse aggregates result in the reduction of stiffness degradation. The reduction of stiffness degradation is desirable in improving the fatigue performance of SMA mixtures. In Figure 6.12 (b), the opposite trend was found between flat and elongated ratio and seismic modulus difference: as the flat and elongated ratio increases, the seismic modulus difference tends to increase, indicating that using more flat coarse aggregates facilitates the stiffness degradation. The acceleration of stiffness degradation is undesirable in improving the fatigue life of the SMA mixtures. This observation demonstrated that SMA mixtures with flaky aggregates can exhibit lower fatigue life than the ones with non-flaky aggregates. In Figure 6.12 (c), though the correlation is poor, the seismic modulus difference decreases with increased angularity, indicating that using more angular aggregates can reduce the stiffness degradation. In figure 6.12 (d), the seismic modulus difference also decreases with increased texture, which indicates that using more rougher aggregates can lead to less stiffness degradation. Therefore, the results indicated that using more spherical, less flaky shaped and angular coarse aggregates with rough texture decreased the stiffness degradation for the SMA mixtures in this study, improving the fatigue life of SMA mixtures.

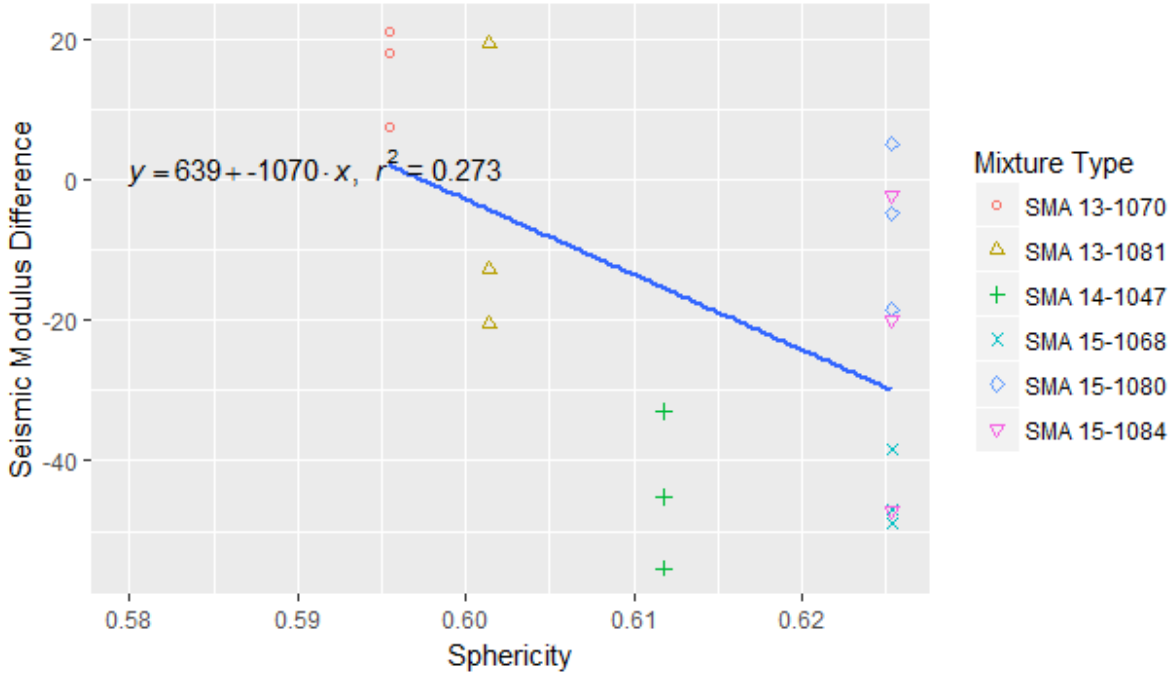

(a)

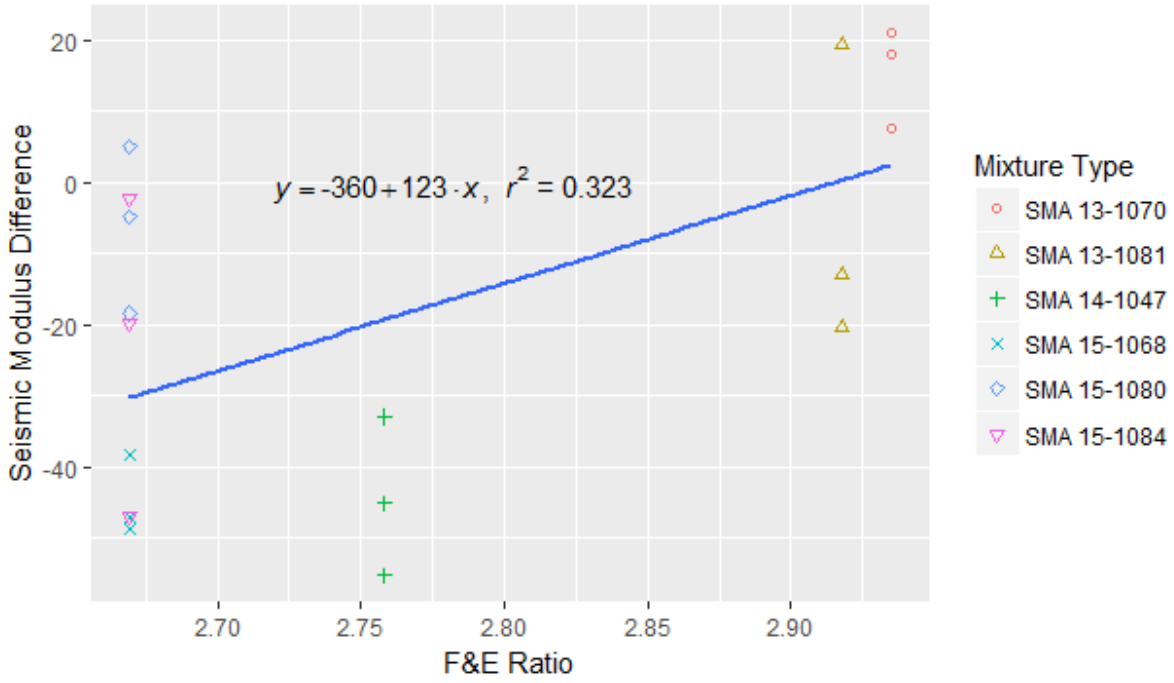
20
0
-20
-40
Seismic Modulus Difference
y = -360 + 123 · x, r² = 0.323
2.70
2.75
2.80
2.85
2.90
F&E Ratio
Mixture Type
SMA 13-1070
SMA 13-1081
SMA 14-1047
SMA 15-1068
SMA 15-1080
SMA 15-1084

(b)

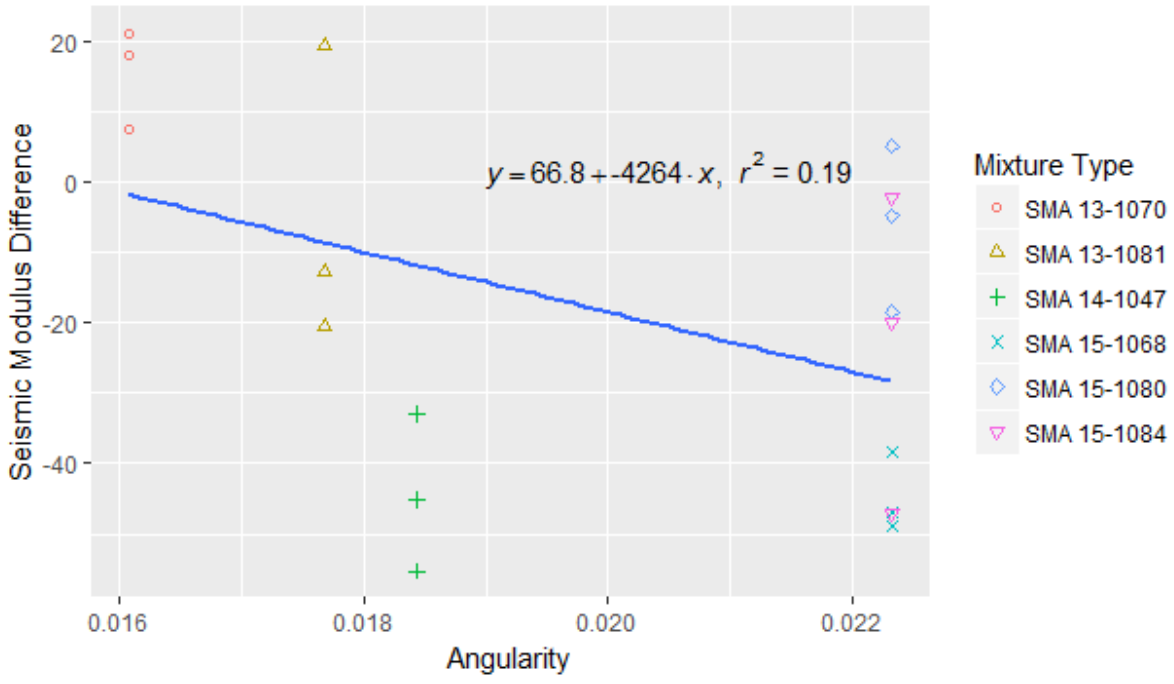
20
0
-20
-40
Seismic Modulus Difference
y = 66.8 + -4264 · x, r² = 0.19
0.016
0.018
0.020
0.022
Angularity
Mixture Type
SMA 13-1070
SMA 13-1081
SMA 14-1047
SMA 15-1068
SMA 15-1080
SMA 15-1084

(c)

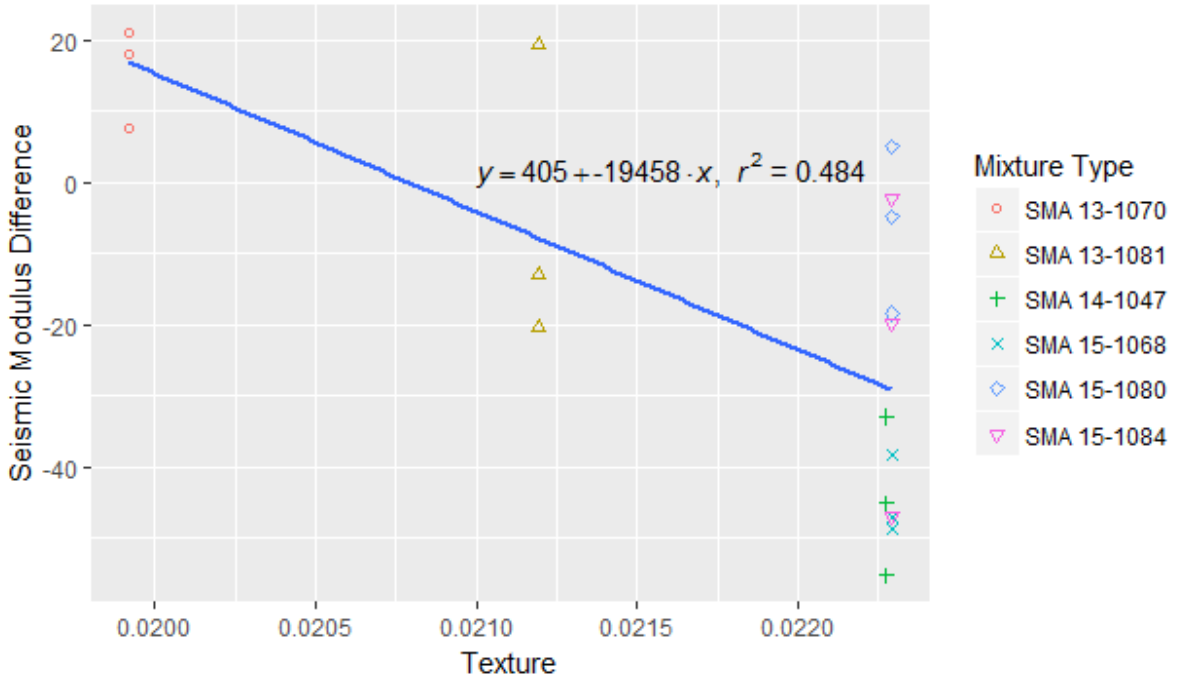

(d)

Figure 6.12 Relationships between Seismic Modulus Difference and Morphological Characteristics. (a) Sphericity, (b) Flat and elongated ratio; (c)Angularity; (d) Texture.

Relationship between the Morphological Characteristics and the Uncompacted Void Content of Coarse Aggregates

Figure 6.13 presents the distributions of five morphological parameters for the first sixteen aggregate fractions, including sphericity, flatness ratio, elongation ratio, angularity and texture. Those aggregates were selected randomly without sieving. A total of 120 aggregates were selected for each type of aggregate. This figure shows the ranges and the mean values of morphological characteristics for sixteen types of aggregates. As shown in Figure 6.13A, 13-1073 Staunton #68 has the greatest sphericity, and 13-1078 Staunton #8 has the smallest sphericity. This difference is statistically significant, as determined by an ANOVA test for all locations and a Tukey honest significant difference test between all pairs of locations. This may be because 13-1073 Staunton #68 was produced with an impact crusher, where particles impact against each other, therefore, producing more equant particles, whereas 13-1078 Staunton #8 was processed using a jaw crusher, which cannot produce particles as equant as the impact crusher. From Figure 6.13A, it can be seen that 13-1071 Bealeton aggregates have close mean values of sphericity, so does 14-1019 Leesburg aggregates. This indicates that aggregates from the same origin might have the same morphological characteristics. In Figure 6.13B, the 13-1071 Bealeton aggregate fractions have smaller flatness ratio than the other aggregate fractions, which implies that 13-1071 Bealeton aggregates are the flattest. It is obvious that 13-1073 Staunton aggregates, 13-1071 Bealeton aggregates, 14-1048 Bealeton aggregates and 14-1019 Leesburg aggregates have different flatness ratio values although they are all diabase. These differences are also statistically significant using the same ANOVA test as before. One possible

explanation is that aggregates with the same rock type but from different origins have different morphological characteristics. From Figure 6.13C, it can be seen that 13-1073 Staunton #68 has the greatest elongation ratio and 13-1078 Staunton #8 has the smallest. This difference is statistically significant. This also might be due to the use of different crushers. In Figure 6.13D, it can be seen that 14-1048 Bealeton # 60 is the most angular aggregate, followed by 14-1019 Leesburg #78, 13-1073 Staunton #68, which are all coarse aggregates. 13-1073 Staunton #10 is the least angular, which is fine aggregate. It indicates that coarse aggregates might have more angular particles than fine aggregates, which further implies that different sized aggregates might have different morphological characteristics. In Figure 6.13E, it can be seen that 13-1071 Bealeton RAP, 14-1048 Bealeton RAP and 14-1019 Leesburg RAP have the greatest texture. It might be due to the fact that RAP is a special material type, which is a mixture of aggregates and asphalt binder that have been pulled apart. 13-1073 Staunton aggregates show different texture values, this might be because each type of them has different material type although with same crush techniques. All the other types of aggregates tend to have very close texture values. Overall, it can be concluded that the aggregate morphological characteristics will be influenced by its size, material type, origins and the production technology.

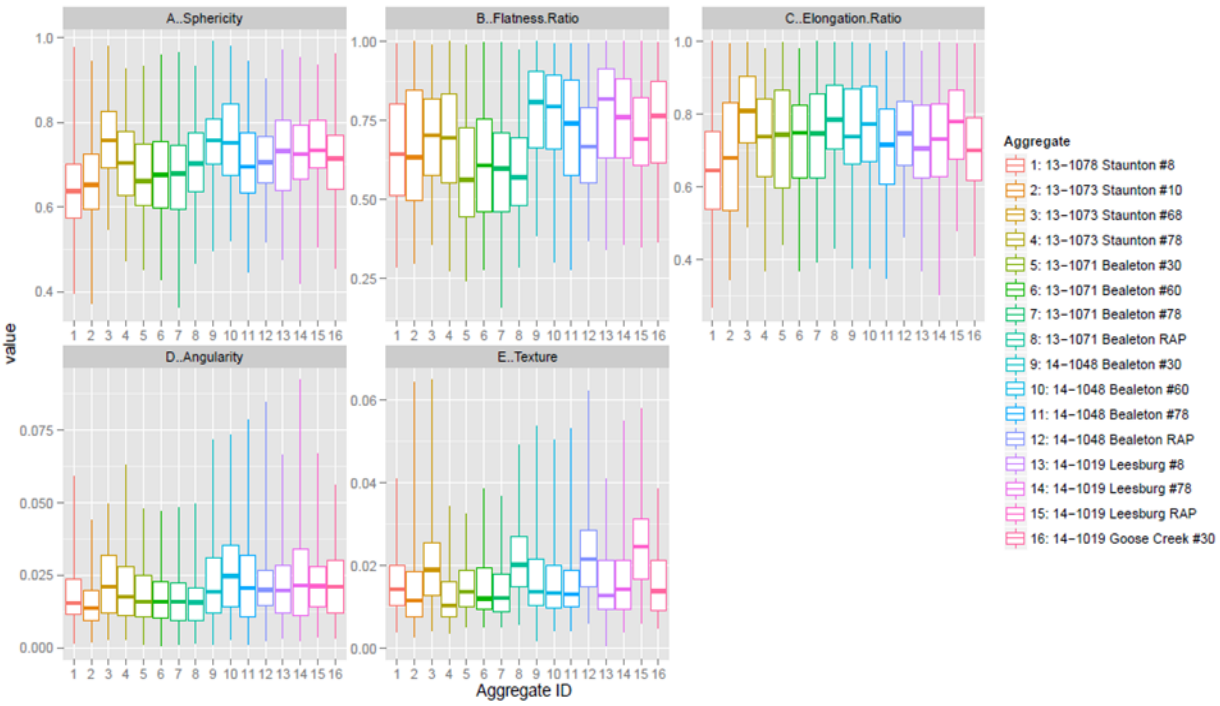

Figure 6.13 The Improved FTI morphological characteristics distributions of sixteen aggregate fractions

Aggregates with the size ranges of 4.75-9.5mm and 9.5-12.5 mm were analyzed to evaluate the relationship between morphological characteristics and uncompacted void content of coarse aggregates. To examine the effects of the morphological characteristics on the uncompacted void content of coarse aggregates, the void contents were measured for aggregates in two size ranges: 8 types of aggregates were measured for particles that pass the 9.5 mm sieve but are retained on the 4.75 mm sieve, and 11 types of aggregates were examined for particles that pass the 12.5 mm sieve but are retained on the 9.5 mm sieve. The uncompacted void content of each

aggregate fraction was measured in accordance with AASHTO T326 (Coarse Aggregate). The coarse aggregates were tested using a cylindrical metal measure with a diameter of 152 mm and a height of 160 mm. The morphological characteristics, including sphericity, flatness ratio, elongation ratio, angularity, and texture, of these aggregates tested above were obtained using the improved FTI system. The effects of the morphological characteristics (the independent variables) described above on the uncompacted void content (the dependent variable) were examined using linear regression analysis.

Tables 6.9 presents the correlation matrix between average uncompacted void contents and mean values of five morphological characteristics for aggregates passing 9.5 mm sieve and retaining on 4.75 mm sieve. As can be seen in Table 6.9, for coarse aggregates retained on 4.75mm, angularity and texture have the strongest correlation; flatness ratio, elongation ratio and texture have a great influence on uncompacted void content.

Table 6.10 presents the correlation matrix between average uncompacted void contents and mean values of five morphological characteristics for aggregates passing 12.5 mm sieve and retaining on 9.5 mm sieve. For coarse aggregates retained on 9.5mm, sphericity and elongation ratio have the strongest correlation. Elongation ratio and angularity show the highest correlation with uncompacted void content, although it is weak due to the limited number of aggregate type in this study.

As shown in Figures 6.14 and 6.15, coefficients of determination (R^2) for the 4.75 to 9.5 mm sieve size and 9.5 to 12.5 mm sieve size were 0.99 and 0.75, respectively, after removing the outlier. The outlier is the data from 13-1078 Staunton #8 in both figure 6.14 and figure 6.15. It is distinct because 13-1078 Staunton #8 aggregates were produced by a jaw crusher, different from the other aggregates that were produced by cone and impact crushers. Regression analysis shows that those five morphological characteristics correlate well with the uncompacted void content of coarse aggregates measured for individual sieve sizes. The respective calculated regression equations are as follows:

For aggregates retained on 4.75mm sieve (4.75-9.5mm):
Uncompact void content (%) = 54.278 - 100.121 (sphericity) + 26.026 (flatness ratio) + 61.579 (elongation ratio) – 46.896 (angularity) + 180.147 (texture)
For aggregates retained on 9.5mm sieve (9.5-12.5mm):
Uncompact void content (%) = 59.288 + 200.82 (sphericity) – 59.16(flatness ratio) – 144.612 (elongation ratio) – 288.913 (angularity) – 63.763 (texture)

For aggregates with the size range of 4.75-9.5mm, the regression indicates that predicted uncompacted void content increases with a decrease in sphericity and angularity and an increase in flatness ratio, elongation ratio, or texture. For aggregates with the size range of 9.5-12.5mm, the regression indicates that predicted uncompacted void content increases with an increase in sphericity and with a decrease in flatness ratio, elongation ratio, angularity and texture. Both regressions indicate that the void content can vary with various morphological

characteristics and increase with a decrease of angularity for coarse aggregates of both size ranges. However, for fine aggregates, the void content increases with an increase in angularity and roughness for two size ranges of No. 16 to No. 30 and No. 30 to No. 50 (Kuo et al., 2000).

Overall, the regression models for coarse aggregates with size ranges of 4.75-9.5mm and 9.5-12.5 mm indicate that the morphological characteristics have a great impact on the uncompacted void content of coarse aggregates, as the coefficients of determination for the regression models are 0.99 and 0.76, respectively. Previous research on fine aggregates has been conducted on the relationship between shape characteristics and void content, which also validates such a finding (Kuo et al., 2000; Dilek et al., 2004). However, this study investigates the relationship between morphological characteristics and uncompacted void content of coarse aggregate for the first time. The effects of shape characteristics of different sized particles on uncompacted void content tend to be consistent for fine aggregates (Kuo et al., 2000; Dilek et al., 2004), but it is a different case for coarse aggregates in Virginia. The regression models show that the effects of morphological characteristics of different sized coarse aggregates on void content vary greatly. Different imaging indices have different levels of impact on the uncompacted void content. For example, the uncompacted void content increases with a decrease of sphericity for aggregates with size range of 4.75-9.5 mm, and also increases with a decrease in angularity for aggregates with size range of 9.5-12.5 mm. To better understand the relationship between morphological characteristics and uncompacted void content of coarse aggregates, further research can be conducted by collecting a larger number of coarse aggregates from a wider range of origins with different rock types and produced by different crushing techniques.

Table 6.9 Summary data and correlation matrix for the 4.75 mm sieve size

Aggregates	Uncompacted Void Content (%)	Sphericity	Flatness Ratio	Elongation Ratio	Angularity	Texture
13-1078 Staunton #8	54.4000	0.5932	0.7072	0.5689	0.0197	0.0157
13-1073 Staunton #68	48.7000	0.5526	0.5113	0.5745	0.0135	0.0092
13-1073 Staunton #78	48.3000	0.6280	0.6324	0.6444	0.0139	0.0079
13-1071 Bealeton #60	49.7000	0.5683	0.5867	0.5793	0.0166	0.0118
14-1048 Bealeton #60	51.0000	0.6624	0.7049	0.6591	0.0247	0.0147
14-1048 Bealeton #78	49.9000	0.5693	0.6018	0.5607	0.0163	0.0120
14-1019 Leesburg #8	48.8000	0.6033	0.6859	0.5823	0.0189	0.0129
14-1019 Leesburg #78	49.2000	0.6039	0.9064	0.4962	0.0204	0.0065
Correlation Matrix						
Void Content	1.0000	-0.0700	-0.4767	0.5676	0.0934	0.4780
Sphericity		1.0000	0.6675	0.4364	0.1872	0.3543
Flatness Ratio			1.0000	-0.3717	0.4649	0.4140
Elongation Ratio				1.0000	-0.2947	-0.0066
Angularity					1.0000	0.7656
Texture						1.0000

Table 6.10 Summary data and correlation matrix for the 9.5 mm sieve size

Aggregates	Uncompacted Void Content (%)	Sphericity	Flatness Ratio	Elongation Ratio	Angularity	Texture
13-1078 Staunton #8	53.8000	0.6338	0.6559	0.6447	0.0178	0.0157
13-1073 Staunton #68	49.1000	0.7537	0.7071	0.7891	0.0145	0.0169
13-1073 Staunton #78	46.8000	0.6625	0.6565	0.6888	0.0193	0.0116
13-1071 Bealeton #30	49.6000	0.5925	0.5689	0.6207	0.0168	0.0122
13-1071 Bealeton #60	47.8000	0.6521	0.5715	0.7179	0.0145	0.0135
14-1048 Bealeton #30	49.2000	0.7040	0.7664	0.7006	0.0151	0.0141
14-1048 Bealeton #60	48.8000	0.7152	0.7515	0.7089	0.0247	0.0151
14-1048 Bealeton #78	47.5000	0.6642	0.6992	0.6658	0.0227	0.0151
14-1019 Leesburg #8	48.0000	0.7088	0.7788	0.6878	0.0227	0.0166
14-1019 Leesburg #78	47.2000	0.6620	0.6957	0.6656	0.0225	0.0144
14-1019 Goose Creek #30	49.4000	0.6092	0.6823	0.5848	0.0216	0.0133
Correlation Matrix						
Void Content	1.0000	-0.0594	0.0265	-0.1403	-0.3007	0.0872
Sphericity		1.0000	0.6949	0.8636	-0.0455	0.7678
Flatness Ratio			1.0000	0.2449	0.4434	0.6544
Elongation Ratio				1.0000	-0.3999	0.5457
Angularity					1.0000	0.1792
Texture						1.0000

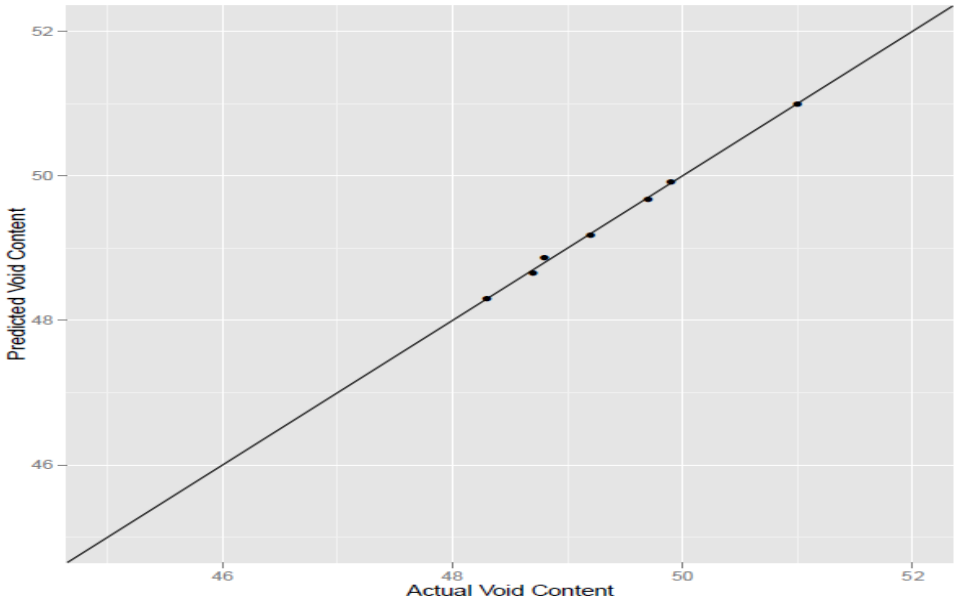

Figure 6.14 Actual versus predicted uncompacted void content for aggregates passing 9.75 mm sieve and retaining on the 4.75 mm sieve (=0.99)

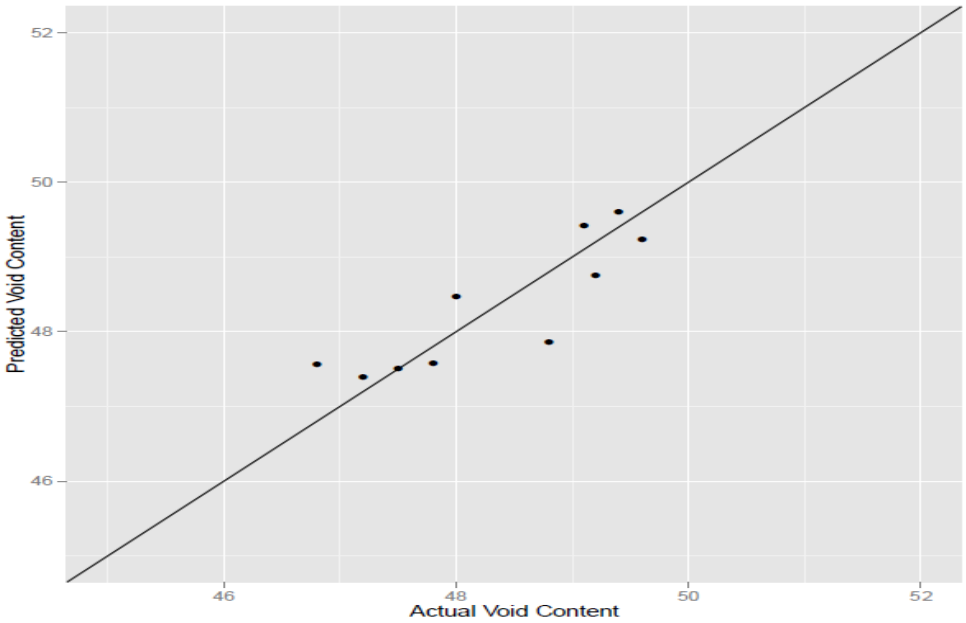

Figure 6.15 Actual versus predicted voids for aggregates passing 12.5 mm sieve and retaining on the 9.5 mm sieve (=0.76)

CHAPTER 7 DISCRETE ELEMENT METHOD SIMULATION

The effect of aggregate shape on the mechanical properties of granular materials

DEM Model Generation

The effect of aggregate shape on the mechanical properties of granular materials and asphalt concrete was investigated by simulating a series of axial compression tests. Different aggregate shapes with different sphericity values and flat and elongated ratio values were selected to generate different discrete element models. The DEM software PFC 3D treats different particle shapes as different combinations of small particles, which are primary particles. Four different particle shapes were modeled to examine the effect of aggregate shape on the mechanical properties of unbounded granular aggregates. The clump logic was used in the discrete element software PFC3D. These four types of aggregates are peanut, pentagonal, triangular, and quadrilateral clumped particles constituted by different numbers of primary circular particles with different arrangements. The peanut shape is composed of three primary particles with one bigger in the middle and two smaller at the ends. The pentagonal shape is composed of five small primary particles with the same size. The triangular shape is composed of three primary particles with three same size particles, two at the bottom and one at the top middle. The quadrilateral shape is composed of four primary particles of the same size. Figure 7.1 shows all the representative clumped particle types. The clumped aggregates have the same volume as the original aggregates replaced and share the centroid with the replaced aggregate. The porosity of sample remains constant after replacement. Each clumped particle is arranged randomly. Particles were represented by clumps. An assembly of clumped particles was generated in the cylindrical model. Aggregates smaller than 2.36 mm were not considered in order to achieve computational efficiency. The minimal radius of the aggregates is 2.36 mm, and the maximum radius is 19 mm. Figure 7.2 shows the gradation curve of the aggregate sample for simulation. The porosity of the sample was set to 0.3.

In the PFC3D model, a cylindrical mold with top, bottom and lateral walls was developed with a diameter of 100 mm and height of 200 mm. Three rigid walls were created as the boundary constraining the model. The top platen was applied with load to the model by specifying a wall velocity of 0.1 m/s. The bottom platen was fixed. The confining pressure was kept constant by adjusting the lateral velocity of the cylindrical wall. The triaxial compression test was simulated under the confining pressure of 0.1 MPa. The whole model was loaded in a stress-controlled mode by applying a velocity on the top wall. A numerical “servo-mechanism” implemented visa the FISH function was used to control the stress. The lateral cylinder is a servo plane, which maintains the confining pressure constant by specifying a lateral velocity to expand or contract the lateral wall. The axial stress was computed by dividing the total force acting on the top wall by the top wall area. The axial strain was calculated by diving the final displacement of the top wall by the original height of the cylinder. Figure 7.3 shows the generated models for all the samples with different particle shapes. For comparison, all the basic information of the models was kept the same, particle shape was considered as the only variable.

Determination of Parameters

The contact model used here is linear contact model, which is suitable to describe contact behavior among granular materials without bonds. The input model parameters were set based on previous research as shown in Table 7.1. The linear contact model can simulate the aggregate-to-aggregate contacts. The linear contact model is described using the normal secant stiffness (Kn) and the shear tangent contact stiffness (Ks) of the two contacting entities, normally either particle-to-particle or particle-to-wall. The aggregate contact friction coefficient was set to simulate the aggregate surface roughness and the slippage in the aggregate-to-aggregate contact.

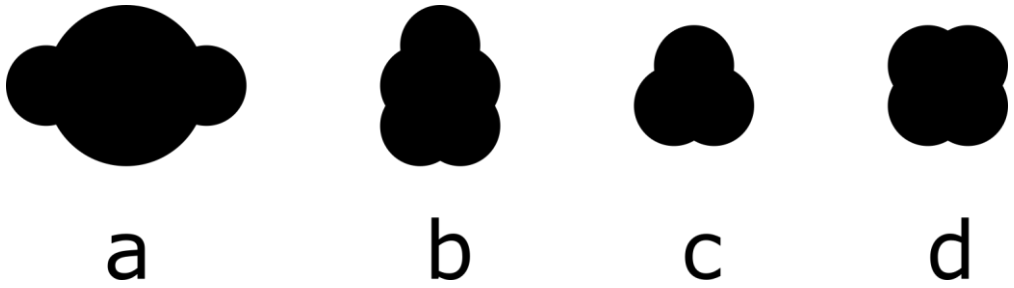

Figure 7.1 The representative particle shapes. (a) peanut; (b) pentagon; (c) triangle; (d) quadrilateral

Table 7.1 Material Parameters

Micromechanical parameters	Values
Contact normal stiffness of particle-particle, Kn (N/m)	4×10^5
Contact shear stiffness of particle-particle, Ks (N/m)	2.4×10^5
Friction coefficient of the particles, μ	0.5
Contact normal stiffness of particle-wall, Kn-wall (N/m)	1×10^{10}
Contact shear stiffness of particle-wall, Ks-wall (N/m)	1×10^{10}
Particle density (kg/m3)	2700

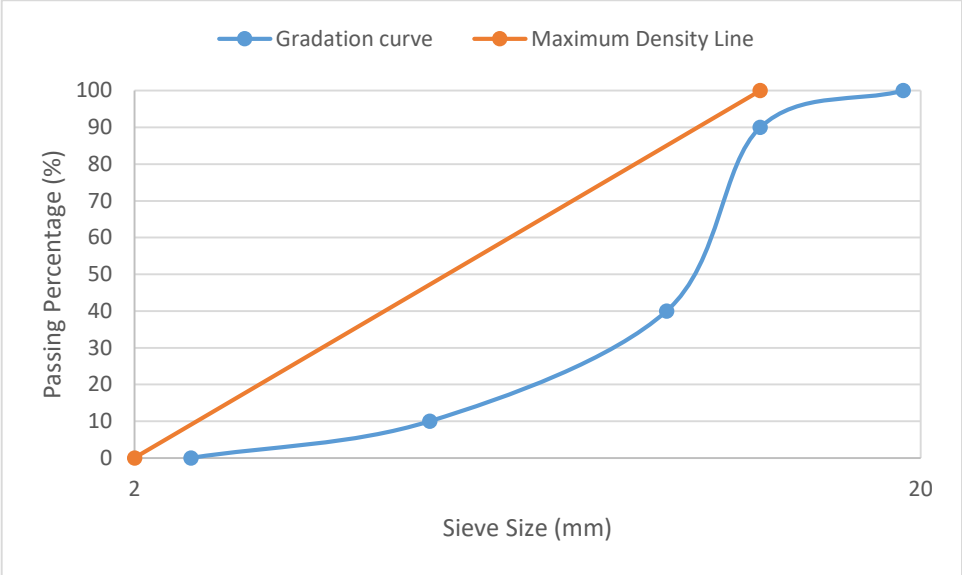

Figure 7.2 Gradation curve for all the sample models

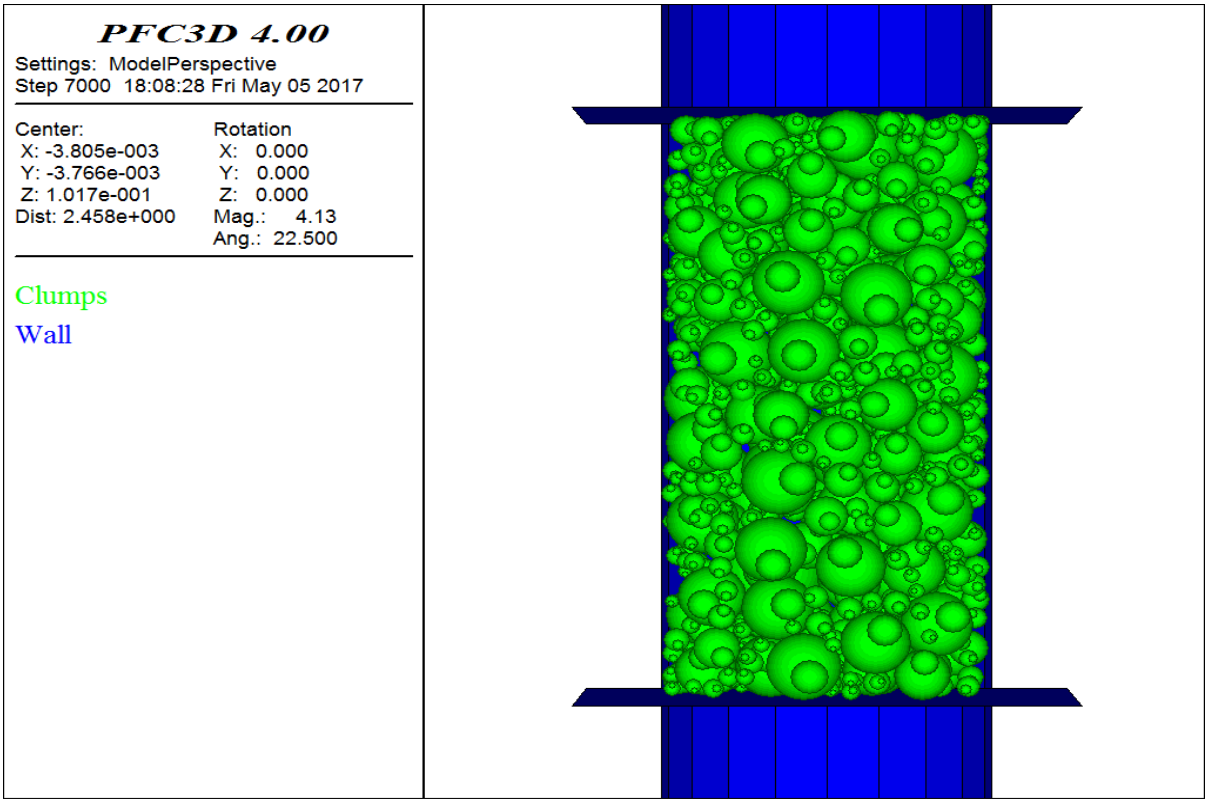

(a) Peanut

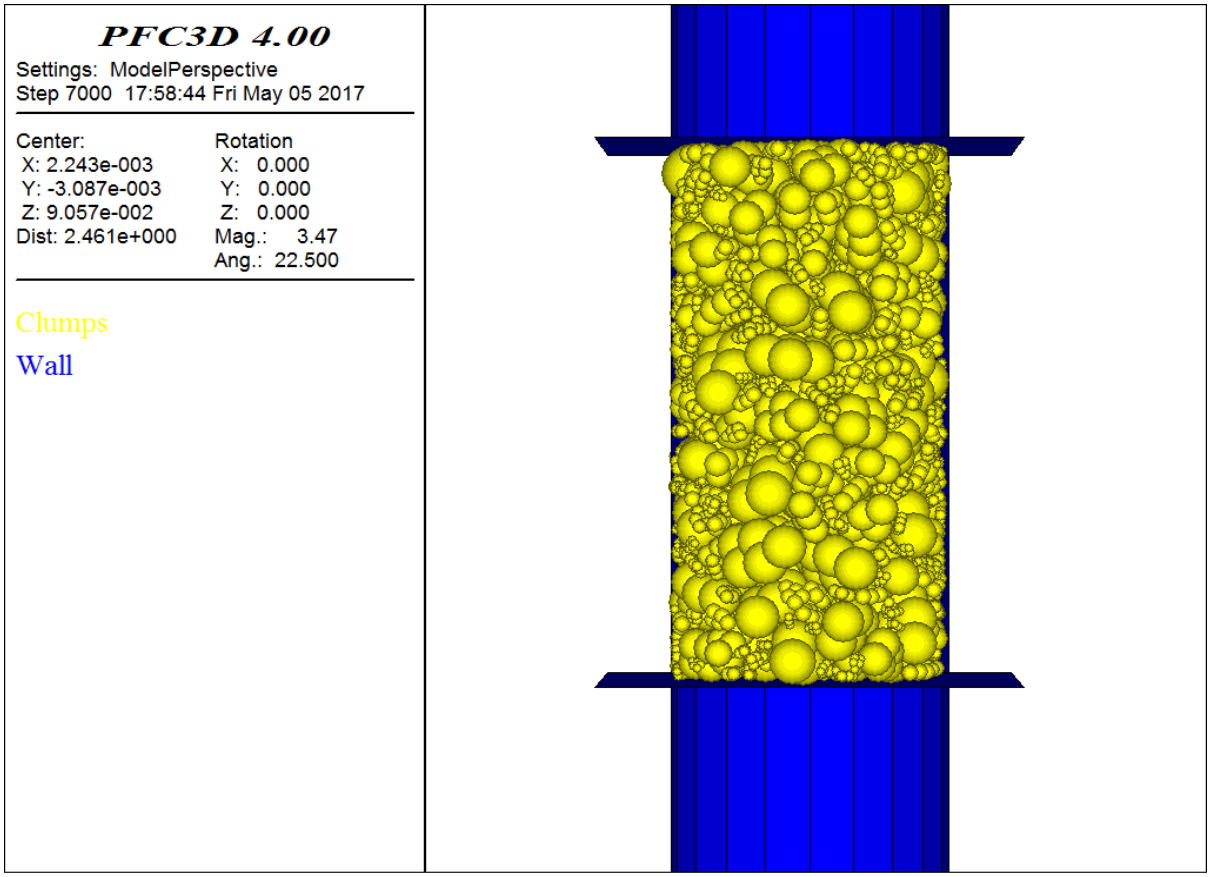

(b)Pentagonal

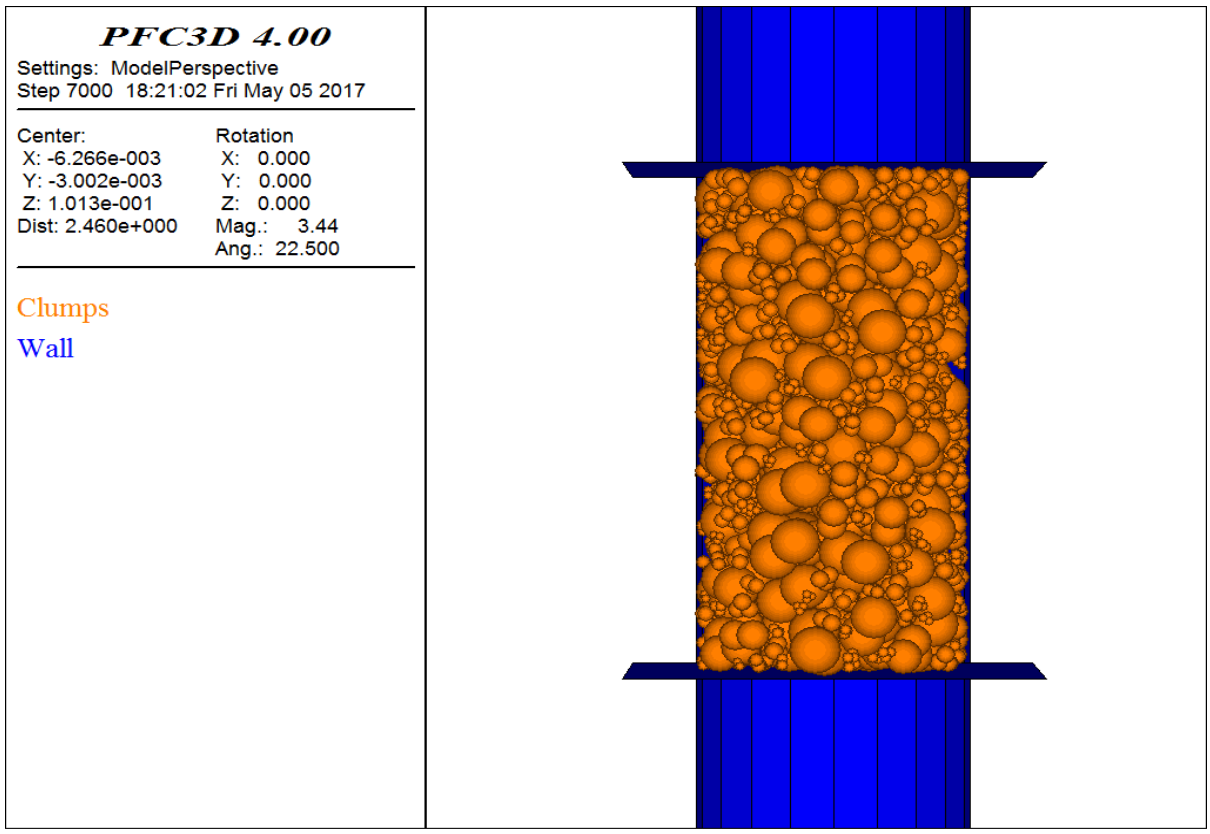

(c) Triangle

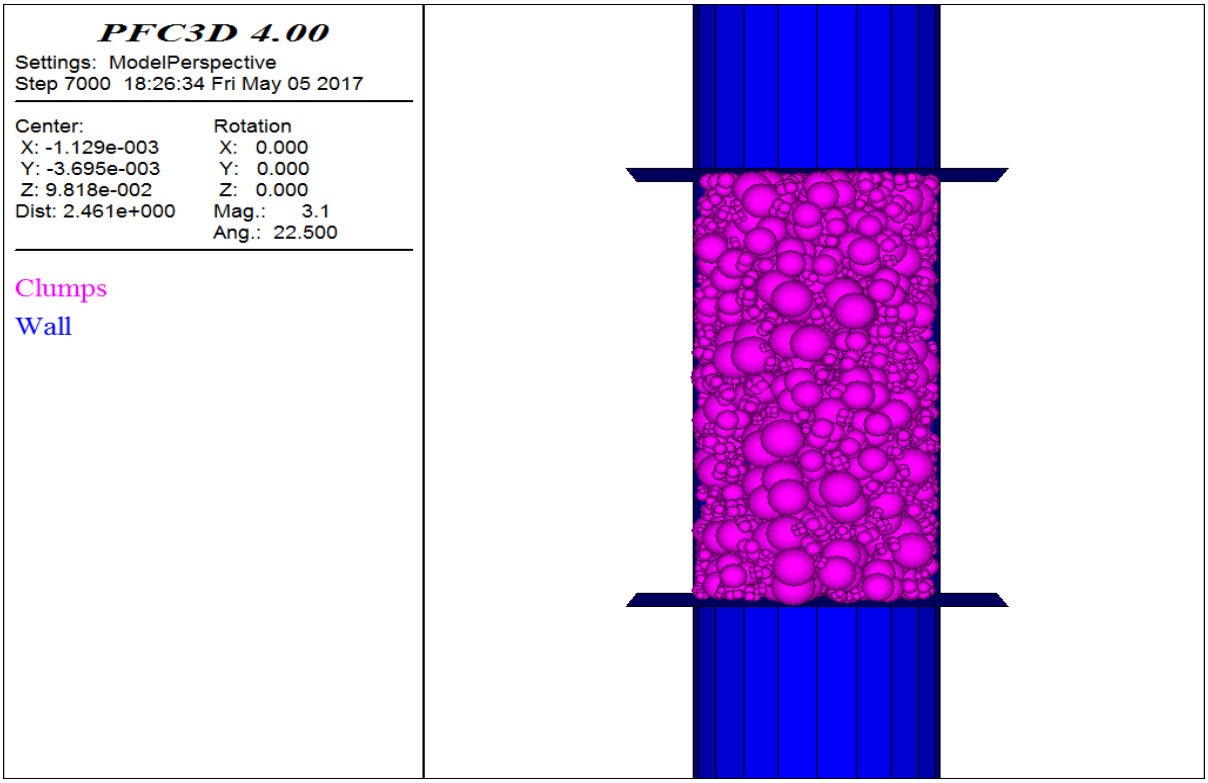

(d) Quadrilateral

Figure 7.3 PFC 3D Models for different shaped particles. (a)Peanut; (b)Pentagonal; (c)Triangle; (d)Quadrilateral

Results and analysis

Figure 7.3 presents the plots of axial deviatoric stress versus axial strain for all the DEM sample models with different representative aggregate shapes. As Figure 7.1 shows, the quadrilateral particle is the most equi-dimensional one and has the greatest sphericity value, the peanut is the longest and least spherical shape, which indicates that the peanut has the greatest FER ratio value and the smallest sphericity value, the triangle is the second most equi-dimensional and has the second greatest sphericity value, and the pentagon is longer than the triangle, which means the FER value of the pentagon is greater than that of the triangle. As shown in figure 7.4, the peanut-shaped sample has the lowest peak strength, the pentagon-shaped sample has the second lowest peak strength, the quadrilateral shaped sample shows the greatest peak strength, and the triangle shows the second greatest peak strength. Table 7.2 summarizes the sphericity, flat and elongated ratio, and peak strength ranks of the DEM sample models. As shown in Table 7.2, the greater the particles' sphericity, the greater the peak strength; the lower the particles' flat and elongated ratio, the greater the peak strength. Research has shown that the more spherical or cubical the aggregate, the better the interlocking between the aggregates (Jian-Shiuh et al, 2005), and correspondingly, the stronger the peak strength. It is well known that the flat and elongated particles tend to breakdown and have lower compactibility, which results in lower peak strength. This conclusion is in good agreement with the experimental results obtained in Chapter 6.

Table 7.2 Summary of sphericity, FER and peak strength rank

Particle Shape	Sphericity Rank	FER Rank	Peak Strength (N/m^2)	Peak Strength Rank
Quadrilateral	1	4	1.4×10^4	1
Triangle	2	3	1.72×10^5	2
Pentagon	3	2	1.9×10^5	3
Peanut	4	1	2.43×10^5	4

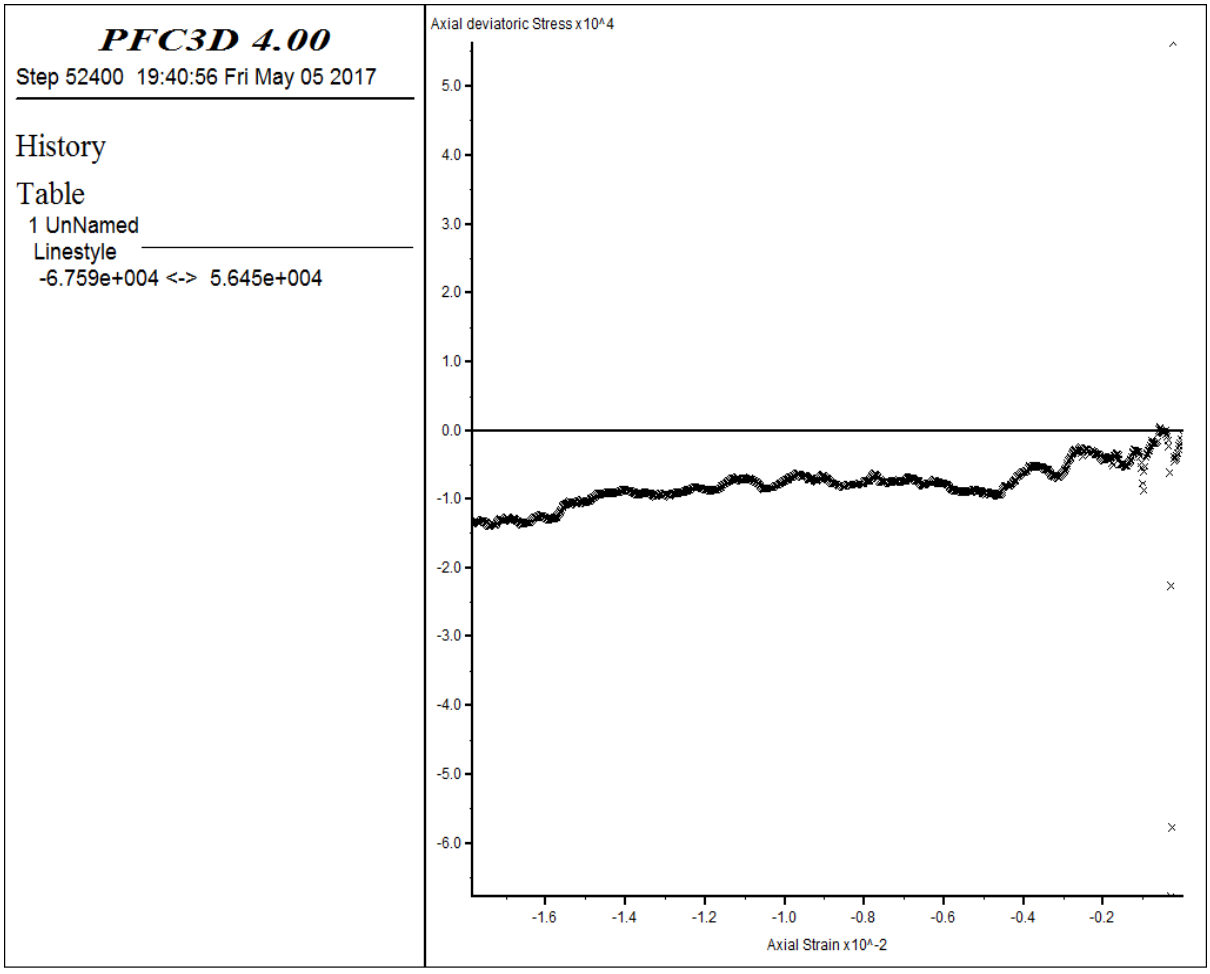

(a)Peanut Sample

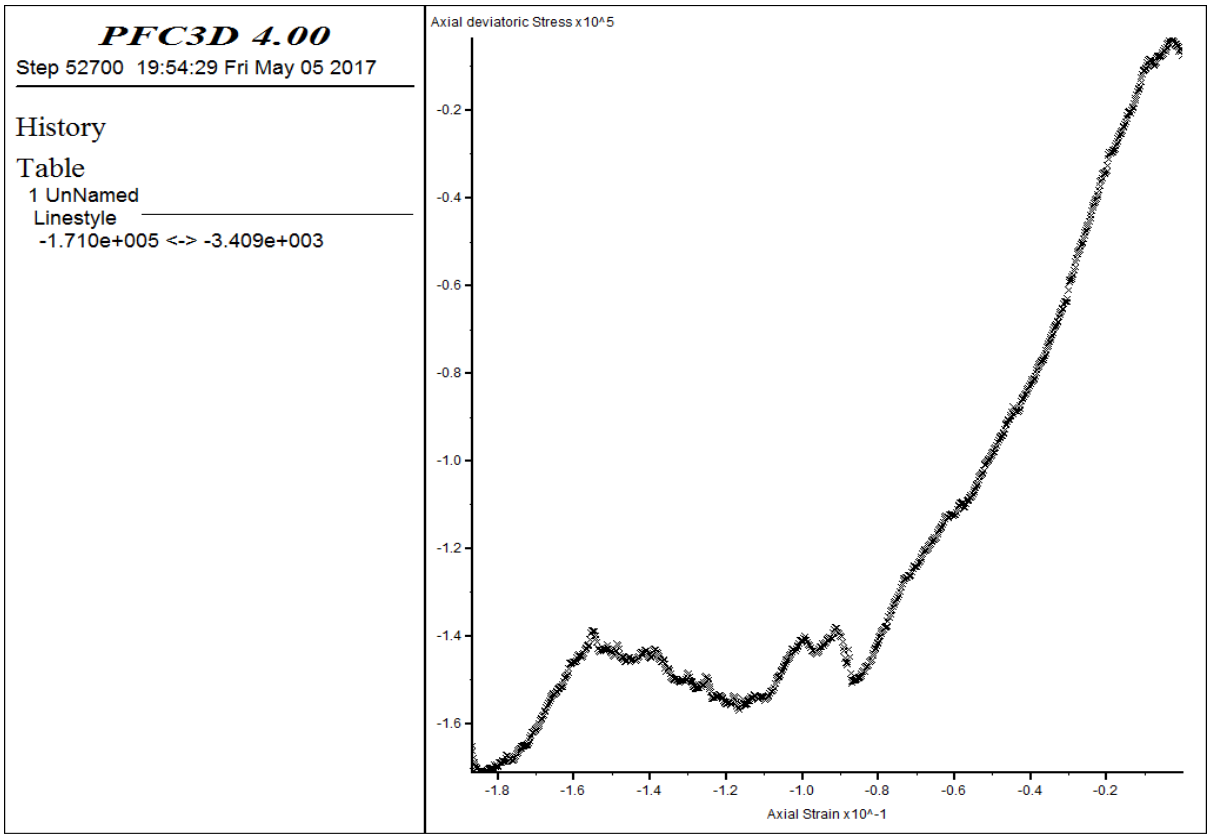

(b)Pentagon Sample

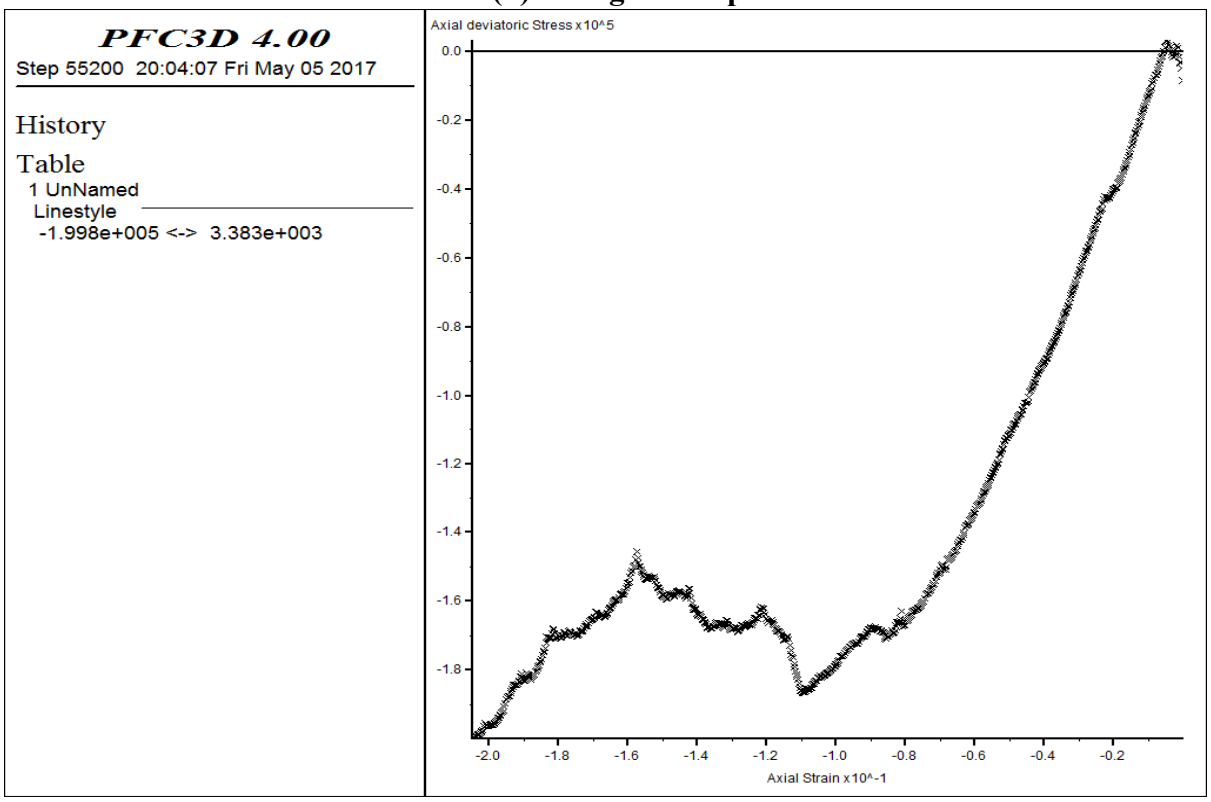

(c)Triangle Sample

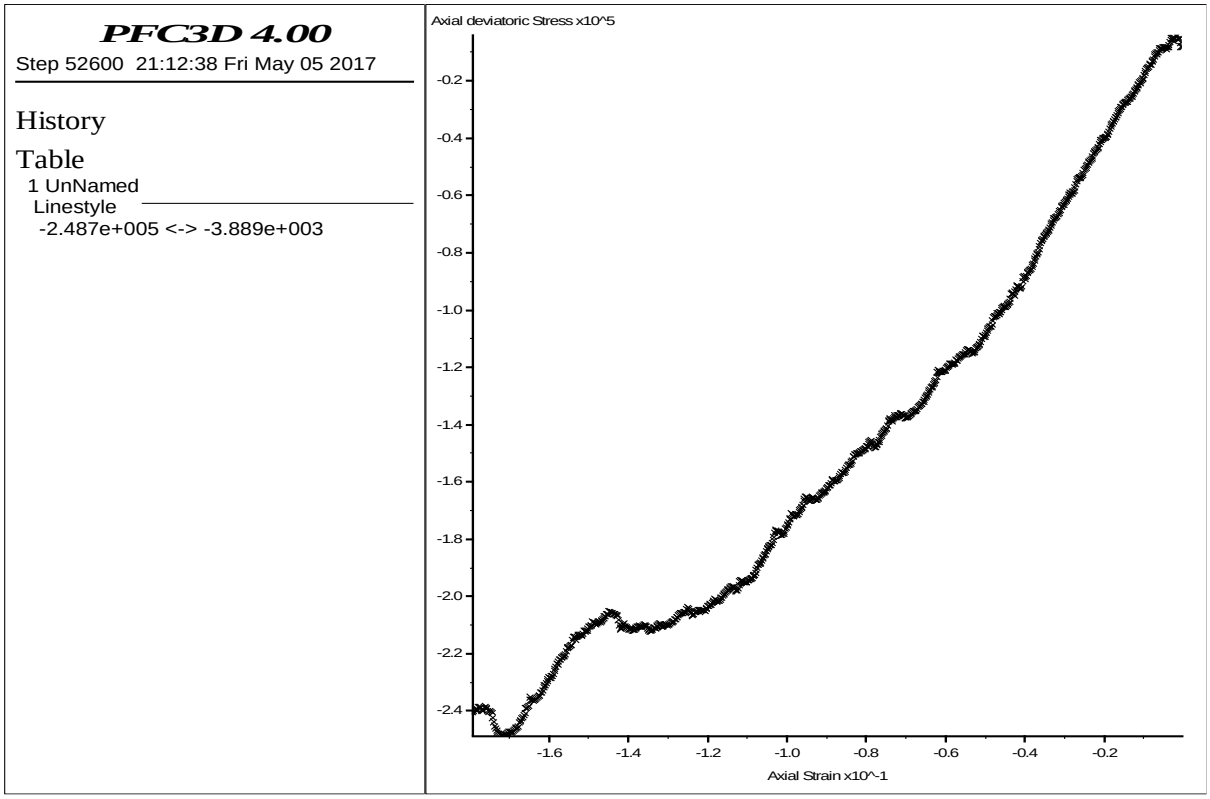

(d)Quadrilateral Sample

Figure 7.4 Axial deviatoric stress versus axial strain for all the samples with different particle shapes. (a) Peanut; (b) Pentagon; (c) Triangle; (d) Quadrilateral

The effect of aggregate roughness and asphalt binder on the mechanical responses of asphalt concrete

Power law contact model

A power-law contact model developed by Cheung (Cheung et al, 1997) was used to examine the effect of the aggregate roughness and asphalt binder on the mechanical response of asphalt concrete. A thin film asphalt was sandwiched between adjacent aggregates. The geometry contact was shown in Figure 7.5. The non-linear constitutive contact model is expressed as:

$$\dot{\varepsilon}_n^0 = \dot{\varepsilon}_n^e + \dot{\varepsilon}_n^v = \frac{\dot{\sigma}_n}{E_n} + \dot{\varepsilon}_0[\left(\frac{1}{n+2}\right)\left(\frac{2n+1}{n}\right)^n \left(\frac{\sqrt{3}}{A}\right)^{n+1}](\frac{\sigma_n}{\sigma_0})^n \quad (7.1)$$

Where: $\dot{\varepsilon}_n^0$ is the total strain, which is composed of the elastic and viscous components; σ_n is the total stress; $\dot{\sigma}_n$ is the stress rate; and n represents the property of asphalt binder: when $n = 1$, asphalt binder is linear viscous; and when $n > 1$, the asphalt binder is non-linear. A is the aspect ratio of width to thickness, $A = a/h$, a and h are width and thickness of the asphalt layer. E_n is the aggregate stiffness; $\dot{\varepsilon}_0$, σ_0 are model constants.

The details of this contact model can be found in somewhere else (Cheung et al, 1997; Bo, 2013). This contact model was coded with the C++ language and was incorporated into PFC 3D. For convenience, a two-ball DEM model incorporated with this new contact model was

created to investigate the aggregate roughness and asphalt binder thickness on the mechanical response of asphalt concrete. Figure 7.6 shows the two-ball model before and after simulation. These two balls can be considered as aggregates coated with asphalt binder after incorporating the new contact model. A constant speed of 0.7 μm/s was applied to the top aggregate. A series of uniaxial compression tests with different model parameters were simulated. Table 7.3 lists all the model parameters used in the simulations. The model parameters used here were estimated based on the experiments done by Bo (Bo, 2013).

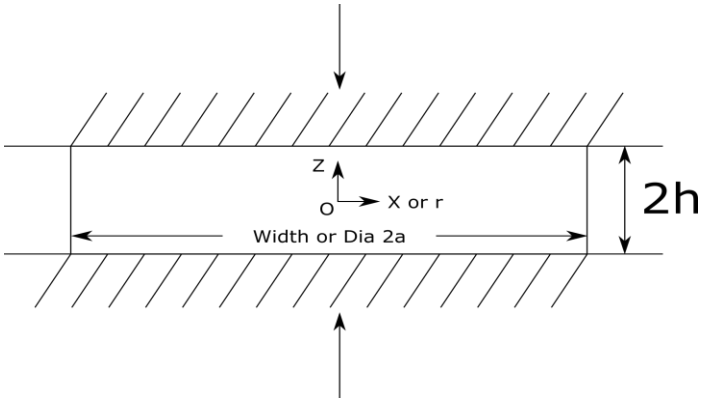

Figure 7.5 Geometry of power-law contact model (Cheung, et al, 1997)

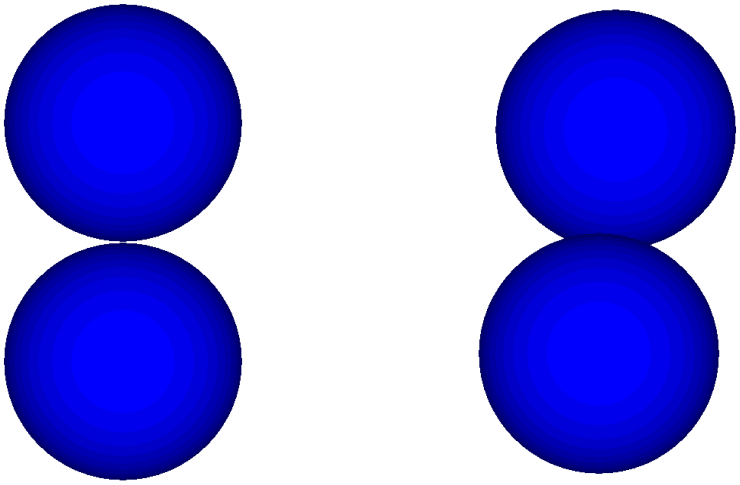

Figure 7.6 The two-ball model before and after simulation

Table 7.3 Pow-law contact model parameters

Cases	Thickness of asphalt layer (h μm)	Width of asphalt layer (a mm)	Aspect ratio of asphalt layer (A)	E_n (N/m)	$\dot{\varepsilon}_0$	σ_0
Case 1	156	3.92	25.13	1.7×10^4	3.72×10^{-5}	100
Case 2	156	3.5	22.44	1.7×10^4	3.72×10^{-5}	100
Case 3	156	2.603	16.69	1.7×10^4	3.72×10^{-5}	100

Case 4	100	2.603	26.03	1.7×10^{4}	3.72×10^{-5}	100
Case 5	50	2.603	52.06	1.7×10^{4}	3.72×10^{-5}	100
Case 6	156	2.603	16.69	1.63×10^{4}	1.29×10^{-4}	100
Case 7	156	2.603	16.69	2.62×10^{4}	1.29×10^{-4}	100
Case 8	156	2.603	16.69	1.0×10^{5}	1.29×10^{-4}	100

Results and analysis

A total of eight two-ball compression tests were simulated using contact models with different asphalt layer widths, different asphalt film thicknesses, and different aggregate stiffnesses. Figure 7.7 shows plots of axial stress versus time step for all the simulation cases. Figure 7.7(a)-(c) shows the axial stress results of compression tests with different asphalt layer widths. As shown in figure 7.7(a)-(c), the wider the asphalt layer, the greater the peak stress. This might be due to the fact that the wider the asphalt layer, the more contact area between aggregates and asphalt, the rougher the aggregates, and the greater the peak stress. Figure 7.7(c)-(e) shows the axial stress results of compression tests with different asphalt film thicknesses. Previous research has also shown that peak stress increases with decreased film thickness (Li, 2015). As shown in figure 7.7(c)-(e), the thicker the asphalt film, the smaller the peak stress. Figure 7.7(f)-(h) shows the axial stress results of compression tests with different aggregate stiffnesses. As shown in figure 7.7 (f)-(h), the stiffer the aggregate, the greater the peak stress. A possible explanation is that the stiffer aggregates tend to be rougher.

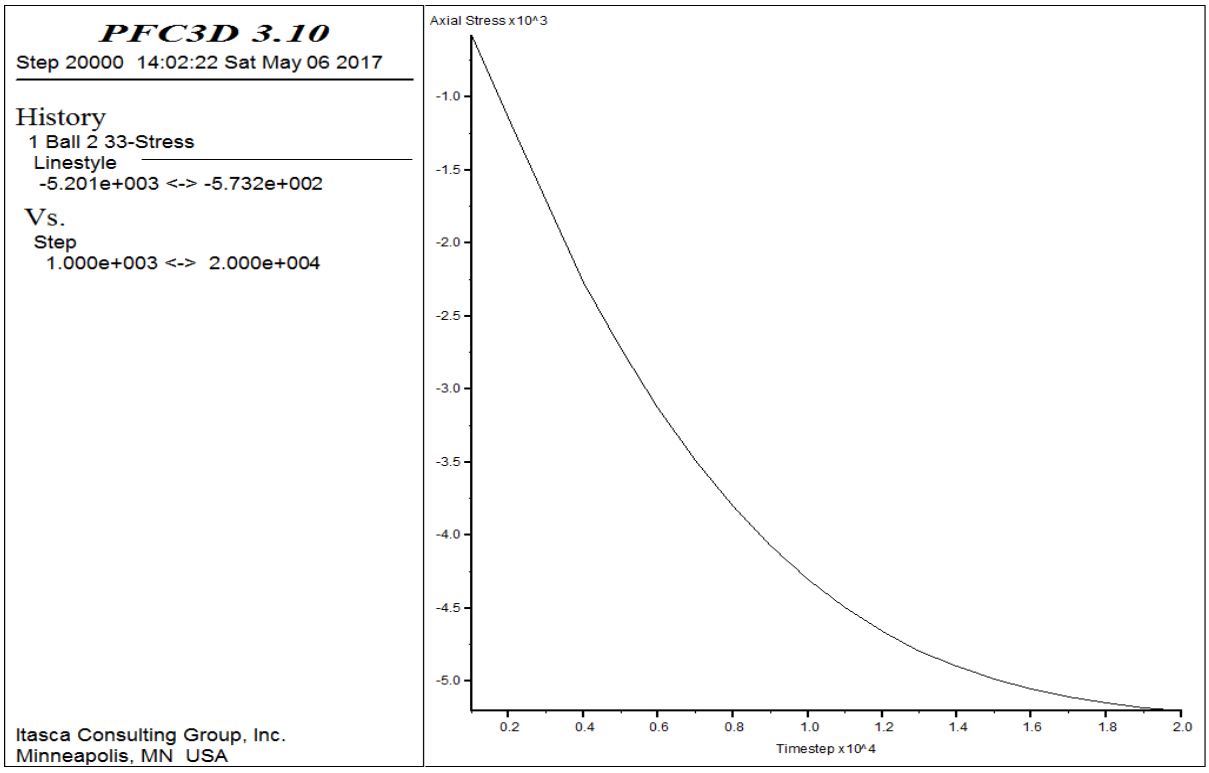

(a) Case 1 (h=156, a=3.92, E_n=1.7×10^{4}, $\dot{\varepsilon}_0$ = 3.72×10^{-5}, σ_0 =100)

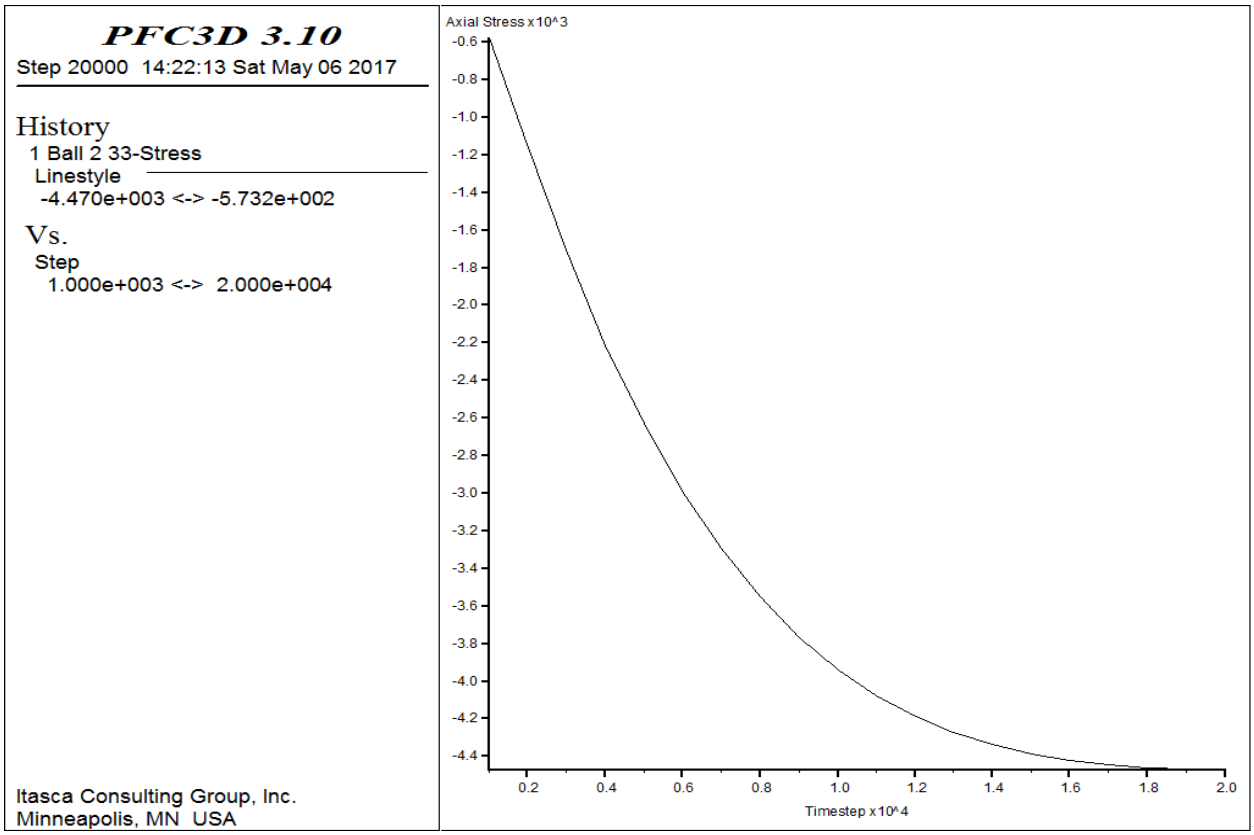

(b) Case 2 (h=156, a=3.5, E_n=1.7×10^4, $\dot{\varepsilon}_0$ = 3.72×10^{-5}, σ_0 =100)

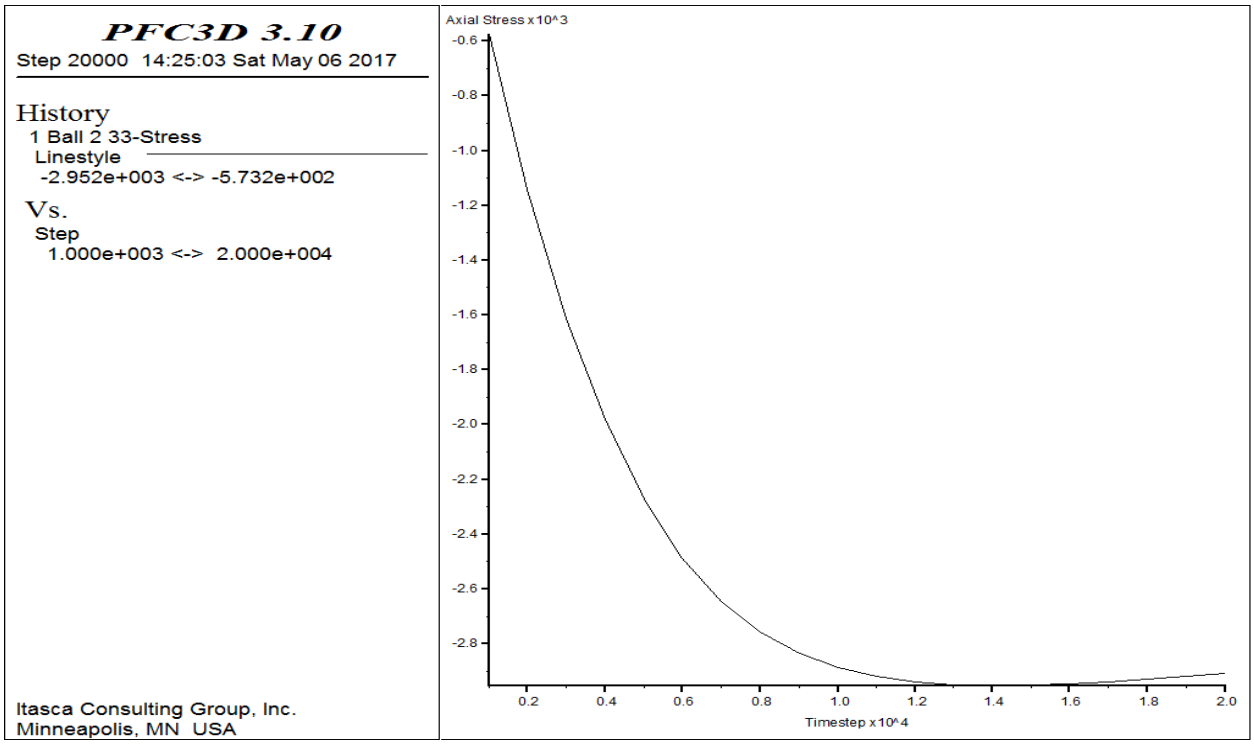

(c) Case 3 (h=156, a=2.603, E_n=1.7×10^4, $\dot{\varepsilon}_0$ = 3.72×10^{-5}, σ_0 =100)

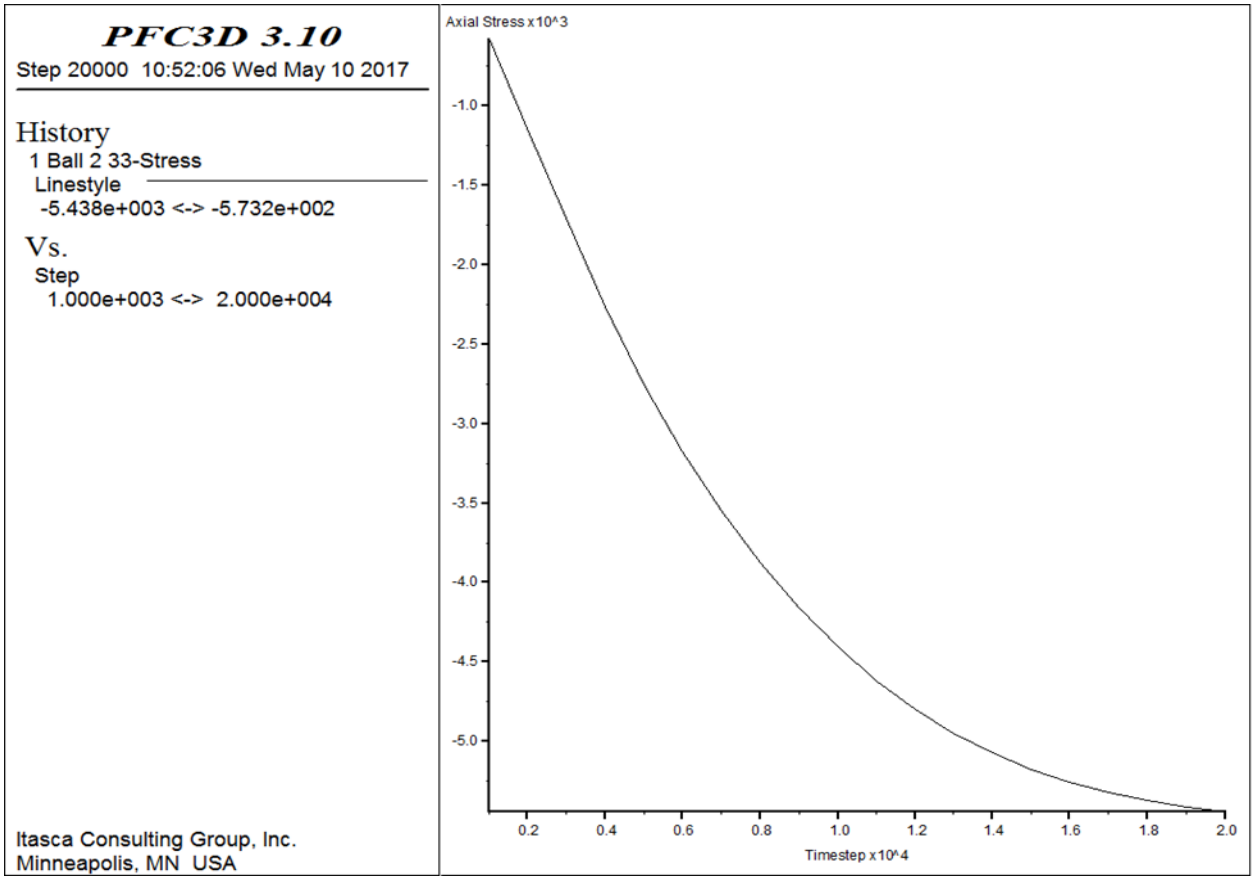

(d) Case 4 (h=100, a=2.603, E_n=1.7×10^4, $\dot{\varepsilon}_0$ = 3.72×10^{-5}, σ_0 =100)

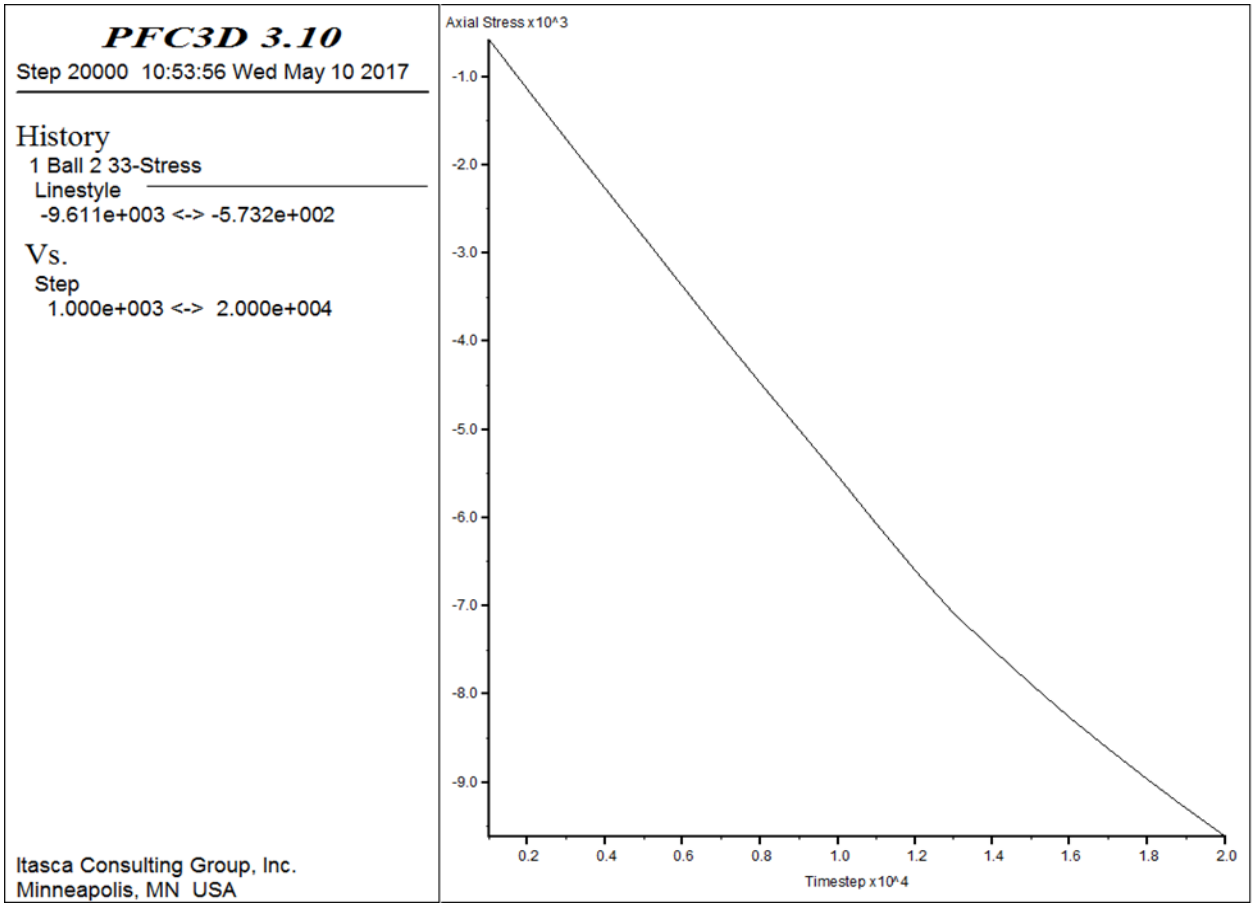

(e) Case 5 (h=50, a=2.603, E_n=1.7×10^4, $\dot{\varepsilon}_0$ = 3.72×10^{-5}, σ_0 =100)

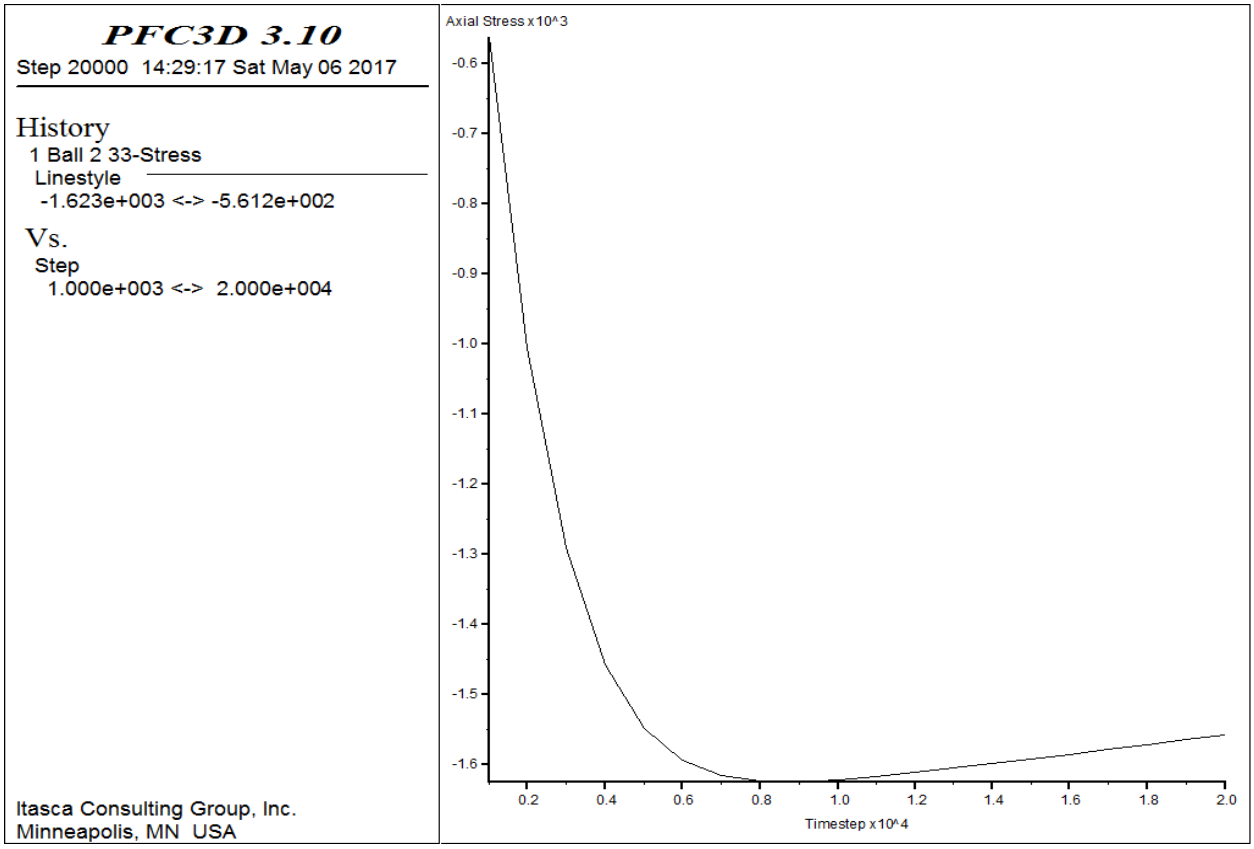

(f) Case 6 (h=156, a=2.603, E_n=1.63×10^4, $\dot{\varepsilon}_0$ = 1.29×10^{-4}, σ_0 =100)

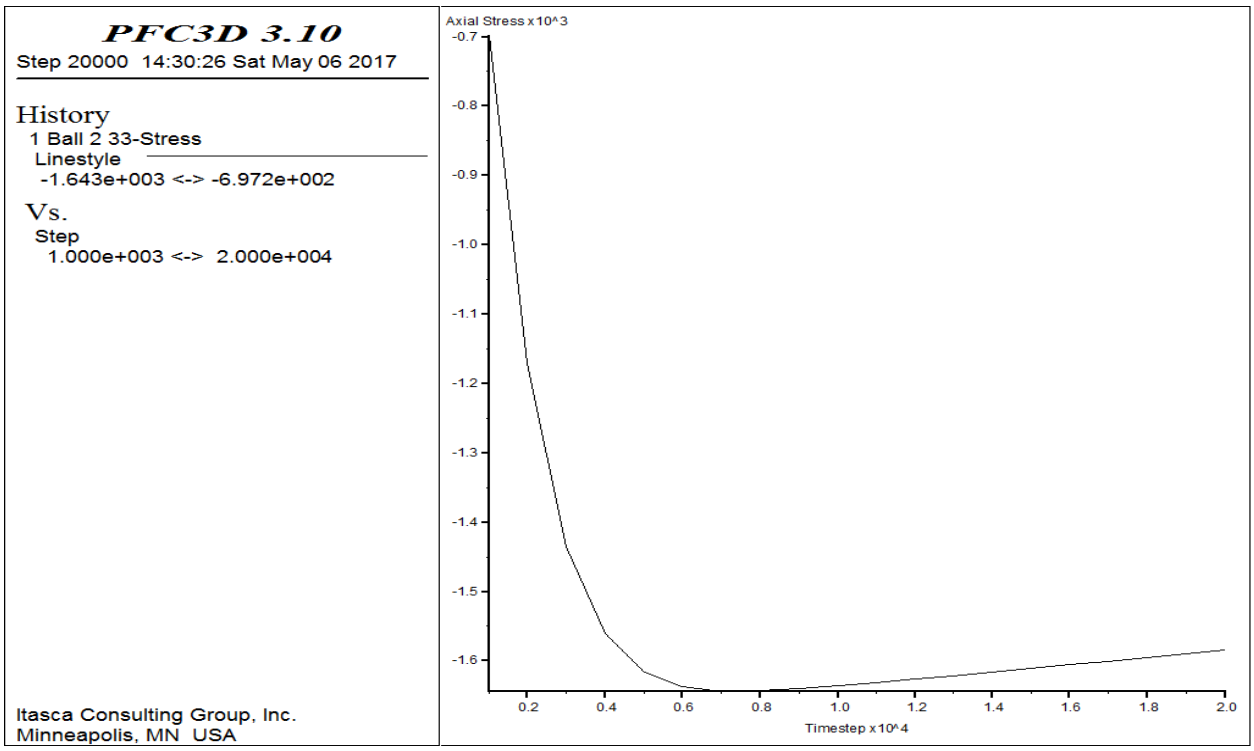

(g) Case 7 (h=156, a=2.603, E_n=2.62×10^4, $\dot{\varepsilon}_0$ = 1.29×10^{-4}, σ_0 =100)

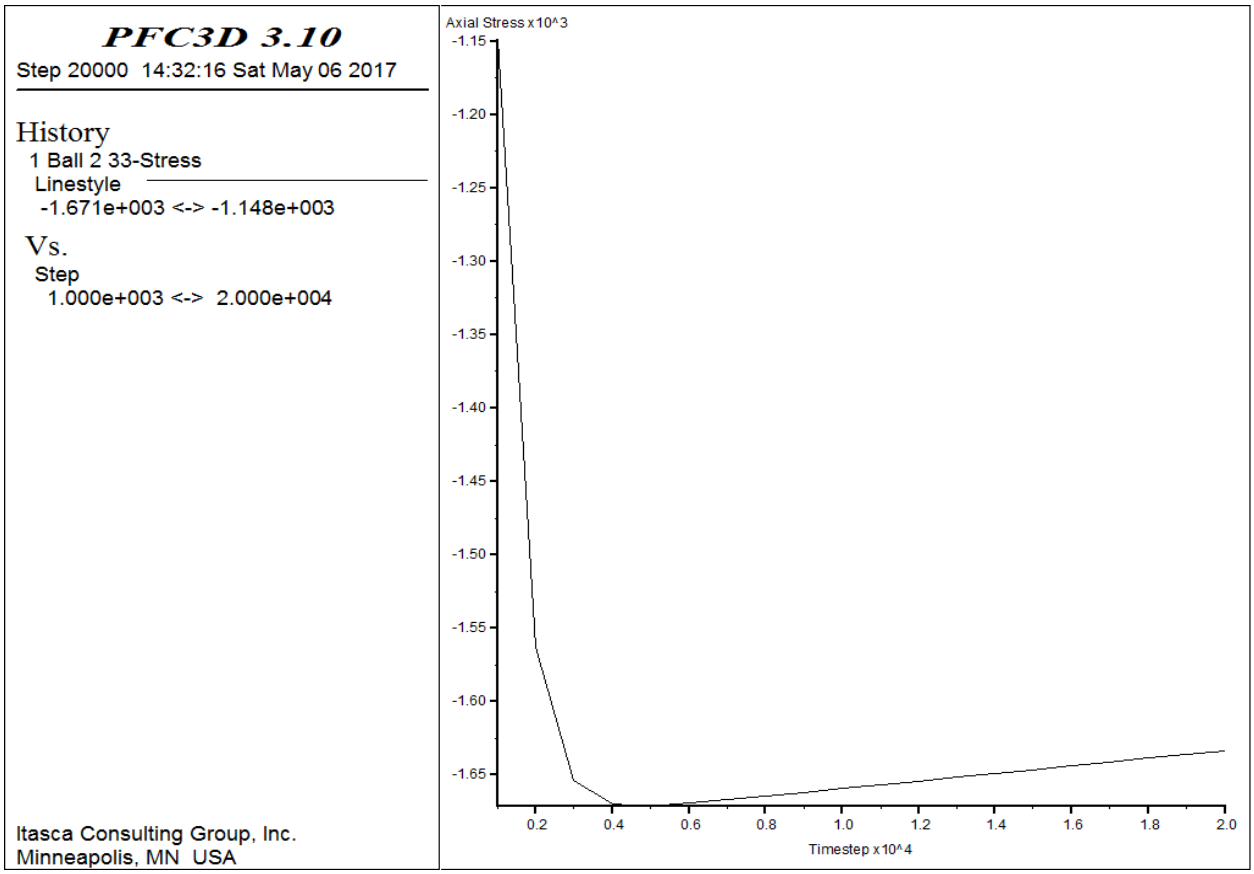

(h) Case 8 (h=156, a=2.603, E_n=1.0×10^5, $\dot{\varepsilon}_0$ = 1.29×10^{-4}, σ_0 =100)

Figure 7.7 Axial compressive stress versus time step for all the simulation cases

CHAPTER 8 CONCLUSIONS

Conclusions

The main objective of the proposed research is to investigate the effects of coarse aggregate morphological characteristics on the mechanical performance of small-size SMA mixtures constituted by those aggregates. A total of 22 aggregate fractions produced from different quarries in Virginia were selected for SMA mixtures. The morphological characteristics of the aggregates were measured by the three dimensional high-resolution Improved FTI image analysis system, including sphericity, flatness ratio, elongation ratio, angularity and texture. Uncompacted void content tests were conducted on different aggregate fractions to relate the morphological characteristics of coarse aggregates with the uncompacted void content.

To evaluate the influence of morphological characteristics on fatigue and rutting performance, simple performance tests and wheel-tracking tests were performed on the SMA mixtures designed with different aggregate blends and different asphalt contents. Dynamic modulus tests, flow number tests, beam fatigue tests and APA tests were conducted on eight types of SMA mixtures, each with three replicates. MMLS test was conducted on six types of SMA mixtures, each with three replicates. Mechanical properties such as dynamic modulus, flow number, flow number slope, the number of loading cycles to failure, rut depth, creep slope and seismic modulus difference were obtained from these laboratory performance-based tests to evaluate the fatigue and rutting resistance of all types of SMA mixtures prepared using a total of 22 aggregate fractions. The morphological characteristics of coarse aggregates were linked to the mechanical performance of the SMA mixtures with different aggregate morphologies through regression analysis. Regression analyses were first conducted on the weighted mean morphological characteristics of aggregate blends used in the SMA mixtures and both the asphalt contents and asphalt binder performance grade. The correlations of weighted mean morphological characteristics of coarse aggregates with the fatigue and rutting parameters were examined to investigate the effects of morphologies on the mechanical performance of the SMA mixtures. The regression analyses between coarse aggregate morphologies and uncompacted void content were performed on two aggregate size ranges to examine the effects of various morphologies on the uncompacted void content. Selection of aggregates with appropriate morphological characteristics ensures adequate performance of pavement surface layers. The main findings from this research are as follows:

- Morphological characteristics of 22 aggregate fractions from different sources and processing methods were measured using the improved FTI image analysis system, a total of 60 aggregates were scanned for each aggregate size range. Image resolution in captured images from the Improved FTI system is 28.47 μm per pixel in both the x and y directions using a new CCD camera. The measured resolution in the z-axis is 22.00 μm per pixel.
- The Improved FTI shape factor results, including sphericty and flatness ratio, were in good agreement with manual measurement results using a vernier caliper, indicating that the Improved FTI results are very reliable and accurate, and the FFT2 method can accurately quantify morphological characteristics of aggregates.
- The F&E ratios were calculated for sixteen aggregate fractions. A plot of the distribution of F&E ratio for each aggregate fraction was presented to show the percentage of flat and

elongated aggregates with F&E ratio greater than 3:1 and 5:1.

- The fatigue parameter |E*|sinφ and the rutting parameter |E*|/sinφ obtained from the dynamic modulus tests under a frequency of 10 Hz were used to evaluate the fatigue and rutting performance of the eight types of SMA mixtures. The statistical results showed the asphalt binder performance grade had correlations with both fatigue parameter and rutting parameter. The SMA mixtures were grouped based on the high temperature performance grade. The regression analyses indicated that the fatigue parameter and rutting parameter of SMA mixtures with asphalt binder stiffness PG 70 had good correlations with morphological characteristics, second-order polynomials were found to be the best fits between aggregate morphological characteristics and both fatigue parameter and rutting parameter**.**
- Statistical results showed the flow number test parameter Log(FN) was correlated with the morphological characteristics (S, FER, AF and TF). Regression analyses between the weighted mean morphological characteristics (S, FER, AF and TF) and the flow number test parameters Log(FN) were performed for eight types of SMA mixtures. The linear regression results indicated that using spherical, less flaky coarse aggregates with angular and rough surfaces in asphalt mixtures, as indicated by higher S, AF, and TF values and lower FER value, can improve the rutting resistance of SMA, as indicated by higher rutting parameter Log(FN) values.
- The linear regression analyses between the weighted mean morphological characteristics (S, FER, AF and TF) and flow number slope (FNS) of all SMA mixtures were performed with or without grouping FNS data based on PG grades. FNS increases with increased weighted mean FER values and decreases with increased weighted mean S, AF and TF values. The lower the flow number slope, the better the rutting performance. The SMA mixtures consisting of more spherical, less flaky aggregates with more angular and rougher textured surfaces exhibited better rutting resistance.
- Statistical results showed the fatigue parameter Log(NOC) was correlated with the morphological characteristics (AF and TF). Linear regression analyses were conducted to investigate the relationships between the weighted mean morphological characteristics (AF and TF) and the measured fatigue parameters Log(NOC) of all SMA mixtures under three different strain levels. The regression results showed that the fatigue parameter Log(NOC) tends to increase as the angularity and texture increase, indicating better fatigue life using more angular and rougher aggregates in SMA mixtures.
- On the basis of the laboratory performance-based test results from the eight types of SMA mixtures, it was observed that the rutting and fatigue resistance of SMA mixtures could be enhanced considerably by the selection of coarse aggregates with appropriate morphological characteristics. In the regression analyses, sphericity and flat and elongated ratio were shown to have some decent linear relationships with the rut depth, and the regressions indicated that using more spherical, less flat and elongated coarse aggregates improved the rutting performance of SMA mixtures. Angularity and texture were shown to have no measurable effects on rut depth of SMA mixtures. However, negative trends exist between rut depth and both angularity and texture, indicating using more angular and rougher coarse aggregates is necessary for improving the rutting resistance ability of SMA mixtures.

- APA creep slope has a negative correlation with the weighted mean sphericity, and has a positive correlation with the weighted mean flat and elongated ratio, indicating using more spherical, less flaky and elongated aggregates is favorable to slower creep slope. Slow creep slope indicates low rate of change of rut depth, which is desirable for improving the rutting resistance potential. Although the low correlation between the weighted mean texture and creep slope, the negative trend exists. Using more rougher aggregates can slow the creep slope, which improves rutting performance of SMA mixtures.
- In the regression analyses, angularity showed little influence on the seismic modulus difference, sphericity and texture exhibited same trends with seismic modulus difference, while flat and elongated ratio exhibited distinct trend with seismic modulus difference in comparison to sphericity and flat and elongated ratio, the correlations indicated that using more spherical, less flaky and rougher coarse aggregates reduced the stiffness degradation, which improved the fatigue life of SMA mixtures. Considering both rut depth and seismic modulus difference, flat and elongated aggregates should only be used within a limited amount in the SMA mixture to achieve desirable mechanical performance.
- Linear regression analyses indicate that the morphological characteristics correlate well with the uncompacted void content of coarse aggregates with size ranges of 4.75-9.5 mm and 9.5-12.5 mm. Both regression models for these two aggregate size ranges show that the uncompacted void content increases with a decrease of angularity for coarse aggregates. The other morphological characteristics show an inverse relationship with uncompacted void content for coarse aggregates at the two size ranges. Among these morphological characteristics, flatness ratio, elongation ratio and texture have the greatest effect on uncompacted void content for coarse aggregates retained on the 4.75 mm sieve, whereas elongation ratio and angularity have the greatest effect on void content for coarse aggregates retained on the 9.5 mm sieve.
- Most of the regression analyses in this study are linear regression analyses with somewhat decent but not strong correlation coefficients between rutting and fatigue performance parameters and aggregate morphological characteristics. The non-linear regression analyses such as parabolic functions might lead to better correlation coefficients.
- The DEM compression test simulations indicated that using more spherical, less flay and elongated, and rougher aggregate particles is favorable to the mechanical response of aggregates and asphalt concrete, which is in good agreement with the experimental results.
- Based on these findings, sphericity value of at least 0.56 is recommended, F&E ratio of at most 3.2 is recommended, angularity value of at least 0.016 is recommended, texture value of at least 0.02 is recommended.

References

AASHTO (American Association of State Highway and Transportation Officials). (2005). "Standard Method of Test for Uncompacted Void Content of Coarse Aggregate (As Influenced by Particle Shape, Surface Texture, and Grading)." AASHTO T326, Washington D.C.

AASHTO (American Association of State Highway and Transportation Officials). (2007). "Standard method of test for determining the fatigue life of compacted Hot-mix Asphalt (HMA) subjected to repeated flexural bending." AASHTO T321, Washington D.C.

AASHTO (American Association of State Highway and Transportation Officials). (2011). "Standard method of test for determining dynamic modulus of Hot-Mix asphalt concrete mixtures." AASHTO T342, Washington D.C.

Akbuluta, S., Yenera, E., Arasan, S., Hinislioglua, S., and **Hattatoglu, F.** (2011). "Correlation between shape of aggregate and mechanical properties of asphalt concrete: Digital image processing approach." Road Materials and Pavement Design, 12(2), 239-62.

Al-Rousan, T., E. Tutumlmuer, and **T. Pan.** (2006). Evaluation of image analysis techniques for quantifying aggregate shape characteristics. Construction and Building Materials, Vol. 21, pp. 978-990.

Al Rousan, T. M. (2005). Characterization of aggregate shape properties using a computer automated system (Doctoral dissertation, Texas A&M University).

Al-Rousan, T., Masad, E., Tutumluer, E., and **Pan, T.** (2007). Evaluation of image analysis techniques for quantifying aggregate shape characteristics. Construction and Building Materials, 21(5), 978-990.

ASTM (American Society for Testing and Materials). (2006). "Standard test method for index of aggregate shape and texture." ASTM D3398, West Conshohocken, PA.

ASTM (American Society for Testing and Materials). (2010). "Standard test method for flat aggregates, elongation aggregates, or flat and elongated aggregates in coarse aggregate." ASTM D4791, West Conshohocken, PA.

ASTM (American Society for Testing and Materials). (2013). "Standard test method for determining the percentage of fractured aggregates in coarse aggregate." ASTM D5821, West Conshohocken, PA.

ASTM. (1999). "Standard test method for flat particles, elongated particles, or flat and elongated particles in coarse aggregate." Annual book of ASTM standards: ASTM D 4791-99, Vol. 04.03, ASTM, Philadelphia.

Bessa, I., Branco, V., Soares, J., and **Neto, J.** (2014). "Aggregate Shape Properties and Their Influence on the Behavior of Hot-Mix Asphalt." J. Mater. Civ. Eng., 27(7), 04014212.

Peng, B. (2014). Discrete element method (DEM) contact models applied to pavement simulation (Doctoral dissertation, Virginia Tech).

Brandon, D., and **Kaplan, W. D.** (1999). Microstructural Characterization of Materials. Wiley, New York.

Buchanan, M. S. (2000). Evaluation of the effects of the flat and elongated particles on the performance of hot asphalt mixtures. NCAT Rep. No. 2000-03, 18–21.

Chen, J., Hsieh, W., and **Liao, M. (2013).** Effect of coarse aggregate shape on engineering properties stone mastic asphalt applied to airport pavements. International Journal of Pavement Research and Technology, 6(5), 595-601.

Chen, J. S., Chang, M. K., and **Lin, K. Y.** (2005). "Influence of coarse aggregate shape on the strength of asphalt concrete mixtures." Journal of the Eastern Asia Society for Transportation Studies, 6, 1062-1075.

Cheung, C. Y., and **Cebon, D.** (1997). Thin film deformation behavior of power-law creeping materials. *Journal of engineering mechanics*, *123*(11), 1138-1152.

Dilek, U., and **Leming, M.** (2004). Relationship between particle shape and void content of fine aggregate. Cement, Concrete, and Aggregates, 26(1), 1-7. Doi:10.1520/CCA11916

Doyle, J. D. (1971). Effects of flat and elongated particles upon properties of mixtures containing glass aggregates.

Fernlund, J. M. R. (2005). "Image analysis method for determining 3-D shape of coarse aggregate." Cement and Concrete Research, 35(8), 1629-1637.

Fletcher, T., et al. (2002). Measurement of aggregate texture and its influence on hot mix asphalt (HMA) permanent deformation. Journal of Testing and Evaluation, 30 (6), 524– 531.

Fletcher, T., Chandan, C., Masad, E., and **Sivakumar, K.** (2003). "Aggregate imaging system for characterizing the shape of fine and coarse aggregates." Transportation Research Record: Journal of the Transportation Research Board, 1832, 67–77.

Francisco Thiago Sacramento Abraham Ricardo Guerrero Pazos, Laura Maria Goretti da Motta, Yong-Rak Kim, Luis Alberto Herrmann do Nascimento (2016). Effects of morphological characteristics of aggregate particles on the mechanical behavior of bituminous paving mixtures. Construction and Building Materials, Volume 122, pp 444-453.

Huang, B., Chen, X., Shu, X., Masad, E., and **Mahmoud, E.** (2009). Effects of coarse aggregate angularity and asphalt binder on laboratory-measured permanent deformation properties of HMA. International Journal of Pavement Engineering, 10(1), 19-28.

Huang, Y., Hugo, F., Steyn, W., Xiong, H, and **Wang, L.** (2016). Comparative evaluation of performance of warm mix RAP asphalt under accelerated unidirectional wheel load trafficking. Accelerated Pavement Testing International Conference, San José, Costa Rica.

Janoo, V.C. (1998). Quantification of shape, angularity, and surface texture of base course materials. USA Cold Regions Research and Engineering Laboratory, Special Report 98-1.

Jian-Shiuh, C. H. E. N., Chang, M. K., and **Lin, K. Y**. (2005). Influence of coarse aggregate shape on the strength of asphalt concrete mixtures. *Journal of the Eastern Asia Society for Transportation Studies*, *6*, 1062-1075.

Jurado, M., Gibson, N., Celaya, M., and **Nazarian, S.** (2012). Evaluation of asphalt damage and cracking development with seismic pavement analyzer. Journal of the Transportation Research Board, 2204, 47–54.

Kandhal, P. S., and **Parker, F.** (1998). "Aggregate tests related to asphalt concrete performance in pavements." NCHRP Report No. 405, Transportation Research Board, Washington, D.C.

Kim, Y. R., and **Souza, L. T.** (2009). Effects of aggregate angularity on mix design characteristics and pavement performance. Technical Report, No. MPM-10, Department of Civil Engineering, University of Nebraska-Lincoln, Lincoln, Nebraska, United States.

Krumbein, W.C. (1941). "Measurement and geological significance of shape and roundness of sedimentary aggregates." J. Sed. Petrol., 11, 64–72.

Kuo, C., and **Freeman, R.** (2000). Imaging indices for quantification of shape, angularity, and surface texture of aggregates. Transportation Research Record: Journal of the Transportation

Research Board, 1721, 57-65. Doi:10.3141/1721-07.
Lally, E. M. (2010). "Fourier transform interferometry for 3D mapping of rough and discontinuous surfaces." PhD dissertation. Virginia Polytechnic Institute and State University, Blacksburg.
Lally, E. M., Gong, J., and **Wang A.** (2010). "Method of multiple references for 3D imaging with fourier transform interferometry." Optic Express, 18(17), 17591–17596.
Li, Y. (2015). Digital Mix Design for Performance Optimization of Asphalt Mixture. PhD dissertation. Virginia Polytechnic Institute and State University, Blacksburg.
Little, D., Button, J., Jayawickrama, P., Solaimanian, M., and **Hudson, B.** (2003). "Quantify shape, angularity and surface texture of aggregates using image analysis and study their effect on performance." Report No. 0-1707-4, Texas Dept. of Transportation, Austin, TX.
Liu, Y., Sun, W., Nair, H., Lane, S., and **Wang, L.** (2016). Quantification of aggregate morphological characteristics as related to mechanical properties of asphalt concrete with improved FTI system. Journal of Materials in Civil Engineering, 28(8), 04016046.
Mahmoud E, and **Ortiz E.** (2014). Implementation of AIMS in measuring aggregate resistance to polishing, abrasion, breakage. Illinois Center for Transportation, Rantoul (IL) Report # FHWA-ICT-14-014.
Masad, E. (2003). The development of a computer controlled image analysis system for measuring aggregate shape properties. NCHRP-IDEA Project 77 Final Report, Transportation Research Board, Washington, DC.
Masad, E. and **Button, J.W.** (2000). Unified imaging approach for measuring aggregate angularity and texture. Computer Aided Civil Infrastructure Engineering, 15 (4), 273–280.
Masad, E., Olcott, D., White, T. and **Tashman, L.** (2001). "Correlation of fine aggregate imaging shape indices with asphalt mixture performance." Transp. Res. Record, 1757, 148–56.
Meininger, R. C. (1998). "Aggregate test related to performance of portland cement concrete pavement." NCHRP Report No. 281, Transportation Research Board, Washington, D.C.
Mohammad, L., et al. (1999). Laboratory performance evaluation SMA, CMHB AND dense graded asphalt mixtures. Journal of the Association of Asphalt Paving Technologists, 68, 252–280.
Naidu, G., and **Adiseshu, S.** (2011). Influence of coarse aggregate shape factors on bituminous mixtures. In International Journal of Engineering Research and Applications (IJERA).
ÖZEN, M. (2007). Investigation of relationship between aggregate shape parameters and concrete strength using imaging techniques (Doctoral dissertation, Middle East Technical University).
Pan, T (2006). "Investigation of coarse aggregate morphology affecting hot mix behavior using image analysis." PhD dissertation. University of Illinois at Urbana-Champaign, Champaign.
Pan, T., Tutumluer, E., and **Carpenter, S.** (2005). Effect of coarse aggregate morphology on the resilient modulus of hot-mix asphalt. Transportation Research Record: Journal of the Transportation Research Board, 1929, 1-9. Doi:10.3141/1929-01.
Pan, T., Tutumluer, E., and **Carpenter, S. H.** (2006). Effect of coarse aggregate morphology on permanent deformation behavior of hot mix asphalt. Journal of transportation engineering, 132(7), 580-589.
Prowell, B.D., Watson, D. E., Hurley, G. C., and **Brown, E. R.** (2009). Evaluation of Stone

Matrix Asphalt (SMA) for Airfield Pavements. Final Report 04-04, Airfield Asphalt Pavement Technology Program, Auburn, AL.

Rao, C., and **Tutumluer, E.** (2000). "Determination of volume of aggregates: new image analysis approach." Transportation Research Record: Journal of the Transportation Research Board, 1721, 73–80.

Rao, C., Tutumluer, E. and **Kim, I.T.** (2002). Quantification of coarse aggregate angularity based on image analysis. Transportation Research Record, 1787, Washington, DC: Transportation Research Board, 117 –124.

Rao, C., Tutumluer, E. and **Stefanski, J.A.** (2001). Flat and elongated ratios and gradation of coarse aggregates using a new image analyzer. ASTM Journal Testing Standard, 29 (5), 79– 89.

Roy, N., Veeraragavan, A., and **Krishnan, J.** (2015). "Interpretation of flow number test data for asphalt mixtures." Proceedings of the Institution of Civil Engineers-Transport, 168(3), 191-199.

Saeed, A., Hall, J. W., and **Barker, W. R.** (2001). "Performance-related tests of aggregates for use in unbound pavement layers." NCHRP Report 453, Transportation Research Board, Washington, D.C.

Shu X, Huang B, and **Vukosavljevic D.** (2008). Laboratory evaluation of fatigue characteristics of recycled asphalt mixture. Construction and Building Materials, 22(7), 1323–1330.

Sime, L. C., and **Ferguson, R. I.** (2003). "Information on grain sizes in gravel-bed rivers by automated image analysis." Journal of Sedimentary Research, 73(4), 630-636.

Smith, M. R., and **Collis, L.** (1993). Aggregates: Sand, gravel and crushed rock aggregates for construction purposes (2nd ed.). Geological Society, London, Engineering Geology Special Publications.

Souza, L. T. (2009). Investigation of aggregate angularity effects on asphalt concrete mixture performance using experimental and virtual asphalt samples. M.S. thesis, Univ. of Nebraska, Lincoln, NE.

Stiady, J., Hand, A., and **White, T.** (2001). Quantifying contribution of aggregate characteristics to HMA performance using PURWheel laboratory tracking device. ASTM STP 1412, West Conshohocken, PA.

Sun, W., Wang, L., and **Tutumluer, E.** (2012). "Image analysis technique for aggregate morphology analysis with two-dimensional fourier transform method." Transportation Research Record: Journal of the Transportation Research Board, 2267, 3-13.

Tafesse S., Robison Fernlund, J. M., Sun, W., et al. (2013). "Evaluation of image analysis methods used for quantification of aggregate angularity." Sedimentology, 60(4), 1100-1110.

Tutumluer, E., Pan, T., and **Carpenter, S. H.** (2005). Investigation of aggregate shape effects on hot mix performance using an image analysis approach.UILU-ENG-2005-2003.

Unal, H., and **Mimaroglu, A.** (2014). "Evaluation of morphologic characteristics and mechanical performance of rockforce mineral fiber- and glass fiber-reinforced polyamide-6 composites." Science and Engineering of Composite Materials, 21(3), 323-328.

Virginia Department of Transportation (2007). Virginia Test Method 110: Sample Preparation and Calculations for Flat and Elongated Testing by ASTM D 4791 – (Asphalt Lab).

Virginia Department of Transportation (2009). Virginia Test Method 110: Virginia Test Method for Determining Rutting Susceptibility Using the Asphalt Pavement Analyzer.

Richmond.
Walubita, L. F., Hugo, F., and **Epps, A. L.** (2000). Performance of rehabilitated lightweight aggregate asphalt concrete pavements under wet and heated model mobile load simulator trafficking: a comparative study with the TxMLS (No. FHWA/TX-00/0-1814-3). Center for Transportation Research, Bureau of Engineering Research, University of Texas at Austin.
Wang, H., Bu, Y., Wang, Y., Yang, X., and **You, Z.** (2016). The Effect of Morphological Characteristic of Coarse Aggregates Measured with Fractal Dimension on Asphalt Mixture's High-Temperature Performance. Advances in Materials Science and Engineering, 2016(2016), 1-9.

Wang, L., Wang, X., Mohammad, L., and **Abadie C.** (2005). "Unified method to quantify aggregates shape angularity and texture using fourier analysis." Journal of Material in Civil Engineering, 17(5), 498–504.
Wang, L., Sun, W., Lally, E. M., Wang, A., Druta, C., and **Tutumluer, E.** (2012). Application of LADAR in the analysis of aggregate characteristics. NCHRP Rep. No. 724, Transportation Research Board, Washington, DC.
Wang, R. Y. (2007). "Two-dimensional fourier transform." <http://fourier.eng.hmc.edu/e101/lectures/Image_Processing/node6.html> (Nov. 5, 2007)

Appendix A

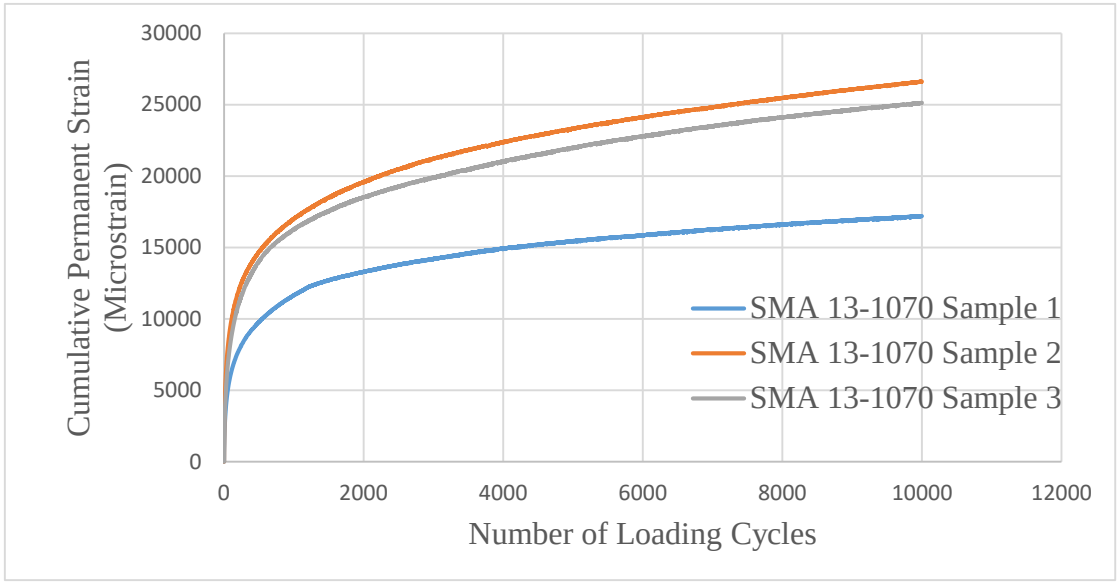

(a)

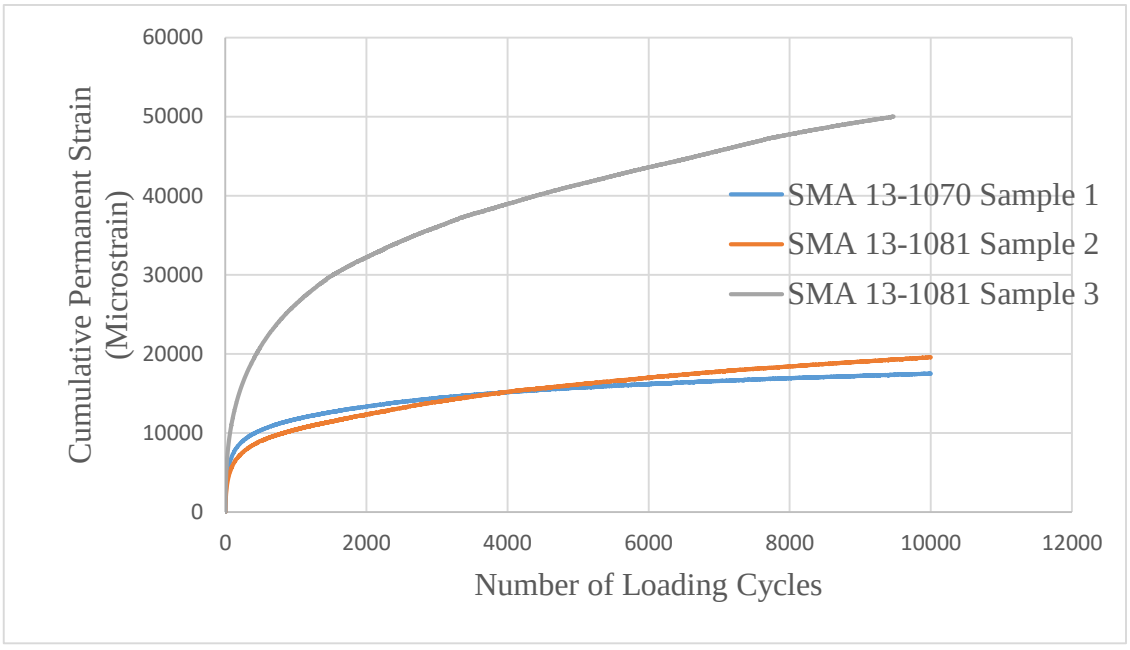

(b)

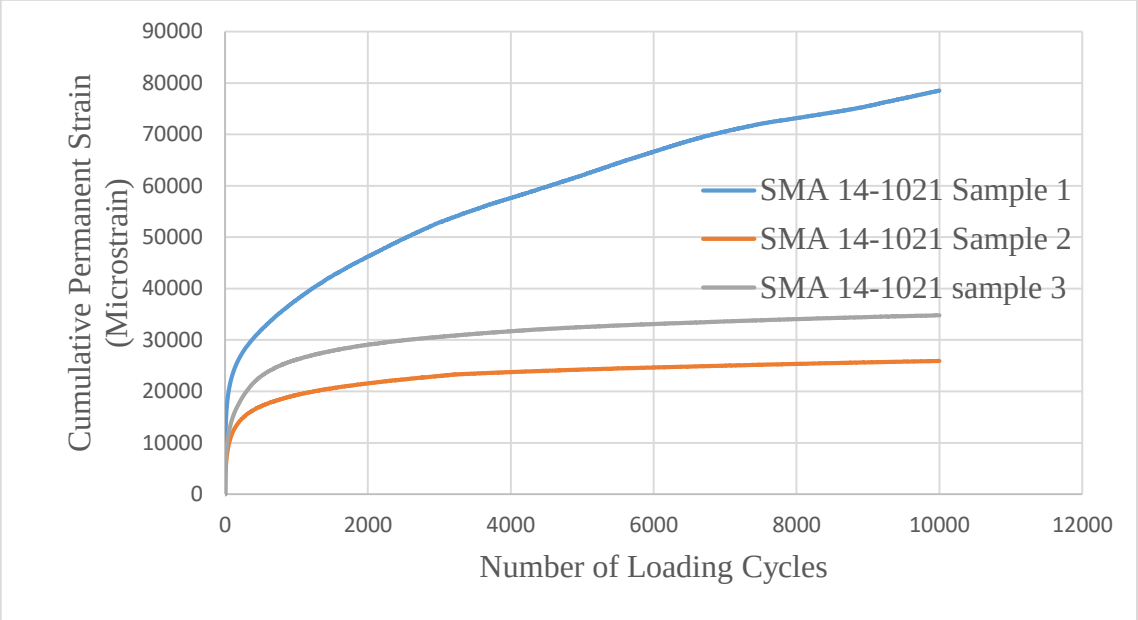
Cumulative Permanent Strain (Microstrain)
90000
80000
70000
60000
50000
40000
30000
20000
10000
0
0
2000
4000
6000
8000
10000
12000
Number of Loading Cycles
SMA 14-1021 Sample 1
SMA 14-1021 Sample 2
SMA 14-1021 sample 3

(c)

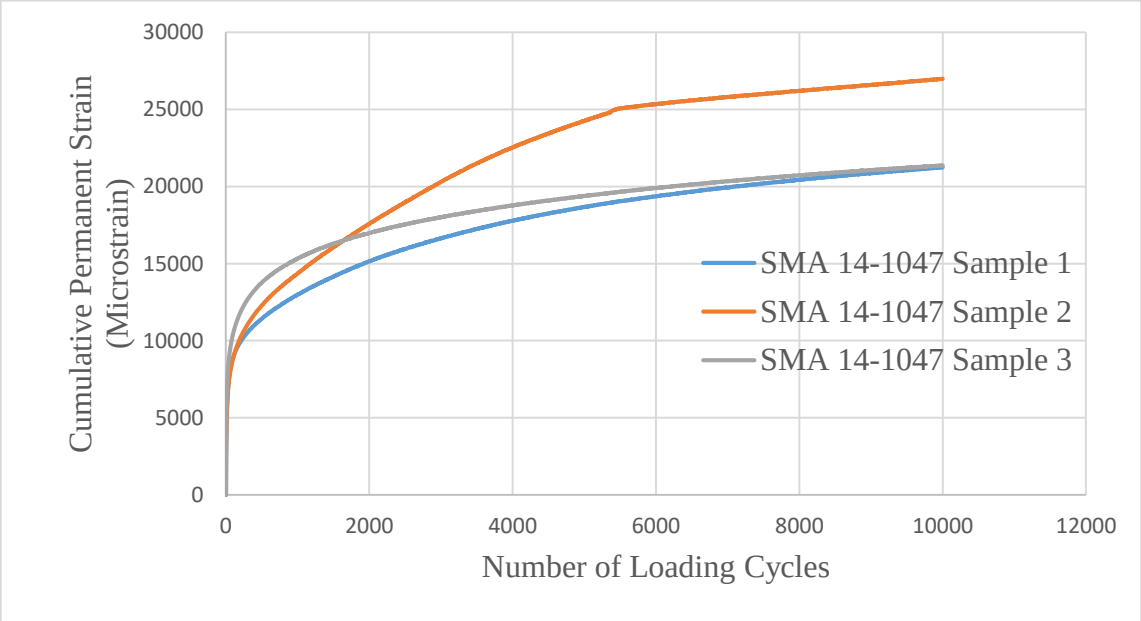
Cumulative Permanent Strain (Microstrain)
30000
25000
20000
15000
10000
5000
0
0
2000
4000
6000
8000
10000
12000
Number of Loading Cycles
SMA 14-1047 Sample 1
SMA 14-1047 Sample 2
SMA 14-1047 Sample 3

(d)

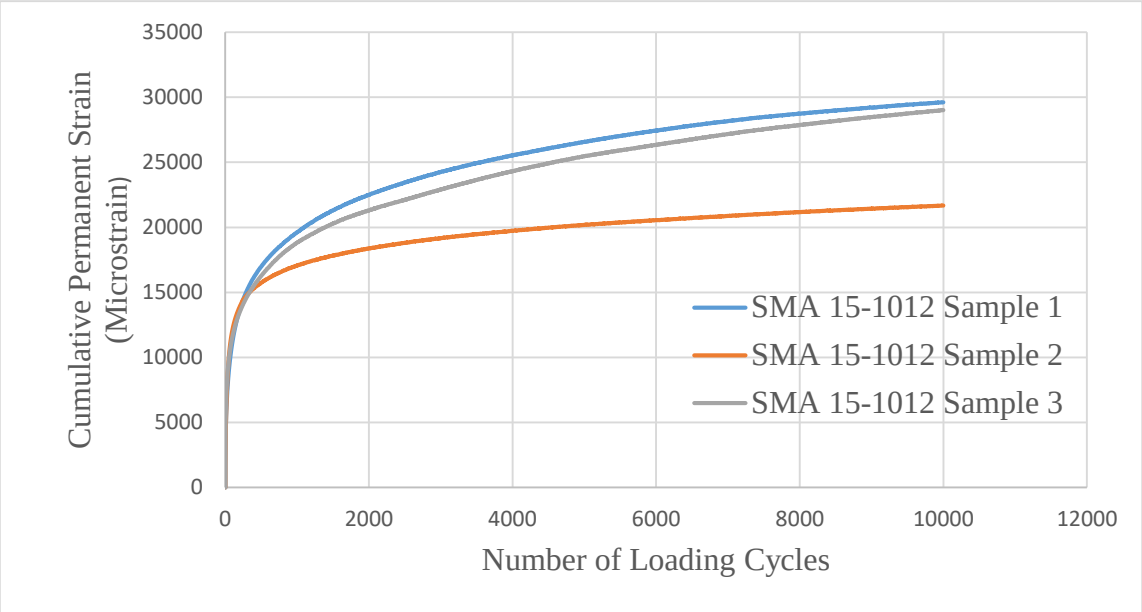
Cumulative Permanent Strain (Microstrain)
35000
30000
25000
20000
15000
10000
5000
0
0
2000
4000
6000
8000
10000
12000
Number of Loading Cycles
SMA 15-1012 Sample 1
SMA 15-1012 Sample 2
SMA 15-1012 Sample 3

(e)

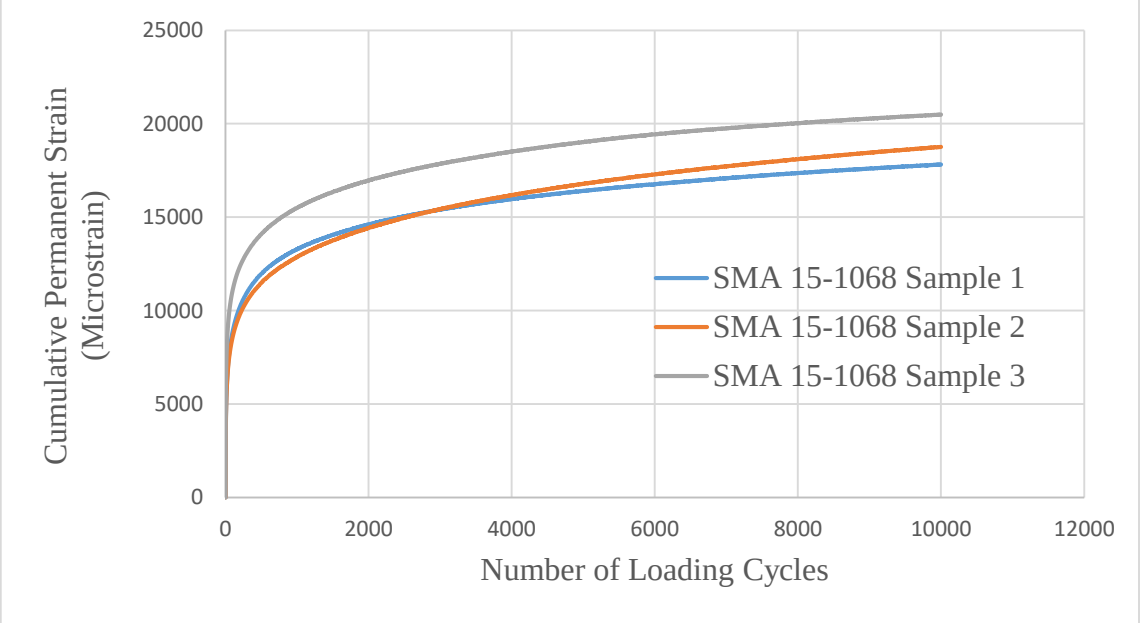
Cumulative Permanent Strain (Microstrain)
25000
20000
15000
10000
5000
0
0
2000
4000
6000
8000
10000
12000
Number of Loading Cycles
SMA 15-1068 Sample 1
SMA 15-1068 Sample 2
SMA 15-1068 Sample 3

(f)

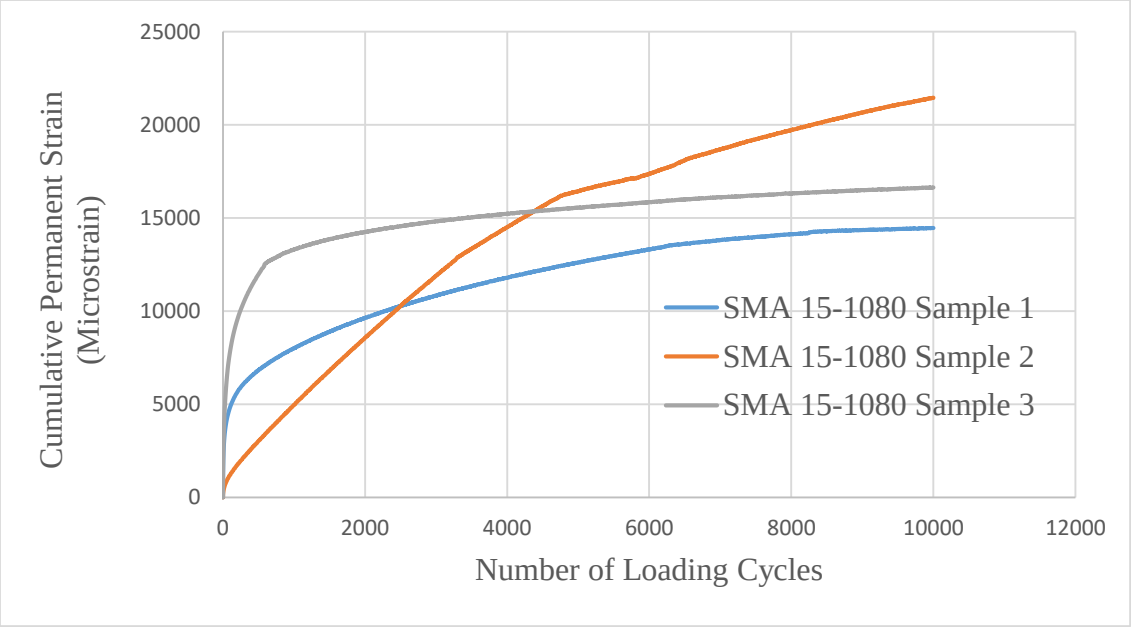

(g)

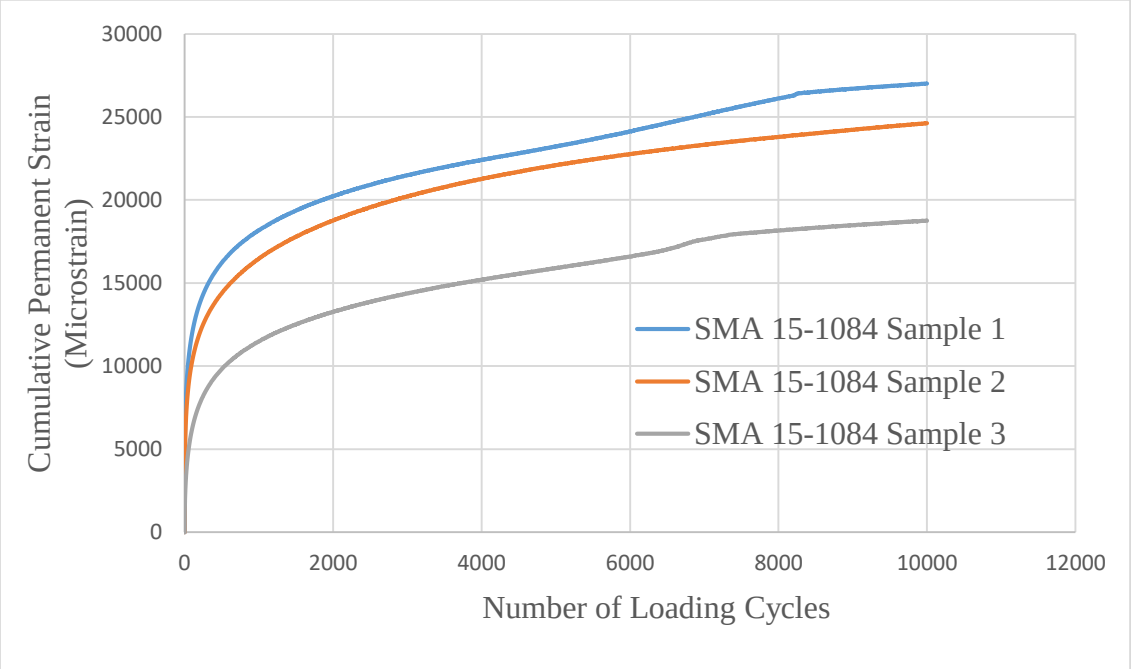

(h)

Plots of the cumulative permanent strain versus number of loading cycles for flow number test under confined condition for each type of SMA mixture. (a) SMA 13-1070; (b) SMA 13-1081; (c) SMA 14-1021; (d) SMA 14-1047; (e) SMA 15-1012; (f) SMA 15-1068; (g) SMA 15-1080; (h) SMA 15-1084.

Appendix B

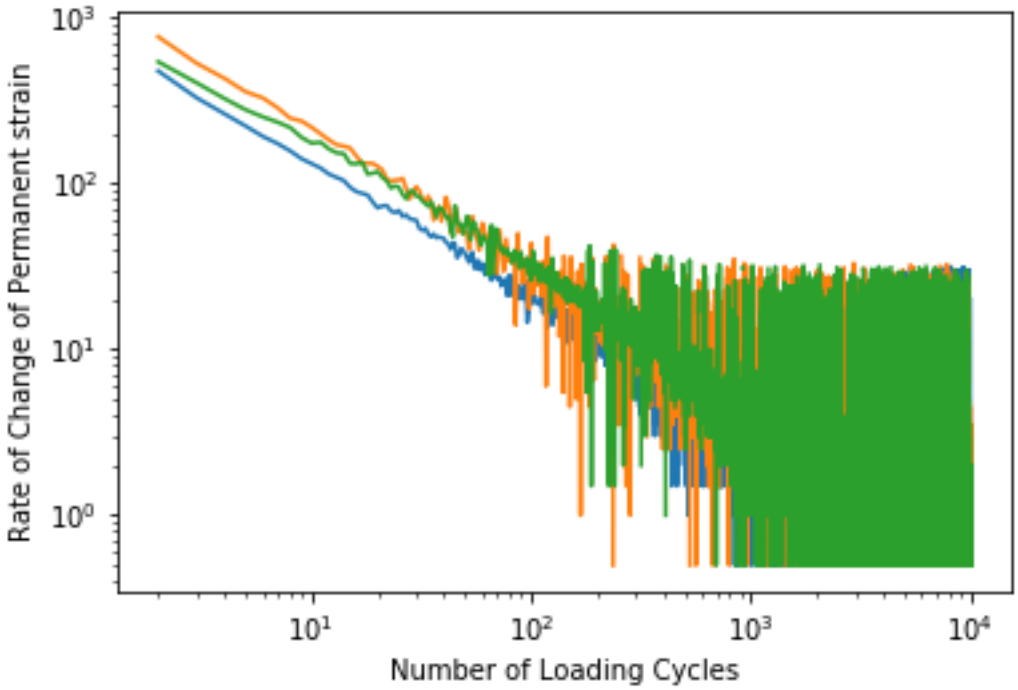

(a)

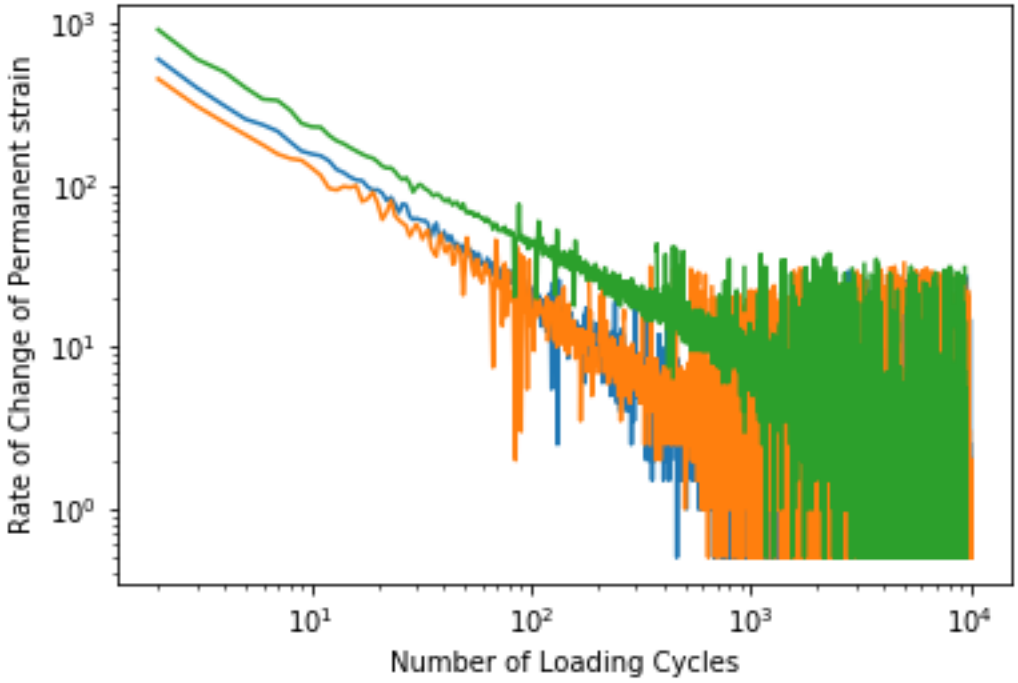

(b)

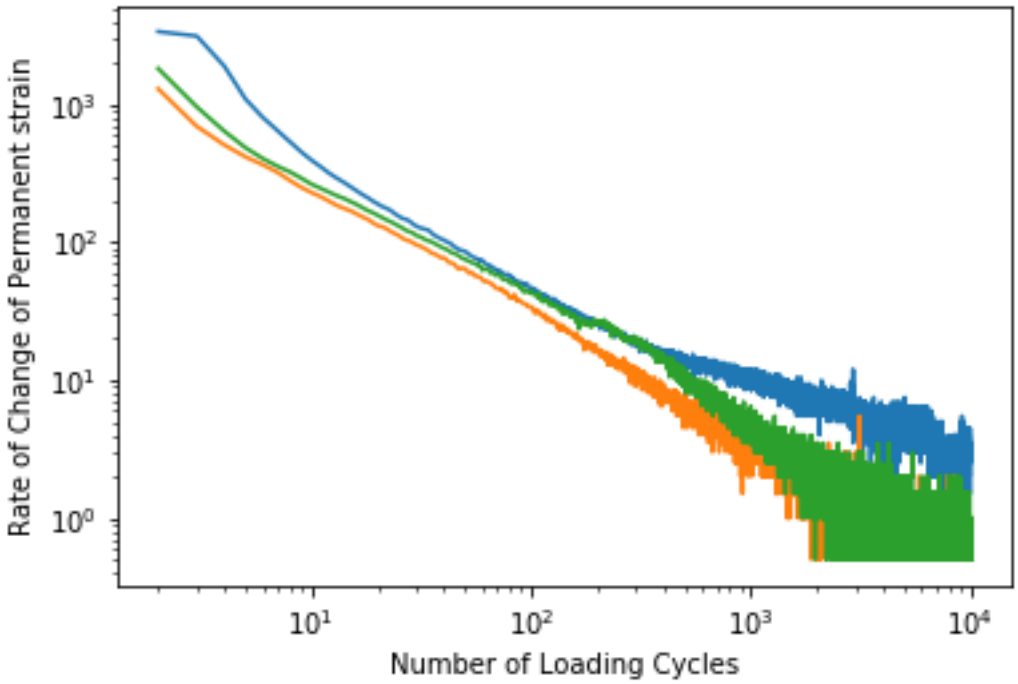
Rate of Change of Permanent strain
10^3
10^2
10^1
10^0
10^1
10^2
10^3
10^4
Number of Loading Cycles

(c)

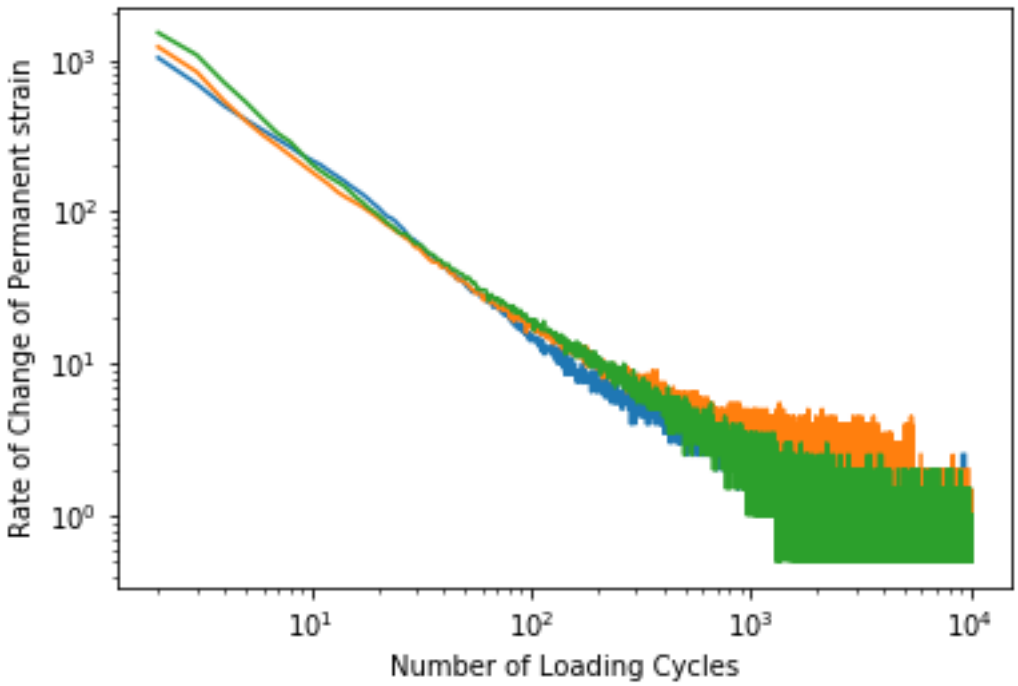
Rate of Change of Permanent strain
10^3
10^2
10^1
10^0
10^1
10^2
10^3
10^4
Number of Loading Cycles

(d)

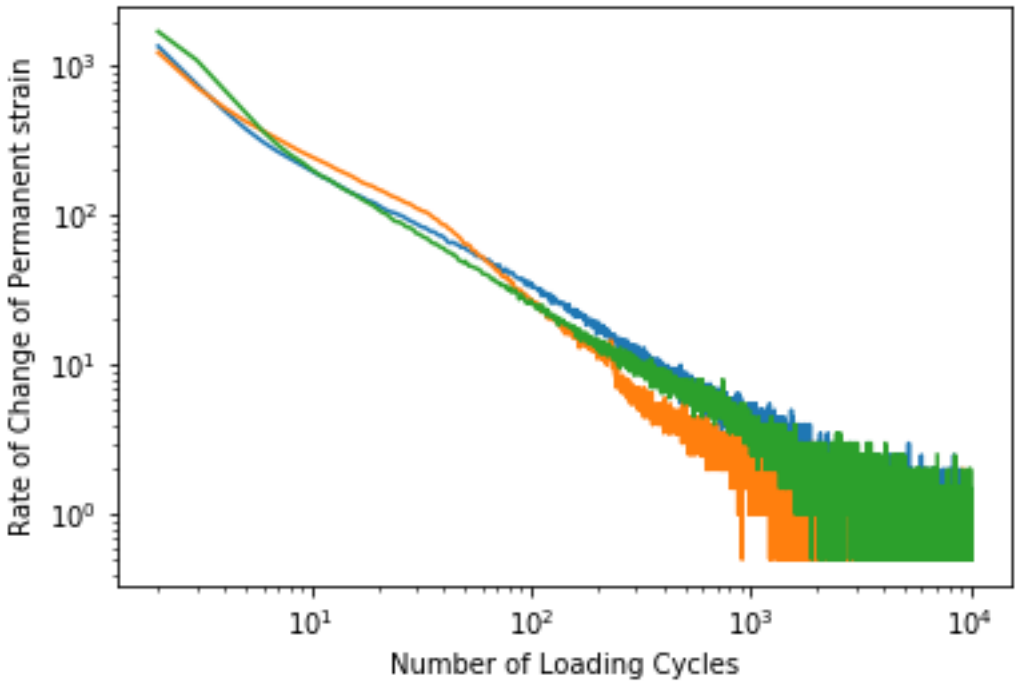
Rate of Change of Permanent strain
10^3
10^2
10^1
10^0
10^1
10^2
10^3
10^4
Number of Loading Cycles

(e)

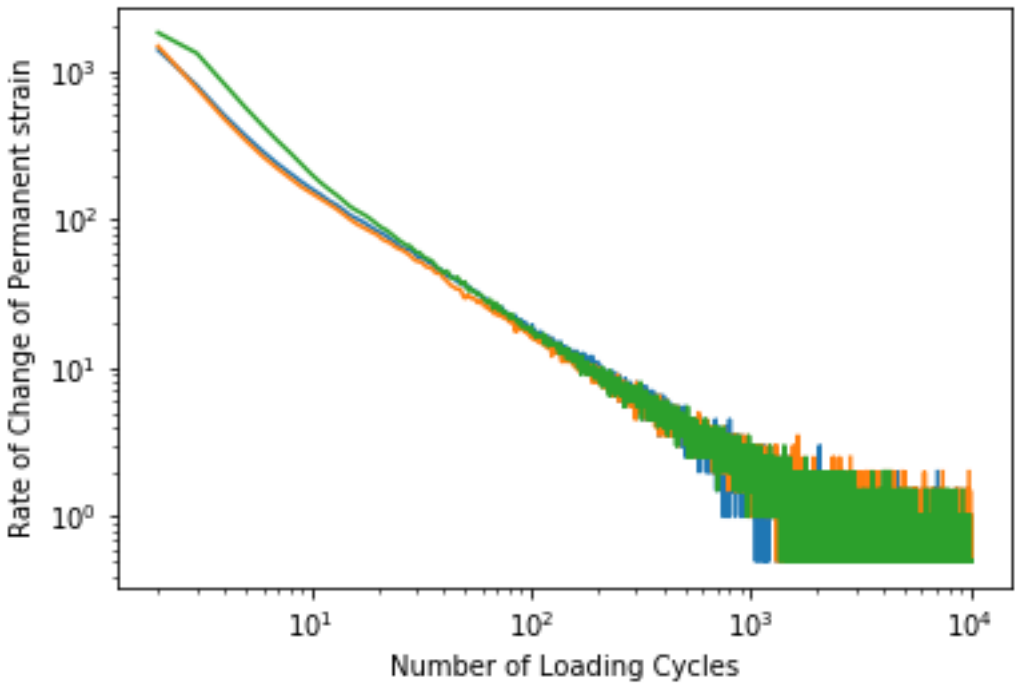
Rate of Change of Permanent strain
10^3
10^2
10^1
10^0
10^1
10^2
10^3
10^4
Number of Loading Cycles

(f)

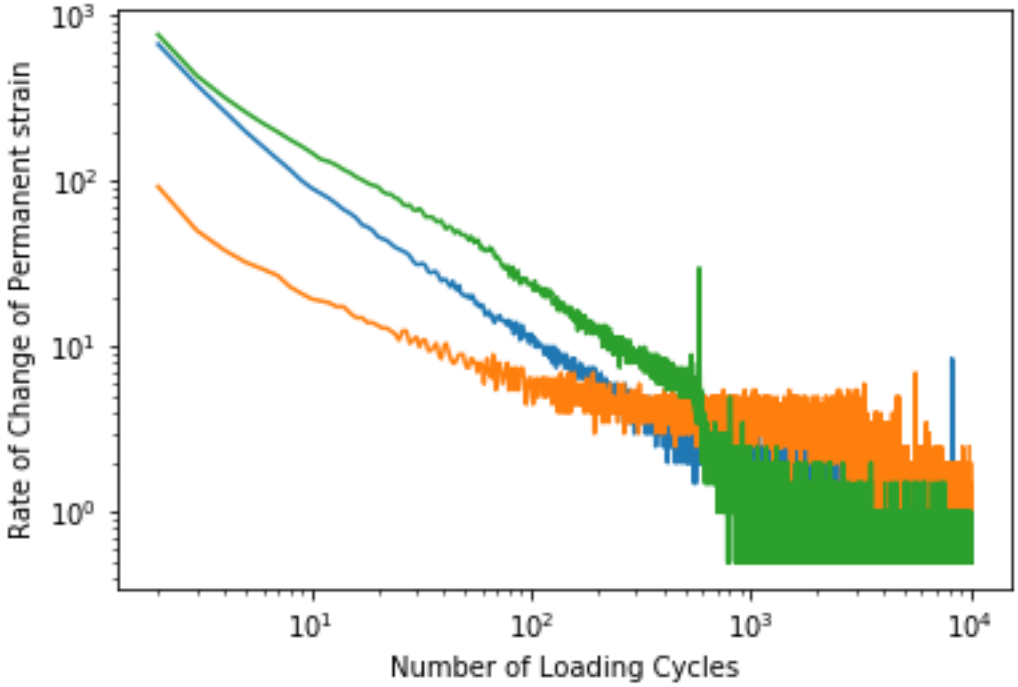

(g)

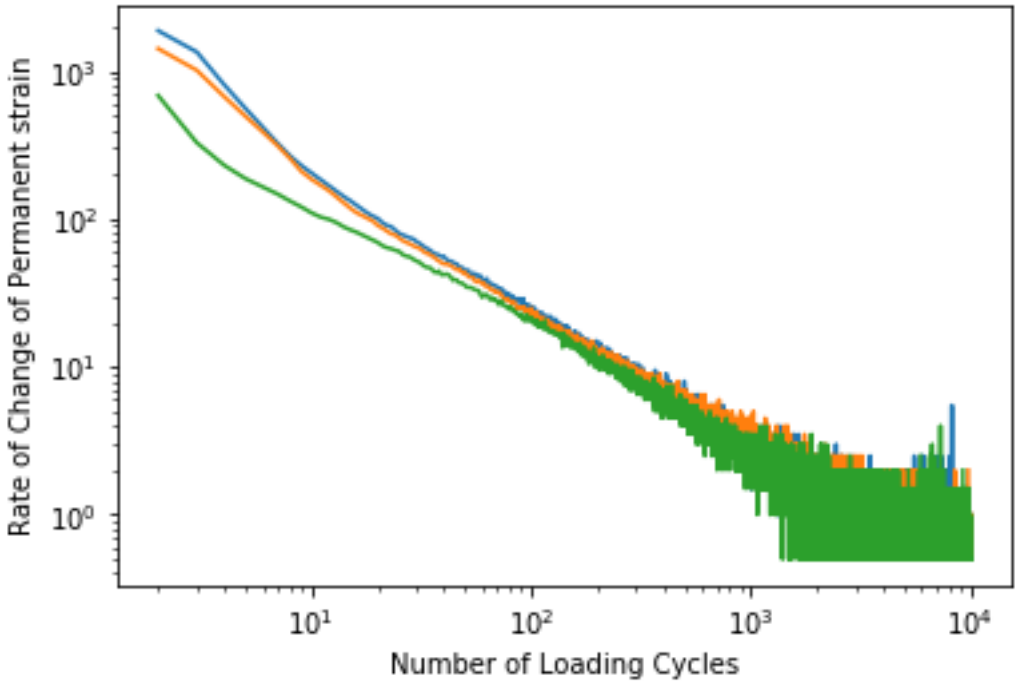

(h)

Plots of the rate of change of permanent strain versus number of loading cycles for flow number test under confined condition for each type of SMA mixture. (a) SMA 13-1070; (b) SMA 13-1081; (c) SMA 14-1021; (d) SMA 14-1047; (e) SMA 15-1012; (f) SMA 15-1068; (g) SMA 15-1080; (h) SMA 15-1084.

Appendix C

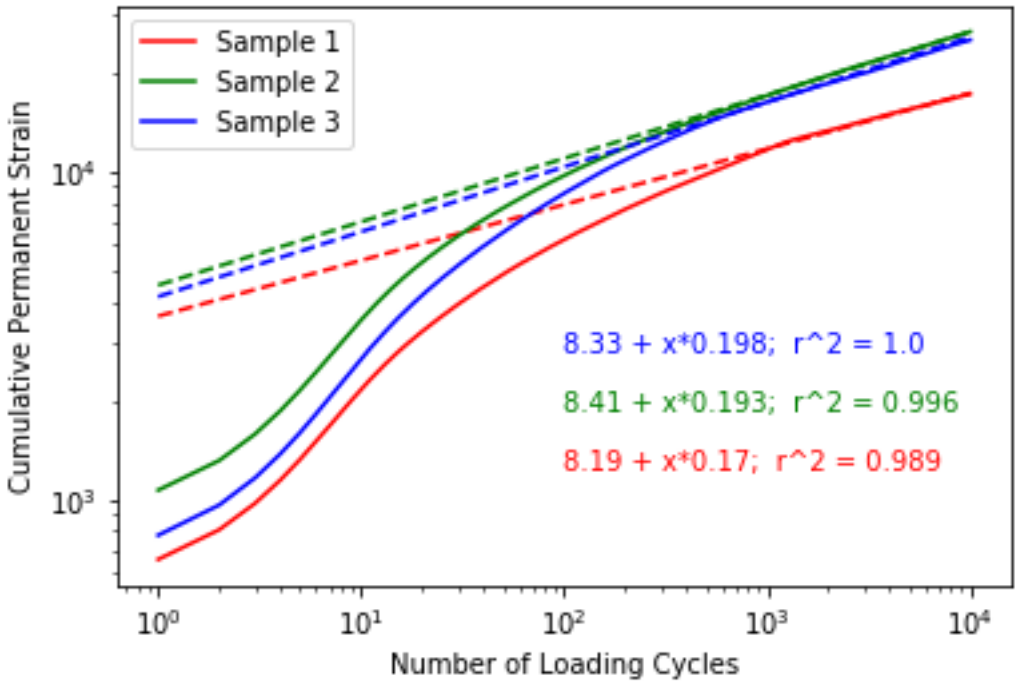

(a)

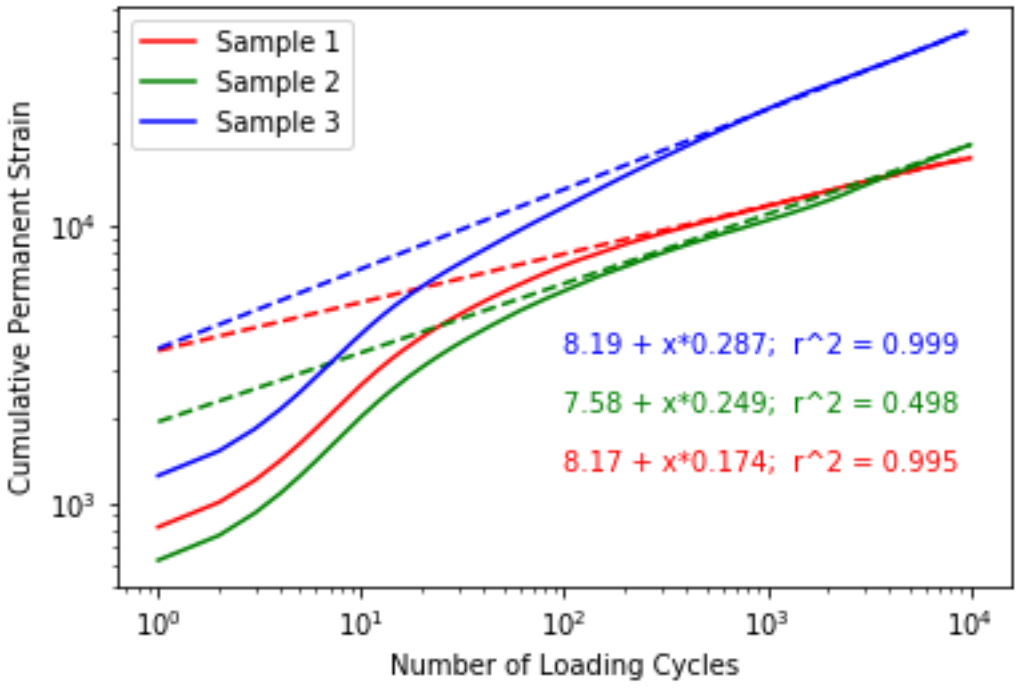

(b)

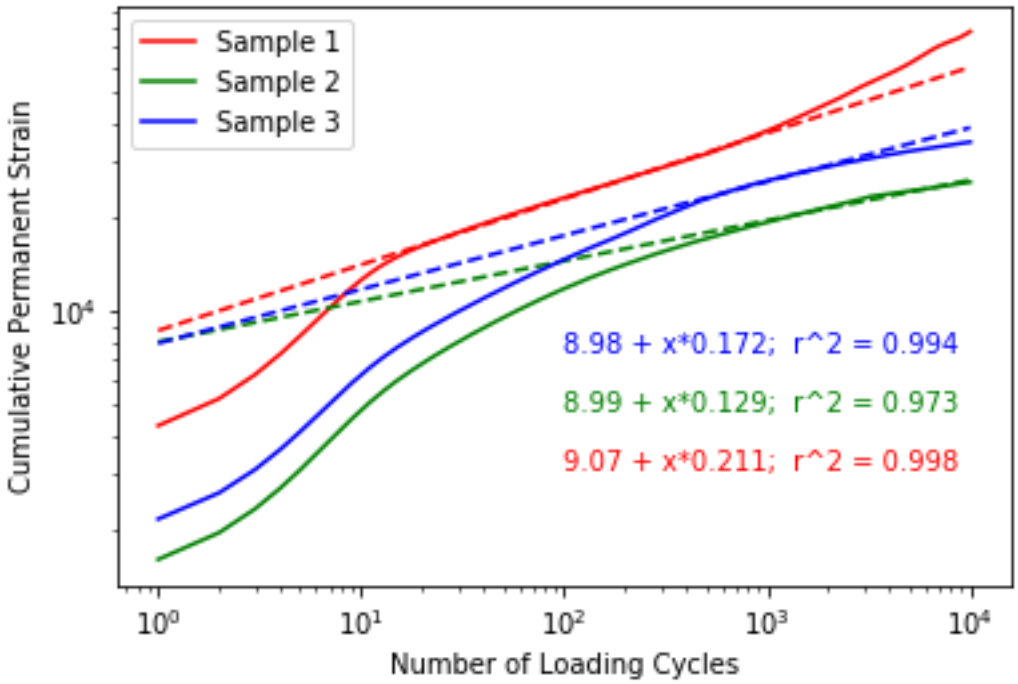
Sample 1
Sample 2
Sample 3
8.98 + x*0.172; r^2 = 0.994
8.99 + x*0.129; r^2 = 0.973
9.07 + x*0.211; r^2 = 0.998
Cumulative Permanent Strain
Number of Loading Cycles

(c)

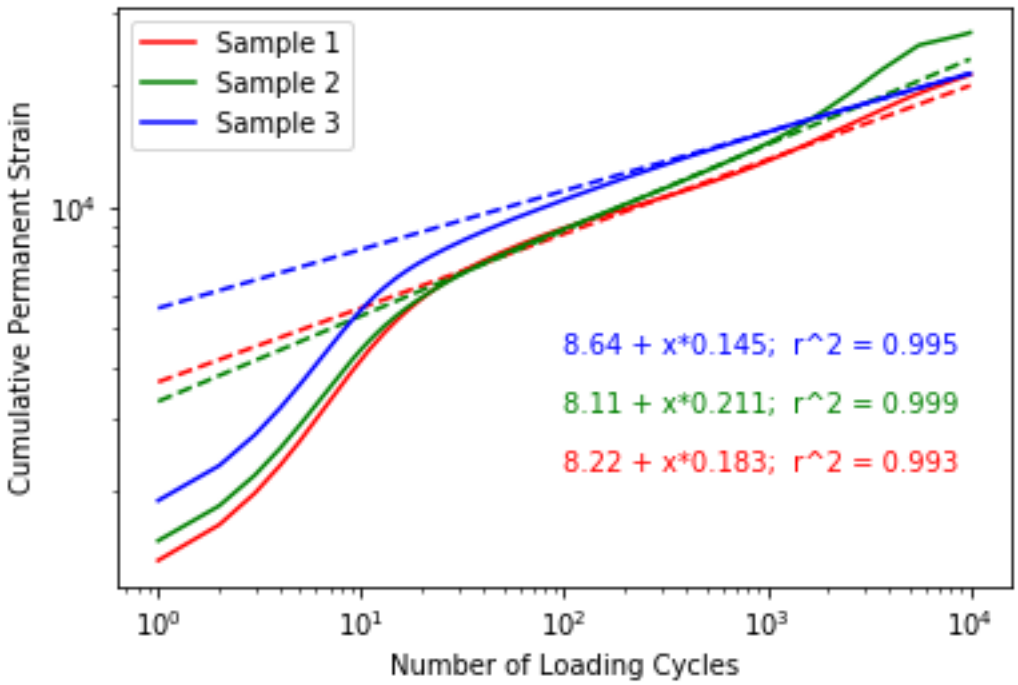
Sample 1
Sample 2
Sample 3
8.64 + x*0.145; r^2 = 0.995
8.11 + x*0.211; r^2 = 0.999
8.22 + x*0.183; r^2 = 0.993
Cumulative Permanent Strain
Number of Loading Cycles

(d)

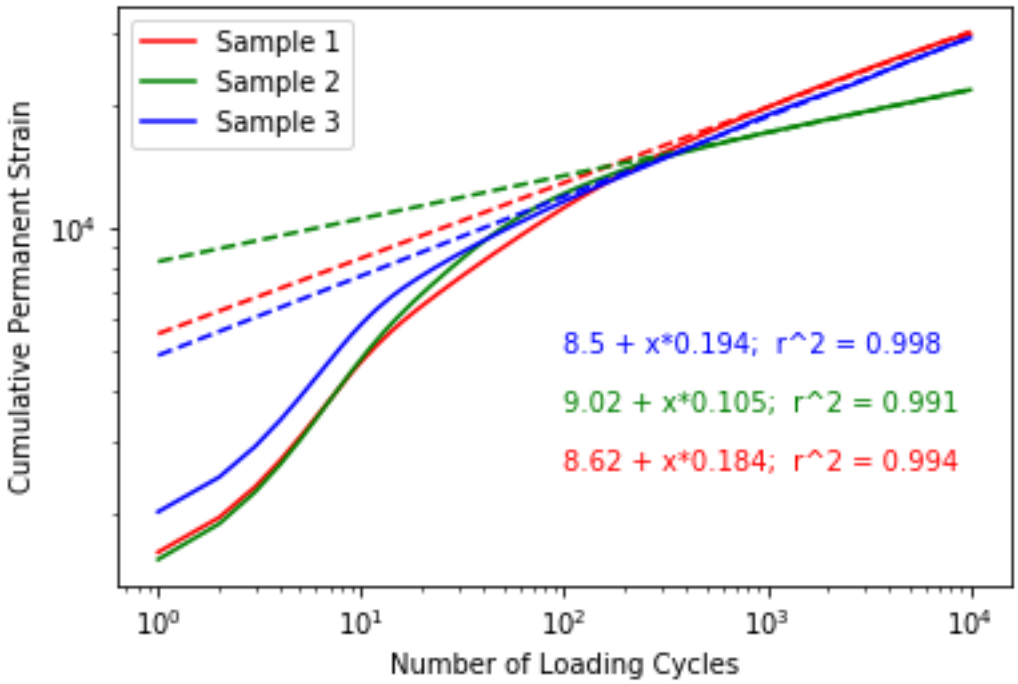
Sample 1
Sample 2
Sample 3
Cumulative Permanent Strain
10^4
8.5 + x*0.194; r^2 = 0.998
9.02 + x*0.105; r^2 = 0.991
8.62 + x*0.184; r^2 = 0.994
10^0
10^1
10^2
10^3
10^4
Number of Loading Cycles

(e)

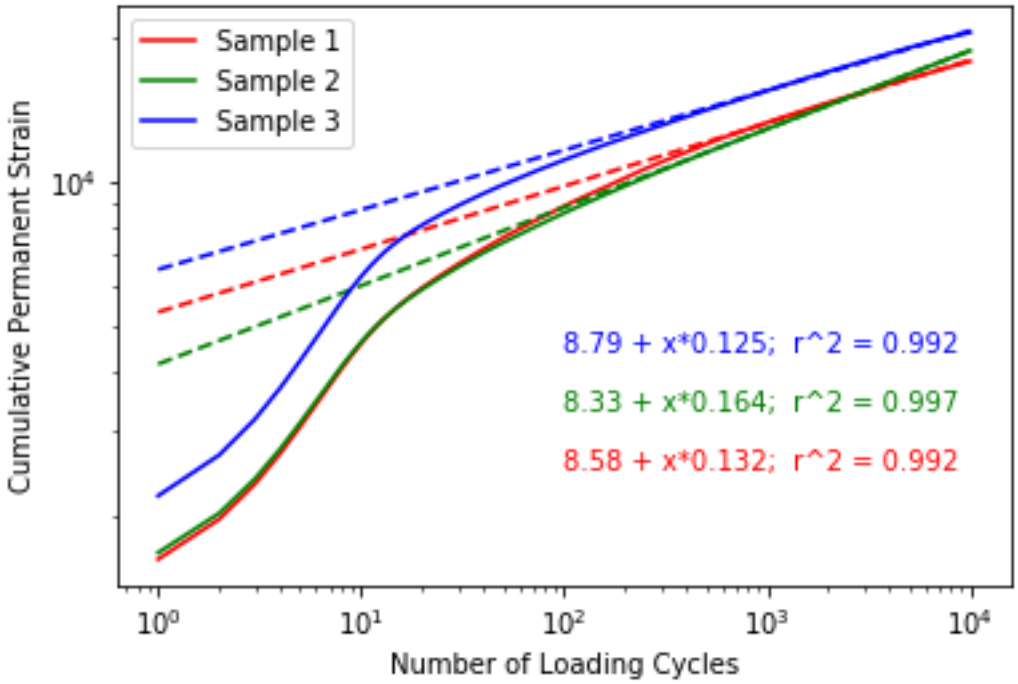
Sample 1
Sample 2
Sample 3
Cumulative Permanent Strain
10^4
8.79 + x*0.125; r^2 = 0.992
8.33 + x*0.164; r^2 = 0.997
8.58 + x*0.132; r^2 = 0.992
10^0
10^1
10^2
10^3
10^4
Number of Loading Cycles

(f)

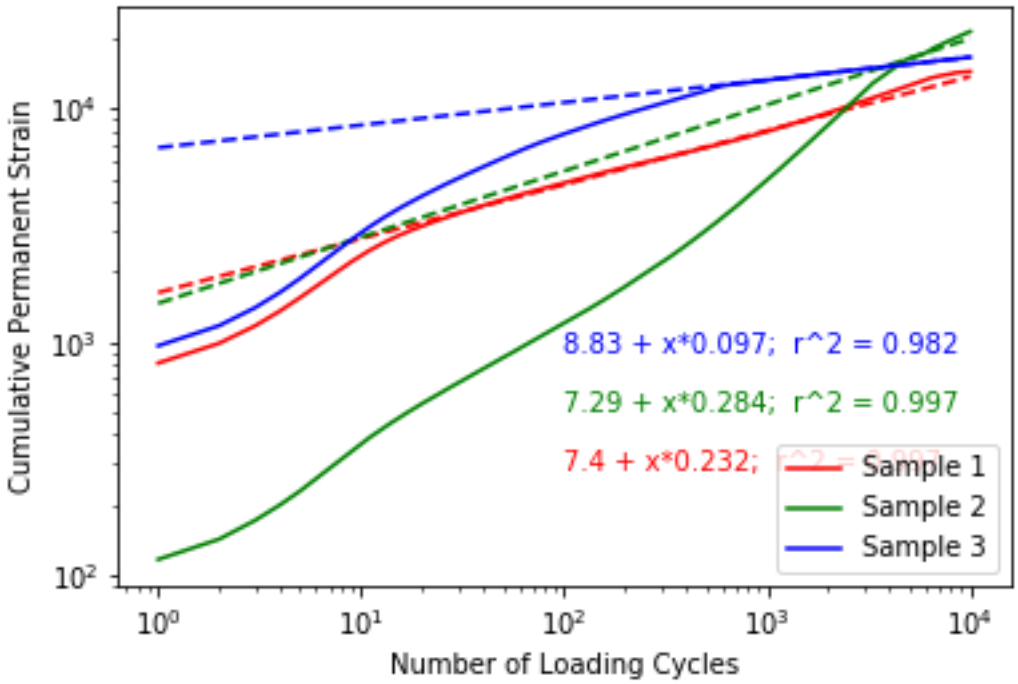

(g)

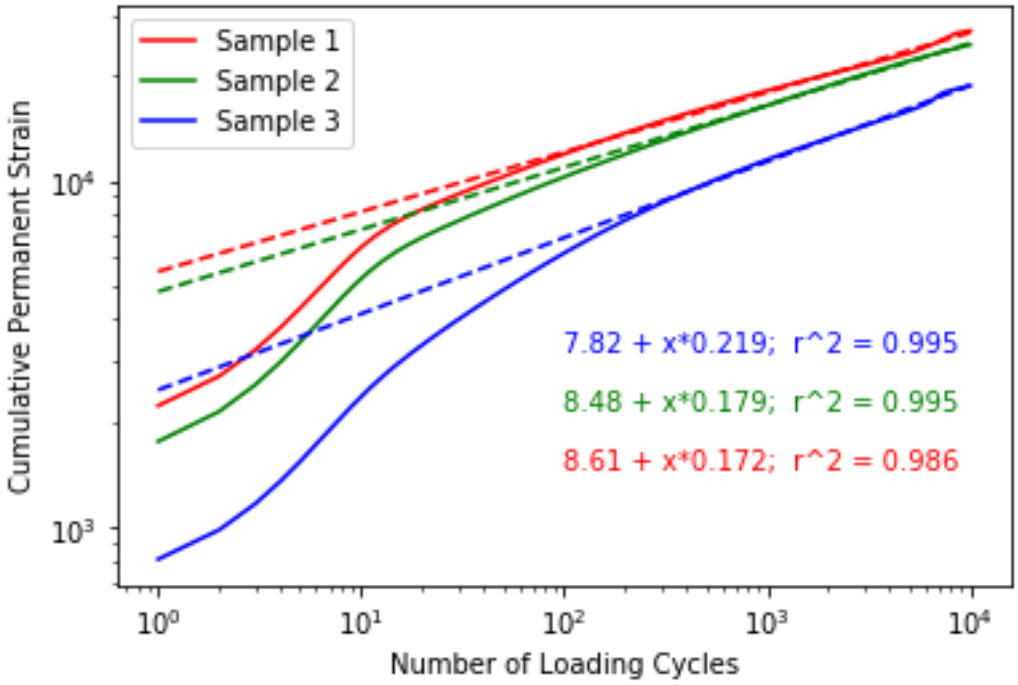

(h)

Flow number slope from plot of permanent strain versus number of loading cycles on log-log scale for flow number test under confined condition for each type of SMA mixture. (a) SMA 13-1070; (b) SMA 13-1081; (c) SMA 14-1021; (d) SMA 14-1047; (e) SMA 15-1012; (f) SMA 15-1068; (g) SMA 15-1080; (h) SMA 15-1084.

Appendix D

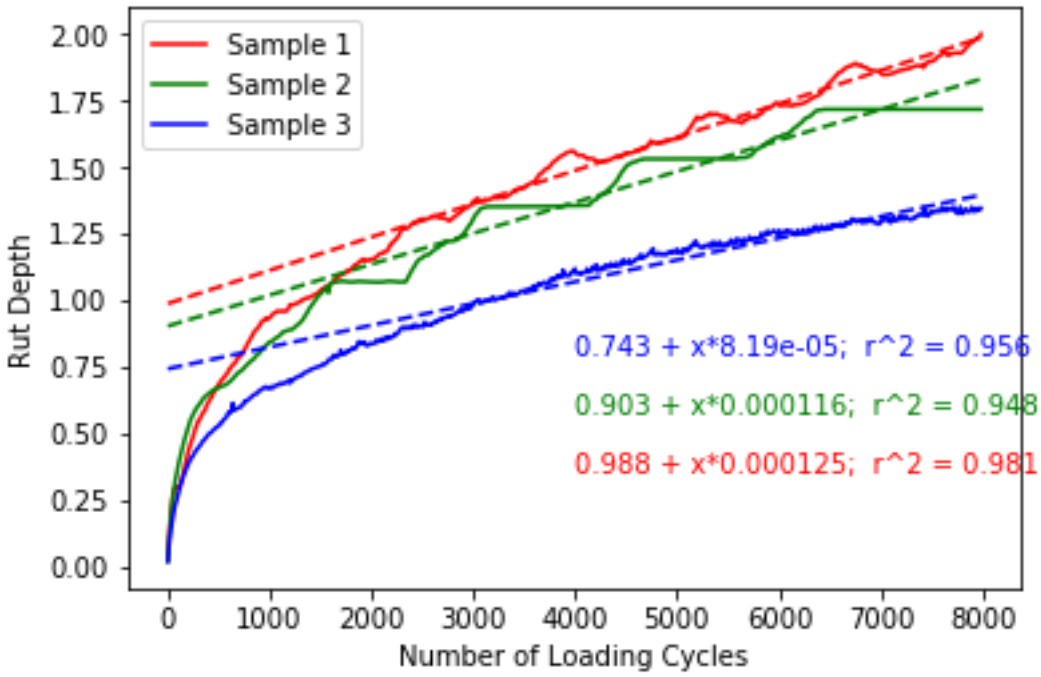

(a)

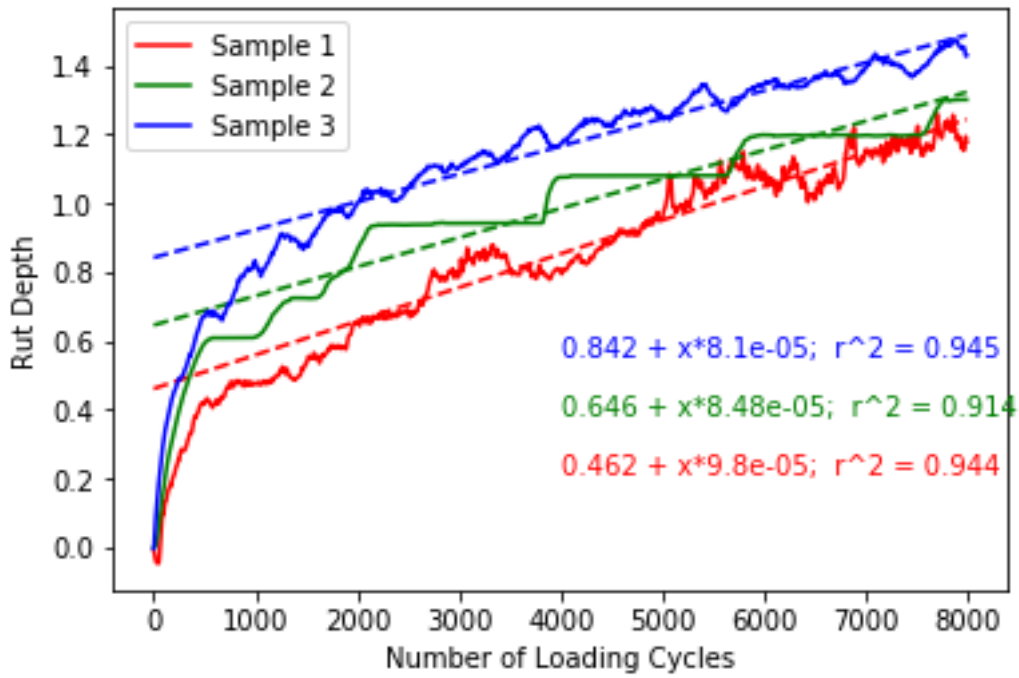

(b)

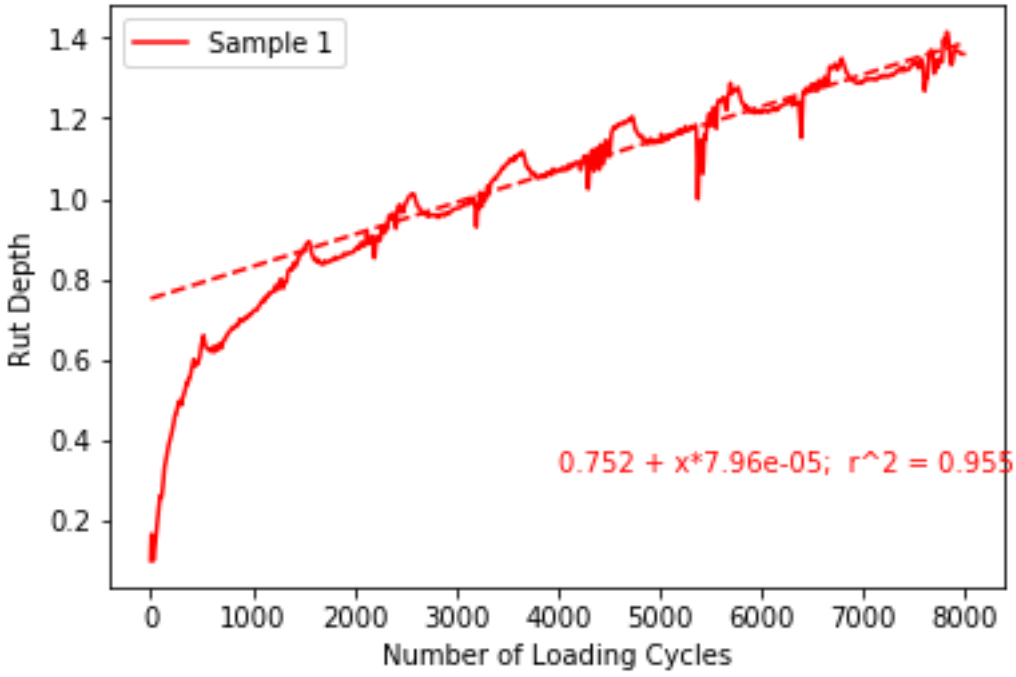
Sample 1
Rut Depth
Number of Loading Cycles
0.752 + x*7.96e-05; r^2 = 0.955

(c)

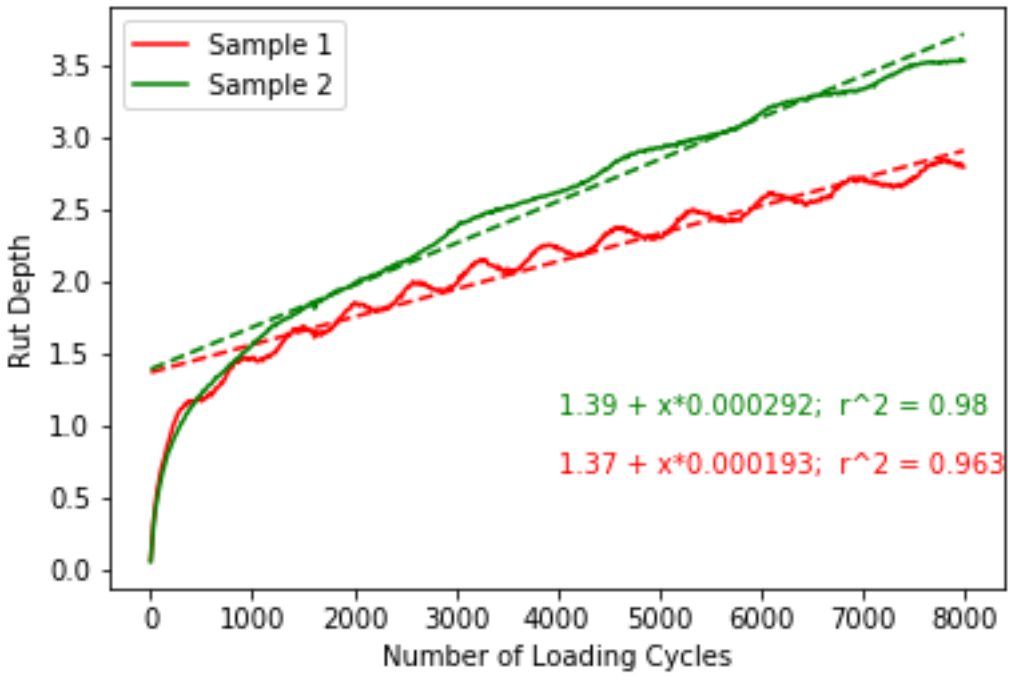
Sample 1
Sample 2
Rut Depth
Number of Loading Cycles
1.39 + x*0.000292; r^2 = 0.98
1.37 + x*0.000193; r^2 = 0.963

(d)

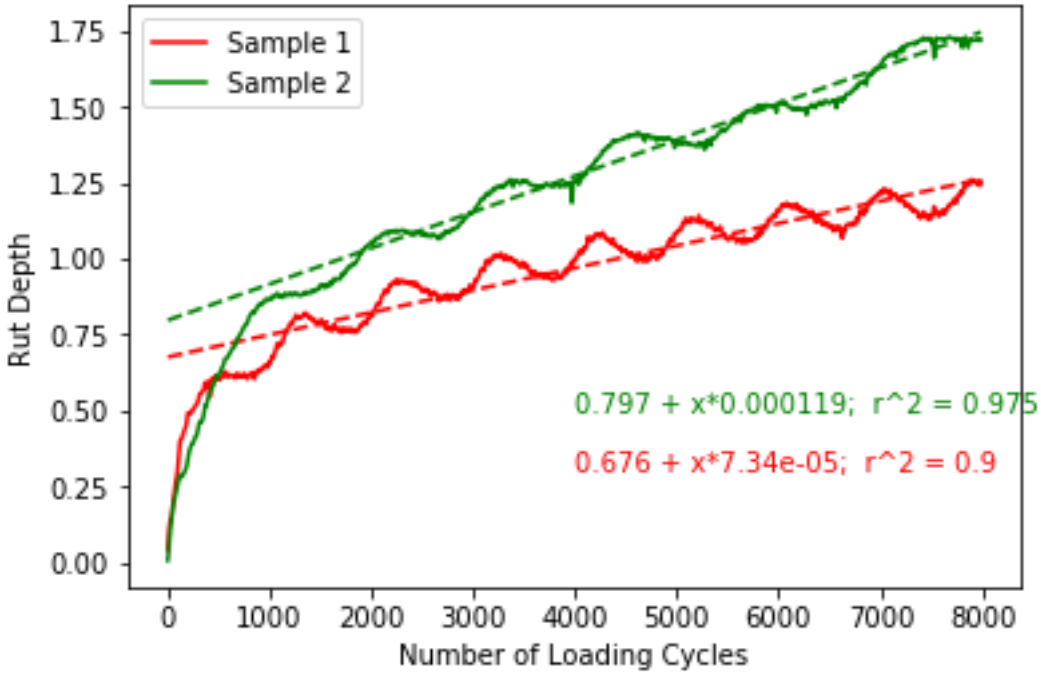
Sample 1
Sample 2
Rut Depth
Number of Loading Cycles
0.797 + x*0.000119; r^2 = 0.975
0.676 + x*7.34e-05; r^2 = 0.9

(e)

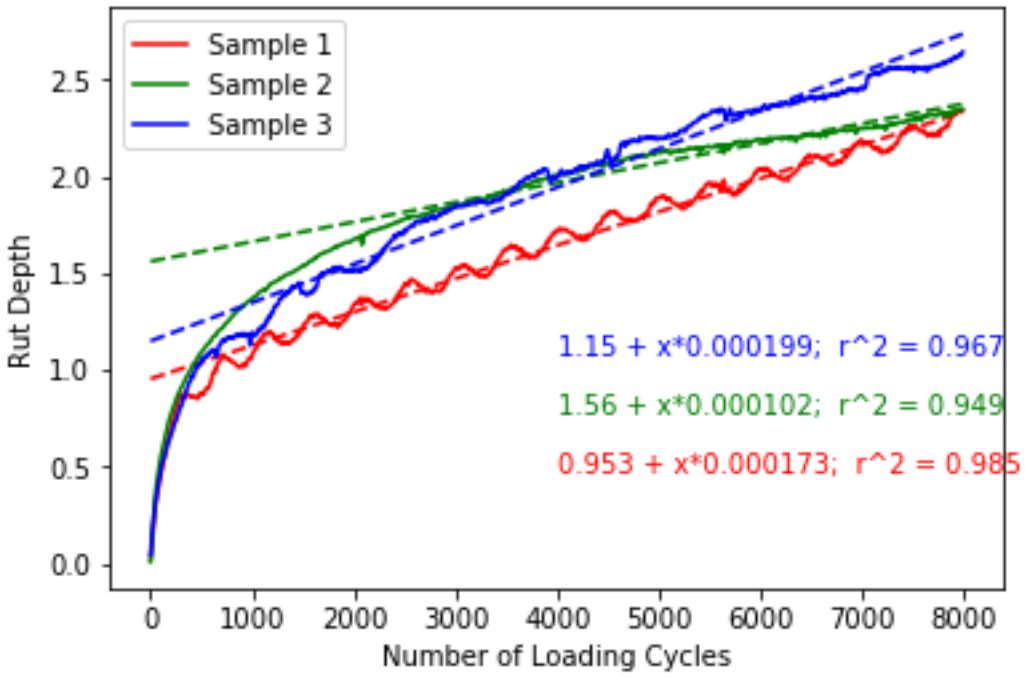
Sample 1
Sample 2
Sample 3
Rut Depth
Number of Loading Cycles
1.15 + x*0.000199; r^2 = 0.967
1.56 + x*0.000102; r^2 = 0.949
0.953 + x*0.000173; r^2 = 0.985

(f)

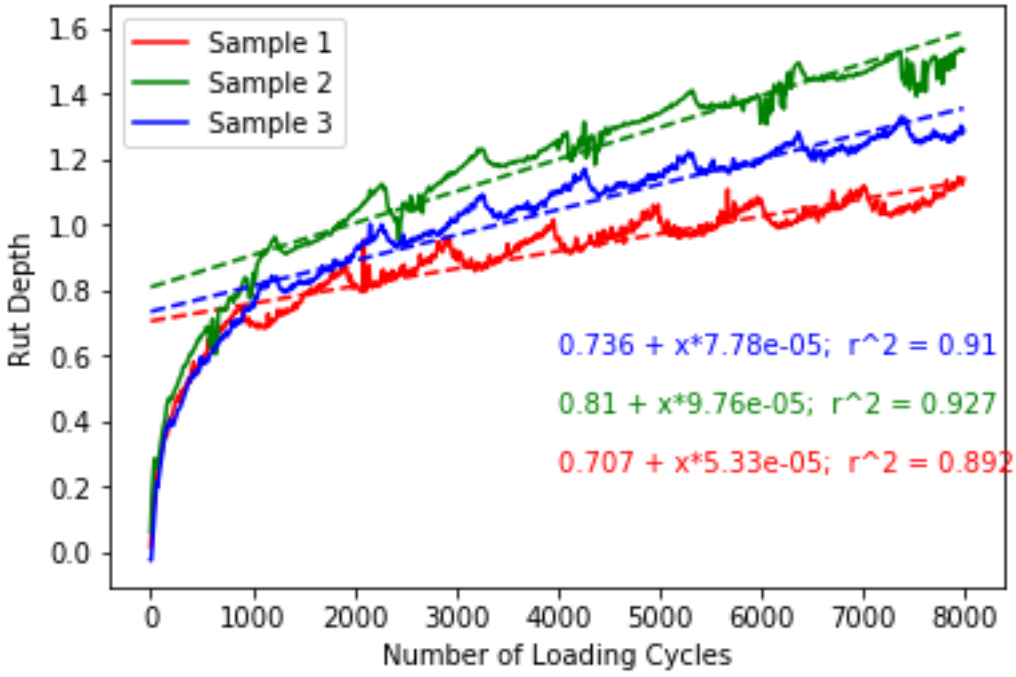

(g)

APA creep slope determination for SMA mixtures. (a) SMA 13-1070; (b) SMA 13-1081; (c) SMA 14-1021; (d) SMA 15-1012; (e) SMA 15-1068; (f) SMA 15-1080; (g) SMA 15-1084.